2022

Nanoplasmonics: properties and applications in photocatalysis, antimicrobials and surface-enhanced Raman spectroscopy

https://hdl.handle.net/2144/45225

BOSTON UNIVERSITY

GRADUATE SCHOOL OF ARTS AND SCIENCES

Dissertation

NANOPLASMONICS: PROPERTIES AND APPLICATIONS IN PHOTOCATALYSIS, ANTIMICROBIALS AND SURFACE-ENHANCED RAMAN SPECTROSCOPY

by

XINGDA AN

B.S., University of Science and Technology of China, 2016

Submitted in partial fulfillment of the

requirements for the degree of

Doctor of Philosophy

2022

Approved by

First Reader ______________________________
Björn M. Reinhard, Dr. rer. nat.
Professor of Chemistry
Professor of Materials Science and Engineering

Second Reader ______________________________
Xi Ling, Ph.D.
Assistant Professor of Chemistry
Assistant Professor of Materials Science and Engineering

DEDICATION

I would like to dedicate this work to my beloved mom, dad and Ning. Their love and support have carried me through the most difficult times in my life. This work would not have been possible without them.

ACKNOWLEDGMENTS

First and foremost, I would like to express my sincere gratitude towards my advisor, Prof. Björn M. Reinhard, for the advice, guidance and help that he provided over the years of my PhD. Joining his research group as a transfer student, I have truly benefited a lot from the patience and understanding both in and outside of the lab. His enthusiasm towards new science and incredible work ethic have and will continue to inspire and motivate me along the path as a scientific researcher.

I would like to extend my thanks to my Dissertation Advisory Committee, Profs. Xi Ling, Shyamsunder Erramilli, David Coker, and John Snyder for their valuable advice and insights; as well as collaborators Prof. Tom Keyes, Dr. David Stelter, Prof. Pinghua Liu, Dr. Nathchar Naowarojna, Dr. Ronghai Cheng, Dr. Mina Nazari, Ramprasath Rajagopal, Prof. John Straub, Ayan Majumder, Dr. James McNeely, Taranee Puri, Taimeng Liang, Zhiliang He, Jayraj Patel, Sara Mason, Prof. Allison Dennis, Dr. Joshua Kays, Dr. Ian Lightcap, Dr. Ranjith Premasiri, Prof. Lawrence Ziegler, Dr. Yimin Huang, Dr. Ying Jiang, Dr. Melissa Cardona et al., without whom many parts of the projects in this dissertation could not have been accomplished. I would also like to thank Profs. Chen Yang and Ji-Xin Cheng for their help in the first years of my PhD, as well as their understanding of my personal choices.

I am very grateful to all of the past and current members of the Reinhard group for their help throughout my PhD. I wish to specially thank Dr. Fangda Xu, Dr. Qianyun Zhang and Han Zang for their help and company as both labmates and friends in and out of the lab. Dr. Behnaz Eshaghi and Dr. Sandy Zhang have had much overlap with me and I have truly benefited from the discussions and experiments with them. Dr. Sarah Lerch, Dr. Ali Khanezar, Dr. Xin Zhao, Dr. Min Xi, Anna Duboff, and Jihad Allami have provided me with help and advice in the earlier years of my PhD; Taejun Han, Leslie Velasco, Erik Schiferle, Zhongkun Zhang, Jialing Yang, Aidan Oi, Tianhong Ouyang, Yuanqing Gu and Yixin Mei have offered help in the last few years of my PhD, for these I am very grateful. I'd also like to thank Boston University (BU) Photonics Center, BU Chemistry, Purdue Chemistry, and additional collaborating shared facilities faculty and staff for their help with my experiments. Anlee Krupp and Dr. Alexey Nikiforov have offered me excellent training and help on electron microscopes among other instruments, which are crucial for my projects. Dr. Norman Lee, Dr. Paul Mak, Serge Zdanovich, Dr. Jeffrey Bacon, Dr. Mounika Vutukuru, Dr. Zhuofa Chen, Dr. Greg Lin, Dr. Thomas Ireland, Dr. Arthur McClelland, Dr. Esther Bullitt among others assisted me on different instrument at BU Chemical Instrumentation Center, BU Photonics Center, BU Department of Earth and Environment, the Center for Nanoscale Systems at Harvard University, and BU medical campus. I'm also thankful to Kaitlin Valli, Marley O'Neil, Cecilia Handy from BU Chemistry; and Marybeth Miller and Candice Kissinger from Purdue Chemistry among many others for help with administrative affairs.

I also wish to thank all medical workers that contributed to the combat of Covid-19, especially those in China, US, and Boston University in particular, without whom our normal lives and my PhD studies could not have been restored.

Last but not least, I would like to sincerely thank my family and friends, whose support carries me through the arduous years of PhD studies. Mom, dad, and Ning have always shown me the strong side and provided me with enormous emotional support, without which I could not have managed to overcome the challenges I faced in the past years. I am also thankful to my amazing friends Jun Cao, Dr. Xinpei Cai, Dr. Xiaofeng Wu, Weijun Luo, Wenjie Zhou, Li Zhang, Linli Shi, Feiyuan Yu, Ziyi Quan, Haoran Lei, Youlin Liu among others for their support and help. And I want to thank myself for not giving up in the most difficult times in the past years, and for gradually becoming stronger in the process into my present-day self.

NANOPLASMONICS: PROPERTIES AND APPLICATIONS IN PHOTOCATALYSIS, ANTIMICROBIALS AND SURFACE-ENHANCED RAMAN SPECTROSCOPY

XINGDA AN

Boston University Graduate School of Arts and Sciences, 2022

Major Professor: Björn M. Reinhard, Professor of Chemistry

ABSTRACT

Localized surface plasmon resonance (LSPR) describes the collective oscillation of conductive electrons in noble metal nanostructures, such as gold, silver and copper; or in selected doped semiconductor nanocrystals. Nanoplasmonics is emerging as a useful and versatile platform that combines the intense and highly tunable optical responses derived from LSPR with the intriguing materials properties at the nanoscale, including high specific surface areas, surface and chemical reactivity, binding affinity, and rigidity. LSPRs in plasmonic nanoparticles (NPs) can provide large optical cross-sections, and can lead to a wide variety of subsequent photophysical responses, such as localization of electric (E-)fields, production of plasmonic hot charge carriers, photothermal heating, etc. Plasmonic NPs can also be combined with other molecular or nanoscale systems into plasmonic heterostructures to further harvest the resonant E-field enhancement or to prolong the lifetime of plasmonic charge carriers.

In this dissertation, we study the photophysical properties of plasmonic Ag and Au NPs, particularly E-field localization and hot charge carrier production performances; and illustrate how they can be optimized towards plasmonic photocatalysis, development of nano-antimicrobials, and surface-enhanced Raman spectroscopy (SERS) sensing. We demonstrate that with a lipid-coated noble metal nanoparticle (L-NP) model, the E-field localization properties could be optimized through positioning molecular photosensitizers or photocatalysts within a plasmonic "sweet spot". This factor renders the plasmonic metal NPs efficient nanoantenna for resonant enhancement of the intramolecular transitions as well as the photocatalytic properties of the molecular photocatalysts. The enhanced photoreactivity have been applied to facilitate fuel cell half reactions for the enhancement of light energy conversion efficiencies; as well as to facilitate the release of broad-band bactericidal compounds that enables plasmonic nano-antimicrobials. Localized E-fields in L-NPs also enhance the inelastic scattering from molecules through SERS. This is utilized to obtain molecular-level information on the configuration of sterol-based, alkyne-containing Raman tags in hybrid lipid membranes, which enables spectroscopic sensing and targeted imaging of biomarker-overexpressing cancer cells at the single-cell level. In contrast to the localized E-field, plasmonic charge carrier generation mechanism relies on non-radiative decay pathways of the excited plasmons that lead to production of ballistic charge carriers. The plasmonic hot charge carriers directly participate in chemical redox processes with degrees of controllability over the nature of the charge carrier produced and direction of their transfers. The implementation and optimization of these mechanisms are explored, and the significances of some relevant applications are discussed.

TABLE OF CONTENTS

LIST OF TABLES

LIST OF FIGURES

LIST OF ABBREVIATIONS

$\cdot OH$	Hydroxyl radicals
$^1O_2$	Singlet oxygen
AB	Antibody
ABDA	9,10-anthracenediylbis(methylene)dimalonic acid
BP	Bipyramid
CA	Chronoamperometry
CB	Conduction band
CFU	Colony-forming unit
CID	Chemical Interface Damping
CPCM	Conductor-like polarizable continuum model
CW	Continuous-wave
DCM	Dichloromethane
DF	Darkfield
DIPEA	N,N-diisopropylethylamine
DLS	Dynamic light scattering
DMAP	4-N,N-dimethylaminopyridine
DMEM	Dulbecco’s Modified Eagle Medium
DMF	dimethylformamide
DMSO	Dimethyl sulfoxide
DOPS	1,2-dioleoyl-sn-glycero-3-phospho-L-serine
DPPC	1,2-dipalmitoyl-sn-glycero-3-phosphocholine

DSPA	1,2-distearoyl-sn-glycero-3-phosphate
E. coli	*Escherichia coli*
E-Field	Electric field
ECM	Extracellular matrix
EDCI	1-ethyl-3-(3-dimethylaminopropyl)-carbodiimide
EDX	Energy-dispersive X-ray spectroscopy
EF	Enhancement factor
EGF	Epidermal Growth Factor
EGFR	Epidermal Growth Factor Receptor
EPC	1,2-dioleoyl-sn-glycero-3-ethylphosphocholine
ESI	Electrospray ionization
FBS	Fetal bovine serum
FCA	Fluorescent click assay
FDTD	Finite-difference time-domain
FL	Fluorescence
FWHM	Full width at half maximum
H&E	Hematoxylin and eosin
HBN	Hydrogen-bonding network
HBSS	Hank’s Balanced Salt Solution
HER	Hydrogen Evolution Reaction
HRMS	High-resolution mass spectrometry
HRTEM	High-resolution transmission electron microscopy

IB	Intermediate band
IC$_{50}$	Half-maximal inhibitory concentration
ICG	Indocyanine Green
ICP-MS	Inductively Coupled Plasma-Mass Spectrometry
ISC	Intersystem Crossing
J_{photo}	Photocurrent density
L-Ag	Lipid-coated Ag nanospheres
L-Ag-NCs	Lipid-Ag nanosphere-nanocrystal photocatalyst control
L-Au-NCs	Lipid-Au nanosphere-nanocrystal photocatalyst control
L-NP	Lipid-coated noble metal nanoparticle
L-NP-Tag-1/2/3	Lipid-coated Ag nanosphere with Tag-1, -2 or -3
L-NP$_{Au}$-Tag-1	Lipid-coated Au nanosphere with Tag-1
L-NR	Lipid-coated Au nanorod
L-NR-NCs	Lipid-Au nanorod-chalcopyrite nanocrystal hybrid plasmonic photocatalyst
LDOS	Local density of electromagnetic states
LDPE	Low-density polyethylene
L$_{DSPA}$-NP-Tag-1	DSPA-containing lipid-coated Ag nanosphere with Tag-1
LDUFC	Light-driven direct urea fuel cell
LED	Light-emitting diode
LEVO	Levofloxacin
LRV	Log reduction value
LSPR	Localized Surface Plasmon Resonance

LSV	Linear Sweep Voltammetry
M_1	Manders’ colocalization coefficient 1
M_2	Manders’ colocalization coefficient 2
MD	Molecular dynamic
MeOH	Methanol
MLCT	Metal-to-Ligand Charge Transfer
MP-AES	Microwave Plasma-Atomic Emission Spectroscopy
MSN	Mesoporous silica nanoparticle
M_W	Molecular weight
NC	Nanocrystal
NHE	Normal hydrogen electrode
NIR	Near-infrared
NMR	Nuclear Magnetic Resonance
NP	Nanoparticle
NR	Nanorod
NS	Nanosphere
$O_2^{\cdot -}$	Superoxide anion
OCP	Open Circuit Potential
OD_{600}	Absorbance optical density at 600 nm
ODT	Octadecanethiol
OER	Oxygen evolution reaction
PBS	Phosphate-buffered saline

PC	Photocatalytic
PDCT	Photodynamic Chemotherapy
PEC	Photoelectrochemical
PEG	Polyethylene glycol
PI	Propidium iodide
PL	Photoluminescence
PLA	Polylactic acid
PLL	poly-L-lysine
PMF	Potential of mean force
PPT	Plasmonic Photothermal
PS	Photosensitizer
PVC	Polyvinyl chloride
QD	Quantum Dot
Qtof	Quadrupole time-of-flight
QY	Quantum Yield
ROS	Reactive oxygen species
RT	Room temperature
SEM	Scanning electron microscopy
SERS	Surface Enhanced Raman Spectroscopy
SR	Sacrificial reductant
TBTU	2-(1H-benzotriazole-1-yl)-1,1,3,3-tetramethylaminium tetrafluoroborate
TEM	Transmission electron microscopy

TLC	Thin-layer chromatography
TPrA	Tripropylamine
UOR	Urea oxidation reaction
UV	Ultraviolet
UV-vis	Ultraviolet-visible
VB	Valence band
XPS	X-Ray Photoelectron Spectroscopy
XRD	X-Ray Diffraction Spectroscopy

Chapter 1. INTRODUCTION

Nanomaterials have emerged as a useful and promising materials platform in the recent decade both for studies of fundamental materials physical and chemical properties that are absent at the macroscale, and to enable various functionalities and fields of applications. Due to the nanoscale size typically confined to 1 - 100 nm at one or multiple dimensions, nanomaterials typically possess extremely large specific surface areas. This is beneficial for increasing the effectiveness and efficiency of processes happening at the interfaces of the nanostructures with aqueous medium, molecular adsorbates, and/or biological cells. This have enabled a series of applications of the nanomaterials, for instance, as nano-catalysts,[1-4] nano-reactors,[5-7] nano-carriers,[8-9] nano-devices for energy harvesting and storage,[10-11] and nano-medicines.[12-14] Through effective modulation approaches such as structural,[3-4] phase,[15] and defect engineering;[4, 16] surface functionalization[17-18] and etc., the specific composition, structure, hydrophilicity, binding affinity, size and shape of nanostructures could be feasibly tuned, which, in turn, allows them to display a wide variety of chemical,[2-3] electrical,[16, 19] mechanical,[20-21] dielectric,[22-23] and optical[24-27] properties that can be customized towards distinct applications.

Plasmonic nanoparticles (NPs) are an intriguing category of nanomaterials that sustain the localized surface plasmon resonance (LSPR) effect, which describes the coherent collective oscillation of conduction electrons upon resonant electromagnetic excitation within the close vicinity of the NPs.[2, 22, 28] LSPR is typically observed in noble metal NPs, such as gold (Au),[2] silver (Ag),[29] and copper (Cu);[30] and in selected doped semiconductor nanocrystals (NCs) or quantum dots (QDs).[31-33] LSPR can give rise to intense optical responses, manifested by high optical scattering and absorption cross-sections of plasmonic NPs;[22, 25, 34] as well as a series of radiative and non-radiative photophysical properties, such as the localization of plasmonic electric (E-)field,[29, 35-36] production of hot charge carriers,[1, 37] and plasmonic photothermal heating.[13, 38-39] Under femtosecond pulsed laser irradiation, plasmonic NPs have also been shown to sustain additional photonic response, such as shockwave formation.[40-43] Therefore, plasmonic NPs combine the diverse and intense light response with the favorable materials properties at the nanoscale, and presents a unique platform to enable a series of applications.

Plasmonic metals have been extensively utilized by humans since ancient times, such as on the classic Lycurgus cup,[44] whose color change based on the absorption and scattering properties of the Au and Ag NP coating on the surface. Another example is the use of silver kitchenware through the ages for their antimicrobial properties, and for wound healing properties dating back to Hippocrates as early as 400 B.C.[45] In more recent studies, plasmonic NPs have been utilized in plasmonic photocatalysis to either provide enhancement of molecular or nanoscale photocatalyst through resonant energy transfer pathways,[29, 46-49] or to directly participate in chemical redox reactions with photo-generated hot charge carriers;[1, 37] as plasmonic nano-antimicrobials that entail broad-band and multi-modal microbicidal effect;[41, 50-53] to enable or assist in delivery and release processes;[54-55] and to provide chemical sensing and high-contrast bioimaging modalities for diagnostic applications;[56-58] and to enable studies of the physiological mechanisms in biology, such as the distribution of surface molecular biomarkers,[58-59] NP-induced endocytotic or apoptotic pathways,[18, 60] and immune response.[17, 61-62] Plasmonic NPs can also be combined with other molecular or nanoscale systems to form various types of nanocomposites or heterostructures. For instance, Schottky heterostructures between plasmonic metals and semiconductors, or plasmonic heterostructures comprising of multiple plasmonic building blocks have been designed to harvest the resonant E-field enhancement or to prolong the lifetime of charge carriers.[63-65]

Nanoplasmonics concern the study of the physicochemical properties and applications of plasmonic NPs and the LSPR. Two particularly interesting photophysical properties of nanoplasmonics, E-field enhancement and plasmonic charge carrier, forms the basis of this dissertation. Intense E-field localization properties render plasmonic NPs efficient nanoantenna for enhancement of important intramolecular transition processes, such as the excitation of metal-to-ligand charge transfers (MLCT) in molecular dyes or the interband transition in semiconductors.[29, 35, 66] This enhancement can be harvested for improved redox catalytic properties,[29, 35, 46, 48-50, 67] which can contribute to the design of light-driven fuel cells and to efficient energy harvesting and conversion purposes. Besides, the field enhancement can also augment molecular microscopy or spectroscopy,[58, 68-71] such as through surface-enhanced Raman spectroscopy (SERS).[56, 72-75] Plasmon-enhanced microscopy and spectroscopy have been shown to provide reliable imaging and sensing modality for biomolecules,[76-77] bacteria[71, 73-74] as well as cells.[56, 72] On the other hand, plasmonic hot charge carrier production also possesses great promise in modulating the specific redox process in a wavelength-dependent manner,[78] which finds applications in catalysis,[79] energy conversion,[36, 80] and for photocatalytic microbial inactivation.[81-83]

Despite extensive studies and great achievements with plasmonic NPs, important questions and challenges still exist. For one, efficient harvesting of the plasmonic field-enhancement requires careful placement of the photocatalyst at certain distances to the metal surface in order to attain efficient balancing of the tradeoff between (a) the plasmonic E-field enhancement of molecular excitation, and (b) the quenching of the excited state population through metal-associated non-radiative decay pathways.[29, 84-85] This could be challenging as intricate fabrication and synthesis approaches might be required to fulfill the precise distance dependency. Additionally, achieving a spatial and temporal control of the nature and direction of the charge transfer processes induced by plasmonic hot charge carriers is beneficial to increase the selectivity and efficiency of the reactions, but can also be challenging. In this chapter, we outline the aforementioned properties of nanoplasmonics as well as introduce potential grounds of application of plasmonic NPs and plasmonic NPs-based nanocomposites.

1.1 LSPR and Nanoplasmonics

A number of optical properties as well as photophysical responses are enabled by LSPR in nanoplasmonics. One of the most fundamental properties that describes the response of plasmonic NPs upon incident irradiation is their polarizability (α). Polarizability is an intrinsic property of NPs, and is determined by their shape, size, and dielectric function (ε). The dielectric function of an NP can be approximated by the Drude model according to **Eq. (1.1)**:[28, 86]

$$\varepsilon_{Drude} = 1 - \frac{\omega_p^2}{\omega^2 + i\gamma\omega} \qquad \textbf{Eq. (1.1)}$$

where ω is the angular frequency of the excitation light, and γ is the frequency of electron collisions in the bulk of the material. ω_p is the bulk plasma frequency and is, in turn, determined by intrinsic properties of the material including the density of free electrons (n), permittivity of free space (ε_0), electron unit charge (e) and effective mass (m_e) according to **Eq. (1.2)**:[22, 33]

$$\omega_p = \sqrt{\frac{ne^2}{\varepsilon_0 m_e}} \qquad \textbf{Eq. (1.2)}$$

Together with the dielectric function of the surrounding medium (ε_m) and the incident electric field ($\boldsymbol{E_0}$), polarizability determines the polarization vector ($\boldsymbol{P}$) as **Eq. (1.3)**:

$$\boldsymbol{P} = \varepsilon_0 \varepsilon_m \alpha \boldsymbol{E}_0 \qquad \textbf{Eq. (1.3)}$$

For a spherical NP, when the particle diameter is much smaller than the incident wavelength (λ), its plasmon resonance can be approximated as a first-order dipolar resonance, and denoted by the Clausius-Mossotti relation as **Eq. (1.4)**:[28, 86-87]

$$\alpha = 4\pi R^3 \frac{\varepsilon - \varepsilon_m}{\varepsilon + 2\varepsilon_m} \qquad \textbf{Eq. (1.4)}$$

where R is the radius of the NP. When the real part of the dielectric function of the NP equals to -2ε_m, the polarizability reaches a pole, indicative of an extremely intense light response by the plasmonic NPs. This is known as the Fröhlich resonance condition,[28] which is a fundamental prerequisite for the occurrence of LSPR. Plasmonic Au, Ag and Cu NPs are observed to meet the Fröhlich resonance condition is the visible range of the electromagnetic spectrum.[88-89] Some doped semiconductor nanocrystals (NCs) also meet this requirement within some wavelength ranges, for instance, chalcopyrite $CuFeS_2$ NCs

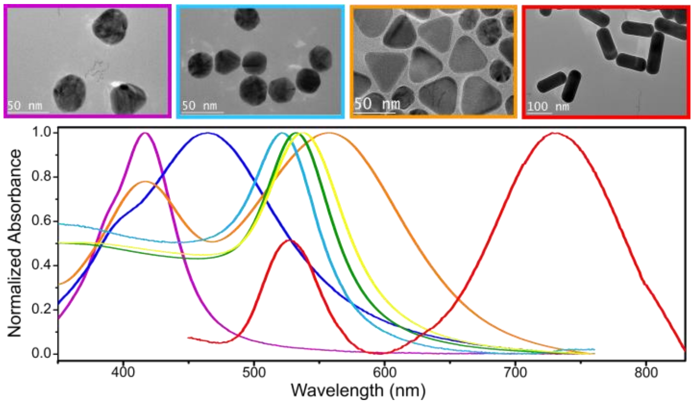

Figure 1.1 TEM Micrographs (top) and Absorbance Spectra (bottom) of Different Plasmonic Nanostructures. Color code: 40 nm (purple) and 80 nm (blue) Ag nanospheres; 40 nm (cyan), 60 nm (green) and 80 nm (yellow) Au nanospheres; Ag nanoplates (orange); and Au nanorods (red). Reproduced with permission from Ref. 109, Copyright (2021) by The Royal Society of Chemistry.

around 490 nm.[90-92] They have, thus, been considered to also sustain a quasistatic coherent resonance, although the light response in the semiconductors would typically be less intense than in plasmonic metal NPs due to a lower concentration of free charge carriers.[33]

The polarizability, as well as additional optical properties of plasmonic NPs, including the plasmon resonance wavelengths and optical cross-sections, can be feasibly modulated by altering the size, shape, and composition of the material (**Fig. 1.1**).[24-26, 93] For instance, the Clausius-Mossotti relation for a spherical NP in **Eq. (1.4)** can be generalized to **Eq. (1.5)** for non-spherical NPs:

$$\alpha = (1+\kappa)V\,\frac{\varepsilon-\varepsilon_m}{\varepsilon+\kappa\varepsilon_m} \qquad \textbf{Eq. (1.5)}$$

where V is the volume of the NP, and κ is an added term for shape factor.[94] For spherical NP, $\kappa = 2$. From the polarizability, the optical scattering, absorption, and extinction cross-sections (σ_{sca}, σ_{abs}, σ_{ext}) can be determined respectively according to **Eq. (1.6) - Eq. (1.8)**.[87]

$$\sigma_{abs} = k\, Im(\alpha) - \frac{k^4}{6\pi}|\alpha|^2 \qquad \textbf{Eq. (1.6)}$$

$$\sigma_{scat} = \frac{k^4}{6\pi}|\alpha|^2 \qquad \textbf{Eq. (1.7)}$$

$$\sigma_{ext} = k\, Im(\alpha) \qquad \textbf{Eq. (1.8)}$$

where $k = \frac{2\pi}{\lambda}$. Furthermore, plasmon resonance frequency can also be modulated by altering the shape of the NP. For instance, two plasmon resonance modes exist for Au nanorods (NRs), a vertical and one longitudinal resonance mode, as opposed to the one plasmon resonance frequency for isotropic spherical Au NPs.[24, 78] In addition, plasmon resonance frequency can also be modulated through different aspect ratios and pointedness in Au nanobipyramids. Our group has demonstrated that epitaxial deposition of Ag onto Au bipyramids (BPs) is able to achieve shifting of the plasmon resonance frequency of the BPs either towards larger or smaller frequencies by means of altering the tip width and/or length of the BPs.[41, 95]

Another factor that can affect the absorption and scattering properties of plasmonic NPs as well as the ratio between absorption and scattering is the size of the NPs.[25, 96] Analyses on the size-dependence of the optical cross-sections of plasmonic NPs have been performed in multiple works. It has been shown that LSPR decay is dominated by radiative decay processes for large NP sizes, but that plasmon decay by dissipation dominates for NPs with smaller diameters.[87, 96] As a specific example, Baffou and Quidant demonstrated that for spherical Au NPs with d < 90 nm, the peak absorption cross-section is larger than the peak scattering cross-section, whereas for larger NPs (d > 90 nm) the peak scattering cross-section is larger than the peak absorption cross-section.[87]

The composition of the plasmonic NPs can also have a strong effect on the plasmon frequency.[24] Together with the size and shape factors, they provide desirable room for modulation of the properties of plasmonic NPs and adapting them towards various applications. For instance, the LSPR bands of spherical Al and Ag NPs lie in the ultraviolet (UV) or the high-energy regime of the visible range,[29, 97] thus, these NPs possess great potential to enhance intramolecular excitation processes, which typically requires higher energy levels that overlaps with the absorbance bands of Al and Ag NPs. In contrast, the LSPR bands of Au nanostructures, such as the longitudinal mode of Au NRs, can be tuned to occur in the near-infrared (NIR) region.[24, 27, 78, 98] As NIR irradiation typically possess larger tissue penetration depth,[99] these materials are favorable platforms for tissue engineering applications or applications of plasmonic nano-antimicrobials in medium or *in vivo*.[40, 100] Due to the large absorption cross-section of Au NRs in the NIR as well as the absorption of surrounding medium, the NIR-responsive plasmonic NPs could also serve as favorable photothermal transducers for heating.[34, 101] Additional structural properties of plasmonic NPs have also proven extremely useful. Plasmonic nanomaterials with high surface areas, for example, have been exploited for surface chemistry and physics-based applications as well as to aid the formation of heterostructures.[102-104]

1.2 Associated Photophysical Properties Nanoplasmonics

The localized surface plasmon resonance grants the plasmonic NPs with a series of intriguing photophysical responses derived from the radiative or non-radiative decay pathways of the excited plasmons. One of the signature properties of plasmonic nanoantenna is E-field localization, which takes place around individual plasmonic NPs, and can be further augmented in plasmonic hot spots formed by dimers of NPs (**Fig. 1.2A, B**).[22, 105-106] The E-field is produced within the vicinity of plasmonic NPs, and possesses very high intensities at short separations from the metal surface, but decays rapidly as the distance to the metal surface increases.[107-108] Plasmonic E-field have been harvested to promote the photoexcitation of fluorophores and the reactivity of photocatalysts or photosensitizers (PSs).[29, 46] Fundamentally, these processes rely on the energy transfer from the excited plasmon to the molecular adsorbates.[49]

In the case of quantum emitter molecules, another factor that accounts for enhancement of the spontaneous decay of their excited states and radiative emission is the increase in local density of electromagnetic states (LDOS) by the presence of plasmonic NPs. According to Fermi's golden rule, the spontaneous decay rate can be estimated based on the LDOS (ρ), the transition frequency (ω), the vectorial transition dipole moment ($\boldsymbol{p}$), and the location of the molecule ($\boldsymbol{r_m}$) by **Eq. 1.9**:[85]

$$\gamma = \frac{2\omega}{3\hbar\varepsilon_0}|\boldsymbol{p}|^2\rho(\boldsymbol{r_m},\omega) \qquad \textbf{Eq. (1.9)}$$

Consequently, it is a combination of both E-field enhancement of the photoexcitation of molecular fluorophores, and increased photoluminescence

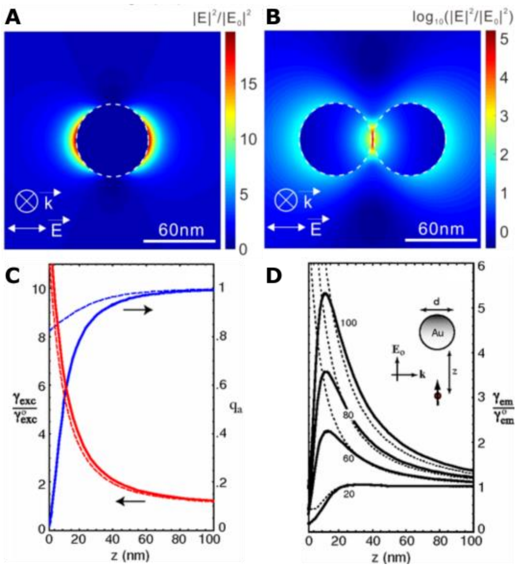

Figure 1.2 Plasmonic E-Field Generation and Enhancement of Molecular Excitation and Emissions. (A, B) Calculated E-field intensity maps for a 60 nm Au NP monomer (A) and dimer (B); reprinted with permission from Ref. 22. Copyright (2019) by IOP Publishing. (C, D) Calculated quantum yield q_a, excitation rate γ_{exc} and fluorescence emission rate γ_{em} normalized with free-space values as a function of fluorophore-metal separation for 80 nm Au NPs (C) and Au NPs with various diameters (D); Solid curves: MMP calculations, dashed curves: dipole approximation; Reprinted with permission from Ref. 85. Copyright (2006) by American Physical Society. https://doi.org/10.1103/PhysRevLett.96.113002.

emission rates from the increased LDOS that defines the overall nanoplasmonic enhancement effect.

Importantly, a tradeoff exists for field-enhancement of dye or PS molecules within the vicinity of plasmonic NPs based on the E-field-induced resonant energy transfer: while high field intensity is present at shorter distances to the metal surfaces for strong field enhancement, there is also more likely to be a higher extent of metal-associated quenching of the photoexcited states.[29, 84-85, 109] For a quantum emitter, the distance-dependent enhancement *versus* quenching of the photo-excited state has been characterized by both calculations and experimental studies. **Fig. 1.2C** contains plots of the excitation rate enhancement and quantum yield for a single dye molecule in the vicinity of an 80 nm Au NP as function of separation.[85] As the distance to the metal surfaces increase, both the quenching efficiency (indicated by the increase in quantum yield) and the E-field mediated excitation rate enhancement decrease. As the former decreases more rapidly than the latter, an optimal separation behavior that balances the two photophysical processes exists for fluorescence emission rate enhancement (**Fig. 1.2D**). Similar distance dependence of the enhancement *versus* quenching effects have also been found with molecular photosensitizers or photocatalysts as discussed in detail in section **1.3**, where a more precise work range of 2-10 nm have been determined.[29, 50-51, 108]

Another important photophysical response of plasmonic NPs with resonant irradiation is the production of charge carriers, namely, electrons (e^-) and holes ($h^{\cdot}$). Plasmonic charge transfers can occur through either indirect or direct mechanisms (**Fig. 1.3**).[1, 37, 109] In indirect plasmonic charge transfer pathways, kinetically excited "hot" charge carriers are produced in the non-radiative decay of excited plasmons through Landau damping, and the charge carriers produced in this process can be thermalized and have an energy distribution that resembles a Fermi-Dirac distribution at a much higher temperature.[110-111] These charge carriers are thus referred to as "hot" electrons and holes. The elevation in the carrier energy levels can consequently facilitate them to overcome the work function and interfacial energy barriers and transfer into higher-lying unoccupied molecular orbitals or acceptor bands of semiconductors that are within the vicinity with the NP, resulting in a charge separation and prolonged lifetimes of the generated e^- and $h^{\cdot}$.[64-65] Generation of kinetically excited charge carriers for indirect transfer processes is, in

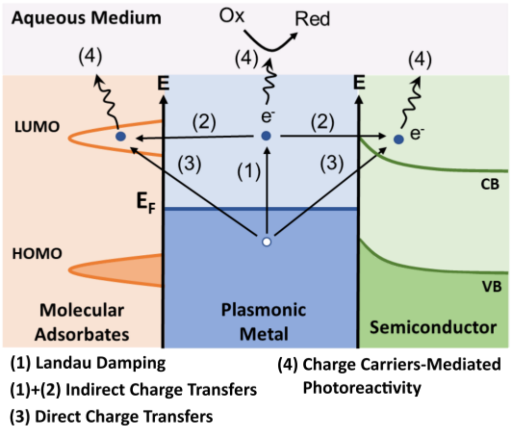

Figure 1.3 Mechanisms of Plasmonic Charge Carrier Production. Reproduced with permission from Ref. 109, Copyright (2021) by The Royal Society of Chemistry.

general, favored by smaller plasmonic NPs with diameters (d) < 20 nm,[112] partly due to the less loss of kinetic energy during diffusion.

The other notable plasmonic charge transfer mechanism is the direct transfer pathway, in which electrons directly hop into a higher lying adsorbate molecular levels or semiconductor acceptor bands possessing matching energy levels without the prior generation of an excited electron energy distribution in the metal. If the direct electron transfer results in the population of vacant adsorbate molecular levels, it is referred to as Chemical Interface Damping (CID).[37, 113] Plasmonic charge transfers in Au or Ag nanostructures have been characterized with both experimental spectroscopy and simulations,[36, 79, 113-114] and are frequently exploited for photocatalytic applications.[1-2] Intriguingly, some plasmonic semiconductors, such as chalcopyrite $CuFeS_2$ nanocrystals, which possess a coherent resonance within the visible range, have also been shown to sustain hot charge carrier production through ultrafast spectroscopic studies.[90]

Plasmonic photothermal heating is another signature property of nanoplasmonics induced by the dissipation of photon energy to the interface between the NPs and the surrounding media. The mechanism and efficiency of plasmonic photothermal heating have been extensively monitored and modelled through both experimental measurements and calculations.[34, 38-39, 87] In the case of continuous-wave (CW) excitation, the temperature increase around an individual NP can be estimated based on its absorption cross-section (σ_{abs}), incident irradiance (I), the surrounding medium's thermal conductivity (κ_s), and the equivalent NP radius (R_{eq}) as:

$$\Delta T = \frac{Q}{\beta 4\pi \kappa_s R_{eq}} = \frac{\sigma_{abs} I}{\beta 4\pi \kappa_s R_{eq}} \qquad \textbf{Eq. (1.10)}$$

where Q is the absorbed light power given by the product of σ_{abs} and I; and β is a geometrical correction factor.[87] For spherical NPs, $\beta = 1$ and $R_{eq} = R$. According to **Eq. 1.10**, smaller NPs with large absorption cross-sections are potentially more efficient plasmonic photothermal transducers. In the case of resonant pulsed irradiation of the LSPR in plasmonic NPs, the thermalization occurs in a few consecutive steps.[39, 87] Firstly, the initial irradiation pulse renders the electron gas in a non-equilibrium state, which then could thermalize into a Fermi-Dirac distribution within ~500 fs; subsequently, the phonons in the metal can interact with the thermalized electrons within a time scale of 1-3 ps accompanied by the relaxation of the hot electrons; lastly, a heat diffusion step transfers the energy from the metal into the surrounding medium. The steps can be considered to happen successively when the pulse is short (< 0.1 ns), and/or the NP is small (d < 100 nm). The maximal temperature increase of the NP with pulsed illumination can be estimated based on **Eq. 1.11**:[87]

$$\Delta T = \frac{\sigma_{abs} F}{V \rho_m c} \qquad \textbf{Eq. (1.11)}$$

where F is the fluence of the laser pulse; V, ρ_m and c are the volume, mass density and specific heat capacity of the NP, respectively.

In addition to the light-induced responses described above for nanoplasmonics, when located in an aqueous medium, plasmonic NPs can also sustain additional hydrodynamic responses, such as nanocavitation and nanocavitation-mediated shockwave generation.[40, 115] Nanocavitation can be induced in the dielectric medium by tightly focused pulsed irradiation through photoionization of the medium at the focal spot;[116] and the presence of plasmonic NPs have been shown to greatly augment this process and reduce the fluence required to induce the nanocavitation, due to their capability of focusing the irradiation into nanoscale volumes with intense E-fields.[40-41] The photoionization and subsequent recombination of the formed plasma can trigger a shockwave and initiate cavitation-induced bubble nucleation, which would then expand and collapse. In addition, the photothermal heating in the medium, particularly in the presence of plasmonic NPs, is likely to provide another pathway for the bubble formation, namely the thermal-induced mechanisms.[43, 117] In this case, the heat generated by an irradiated NP results in an evaporation of the surrounding medium. The preference of the E-field-enhanced and the photothermal mechanisms and the efficiency of these processes can be controlled by choice of irradiation wavelengths and fluence of the incident laser, as well as by using plasmonic NPs with distinct absorption, E-field localization, and thermal emission properties.[42, 118]

1.3 Plasmonic Photocatalysis

Plasmonic photocatalysis is one important application of nanoplasmonics that utilizes the plasmonic resonance effects to harvest light and to facilitate energy conversion and chemical transformations. As the plasmon resonance frequency of plasmonic NPs can be feasibly tuned in the visible range,[24-25, 28] plasmonic photocatalysts can often exploit sunlight, which is the most abundant energy source on earth. Plasmonic photocatalysis can occur through different mechanisms, of which i.) E-field enhancement of molecular or nanoscale photocatalysts, ii.) hot charge transfer-induced reactivity, and iii.) plasmonic photothermal catalysis are the most widely exploited.

As is outlined in section **1.2**, plasmonic NPs are capable of localizing a strong, evanescent E-field within the close vicinity of the metal surfaces that decreases in intensity as the distance to the metal surface increase in the case of a single NP, or as the interparticle distance increase in the case of dimers (**Fig. 1.4A**).[22, 108] Thus, plasmonic NPs can be utilized as nanoantennas for E-field-mediated resonant energy transfer to boost the excitation of photocatalysts located in the immediate vicinity of the NPs. As discussed in **Fig. 1.2C, D**, the tradeoff between the field enhancement of the molecular excitation and metal-associated quenching of the photoexcited states determines a strong distance-dependence for the overall enhancement effect of quantum emitters.[85] Similar distance-related arguments have also been made for photosensitizers and molecular or

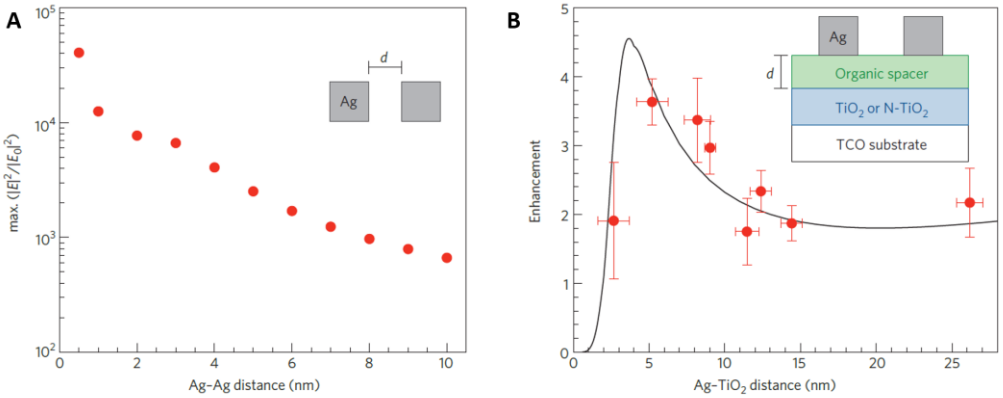

Figure 1.4 E-Field Enhancement Mechanism in Plasmonic Metal-Semiconductor Composite Photocatalysts. Reproduced with permission from reference 108, Copyright (2011) by Springer Nature. (A) Maximum enhancement in the E-field intensity (E^2) as a function of distance between two Ag NPs calculated from finite-difference time-domain (FDTD) simulations. (B) Photocurrent enhancement measured by oxygen evolution rate as a function of distance between the Ag and TiO_2 building blocks, distance controlled by varying the thickness of an organic spacer layer.

nanoscale photocatalysts around plasmonic NPs, where a plasmonic enhancement “sweet spot” is seen, in general, between 2 - 10 nm to the metal surface for both optimized enhancement and limited quenching.[29, 46, 50, 108] Very strong quenching of the photoexcited states through non-radiative decay associated with the metal surfaces exists at separations < 2 nm; whereas the plasmonic E-field intensity is too low to sustain significant enhancement of the photoexcitation of the molecular transition processes at larger distances than 10 nm. Consequently, a crucial factor to efficiently harvest the plasmonic E-field enhancement for photocatalytic reactivity is to place the photocatalyst within these plasmonic “sweet spots” around the metal NPs. Prior examples have utilized strategies including core-shell structures,[50-51] covalent or electrostatic linkers,[46, 119] insulating polymer layers (**Fig. 1.4B**)[108] among other approaches to achieve the precise localization of the photocatalyst within the "sweet spot" distances. Despite their efficacy, a feasible one-pot approach without the need of any complicated fabrication techniques that spontaneously and reliably localizes the photocatalyst around plasmonic metal NPs is still pending.

The second major mechanism of plasmonic photocatalysis involves plasmonic charge transfer processes of the plasmonic component, and plasmonic charge carrier-induced redox catalysis. Under this mechanism, the dephasing of plasmons can be coupled to the direct or indirect charge transfer mechanisms. For Au and Ag NPs, plasmonic hot charge carrier generation and injection have been characterized through *ab initio* calculations as well as ultrafast spectroscopy.[36, 79, 113-114] The size, composition and morphology of the NPs, photoexcitation conditions, and the energetic alignment of excited charge carriers with acceptor levels in adsorbates are all potential determining factors for the likelihood and efficiency of the production and transfer of plasmonic charge carriers and the charge carrier energy.[120-122] In addition, the lifetimes of the excited plasmonic charge carriers also, on a large scale, determine the feasibility of the catalyzed reactions. A relaxation time (τ) of the charge carriers on the order of 1 ps has been reported for Au NPs with diameters < 5 nm, while the lifetimes may become even shorter as the size of the NPs increase.[112, 123]

Charge separation mechanisms that prevent rapid recombination and increase the lifetimes of reactive charge carriers have been exploited, for example, through construction of hybrid plasmonic structures, such as Schottky heterostructures comprising both noble metal NPs and semiconductor components. Due to the spatial separation of the charge carrier pairs in the heterostructures, the reactive charge carriers can then exist long enough to induce

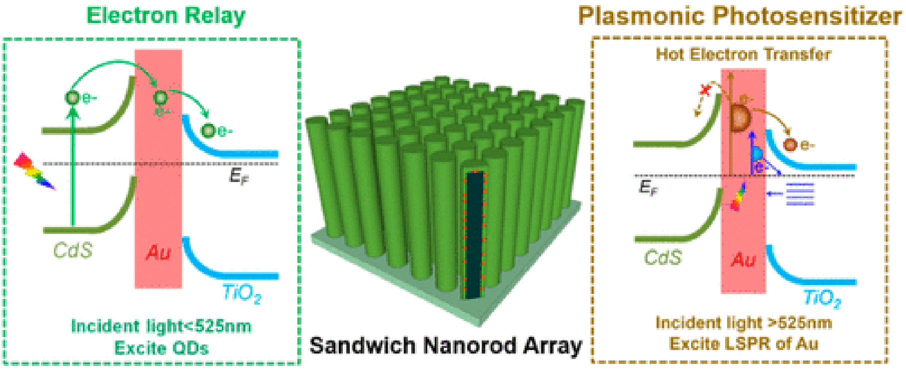

Figure 1.5 Charge Transfer Pathways in a CdS-Au-TiO_2 Sandwich Composite Photocatalyst. Reproduced with permission from Ref. 63, Copyright (2014) by American Chemical Society.

chemical reactions. For instance, lifetimes of excited electrons produced in Au/mesocrystalline TiO_2 nanocomposite have been measured to be around 10 ns.[64] In some cases, vacancies in the crystal lattices of the heterostructures could also trap the photo-generated electrons to further increase τ to up to a few minutes.[65] Semiconductor nanocrystals, including oxides and other chalcogenides,[63-64, 79] perovskites,[124-125] carbon-based QDs[126] among others,[114] have been exploited to assemble functional plasmonic hybrid materials.

Through selective excitation of the plasmonic and/or the semiconductor component in the heterostructure, it is also likely to achieve broad-band charge carrier generation in these composite photocatalysts. For instance, Wu and coworkers designed a CdS-Au-TiO_2 composite sandwich nanocatalyst arrays (**Fig. 1.5**).[63] Under excitation wavelengths shorter than 525 nm, interband transition in the CdS quantum dots (QDs) can be excited, and the conduction band electrons can be then relayed by Au into the TiO_2 for charge separation and catalysis; whereas with lower-energy irradiation than 525 nm and excitation of Au

LSPR, the plasmonic charge carrier production in Au can be induced. The authors thus achieve the broad band production of conduction electrons on the semiconductor shells for solar energy harvesting devices.[63] Schottky heterostructures have proven successful in enabling clean energy conversion and photovoltaic cells,[63, 127-129] optoelectronic devices,[130] catalysis of the synthesis of organic molecules,[131-132] and additional environmental remediation strategies.[64, 125] Moreover, as interesting new functionalities can be expected for semiconductor nanocrystals that by themselves sustain collective resonances, hybrid plasmonic heterostructures that contain multiple plasmonic components also presents a promising strategy to modulate the production and the nature of charge carriers.[78] In such hybrid plasmonic heterostructures, it is foreseeable that a wavelength-controlled plasmonic charge carrier production can be exerted, where different excitation wavelengths could respectively excite distinct building blocks of the heterostructure and could lead to the accumulation of electrons or holes at the interface with the aqueous medium to facilitate different types of redox processes.[78]

In addition to the field-enhancement and plasmonic hot charge carrier mechanisms discussed above, the plasmonic photothermal heating represents another commonly used strategy to enhance chemical reaction rates. The plasmonic photothermal effect could, in some cases, directly accelerate the kinetics of the catalyzed reactions. Plasmonic nanostructures based on Ag,[133] Cu, [134-135] Al[136] and Pd[137] have been utilized as photothermal transducers in promoting photocatalysis through nanoplasmonics-induced heating. Additionally, plasmonic photothermal heating could also promote catalysis through mechanisms that synergistically overlap with the catalytic pathways discussed above,[138-139] such as the field enhancement[136] or the hot charge carrier production[133, 137] pathways. As an example of the latter, Zou *et al.* discovered that with a Pd-CeO_2 hybrid catalyst, charge carriers can be generated in the plasmonic Pd nanostructure, which can then transfer into ceria to lower the catalytic reaction temperature for LSPR-assisted photothermal catalysis of toluene and carbon monoxide oxidation reactions.[137]

1.4 Plasmonic Nano-Antimicrobials

Microbial infections of mammals and colonization on materials surface can both pose serious threats to human health and well-being. The rapid development of microbial resistances against conventional antimicrobials[12, 45] necessitates the development of novel strategies not only for microbial inactivation in mammal hosts, but also to implement active and/or passive antimicrobial properties in water, food, or on materials surfaces. Plasmonic NPs can induce a series of light-dependent or -independent microbial inactivation pathways (**Fig. 1.6**) that are broad-band and efficient against a wide variety of microbial pathogens including bacteria, viruses and fungi, and are thus a promising new category of nano-antimicrobials for combatting microbicidal resistance.[109] For bacterial and fungal pathogens, the inactivation properties discussed in this section is generally characterized through plating and counting the log reduction values (LRVs) of the concentration of colony-forming units (CFUs) of the treatment group (C_t) compared to that of a no-treatment control (C_0) according to **Eq. 1.12**:

$$LRV = log_{10}\left(\frac{C_0}{C_t}\right) \qquad \textbf{Eq. (1.12)}$$

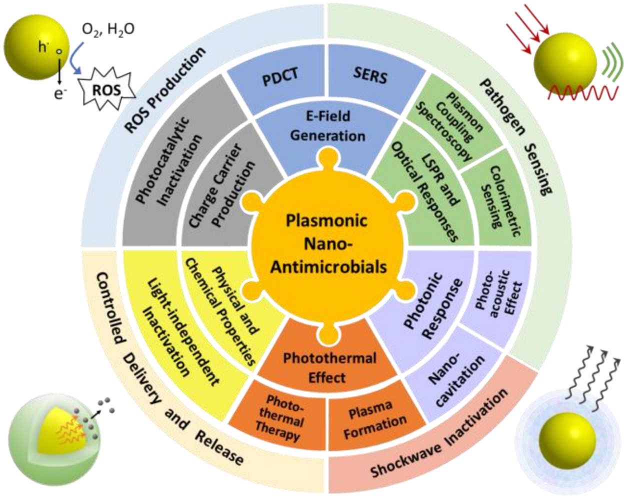

Figure 1.6 Properties and Inactivation Mechanisms of Plasmonic Nano-Antimicrobials. Reproduced with permission from Ref. 109, Copyright (2021) by The Royal Society of Chemistry.

Similarly, viral inactivation can be quantified in LRVs by comparing the reduction in viral load of a treated group (C_t) relative to that of a non-treatment group (C_0) from the same equation.[109] Additional evidence of microbial inactivation by plasmonic nano antimicrobials have also been made through optical and electron microscopy.[52, 140]

The optical, catalytic, photothermal and photonic properties of plasmonic nanostructures outlined in the previous sections form the basis for multiple light-induced plasmonic microbe inactivation pathways. Four major light-dependent inactivation pathways have been proposed for plasmonic nano-antimicrobials, namely, photodynamic chemotherapy (PDCT), photocatalytic (PC) inactivation, plasmonic photothermal (PPT) inactivation, or plasmonic shockwave-based photonic inactivation.[12, 109] PDCT and PC inactivation mechanisms are based on photocatalytic properties of nanoplasmonics outlined in section **1.3**. PDCT harvests the intense plasmonic E-fields for resonant enhancement of the excitation of PSs, such as tris(bipyridine) Ruthenium(II) ($[Ru(bpy)_3]^{2+}$),[52-53] Rose Bengal,[50-51] toluidine blue O,[141] hematoporphyrin,[142] among others; whereas PC inactivation pathways are achieved through plasmonic charge carriers-induced catalytic properties, either with plasmonic NPs only[143-144] or with heterostructures containing both plasmonic and semiconductor components, such as Ag/TiO_2,[81-82] Au/TiO_2,[64-65] or Ag/ZnO.[83] In both cases, strong enhancement over the microbicidal effect of the individual metal, and the photosensitizer and/or the semiconductor components have been measured. Liga *et al.* reported a remarkable 6 - 7 orders of magnitude reduction in the population of bacteriophage MS2 irradiated in the presence of Ag/TiO_2 hybrid structures within 2 min, which represents an almost 5 orders of magnitude improvement in inactivation efficacy of TiO_2 nanostructures alone.[82] Although having fundamentally different reaction pathways, the PDCT and PC mechanisms resemble each other in that they both involve plasmon-enhanced photo-reactivity, and that they could both lead to the production of reactive oxygen species (ROS) as well as other microbicidal compounds, such as peroxidized lipids[52] and Br^0,[81] for microbial surface structural damage and thus achieve inactivation. ROS species produced in these mechanisms include superoxide anion ($O_2^{\cdot -}$), hydroxyl radicals (·OH), singlet oxygen ($^1O_2$) etc.[50, 52, 141] ROS production in PDCT or PC pathogen inactivation studies have been probed directly through photoluminescence measurements[50-51] or with redox dyes;[141, 145] as well as indirectly, for instance, with the help of ROS scavengers.[52] As an example of the former, Heyne and coworkers characterized the ROS formation in Rose Bengal enhanced by Ag nanospheres or nanocubes through measurement of the time-resolved $^1O_2$ luminescence signal.[50-51]

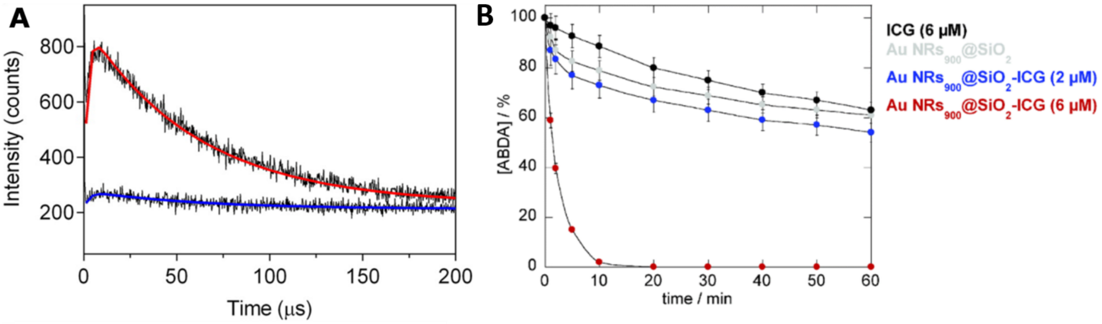

Figure 1.7 Characterization of ROS Formation Facilitated by Plasmonic Nano-Antimicrobials. (A) Time-resolved luminescence of $^1O_2$ and biexponential fits at 1275 nm for hybrid plasmonic nanoparticles (red) and an etched control (blue). Reprinted with permission from Ref. 50. Copyright (2016) by American Chemical Society. (B) ABDA degradation curve with Au NRs@SiO$_2$ nanocomposites incorporating various concentrations of indocyanine green. Reproduced with permission from Ref. 145. Copyright (2016) by The Royal Society of Chemistry.

Significantly increased luminescence intensity for the Ag NP-enhanced hybrid system (red) was observed compared to an etched control (blue) with no metal core (**Fig. 1.7A**). The enhanced production of $^1O_2$ accounted for an improved antibacterial property of the nanocomposite for both Gram-positive and -negative bacteria. The photocatalytic decomposition of dye molecules, such as 9,10-anthracenediylbis(methylene)dimalonic acid (ABDA), has also been used to monitor changes in $^1O_2$ concentration in the PDCT mechanism, such as for Au NRs@SiO$_2$ core-shell nanostructures incorporating indocyanine green (ICG) (**Fig. 1.7B**) or verteporfin as PSs under resonant illumination conditions.[145-146] The decrease of ABDA absorbance at 262 nm provided experimental evidence of $^1O_2$ formation.[145]

The PPT inactivation pathway utilizes the photothermal heating to induce the denaturation of proteins and inhibition of cellular functions in microbes and thus achieve inactivation. As pathogenic bacteria are usually mesophilic and can thrive between 33 - 41 °C,[147] heating to above these temperatures with plasmonic NPs or heterostructures is likely to induce structural damage to the protein or other structural components.[13] And the photonic inactivation involves the plasmon-enhanced generation of shockwaves in the presence of femtosecond-pulsed laser for a dynamic inactivation process.[40-41, 116]

Owing to their nanoscale size and the surface and chemical properties that are independent of the plasmon resonances, plasmonic NPs can also sustain a series of light-independent antimicrobial effects based on these properties. Ag and Au NPs have been known to form covalent bonds with thiol groups of certain amino acids in proteins, disrupt disulfide bonds, impede with microbial binding or sensing functionalities, and cause damage to the surface structures of microbes.[45, 148] Additionally, the release of metal cations through oxidative dissolution of Au,[149] Ag[52, 81] and Cu[150] NPs have also been shown to lead to the formation of microbicidal compounds or complexes. These species, similar to discussed above for PDCT and PC mechanisms, can either damage the surface morphology of the microbes, or enter the microbes and cause damage to the interior structures. Importantly, both Ag NPs and Ag^+ have been demonstrated to also sustain synergistic enhancement for the antibacterial effect of molecular antibiotics.[45, 52, 54] In most cases, this synergy derives from the surface damage and thus the increased likelihood of the antibiotics entering the bacteria cells.

When irradiated, some of the light-dependent and -independent mechanisms described above can occur simultaneously, potentially facilitating a synergistic enhancement of microbe inactivation, and decreasing the likelihood of microbial resistance development.

A combination of both light-induced and -independent mechanisms can also enable some antimicrobial strategies that utilize the plasmonic NPs as scaffolds for controlled delivery and release of microbicidal drugs or complexes.[52, 54-55, 151] The nanoplasmonic optical responses can, in some cases, also facilitate efficient light-controlled release mechanisms.[52]

Plasmonic nano-antimicrobials have proven effective in various different studies against a broad range of microbial pathogens, which includes both enveloped and non-enveloped viruses;[40-41] Gram-positive and -negative bacteria;[41, 50-52] and fungi[152] with LRVs > 3. For light-induced mechanisms and light-controlled release pathways, low-power, ambient white-light illumination sources have been utilized and are proven sufficient to achieve the microbicidal effect. These observations mark yet another great potential of plasmonic nano-antimicrobials in comparison to conventional disinfection and sterilization techniques, such as autoclaving, UV and gamma irradiation, which is to achieve efficient sterilization with relatively low energy consumption and less specified instrumentation. Intriguingly, some plasmonic nano-antimicrobials have been shown to be effective against multiple microbicidal pathogens classes, whereas their effect that are significantly less harmful for mammalian cells or cell components.[41, 53] This selectivity derives from the different size scale, surface structures, and/or surface charge between microbes and mammalian cells. The pan-microbial efficacy, selectivity and decreased likelihood for microbial resistances make plasmonic NPs a promising class of nano-antimicrobials. Consequently, some plasmonic nano-antimicrobials have seen applications *in vivo*, for instance, for the disinfection of bacteria-inflicted wounds in rats or mice models.[153-154]

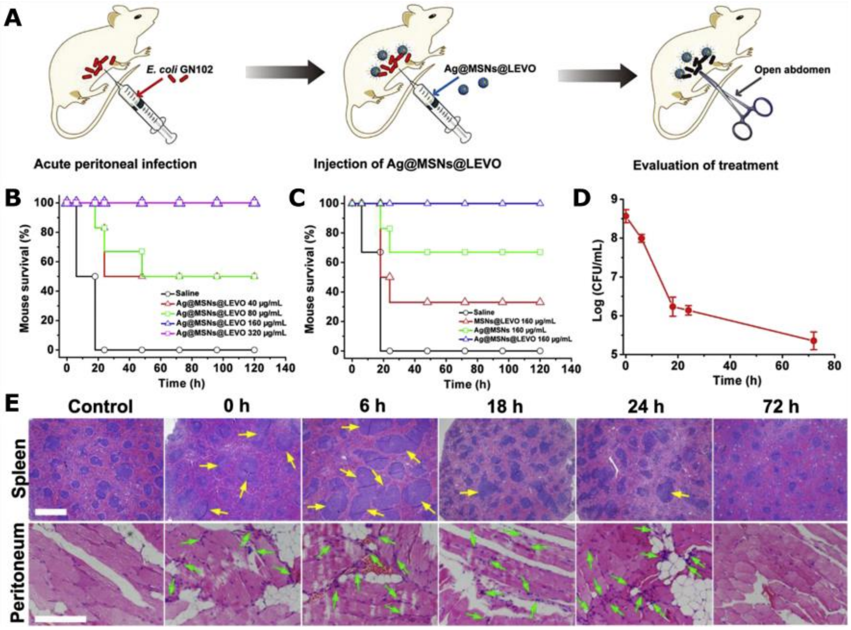

Figure 1.8 ***In vivo*** **Evaluation of** ***E. coli*** **Infected Mice Peritoneal Wound Healing Effect of Ag@MSNs@LEVO.** Reprinted with permission from Ref. 153, Copyright (2016) by Elsevier. (A) Scheme of the *in vivo* infection and treatment procedure. (B, C) Mice survival rates after acute peritoneal infection and treatment with Ag@MSNs@LEVO and control groups. (D) Bacterial counts within the peritoneal cavity of mice after treatment with 160 μg/mL Ag@MSNs@LEVO for different times. (E) H&E staining of histological sections including spleen and peritoneum of mice after acute peritoneal infection and treatment with 160 μg/mL Ag@MSNs@LEVO for different times. Extended lymphoid nodules on spleen and inflammatory cells on peritoneum are respectively marked with yellow and green arrows. Scale bars, 800 μm (top) and 100 μm (bottom).

Wang *et al.* used mesoporous silica NPs (MSNs) with Ag cores as carriers for levofloxacin (LEVO),[153] a common antibiotics that functions through inhibition of DNA gyrase and topoisomerase IV in bacteria. The authors discovered that through the spontaneous release of LEVO and Ag^+ from the NPs, an efficient *in vivo* treatment of *E. coli*-induced peritoneal infection in mice could be achieved (**Fig. 1.8**). Relatively high survival rates (**Fig. 1.8B, C**) as well as significantly reduced bacteria load (LRV = 3) in the peritoneal cavity after 72 hours of treatment (**Fig. 1.8D**) were observed in mice treated with Ag NP cores@MSNs@LEVO. Hematoxylin-eosin (H&E) staining tests performed on the spleen and peritoneum of infected mice also showed reduced degree of enlarged lymphoid nodules (yellow arrows) and inflammatory cells (green arrows), which are signatures of inflammatory responses, within 72 hours after treatment with Ag@MSNs@LEVO (**Fig. 1.8E**).[153]

Plasmonic nano-antimicrobials could also play an important role in mitigating and controlling future pandemic diseases caused by microbes, for which effective antimicrobial compounds are lacking.

1.5 Lipid-Coated Plasmonic Nanocomposites

Despite the distinct and intriguing properties of nanoplasmonics, when applied at high concentrations, some plasmonic NPs can be cytotoxic,[155] which precludes their application in certain fields, such as as nanomedicine or for food and water treatment. Besides, the oxidative dissolution of some plasmonic NPs, such as Cu and Ag,[52, 81, 150] could also impact their efficacy in long-term application as, for example, photocatalysts or antimicrobial coatings. Lipid-coated plasmonic NPs (L-NPs) have emerged as a favorable platform that possess the potential to address these problems by granting the NPs with biomimetic and biocompatible surface properties from the lipid coatings. Typically being amphiphilic and zwitterionic, the lipid architecture is also able to provide structural and chemical stability for the NP cores in aqueous solutions.[29, 52] Furthermore, the lipid membrane could be modulated to incorporate different binding ligands in order to adjust the surface properties of the nanocomposites, or to include specific binding affinity towards different molecules or biological cells.[56, 58-59, 156]

Various categories of L-NPs have been prepared in previous literature using lipid architectures ranging from lipid monolayer or micelles,[29, 56, 157-158] or bilayer liposomes.[159-160] One commonly seen model involves a hybrid lipid membrane that contains an outer lipid monolayer tethered through hydrophobic interactions to an inner alkylthiol layer, such as octadecanethiol (ODT), which is covalently bound to the metal NP surfaces through metal-thiol interaction.[56, 158] In this model, an interdigitation between the lipid tails and the alkylthiol have been evidenced by Transition Electron Microscopy (TEM) measurements of the membrane width in various studies.[56, 158] As the structure of L-NPs closely resemble that of enveloped viruses, their interaction with membrane-based systems is meaningful as a biomimetic system for probing numerous virological pathways, such as pathways for targeting and interaction with host cells,[17, 62] binding and entrance into host cells,[158, 161] and for intracellular trafficking.[61] L-NPs have also been used to provide contrast for the imaging of biomolecules or cells,[56, 76] and for controlled drug or cargo delivery.[159-160]

Sterols, in particular cholesterol, and other terpenoid derivatives are important components of both biological membranes and artificial L-NPs,[56] and, in general, play vital roles in regulating various properties of the lipid architectures, including membrane fluidity,[162-163] domain formation,[164-165] phase behavior,[164, 166] permeability,[52, 163] and etc. Importantly, the functionality of L-NPs can be feasibly tuned towards the distinct applications by altering the structure of the lipid architectures, and/or the compositional aspects of lipid, sterol, or

NP cores including saturation, amphiphilicity, surface charge etc. Consequently, chemical derivatization of the membrane components, such as the sterols, represents one promising approach to modulate the molecular conformation of these molecules, and thus the surface properties of the L-NPs.[56] These modulations are crucial in adapting the L-NPs towards different applications. For instance, when the L-NPs are applied for specific targeting of cell surface receptors in particle-cell interaction studies[58-59, 156] or for enhancing photochemical reactions at the lipid-medium interfaces,[29] it is favorable for the targeting ligands or photocatalysts to be placed close to the membrane surface to facilitate the interfacial processes. Contrarily, when L-NPs are utilized as nanocarriers for drug loading and release,[55, 160] or as nanoprobes that provide imaging or spectroscopy modalities,[76, 167] an integration of optical labels or cargo molecules within the membrane where they are protected from release or chemical reactions is preferred.

Chapter 2. Nanoplasmonics in Photocatalysis

Lipid-coated noble metal nanoparticles (L-NPs) provides a reliable scaffold to incorporate photocatalytic molecules or particles, and to harvest the plasmonic enhancement for plasmonic photocatalysis through the E-field augmentation mechanism, the plasmonic charge carrier-induced catalysis, or additional pathways as introduced in section **1.3**. In this chapter, we discuss two examples that respectively utilize the field-enhancement and charge carrier-mediated plasmonic photocatalysis mechanism to facilitate fuel cell half reactions. This chapter was in part reproduced and adapted with permission from Ref. 29, Copyright (2019) by Elsevier and with permission from Ref. 78, Copyright (2022) by American Chemical Society.

2.1 Plasmonic E-Field Enhanced Photocatalysis of Urea Oxidation by a Plasmonic Nanopigment

In this project, we achieve quantitative optimization of plasmonic catalysis of the urea oxidation reaction (UOR) mediated by E-field-enhanced intramolecular metal-to-ligand charge transfer (MLCT) with a hierarchical nanopigment architecture.[29] The nanopigment consists of (1.) a spherical Ag NP core as an effective nanoantenna; (2.) a molecular photocatalyst, trisbipyridine-ruthenium(II) ($[Ru(bpy)_3]^{2+}$); and (3.) a lipid membrane layer as both a scaffold and molecular spacer. The self-assembled lipid layer provides a facile and effective strategy to pin the photocatalyst at a distance of 2 - 4 nm away from the Ag surface, which represents a plasmonic ‘‘sweet spot’’. At this spot, there are both intense E-fields for resonant enhancement of photoexcitation of the molecular photocatalyst, and limited quenching of photoexcited population.

$[Ru(bpy)_3]^{2+}$ derives its photoreactivity from its MLCT absorption[66] that overlaps the LSPR of the Ag NPs at around 430 nm. The light-harvesting efficiency of $[Ru(bpy)_3]^{2+}$ is fundamentally limited by the moderate extinction coefficient of its MLCT band (4,600–11,000 $M^{-1}cm^{-1}$),[66, 168] which is much lower than those of high-performance dyes (>200,000 $M^{-1}cm^{-1}$).[169] The E-field-mediated enhancement of the MLCT photoexcitation of $[Ru(bpy)_3]^{2+}$ in plasmonic nanopigments is likely to close this gap and achieve a measurable increase in the excitation of $[Ru(bpy)_3]^{2+}$ and thus, the photoreactivity of the nanopigment. We implement a robust visible-light fuel cell that achieves energy conversion through photo-oxidation of urea, a ubiquitous waste molecule.

2.1.1 Design and Preparation

Lipid wrapping was achieved through a modified one-pot synthesis as shown in previous reports.[61-62] A lipid membrane composition was adopted based on a simplified biological membrane model containing 45 mol% zwitterionic lipid 1,2-dipalmitoyl-sn-glycero-3-phosphocholine (DPPC), 5 mol% negatively charged lipid 1,2-dioleoyl-sn-glycero-3-phospho-L-serine (DOPS), 40 mol% cholesterol, and 10 mol% $[Ru(bpy_3)]^{2+}$. The lipids were tethered to the NP core through an intermediate octadecanethiol (ODT) layer conjugated to the Ag NP cores (**Fig. 2.1.1A**). A lipid thin film was first generated in round-bottom flasks through rotary evaporation of chloroform solutions of lipids mixed with a methanol solution of $[Ru(bpy)_3]Cl_2$ (Sigma Aldrich) with a total lipid amount of 1 μmol.

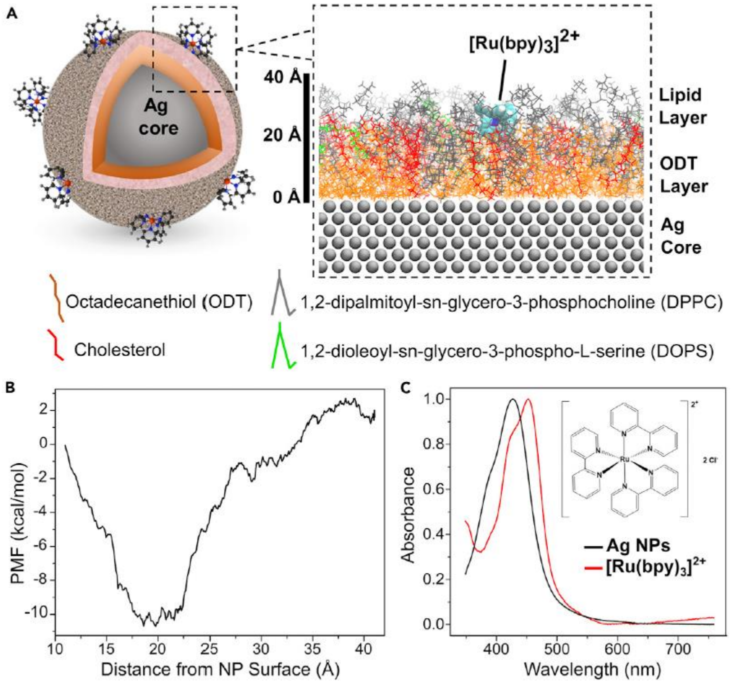

Figure 2.1.1 Design of the Nanopigment. Reprinted with permission from Ref. 29, Copyright (2019) by Elsevier. (A) Scheme of the nanopigment architecture with simulated surface morphology diagram of the surface (right). Water molecules are not shown. (B) Plot of potential of mean force (PMF) of the $[Ru(bpy)_3]^{2+}$ molecule over lipid membrane cross-sectional distance from NP surface. (C) Normalized UV-vis absorbance spectra of 44 nm Ag NP colloid and $[Ru(bpy)_3]^{2+}$ water solution. Inset: molecular structure of $[Ru(bpy)_3]Cl_2$.

After overnight desiccation, the thin films were re-dispersed with 1 ml of water and liposomes were generated through tip sonication under Argon purge. Dynamic Light Scattering (DLS) tests on the liposome suspension after tip sonication show an average diameter of 117.3 ± 5.2 nm. 2mg/ml of octadecanethiol (Sigma Aldrich) in anhydrous ethanol was subsequently added into the liposome suspension. 0.5 ml Ag NPs (Nanocomposix) colloid with approximately 10^{10} NPs and a hydrodynamic diameter of 44.23±0.62 nm (DLS) was subsequently mixed with liposomes/ODT suspension. The 1.5

ml mixture was shaked for 12 h before being washed twice by water and stored in 4 ℃ for later characterizations.

In order to understand the equilibrium of $[Ru(bpy_3)]^{2+}$ in the lipid membrane, our collaborator, Dr. David Stelter and Prof. Tom Keyes performed calculations of the potential of mean force (PMF) of a $[Ru(bpy_3)]^{2+}$ complex from a steered molecular dynamics simulation by Jarzynski's equality (**Fig. 2.1.1B**).[170-172] The nonequilibrium work (W) was calculated as a function of distance of the catalyst molecule to the metal NP surface. The resulting PMF plot exhibits a minimum at around 2 nm, indicating a preferential localization of $[Ru(bpy_3)]^{2+}$ close to the membrane surface at the interface formed by the hydrophilic lipid headgroups and the hydrophobic lipid tails. Ag NPs with diameters of 44.23 ± 0.62 nm were chosen, whose absorption spectrum in aqueous suspension is shown in **Fig. 2.1.1C**.

To validate the successful nanopigment formation, we added small amounts of fluorescent lipid dye (Lissamine rhodamine DSPE, Avanti Polar Lipids) into the lipid membrane and imaged the nanopigments with correlated darkfield (DF) and fluorescence (FL) microscopy (**Fig. 2.1.2A**). The optical colocalization of DF signals from NP cores and FL signals from the membrane dye confirmed a successful membrane assembly around the Ag NP cores. High-resolution transmission electron microscopy (HRTEM) images reveal uniform lipid membrane around the NP core (**Fig. 2.1.2B**). A statistical analysis of the thickness of the membrane for 70 particles showed an average membrane width of 3.8 ± 1.4 nm, defining an upper boundary for the distance between $[Ru(bpy_3)]^{2+}$ and Ag NPs. Energy-dispersive

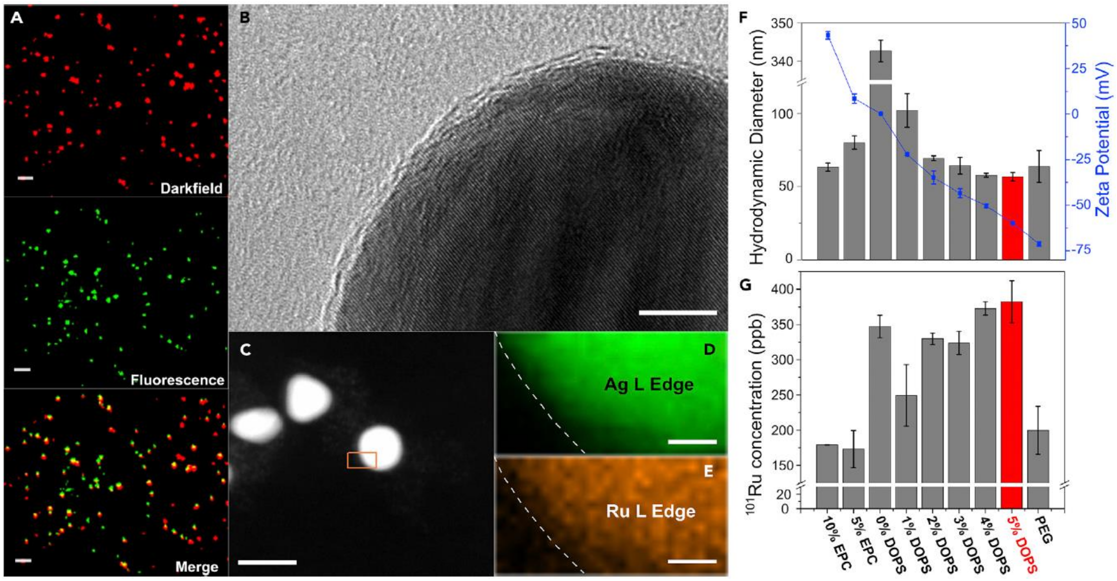

Figure 2.1.2 Structural Characterization of the Nanopigment. Reprinted with permission from Ref. 29, Copyright (2019) by Elsevier. (A) DF (top), FL (middle) images, and a channel merge (bottom) of an area with nanopigments under inverted microscope. Scale bars: 1 μm. (B) HRTEM image of a nanopigment particle. Scale bar: 10 nm. (C) STEM image of nanopigments with scan area (orange rectangle) for EDX element mapping. Scale bar: 50 nm. (D, E) EDX elemental scan maps with (D) Ag L edge and (E) Ru L edge. Scale bars: 5 nm. (F) DLS results of hydrodynamic diameters of nanopigments and nanocomposite controls (columns) and ζ-potentials of corresponding liposomes before incorporation of $[Ru(bpy)_3]^{2+}$ (scatter plot). (G) ICP-MS results of incorporated ^{101}Ru concentrations of nanopigments and nanocomposite controls. Error bars: standard deviations of 3 independent measurements.

X-ray spectroscopy (EDX) further confirmed the coexistence of Ag and Ru (**Fig. 2.1.2D, E**) within the boundary of the particle, providing additional experimental proof of a successful integration of $[Ru(bpy_3)]^{2+}$.

The hybrid lipid membrane provides both electrostatic and hydrophobic binding affinity for $[Ru(bpy_3)]^{2+}$. The electrostatic interaction is evidenced by a series of control L-NPs having different surface charges achieved by varying the amount of negatively charged lipid DOPS or by replacing DOPS with cationic lipid 1,2-dioleoyl-sn-glycero-3-ethylphosphocholine (EPC, Avanti Polar Lipids) in the membrane. In general, with increasing negative charge, an overall increase in ^{101}Ru concentration is measured from the nanocomposite by Inductively Coupled Plasma-Mass Spectrometry (ICP-MS), indicating a contribution from Coulomb attraction in $[Ru(bpy)_3]^{2+}$ binding (**Fig. 2.1.2F, G**). An exception exists for 0% DOPS. This is because under this condition, a lack of any electrostatic repulsion led to strong agglomeration of the nanocomposites, which interfered with the incorporated Ru measurement. The hydrophobic interaction can be evidenced by another control group where thiolated polyethylene glycol (PEG) with carboxyl end groups (HS-PEG$_n$-COOH, M_w=1,000) was used as coating layers instead of the amphiphilic lipids. This control group records a similar ζ potential as the nanopigments, but showed a 48% decrease in ^{101}Ru concentration due to absence of the hydrophobic tail groups of the lipid layer (**Fig. 2.1.2F, G**). These results are in good agreement with the PMF calculations in **Fig. 2.1.1** and indicate a structural model in which $[Ru(bpy_3)]^{2+}$ is pinned to the interface between hydrophobic and hydrophilic membrane regions.

2.1.2 Photophysical Characterizations

UV-vis absorbance spectra of water suspensions of nanopigments and controls with identical Ag and/or Ru concentrations exhibited a clear enhancement of the absorbance of the nanopigments in the MLCT range (**Fig. 2.1.3A**, red). After correcting the absorbance of the nanopigments with the contribution from the "bare" Ag NP, a 35-fold increase at absorbance maxima of 424 nm was calculated compared to $[Ru(bpy_3)]^{2+}$ only. In the control group where Ag NP cores were replaced with Au cores (green), which possess an LSPR around 540 nm and less overlap with the MLCT of the dye molecule, no noticeable

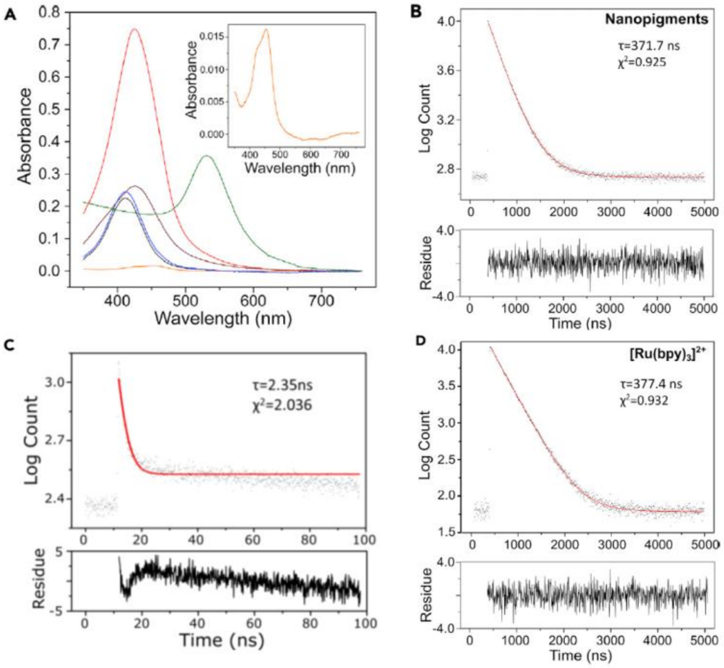

Figure 2.1.3 Photophysical Characterization of the Nanopigment and Controls. Reprinted with permission from Ref. 29, Copyright (2019) by Elsevier. (A) UV-vis absorbance spectra of nanopigment colloid (red), ‘‘bare’’ Ag NPs (black), membrane-wrapped Ag NPs without photocatalyst (brown), aqueous solution of $[Ru(bpy)_3]^{2+}$ (orange, inset), simple mixture of Ag NPs and aqueous $[Ru(bpy)_3]^{2+}$ solution (blue), and control nanopigments with Au NP cores (green). All controls were prepared to have identical Ag and/or Ru concentration as in the nanopigments. (B-D) Photoluminescence decay patterns and monoexponential fit curves (red) for (B) Nanopigments, (C) the HS-PEG$_3$-COOH control, and (D) $[Ru(bpy)_3]^{2+}$ water solution.

resonant enhancement was observed. A simple mixture control of Ag NP colloid and $[Ru(bpy_3)]^{2+}$ solution at identical Ag and Ru concentrations (blue) generated only a weak enhancement of the MLCT band. These observations suggest that spectral overlap and preferential localization of the Ru(II) complex within the evanescent field of the NPs are necessary factors for the resonant energy transfer.

To assess the extent of quenching on reactive photoexcited states, we next measured the photoluminescence (PL) lifetime and quantum yield (QY) for the nanopigments and controls. The measured lifetime is determined by the phosphorescence of the Ru*(II) triplet state that is generated through rapid intersystem crossing (ISC) from the initial short-lived photoexcited singlet state.[66] The measured PL lifetime of the aqueous suspensions of nanopigments was 371.7 ns (**Fig. 2.1.3B**) whereas a much-reduced lifetime of 2.35 ns was seen for a control where the photocatalyst molecule was pinned at around 1 nm distance to the metal surface with HS-PEG$_3$-COOH ($M_w = 238.3$) (**Fig. 2.1.3C**).[173-174]. In comparison, a lifetime of 377.4 ns measured for the $[Ru(bpy)_3]^{2+}$ solution (**Fig. 2.1.3D**); A QY = 4.55% is measured for the plasmonic nanopigments, compared to 1.95% for free $[Ru(bpy)_3]^{2+}$ and 0.02% for the HS-PEG$_3$-COOH control. These results indicate that through the L-NP model, the hybrid lipid membrane around the Ag NPs have achieved the positioning of the $[Ru(bpy_3)]^{2+}$ photocatalyst molecules within the plasmonic ‘‘sweet spot’’ where substantial E-field enhancement of MLCT photoexcitation and limited quenching of the reactive excited state are both attained.

2.1.3 Photoelectrochemical Characterizations

We then characterized the photoredox potentials of the nanopigments with linear sweep voltammetry (LSV) in a three-electrode setup. Nanopigment suspensions and controls were drop-casted onto glassy carbon working electrodes, and current densities (J) were measured in the voltage range of 0 – 1.2 V (*versus* Ag/AgCl reference unless otherwise noted) with illumination from a focused 430 nm light-emitting diode (LED) or in dark. In the LSV measurements, the applied bias induced the oxidation of photogenerated Ru*(II) into Ru(III) (**Fig. 2.1.4A**), which was then available to facilitate the oxidation processes.

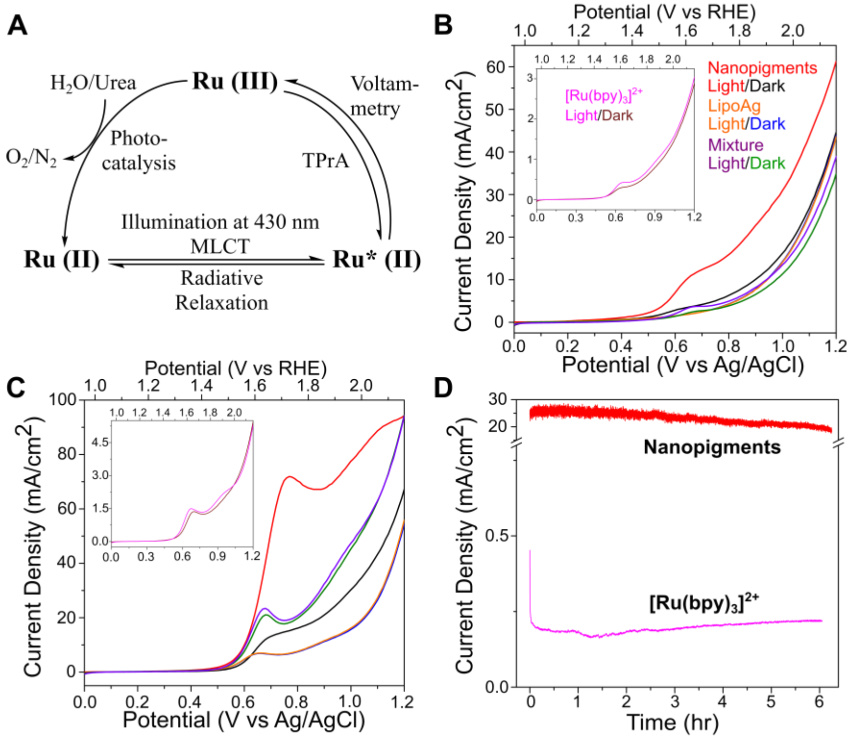

Figure 2.1.4 Photoelectrochemical Characterizations. Reprinted with permission from Ref. 29, Copyright (2019) by Elsevier. (A) Scheme for the photocatalytic reaction mechanism of nanopigments in voltametric measurements. (B, C) LSV curves in (B) 0.1 M NaOH + 0.01 M TPrA, and (C) alkaline urea electrolyte. (D) Chronoamperometry curves for nanopigments (red) and [Ru(bpy)$_3$]$^{2+}$ only (magenta) in alkaline urea electrolyte under 430 nm LED illumination and with 750 mV potential. Color code: nanopigments +/- light, red/black; lipid-wrapped Ag NP control (LipoAg) +/- light, orange/blue; ‘‘mixture’’ control +/- light, purple/green; [Ru(bpy)$_3$]$^{2+}$ only +/- light, magenta/wine (insets).

An electrolyte solution of 0.1 M NaOH + 0.01 M sacrificial reductant (SR) tripropylamine (TPrA) was first used, where the baseline was defined by water oxidation. TPrA is able to rapidly reduce excessive Ru(III) to Ru*(II), which then replenished steady-state Ru(II) through radiative relaxation.[175] LSV for nanopigments with light (**Fig. 2.1.4B**, red) exhibited an early reaction onset at around 350 mV as well as a drastic increase in photocurrent density (J_{photo}) up to 7.03 mA/cm^2, much higher than the control groups, which confirms efficient photo-oxidation of water. The measurable oxidation peak at 650 mV in the nanopigments with light could be assigned to the oxidation of the photogenerated Ru*(II) to Ru(III). Based on the oxidative potential of the Ru species, we next used urea oxidation reaction (UOR) as a test platform for the plasmonic catalysis. Urea ($CO(NH_2)_2$) is a common waste molecule from nitrogen cycles of mammals. Photocatalytic urea oxidation is thus meaningful for urea-containing waste water treatment. Due to the high energy and hydrogen densities of urea, it also possess great potentials for waste-to-energy conversions.[176-177] In UOR, anodic urea oxidation (**Eq. 2.1**) is coupled to cathodic H_2 evolution in neutral or alkaline conditions (**Eq. 2.2**), resulting in the overall reaction **Eq. 2.3**.[176, 178-179]

$$CO(NH_2)_2 + 6OH^- \rightarrow N_2 + 5H_2O + CO_2 + 6e^- \qquad \textbf{Eq. 2.1}$$

$$2H_2O + 2e^- \rightarrow H_2 + 2OH^- \qquad \textbf{Eq. 2.2}$$

$$CO(NH_2)_2 + H_2O \rightarrow N_2 + 3H_2 + CO_2 \qquad \textbf{Eq. 2.3}$$

A human urine equivalent 0.33 M urea was added to 0.1 M NaOH + 0.01 M TPrA as electrolyte (**Fig. 2.1.4C**). A sharp onset of current density for the nanopigments with light was observed at around 450 mV (red), leading to an extended oxidation peak for Ru(III)-mediated urea oxidation. Ru(III)-facilitated urea oxidation peaked at 750 mV, where a maximum J_{photo} of 56.0 mA/cm^2 was recorded. This corresponds to an excellent applied bias photon-to-current efficiency of 4.1%. This value is comparable to previously reported state-of-the-art photoanodes.[180-181]

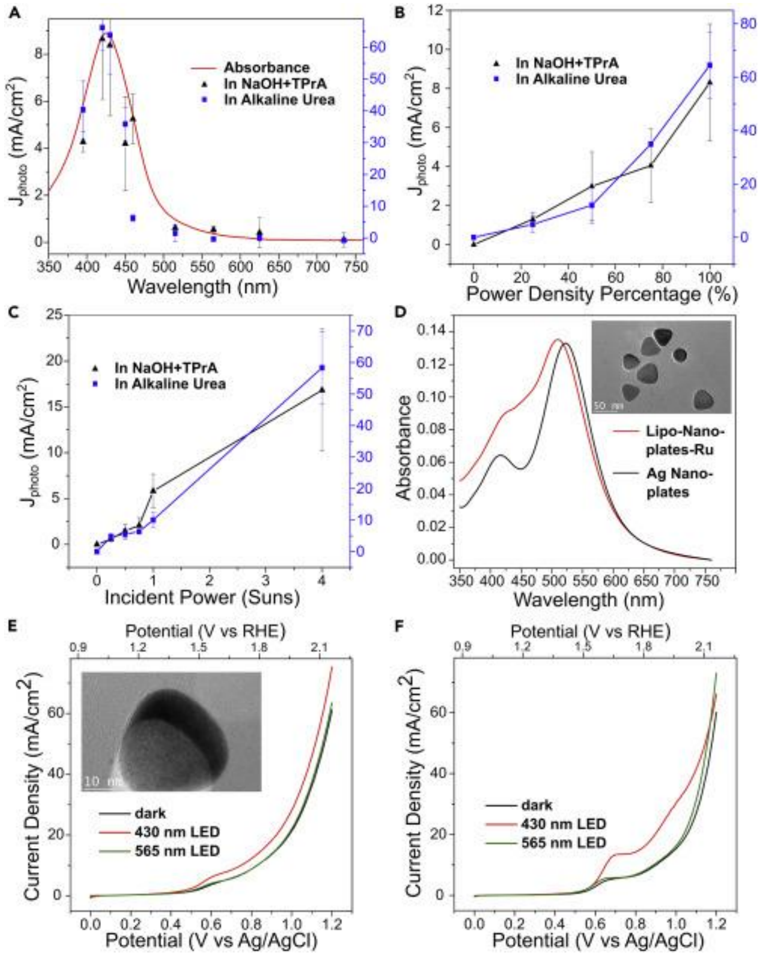

Figure 2.1.5 Characterization of the Plasmonic Photocatalytic Mechanism. Reprinted with permission from Ref. 29, Copyright (2019) by Elsevier. (A) Plots of J_{photo} as a function of incident wavelength for nanopigments in NaOH + TPrA (black triangles) and alkaline urea (blue squares). J_{photo} was calculated from the LSV peaks at 650 mV in NaOH + TPrA and 750 mV in alkaline urea. (B, C) Plot of J_{photo} as a function of incident power density in NaOH + TPrA (black triangles) and alkaline urea (blue squares) electrolytes for (B) 430 nm LED, or (C) a sunlight simulator. (D) UV-vis absorbance spectra of Ag nanoplates (black) and membrane-wrapped Ag nanoplates with $[Ru(bpy)_3]^{2+}$ (Lipo-Ag nanoplates-Ru) (red). Inset: TEM of Ag nanoplates. Scale bar: 50 nm. (E, F) LSV curves for Lipo-Ag nanoplate-Ru in (E) 0.1 M NaOH + 0.01 M TPrA, or (F) alkaline urea electrolyte without illumination (black), with 430 nm LED illumination (red), and with 565 nm LED illumination (green). Inset in (E): TEM image of a Lipo-Ag nanoplate-Ru particle. Scale bar: 10 nm. Error bars: standard deviation from 3 independent measurements.

The hybrid lipid membrane in the nanopigment also provides structural and photoelectrochemical (PEC) stability. To characterize the long-term PEC performance, chronoamperometry measurements were carried out with an applied bias of 650 mV in alkaline urea electrolyte with light. As shown in **Fig. 2.1.4D**, the catalytic current density of nanopigments remained much more stable for 6 hours at significantly higher values than for $[Ru(bpy)_3]^{2+}$. For the latter, J_{photo} drastically decreased over the first 10 min of illumination due to rapid photobleaching and depletion of steady-state Ru(II).

To further elucidate the plasmonic enhancement mechanisms of the enhanced UOR photocatalysis by the nanopigment, the effect of incident wavelength and power was first investigated. J_{photo} in NaOH + TPrA and alkaline urea electrolytes generally followed the UV-vis absorbance spectrum of the nanopigments (**Fig. 2.1.5A**, red) with strong enhancement for incident wavelengths between 395 and 450 nm. A linear dependence of J_{photo} on the incident power was also obtained for both a 430 nm LED (**Fig. 2.1.5B**) and a sunlight simulator (**Fig. 2.1.5C**) in both types of electrolytes. To validate the E-field-enhancement mechanism, we tested another control where triangular Ag nanoplates (**Fig. 2.1.5D**, insets) were used as cores in the nanocomposite. The nanoplates sustained two LSPR modes at 415 and 525 nm with similar dissipation. Only the former mode had good spectral overlap with the $[Ru(bpy)_3]^{2+}$ MLCT to potentially sustain resonant energy transfer and field enhancement; whereas if plasmonic charge carriers or photothermal heating were to play a significant role in the catalysis, both modes could lead to increased performances. Indeed, increase in J_{photo} was only observed with excitation of the 415 nm LSPR mode, confirming that the enhanced photocatalysis of nanopigments is derived from an E-field-driven MLCT excitation enhancement mechanism.

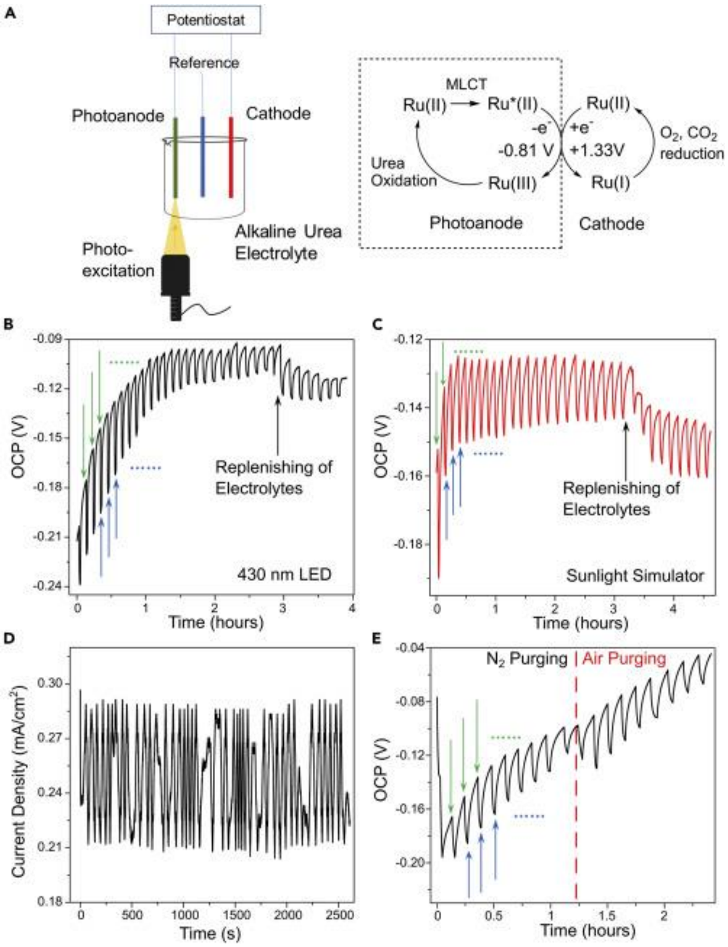

Figure 2.1.6 Characterizations of the LDUFC. Reprinted with permission from Ref. 29, Copyright (2019) by Elsevier. (A) LDUFC setup and cell reactions scheme. (B, C) Open circuit potential (OCP) measurements for nanopigments in 0.33 M urea + 0.1 M NaOH electrolyte with (B) 430 nm LED illumination or (C) sunlight simulator at 1-sun power illumination. Light on and off cycles are indicated by green and blue arrows, respectively. (D) Measurement of short-circuit current density under constant illumination with 430 nm LED. (E) OCP measurements for nanopigments in 0.33M urea + 0.1 M NaOH electrolyte with 430 nm LED illumination and N_2/air purging.

2.1.4 Implementation of a Direct Urea Fuel Cell

Based on the PEC characterizations, a visible light-driven direct urea fuel cell (LDUFC) was next implemented, in which nanopigments served as both the cathode and the photoanode. An electrolyte of 0.33 M urea + 0.1 M NaOH was used, and illumination was focused onto the photoanode, where the photoexcited Ru*(II) undergoes spontaneous oxidation (Ru*(II) - e^- → Ru(III)). The cathode reaction Ru(II) + e^- → Ru(I) occurs on the non-illuminated electrode (**Fig. 2.1.6A**), giving an overall cell potential of +0.52 V.[182] The photo-generated strong oxidizer Ru(III) subsequently facilitates urea oxidation at the photoanode, whereas Ru(I) on the cathode can reduce O_2 or CO_2 in the electrolyte to replenish Ru(II) and complete the redox cycle in the cell. The open circuit potential (OCP) of the LDUFC was measured with illumination from either a 430 nm LED (**Fig. 2.1.6B**) or a sunlight simulator at 1-sun illumination (100 mW cm^{-2}) (**Fig. 2.1.6C**). For both conditions, the cell OCP stabilized with photovoltages between 12 and 15 mV for more than 3 hours. Cell short circuit current density measurements showed a constant oscillation centered around 0.25 mA cm^{-2} (**Fig. 2.1.6D**). This oscillation could be due to the photoelectrochemical cycling on the photoanode that is also observed in some previous studies.[183] Specifically, under continuous illumination, Ru(II) was rapidly consumed but more slowly replenished by the catalyzed 6-electron UOR process, resulting in the formation of consumption-replenishing cycles for the steady-state population and the oscillatory effect.

To further illuminate the nature of the electrode reactions, the cell was purged with nitrogen and recorded cell OCP under oxygen deficient conditions (**Fig. 2.1.6E**). Much decreased photovoltage was observed under this condition, whereas subsequent addition of air triggered a measurable increase in the light response. These observations are consistent with our model of LDUFC reactions in which O_2 and CO_2 from the electrolyte are reduced at the cathode to replenish ground state Ru(II).

In summary, we demonstrate in this section efficient plasmonic E-field enhancement of $[Ru(bpy)_3]^{2+}$-mediated photocatalytic urea oxidation by a hierarchical nanopigment.[29] Our experimental and theoretical analyses suggest that the amphiphilic nature of the self-assembled membrane facilitates both electrostatic and hydrophobic interactions with $[Ru(bpy)_3]^{2+}$ to achieve localization at an electromagnetic ‘‘sweet spot’’ approximately 2 - 4 nm from the metal surface, with both strong E-field intensity for substantial enhancement of photocatalyst excitation, and limited quenching of the photoexcited states. The nanopigments achieved efficient photocatalysis of urea oxidation, and enables a visible light-driven direct urea fuel cell with LED or sunlight illumination. Our proof-of-principle implementations of UOR and LDUFC promise great achievements in both solar energy conversion and waste-water treatment.

2.2 Wavelength-Dependent Bifunctional Plasmonic Photocatalysis in Au/Chalcopyrite Hybrid Nanostructures

In addition to the E-field enhancement mechanism, plasmonic NPs can also be combined with nanoscale catalyst into a heterostructure *via* the L-NP model in order to achieve charge separation and plasmonic charge carrier-mediated photocatalysis. It is conceivable that through construction of hybrid nanostructures that incorporates multiple plasmonic components, the nature and direction of charge transfer can be feasibly tuned through excitation of resonances associated with the different building blocks, making it feasible to produce electrons or holes on the individual components for bifunctional catalysis of different reactions.[78]

In this study, we characterize a hybrid plasmonic photocatalyst comprising Au nanorods (NRs) and chalcopyrite ($CuFeS_2$) nanocrystals (NCs) encapsulated in a lipid membrane for bifunctional catalysis of the water splitting reactions.[78] The $CuFeS_2$ NCs sustain distinct quasistatic resonances when the Fröhlich resonance condition is met at around $\boldsymbol{\lambda_{res}^{NC}}$ = 490 nm,[90-91] and the decay of this resonance results in hot electron production.[90] They also offer a Cu(I)/Cu(II) couple that can complement the plasmonic redox catalysis. The wavelength-dependent redox catalysis provided by the hybrid photocatalysts was assessed using hydrogen evolution (HER) and oxygen evolution reaction (OER) as test platforms. We discovered that excitation of Au NR and $CuFeS_2$ resonances is correlated with HER and OER catalysis, respectively. The observed wavelength-dependent catalysis is rationalized in a model in which light-driven plasmonic electron-transfer and Cu(I)/Cu(II) redox couple-mediated catalysis on the surface of the NCs contribute to the overall catalytic effect.

2.2.1 Design and Preparation

Chalcopyrite $Cu(I)Fe(III)S_2$ nanocrystals (NCs) were synthesized by our collaborators, Prof. Allison Dennis and Dr. Joshua Kays, by hot injection according to literature[184] with slight modifications. Equimolar amounts of iron(II) chloride and copper(II) acetate (0.3 mmol each, Sigma-Aldrich, TM grade) were loaded to a 100 mL round bottom flask with a stir bar in an argon-filled glovebox, along with 6 mL of oleic acid (Sigma-Aldrich) and

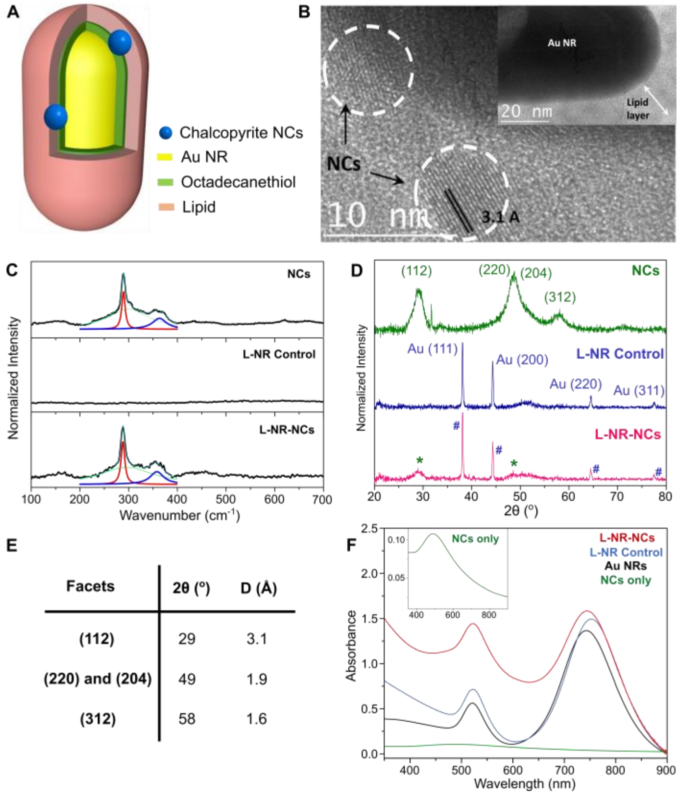

Facets	2θ (°)	D (Å)
(112)	29	3.1
(220) and (204)	49	1.9
(312)	58	1.6

Figure 2.2.1 Characterization of the Hybrid Plasmonic Photocatalyst. Reproduced with permission from Ref. 78, Copyright (2022) by American Chemical Society. (A, B) Structural scheme (A) and TEM micrographs (B) of L-NR-NCs. (C) Raman spectra of drop-casted thin films of chalcopyrite NCs (top), L-NR control (middle), and L-NR-NCs (bottom) with Lorentzian peak fittings of the A_1 (red) and B_2 (blue) phonon modes. Green: a fitted baseline; Cyan: sum of the fit curves. (D) XRD spectra of NCs (top), L-NR control (middle) and L-NR-NCs (bottom). NCs and Au NRs diffraction peaks in L-NR-NCs are denoted respectively with asterisks (*) and pound signs (#). (E) Summary of the XRD diffraction angles (2θ) and interplanar distances (D) of different NCs facets. (F) UV-vis absorbance spectra of L-NR-NCs (red), L-NR control (blue), uncoated Au NRs (black), and NCs only (green, inset); all controls are prepared with the same Au and/or NCs concentrations as in L-NR-NCs.

6mL of octadecene (Sigma-Aldrich). The flask was added to a Schlenk line and heated to 105 °C under vacuum to degas for 30 min. The flask was flushed with argon and heated to 150 °C to dissolve all metal salts, then heated to 180 °C. 3 mL dodecanethiol was injected (causing the solution to change color), and temperature was allowed to recover for 1 min, followed by injection of 3 mL 0.1 M sulfur in oleylamine over 5 min. After this, NCs were left to grow for 10 min then cooled. NCs were cleaned via dilution in hexanes (1:1) and precipitation with ethanol (4-fold excess), followed by centrifugation for 5 min at 21000 rcf. The resulting pellet was then re-suspended in chloroform and stored in a sealed 6-dram vial at 4 °C.

Lipid-Au nanorod-nanocrystal hybrid plasmonic photocatalyst (referred to as L-NR-NCs) was synthesized through a similar one-pot self-assembly as described in section **2.1.1**.[29, 62] L-NR-NCs consists of a Au NR core and $CuFeS_2$ NCs integrated by a hybrid membrane (**Fig. 2.2.1A**). The average width of the hybrid lipid membrane in L-NR-NCs is 8.9 ± 2.7 nm as measured from TEM micrographs of the nanocomposites (**Fig. 2.2.1B**). The chalcopyrite NCs stock have an average diameter of 5.1 ± 0.4 nm and a Fe:Cu ratio of 2.2:1 (Fe: 39353.9 ± 1951.5 ppb, Cu: 18191.5 ± 825.2 ppb), as measured from Microwave Plasma-Atomic Emission Spectroscopy (MP-AES). The membrane encapsulates the NCs and positions them in direct vicinity to the NR core as well as the membrane-solution interface (**Fig. 2.2.1B**). The Au, Cu and Fe concentrations in L-NR-NCs nanocomposite are respectively 70453.4 ± 5705.2, 2301.8 ± 384.6, and 4169.4 ± 1143.1 ppb. Raman spectra of the purified nanocomposites contain characteristic peaks at 288 and 360 cm^{-1} (**Fig. 2.2.1C**), corresponding to the chalcopyrite A_1 and B_2 phonon modes, respectively.[185] Furthermore, X-Ray Diffraction (XRD) spectra for L-NR-NCs exhibit diffraction peaks at $2\theta = 29°$ and 49° (**Fig. 2.2.1D**), respectively corresponding to the chalcopyrite (112), and (220)/(204) peaks (**Fig. 2.2.1E**).[186] The XRD spectra also contain the Au NR (111), (200), (220) and (311) diffraction peaks at $2\theta=38°$, 44°, 65° and 78°,[187] as well as the Si substrate signal at 52°.[188]

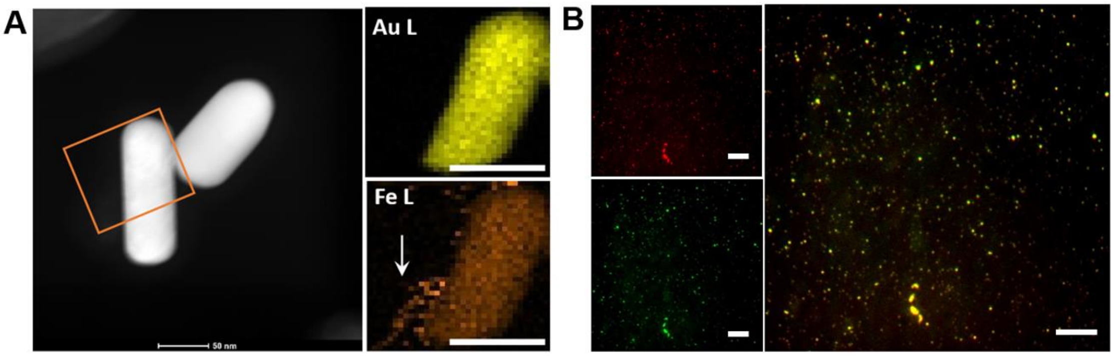

Figure 2.2.2 Supplemental Characterization of the Hybrid Plasmonic Photocatalyst. Reproduced with permission from Ref. 78, Copyright (2022) by American Chemical Society. (A) STEM image (left) and EDX element maps of Au (top right) and Fe (bottom right) L edge of an L-NR-NCs nanocomposite. Orange rectangle: mapped area. Scale bars = 50 nm. (B) Correlated DF (top left), FL (bottom left) images and a channel merge (right) of the L-NR-NCs with a small amount of membrane dye. Scale bars = 10 μm.

A series of characterization results further corroborate successful membrane wrapping and L-NR-NCs formation. EDX element maps confirms the presence of Fe around Au NRs (**Fig. 2.2.2A**). After a membrane dye (Streptavidin Alexa Fluor 594, ThermoFisher) was included in the lipid layer, correlated darkfield (DF) and fluorescence (FL) imaging of L-NR-NCs show strong spatial colocalization between the DF signal from the NR cores and the FL signal from the membrane (**Fig. 2.2.2B**), which offers direct evidence of successful membrane wrapping on a large scale. Manders correlation coefficients M_1 (correlation of DF signals with FL) and M_2 (correlation of FL with DF) were calculated to characterize the degree of colocalization between the DF and FL signals,[189] and high $M_1 = 0.61 \pm 0.02$ and $M_2 = 0.63 \pm 0.06$ are calculated.

Consistent with previous reports, the chalcopyrite NCs sustain a strong quasistatic resonance at around 490 nm (**Fig. 2.2.1F**, inset).[90, 92] The Au NRs possess an intense longitudinal LSPR mode at around 745 nm as well as a vertical mode at around 520 nm, which overlaps with the NC resonance. A significant increase in absorption is observed in the range of the high energy feature of the L-NR-NCs hybrid at around 510 nm. This indicates a resonant plasmonic enhancement of the NC absorption through the vertical NR plasmon mode. The longitudinal NR mode at 745 nm allows for a resonant charge carrier excitation in the NR without overlap with the NC resonance.

2.2.2 Wavelength-Dependent Photocatalysis of HER and OER

Chalcopyrite $CuFeS_2$ possesses an intermediate band (IB) formed by Fe 3d orbitals.[90] In the bulk, the gap between the valence band (VB) and IB has been reported as 0.63 eV;[90, 190] whereas in chalcopyrite NCs, the band gap can be increased due to quantum confinement. For NCs of similar size and Cu/Fe ratios as used in this work, an optical band gap of approximately 1.4 eV was measured,[191-193] which we assign to the VB-IB gap. The electron excited state energy has also been determined by Mott-Schottky plots to be -0.432 V (*vs*. NHE),[191] which we assign to the IB position. Collective electron-hole pair excitations from the VB into the IB give rise to the strong absorption resonance at 490 nm.[90, 190] The VB-IB gap is indirect, but in L-NR-NCs, the vertical plasmon mode of the Au NR that energetically overlaps with the NC resonance can enhance the NC excitation in the near-field.

The presence of distinct NC- and NR-associated resonances in L-NR-NCs provides an experimental strategy for modulating the redox potential of the NCs and for making it commensurable with either oxygen or hydrogen evolution reaction (OER/HER) when different resonance mode is excited (**Fig. 2.2.3**). Specifically, the dephasing of the NC

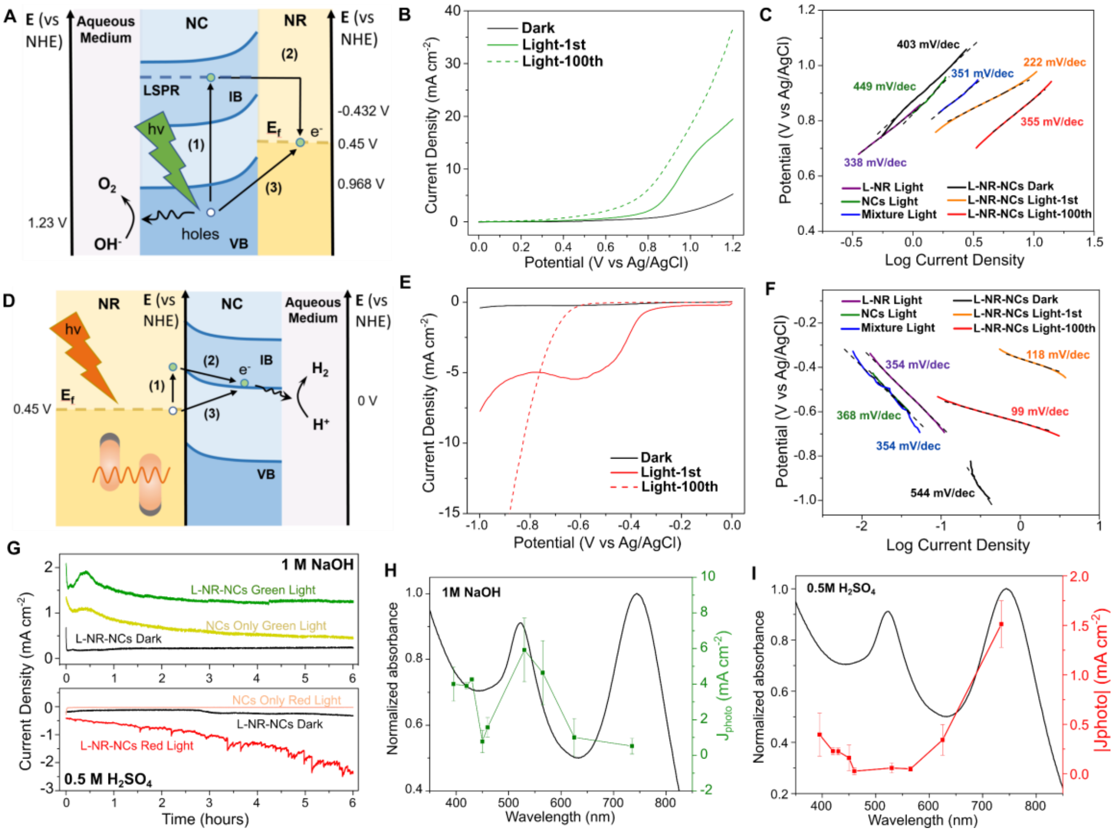

Figure 2.2.3 Photoelectrochemical Characterizations of the Hybrid Plasmonic Photocatalyst. Reproduced with permission from Ref. 78, Copyright (2022) by American Chemical Society. (A-C) Plasmonic charge transfer scheme (A), LSV curves (B), and Tafel Plot (C) for OER photocatalysis in 1 M NaOH by L-NR-NCs with green light irradiation from a 530 nm LED. (D-F) Plasmonic charge transfer scheme (D), LSV curves (E), and Tafel plot (F) for HER photocatalysis in 0.5 M H_2SO_4 by L-NR-NCs with red light irradiation from a 730 nm LED. (G) Chronoamperometry (CA) curves of L-NR-NCs with or without light or NCs only control (with light) in 1M NaOH with 0.8 V (*vs.* Ag/AgCl) applied bias (top), or in 0.5 M H_2SO_4 with -0.7 V applied bias (bottom). (H, I) Wavelength dependence of L-NR-NCs catalytic J_{photo} in 1 M NaOH at 0.8 V applied bias (H), or 0.5 M H_2SO_4 at -0.7 V applied bias (I). Black curves: absorbance spectra of L-NR-NCs water suspension; green/red curves: J_{photo} at different excitation wavelengths after 100 scans of activation. Error bars: Mean ± standard deviation of 3 independent measurements.

resonance in L-NR-NCs can induce plasmonic hot electron transfer from the NCs to the Au NR through direct or indirect charge transfer pathways (**Fig. 2.2.3A**),[90, 191] resulting in charge separation and accumulation of holes on the NC surface. The excessive holes can subsequently facilitate the oxygen evolution catalysis at the surfaces of the nanocomposites according to **Eq. 2.4**. Conversely, excitation of the longitudinal plasmon resonance of the Au NRs at around 745 nm is expected to facilitate hot electron production in the NR and transfer into the NC (**Fig. 2.2.3D**),[98, 194] enabling the proton reduction at the nanocomposite surface (**Eq. 2.5**).

$4OH^- - 4e^- \rightarrow 2H_2O + O_2$ **Eq. 2.4**

$2H^+ + 2e^- \rightarrow H_2$ **Eq. 2.5**

To validate this model, PEC characterizations were performed with L-NR-NCs in a 3-electrode electrochemical setup. 1 M NaOH and 0.5 M H_2SO_4 were used as electrolyte for OER and HER, respectively, and the L-NR-NCs on working electrodes were irradiated with either a 530 nm LED (referred to as green light) or a 730 nm LED (referred to as red light). Control groups include lipid-wrapped Au NRs (L-NRs) without any NCs component, NCs only, and a simple mixture of L-NR and NCs (**Fig. 2.2.4**), all with identical NR and/or NC concentrations as in L-NR-NCs. Importantly, in 1 M NaOH, LSV curves of L-NR-NCs show evident light responses that lead to enhanced J_{photo} as well as earlier onset potentials around 0.3 V (*vs.* Ag/AgCl, same below unless otherwise stated) (**Fig. 2.2.3B**) compared to the dark curve or control groups. In particular, although the simple mixture control contains identical components, L-NR-NCs achieve a higher catalytic performance due to the localization of NCs in close vicinity to the NRs (**Fig. 2.2.4E, F**). The vicinity effect not only enables an efficient plasmonic enhancement of NC excitation, but also facilitates electron transfer between the two components. The superior OER photocatalytic performance for L-NR-NCs with green-light irradiation is further

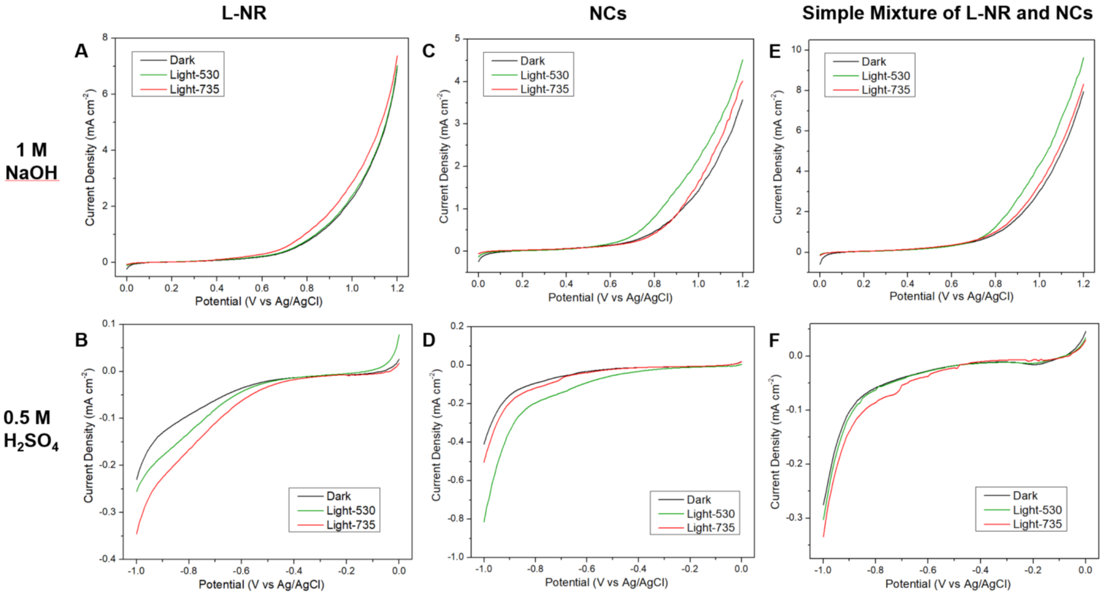

Figure 2.2.4 Photoelectrochemical Characterization of Control Groups. Reproduced with permission from Ref. 78, Copyright (2022) by American Chemical Society. (A-F) LSV curves for lipid-wrapped Au NRs control (L-NR) without the NCs (A, B), NCs only control (C, D), and a simple mixture control of L-NRs and NCs (E, F) in 1 M NaOH (top row) or 0.5 M H_2SO_4 (bottom row), measured after 100 cycles of activation in dark (black), with green-light illumination of a 530 nm LED or red-light illumination of a 730 nm LED.

evidenced by the lowest Tafel slope among all tested conditions (222 mV dec^{-1}, **Fig. 2.2.3C**). Similarly, in H_2SO_4 with red illumination, the early onset potential and high J_{photo} (**Fig. 2.2.3E**), as well as a low Tafel slope of 118 mV dec^{-1} (**Fig. 2.2.3F**) indicate superior HER photocatalytic performance.

Chronoamperometry (CA) measurements in both electrolytes reveal that the L-NR-NCs maintain robust photocatalytic properties for over 6 hours of constant performance (**Fig. 2.2.3G**). The structural and PEC stability of the L-NR-NCs provided by the lipid architecture is impressive in that it overcomes the challenge of chalcopyrite nanocrystals to dissolve quickly in acidic and neutral environments.[191, 195]

To further understand the plasmonic photocatalytic mechanism, we next probed the wavelength dependence of the catalytic J_{photo} for L-NR-NCs in NaOH and H_2SO_4 in the 100th LSV cycle by measuring J_{photo} at 9 discrete wavelengths in the range between 395 and 730 nm. The photocurrent density was then plotted over these different wavelengths. In the alkaline electrolyte, the highest J_{photo} is achieved at 530 nm (**Fig. 2.2.3H**), corresponding to the high-energy absorbance band of the nanocomposite, which corroborates our hypothesis that excitation of the quasistatic NC resonance facilitates OER photocatalysis. The photocurrent density-wavelength plot recorded in H_2SO_4 reveals an increased J_{photo} at wavelengths that coincide with the longitudinal LSPR mode at around 745 nm (**Fig. 2.2.3I**), indicative of the excitation of hot electrons from the NRs.

Additional evidence of the wavelength-dependent enhancement of OER and HER catalysis is provided by the comparison of the PEC performances of L-NR-NCs with control nanocomposites prepared with Au or Ag nanosphere (NS) cores, referred to as L-Au-NCs or L-Ag-NCs. L-Au-NCs have an absorbance band at around 530 nm associated with the resonances in NCs and Au NSs (**Fig. 2.2.5A**); whereas the LSPR of Ag NSs occurs at shorter wavelengths (420 nm) and has a weaker overlap with the NC resonance. Consequently, L-Ag-NCs show a weaker plasmonic enhancement in of the NC absorption range (**Fig. 2.2.5B**). In the alkaline electrolyte, L-Au-NCs show a high J_{photo} as well as an early onset potential of OER around 0.3 V (*vs.* Ag/AgCl) with 530 nm illumination, comparable to L-NR-NCs. This observation indicates that enhanced catalysis under resonant excitation also exists for L-Au-NCs (**Fig. 2.2.5C**). In contrast, LSV curves of L-Ag-NCs controls show only a weak catalytic effect under either green light or 430 nm

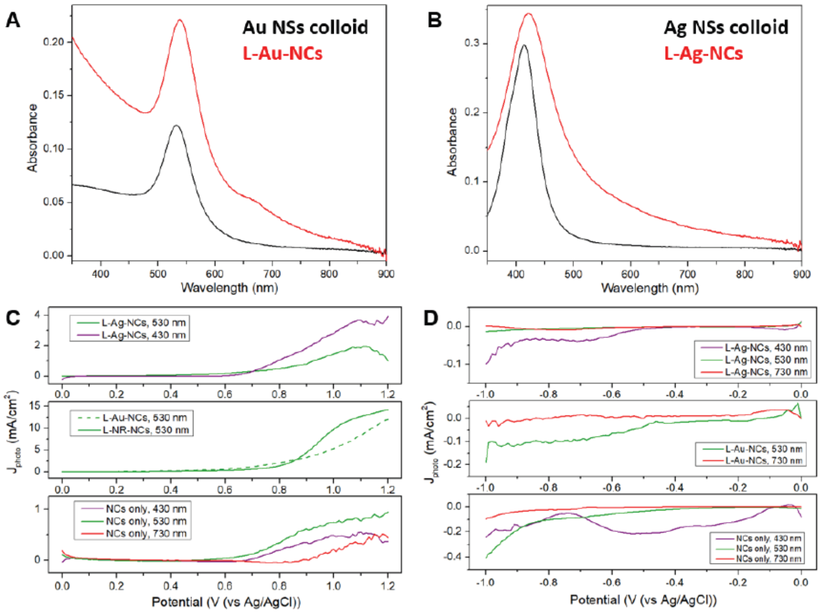

Figure 2.2.5 Characterization of L-Au-NCs and L-Ag-NCs Controls. Reproduced with permission from Ref. 78, Copyright (2022) by American Chemical Society. (A, B) UV-vis absorbance spectra of L-Au-NCs (A) and L-Ag-NCs (B) controls (red curves) prepared with Au or Ag nanospheres (black curves) at the same metal and NCs concentration as in L-NR-NCs. (C) J_{photo} curves for L-NR-NCs, L-Ag-NCs or L-Au-NCs controls, and the NCs only control in 1 M NaOH with different excitation wavelengths. (D) J_{photo} curves for L-Ag-NCs or L-Au-NCs controls and NCs only control in 0.5 M H_2SO_4 with different illumination wavelengths.

irradiation, which corroborates the hypothesis that the OER catalysis observed for L-NR-NCs derives from a plasmon-enhanced excitation of the NC resonance, and not from the metal core resonance. Notably, in acidic electrolyte, neither L-Au-NCs nor L-Ag-NCs achieved any evident HER photocatalysis under resonant excitation (**Fig. 2.2.5D**). This observation suggests that electron accumulation on NCs for HER is only efficient in hybrid structures, such as our L-NR-NCs, under excitation of a second plasmonic building block whose LSPR does not overlap with the NC resonance. The lack of a strong photocatalytic HER response at 530 nm for L-Au-NCs also provides experimental evidence that energy transfer from the metal plasmon to the NC is not a major driving factor for charge carrier

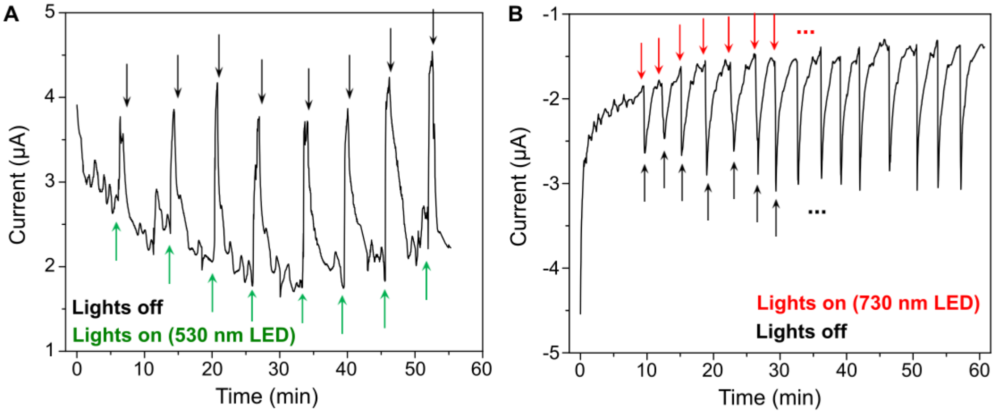

Figure 2.2.6 Photocurrent Measurement of L-NR-NCs Light Response. Reproduced with permission from Ref. 78, Copyright (2022) by American Chemical Society. (A, B) Photocurrent measured from chronoamperometry scans with an applied bias of 0 V (vs Ag/AgCl) NCs in 1 M NaOH electrolyte with or without 530 nm LED illumination (A), or in acidic electrolyte with or without 730 nm LED illumination.

formation and reactivity in case of the HER; besides, it can also evidence that the interband transition in the NCs is also not a major contributing factor for the observed catalytic behavior.

Another potential catalytic mechanism for the L-NR-NCs could be plasmonic photothermal (PPT) heating. To assess the contribution from PPT heating, calculations of the temperature increase in the vicinity of Au NRs and chalcopyrite NCs were performed according to previously reported methods.[87, 91] Given the relatively low power density of the illumination used (9.46 W/m^2), these calculations predict only a modest temperature increase ($\Delta T < 2.4$ K) under our irradiation conditions, which rule out significant contribution from PPT-induced catalysis.

The light response from L-NR-NCs in catalysis of OER and HER, respectively, could be further evidenced by photocurrent measurements from a short circuit current setup of L-

NR-NCs with alternating light-on and -off cycles and 0 V applied bias (**Fig. 2.2.6**). In both cases, steady photocurrents of around 2 μA were observed with multiple on/off cycles.

2.2.3 Cu(I)/Cu(II)-Mediated Photocatalysis

The 1st LSV scan under light irradiation contain a distinct oxidation peak onset around 0.8 V (*vs.* Ag/AgCl) in NaOH (**Fig. 2.2.3B**, solid curve), and a reduction peak onsetting at around -0.3 V in H_2SO_4 (**Fig. 2.2.3E**, solid curve). Based on their redox potentials, these two peaks can be assigned to the oxidation of the Cu(I) species in the NCs to Cu(II), and the reduction of Cu(II) to Cu(I).[196-197] Intriguingly, in the 100th LSV scan under irradiation, these peaks are no longer detected, and the overall current densities are significantly higher than in the 1st cycle for both OER and HER. We attribute the increase to an augmentation of the plasmonic catalysis by a Cu(I)/Cu(II) redox pair-coupled catalysis (**Fig. 2.2.7A**). During the LSV scans in the alkaline electrolyte, LSPR excitation can induce electron transfer from NCs to NRs. Excess electrons associated with the Au NRs subsequently transfer to the electrode under the positive applied bias, generating the anodal photocurrent. The holes remaining on the NCs in this process are neutralized through two complementing mechanisms: i.) direct plasmonic photocatalysis of water oxidation (**Fig. 2.2.7A**, process (1)), and ii.) oxidation of Cu(I) into Cu(II) oxide (process (2)).[198] The Cu(II) species generated according to the second mechanism are known to have favorable binding affinity to oxygen species and can also participate in water oxidation under regeneration of Cu(I).[199] Both OER catalytic pathways can be summarized in **Eq. 2.6**, where "x" denotes the relative contribution of the Cu(I)-mediated catalytic mechanism.[200] Excessive Cu(I)

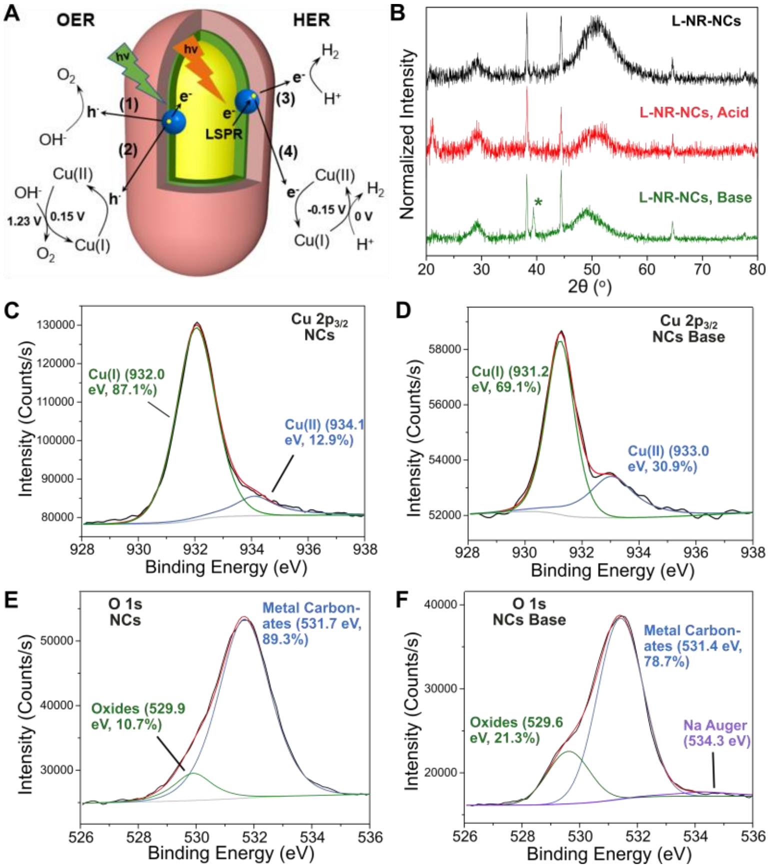

Figure 2.2.7 Characterization of the Cu(I)/Cu(II) Redox Pair After PEC Measurements. Reproduced with permission from Ref. 78, Copyright (2022) by American Chemical Society. (A) Scheme of the charge transfer and redox processes for direct plasmonic charge carrier-induced photocatalysis ((1), (3)), and Cu(I)/Cu(II)-mediated catalysis ((2), (4)). (B) XRD spectra of L-NR-NCs before any treatment (black), after cycling in 0.5 M H_2SO_4 with red light (red), and in 1 M NaOH with green light (green) for 1 hour. NC input concentrations are increased 10-fold in L-NR-NCs in this measurement compared to previous PEC measurements in order to magnify any compositional changes on the NCs. (C, D) Cu $2p_{3/2}$ XPS spectrum (black) and fittings (red) with a Shirley baseline (light grey) for NCs before any treatment (C), and after cycling in 1 M NaOH with green light for 1 min (D). (E, F) O 1s XPS spectrum (black) and fit (red) with a Shirley baseline (light grey) for NCs before any treatment (E), and after cycling in 1 M NaOH with green light for 1 min (F).

oxidation in the process of hole neutralization is, however, expected to deteriorate the optical properties and surface conductivity of the NCs, as it could gradually deteriorate the conductivity and the coherent resonance properties. This effect can account for the observation that the increase in current density in the OER diminishes after approx. 30 min as the scanning continues (**Fig. 2.2.3G**, top).

Conversely, excitation of the longitudinal NR LSPR in L-NR-NCs in H_2SO_4 results in an electron transfer from Au NR to NCs and yields an accumulation of excited electrons at the NC surface. Electron deficits on the NRs are balanced by the electrode. The excess electrons on the NCs are available not only for driving the direct HER plasmonic photocatalysis (**Fig. 2.2.7A**, process (3)), but also for reducing any surface-available Cu(II) back to Cu(I) (process (4)). Cu(I) has a standard oxidation potential of -0.15 V (*vs.* NHE), and is likely to facilitate the proton reduction reaction (0 V *vs.* NHE) while being oxidized to Cu(II) (**Eq. 2.7**), as has been shown in some previous reports.[201] The negative applied bias during HER can drive the reduction of the generated Cu(II) back to the predominant Cu(I) oxidation state in the NCs, preventing an excessive NC oxidation. As a result, different from the OER, the HER shows a steady increase in current density with increasing time (**Fig. 2.2.3G**, bottom).

$$xCu^{2+} + 4OH^- - (4-x)e^- \rightarrow O_2 + xCu^+ + 2H_2O \qquad \textbf{Eq. 2.6}$$

$$xCu^+ + 2H^+ + (2-x)e^- \rightarrow xCu^{2+} + H_2 \qquad \textbf{Eq. 2.7}$$

XRD and X-Ray Photoelectron Spectroscopy (XPS) measurements of L-NR-NCs and NCs confirm the outlined changes in the Cu oxidation states. The signature XRD diffraction peaks of the NCs and Au NRs are still observed after treatment in acid or base, which indicates that the composition of the nanocomposites are retained during the PEC measurements. XRD spectra of L-NR-NCs thin films display a distinct peak at $2\theta = 39^o$

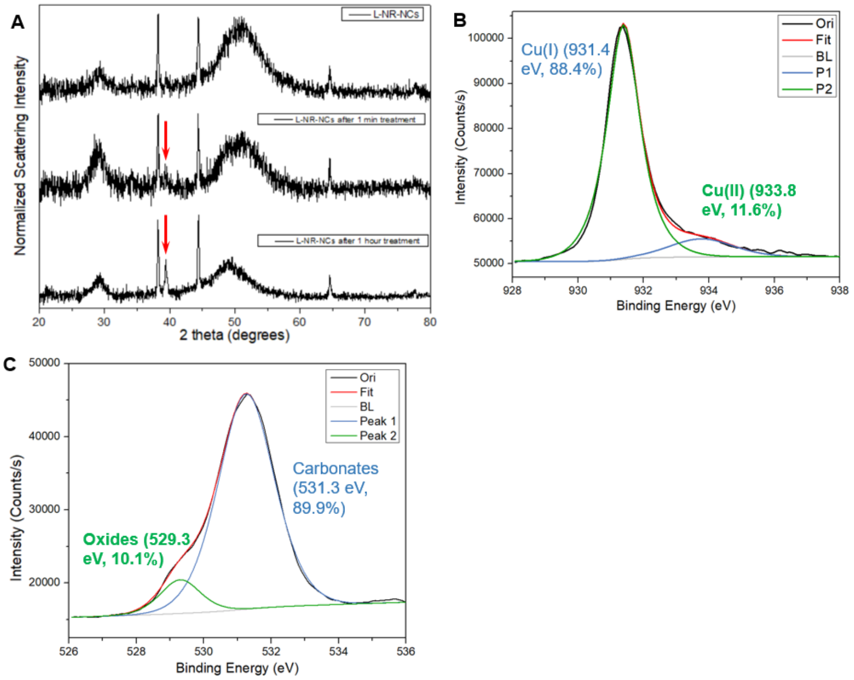

Figure 2.2.8 Supplemental Characterization of the Cu(I)/Cu(II) Redox Pair After PEC Measurements. Reproduced with permission from Ref. 78, Copyright (2022) by American Chemical Society. (A) XRD spectra of a L-NR-NCs thin film with a 10x higher NCs input concentration than in the PEC measurements before treatment (top), after 1 min (middle) and after 1 hour (bottom) scanning in 1 M NaOH, with the same applied bias and illumination conditions as used in OER measurements. (B, C) Cu $2p_{3/2}$ (B) and O 1s (C) XPS spectra of NCs after scanning in 0.5 M H_2SO_4 for 1 min with red light illumination, under the same applied bias as the HER measurements.

that appeared after scanning in base (**Fig. 2.2.7B**, bottom), consistent with the (111) peak of CuO.[202] An examination of this peak over time of treatment in base reveals that the intensity of this peak increased over treatment time (**Fig. 2.2.8A**). The intensity of this peak is very low before treatment and is absent in the spectrum after scanning in H_2SO_4 (**Fig. 2.2.7B**), suggesting that scanning in acid partially removes surface oxides. A similar trend is observed in XPS measurements. The Cu $2p_{3/2}$ XPS spectra of the NCs before any treatment contain a predominant Cu(I) peak at around 932.0 eV with a fitted peak area accounting for 87.1% of the entire signal (**Fig. 2.2.7C**). The Cu(II) contribution (12.9%) at

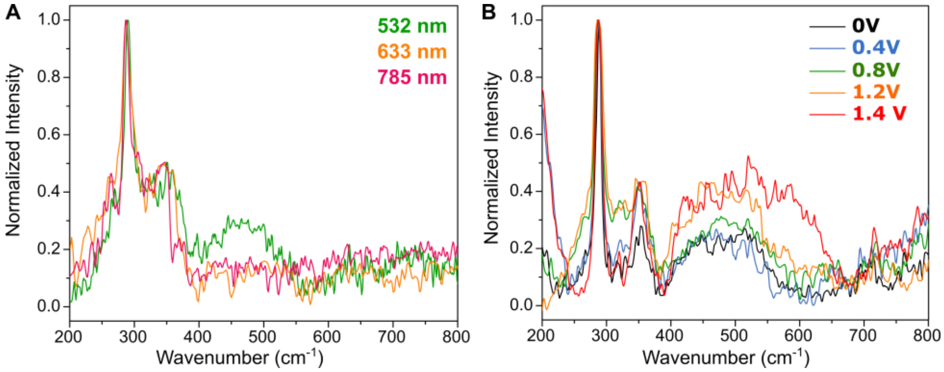

Figure 2.2.9 Raman Characterization of the OER Catalytic Mechanism of the Hybrid Plasmonic Photocatalyst. Reproduced with permission from Ref. 78, Copyright (2022) by American Chemical Society. (A) Raman spectra of L-NR-NCs drop-casted thin film at different excitation wavelengths of 532 nm (green), 633 nm (orange) and 785 nm (red). (B) Raman spectra of L-NR-NCs drop-casted thin film on ITO substrate with different applied bias in the range of 0 - 1.4 V; all spectra were collected with 532 nm excitation.

934.1 eV significantly increased after scanning in 1 M NaOH (933.0 eV, 30.9%; **Fig. 2.2.7D**).[203] A similar increase is also observed in the oxygen 1s spectra. The integrated signal that corresponds to metal oxides[204] at ~530 eV also increased from 10.7% to 21.3% (**Fig. 2.2.7E, F**). In contrast, cycling of NCs in 0.5 M H_2SO_4 reduces the contributions from both Cu(II) (933.8 eV, 11.6%) and oxides (529.3 eV, 10.1%) (**Fig. 2.2.8B, C**). Overall, the XRD and XPS results confirm that Cu(I)/Cu(II) redox pair-coupled catalysis accompanies and enhances the direct plasmonic charge transfer-induced photoreactivity.

The plasmonic charge transfer and Cu-mediated catalytic mechanisms was further evidenced by Raman spectroscopy obtained at different excitation wavelengths on or off resonance, or with on-resonance wavelength and different applied bias (**Fig. 2.2.9A**). For all excitation wavelengths, the A_1 and B_2 modes of the chalcopyrite as discussed earlier are still present, confirming the integrity of the nanocomposites after treatment. Notably, under near-resonant excitation (532 nm) of the high-energy feature of the nanocomposites, a

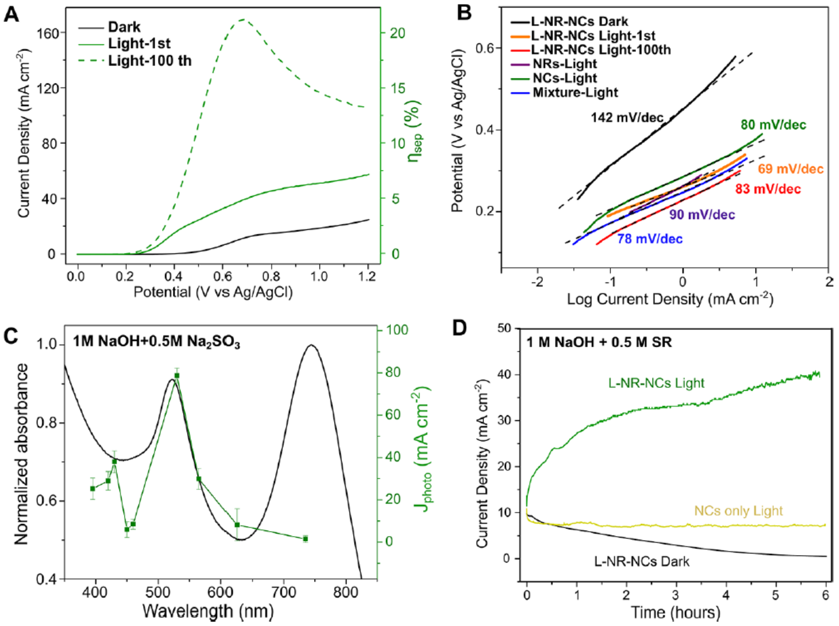

Figure 2.2.10 Study of the Plasmonic Photocatalysis with Sacrificial Reductant. Reproduced with permission from Ref. 78, Copyright (2022) by American Chemical Society. (A-B) LSV curves (A) and Tafel plot (B) of L-NR-NCs in 1 M NaOH + 0.5 M SR electrolyte with or without green light (530 nm LED) irradiation. (C) Wavelength dependence of L-NR-NCs catalytic J_{photo} in 1 M NaOH + 0.5 M SR at 0.8 V applied bias in 1 M NaOH + 0.5 M SR electrolyte. Black curve: absorbance spectrum of L-NR-NCs water suspension. Green curve: J_{photo} at different excitation wavelengths after 100 scans of activation. Error bars: Mean ± standard deviation of 3 independent measurements. (D) CA curves of L-NR-NCs with or without green light (530 nm LED) irradiation or NCs only control with green light irradiation in 1 M NaOH + 0.5 M SR electrolyte with 0.8 V (*vs.* Ag/AgCl) applied bias.

broad band is observed in the Raman spectrum between 400 and 500 cm^{-1}, which can be attributed to the presence of various oxygen species of Cu, such as oxides, hydroxides or hydroxyl radicals.[205-207] This peak is not observed with off-resonance illuminations, which confirms that the photoreactivity is derived from excitation of the NCs quasistatic resonance. We next monitored the intensity of the 400 - 500 cm^{-1} band at an excitation wavelength of 532 nm with different applied bias to probe for signatures of potential reaction intermediates (**Fig. 2.2.9B**).[80] With an applied bias at or above 0.8 V (*vs.* NHE), the intensity of the Cu hydroxide band begins to increase. At an even higher voltage input of 1.4 V, the band further broadens and extends beyond 500 cm^{-1}. This broadening is consistent with hydroxyl intermediate formation on Au as previously reported.[80] Overall, the SERS data confirm that the formation of reactive holes in the NCs of the hybrid plasmonic photocatalyst upon excitation of the NCs quasistatic LSPR band results in a Cu-mediated redox process in the OER catalysis.

To further illuminate the role of the Cu(I)/Cu(II) redox pair, a commonly used sacrificial reductant (SR) for OER photocatalysts, Na_2SO_3,[15, 208] was added into the alkaline electrolyte. The SR reduces generated Cu(II) back to Cu(I) and, thus, prevents an accumulation of oxides on the NC surface. In the 100th LSV scan of L-NR-NCs in 1 M NaOH and 0.5 M SR, a very early onset potential around 0.2 V (*vs.* Ag/AgCl) was observed as well as a high current density (J) that peaks at over 160 mA cm^{-2} at around 0.7 V (**Fig. 2.2.10A**). The Cu(I) oxidation is evidently broadened in the presence of SR due to the redox-coupling with the sulfite oxidation in the SR. The Tafel slope of L-NR-NCs irradiated in the green in the first light cycle is 69 mV dec^{-1}, lower than for all control groups under identical illumination conditions (**Fig. 2.2.10B**). The photocatalysis in the presence of the SR (**Fig. 2.2.10C**) shows a very similar wavelength dependence as observed in NaOH. In the presence of the SR, a continuous increase in J is observed during the chronoamperometry measurement (**Fig. 2.2.10D**) due to a rapid reduction of Cu(II) to Cu(I) caused by the SR. The rapid replenishment of Cu(I) sustains a continuous Cu(I)/Cu(II) catalytic cycle on the NC surface while maintaining the enhanced photocatalysis through excitation of the chalcopyrite NCs quasistatic resonance.

In the presence of the SR, the charge separation efficiency (η_{sep}) of the hybrid plasmonic photocatalyst can be calculated from the LSV curves and **Eq. 2.8**:[15]

$$\boldsymbol{\eta_{sep} = \frac{J_{photo}}{J_{abs} \times \eta_{inj}}} \qquad \textbf{Eq. 2.8}$$

where J_{photo} is the measured photocurrent density; J_{abs} is the theoretical current density, which is determined by the absorbed light power and is calculated in this work to be 799 mA cm^{-2}; and η_{inj} is the charge injection efficiency. For comparison purpose, in the presence of SR, η_{inj} was assumed to be 100% as used in previous researches.[15] These yields a maximum η_{sep} of 21.2% at 0.68 V from the LSV curve after activation.

In summary, we have demonstrated in this section that the hybrid plasmonic photocatalyst L-NR-NCs, which contains chalcopyrite nanocrystals embedded in a protective lipid layer around a Au NR, achieves bifunctional photocatalysis of HER and OER through light-induced, wavelength-controlled charge transfers.[78] The wavelength dependence of the photoelectrocatalysis in the presence of L-NR-NCs in alkaline electrolyte supports a model in which the near-field enhanced excitation of the NC quasistatic resonance at 490 nm results in electron transfer from the NCs to the NR as well as the formation of holes on the NCs surface for an efficient catalysis of the OER; conversely, excitation of the Au NR longitudinal plasmon resonance at 745 nm drives electron transfer from the NR to the NCs for HER photocatalysis in acidic electrolyte. The charge transfer-induced photocatalysis on the NCs is complemented by a Cu(I)/Cu(II) redox pair-mediated catalysis that provides further enhancement of the catalytic performance of the water splitting half reactions.

2.3 Summary of Chapter 2

We demonstrate in this Chapter an example for both (a) the E-field enhanced plasmonic photocatalytic mechanism by a plasmonic nanoantenna in a nanopigment architecture (section **2.1**),[29] and (b) plasmonic charge carrier-mediated photocatalysis in a hybrid Au NRs-chalcopyrite nanocrystal composite (section **2.2**).[78] Our work in (a) characterizes the plasmonic "sweet spot" phenomenon, balances the effects of nanoplasmonics in enhancing the photoexcitation of catalyst molecules through resonant energy transfer and in quenching of excited states, and provides a feasible approach to achieve colocalization of plasmonic nanoantenna and molecular photocatalyst through the hybrid lipid architecture. Our work in (b) broadens the applicability of semiconductor nanocrystals in plasmonic charge carrier-mediated photocatalysis, and introduces a general framework for modulating charge transfer through nanoassemblies containing multiple components with discrete quasistatic resonances at different wavelengths for multifunctional photocatalysis. Both works underline the potential of the L-NP platform for enhancing the efficiency of photocatalysis and sustainable light energy harvesting.

Future efforts to claim the full potential of these strategies should focus on expanding the spectrum of reactions catalyzed by the hybrid plasmonic nanocatalysts. For the E-field enhancement mechanism, other metal NP-catalyst pairs that possess spectral overlap in their absorbance spectra and can thus sustain resonant energy transfer could also be pursued. Although the strong resonant enhancement has enabled the use of very small amounts of $[Ru(bpy)_3]^{2+}$ in the nanopigments of around 100s ppb in our work,[29] yet additional transition-metal complexes could be utilized as alternatives in future works to potentially reduce the cost and collateral cytotoxicity of the system. For the charge transfer mechanism, the interesting possibility of producing different types of charge carrier from the same structural building block in the nanocomposite catalyst could exert favorable spatial and temporal control over the specific reaction that happens on specific parts of the catalyst and potentially facilitate the development of fuel cell whole cells, where both half reactions could be promoted simultaneously. Various different plasmonic components that satisfies the energy level and absorbance requirements could be explored in order to broaden the effective range of visible light response in the electromagnetic spectrum. Further exploration of the lipid-coated NP architecture could also lead to entirely new classes of plasmon-enhanced biomimetic nanoreactors.

Chapter 3. Plasmonic Nano-Antimicrobials

Plasmonic nanoparticles or nanocomposites possess great potentials to combine favorable light-induced antimicrobial effects with light-independent properties that are based on the surface and chemical properties of the NPs.[109] In this chapter, we introduce specific examples of how nanoplasmonic as well as photochemical properties of plasmonic silver NPs could be utilized in bacteria inactivation through simultaneous photodynamic chemotherapy (PDCT) and photocatalytic release of Ag^+ and photosensitizer molecule $[Ru(bpy)_3]^{2+}$. We test the antibacterial effect of a hybrid plasmonic photoreactor in solution, against colonized biofilms, as well as as a coating material on plastic surfaces against both Gram-positive and -negative bacteria species.[52-53] This chapter was in part reproduced and adapted with permission from Ref. 52, Copyright 2020 by American Chemical Society, and with permission from Ref. 53, Copyright 2022 by The Royal Society of Chemistry.

3.1 Plasmonic Photoreactors for Visible Light-Controlled Antibacterial Effect

In this section, we investigate the light-dependent antibacterial effect of a photoreactor bactericide architecture that integrates $[Ru(bpy)_3]^{2+}$ photosensitizer molecule in a lipid membrane around Ag NP cores.[52] The efficacy of the bactericides was tested against planktonic bacteria, including Gram-positive *Arthrobacter sp.* and Gram-negative *Escherichia coli* through systematic *in vitro* studies in solution. We demonstrate that through the plasmon-enhanced, $[Ru(bpy)_3]^{2+}$-mediated photo-oxidation of the protective hybrid lipid membrane around the Ag NP, a release of $[Ru(bpy)_3]^{2+}$, Ag^+, and peroxidized

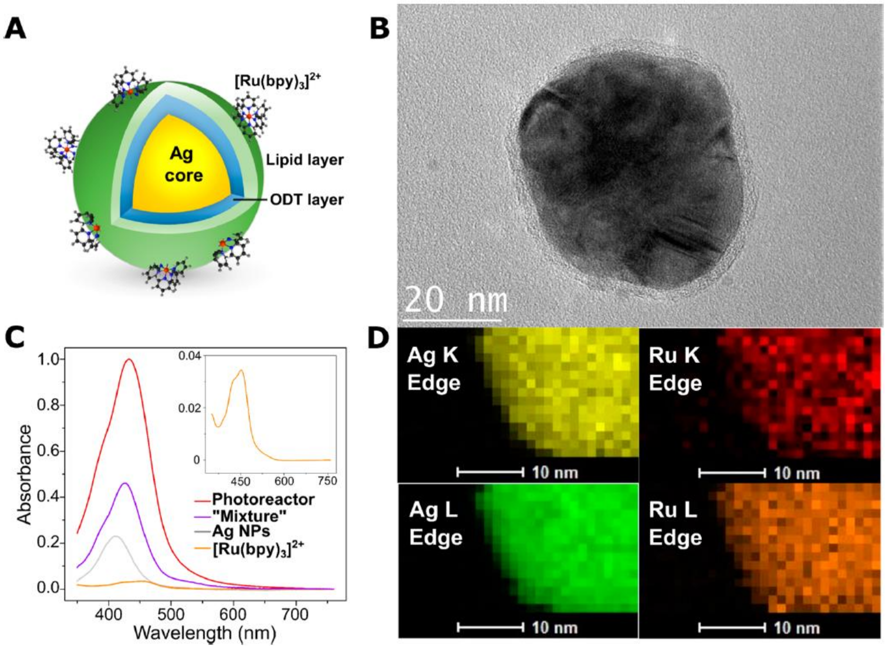

Figure 3.1.1 Structural Characterizations of the Photoreactor Bactericides. Reproduced with permission from Ref. 52, Copyright (2020) by American Chemical Society. (A, B) Scheme (A) and HRTEM micrograph (B) of a photoreactor nanocomposite. (C) UV−vis absorbance spectra of water suspensions of photoreactor nanocomposites (red), Ag NPs alone (light gray), $[Ru(bpy)_3]^{2+}$ solution (orange, inset), and a simple mixture control of Ag NP colloid and $[Ru(bpy)_3]^{2+}$ solution (purple). All controls possess identical Ag and/or Ru concentrations as the photoreactor nanocomposite. (D) EDX element maps in STEM mode for Ag and Ru K and L edges.

lipids into the ambient medium could be triggered, and the released compounds can achieve a synergistic antibacterial effect. The release rate could be controlled by adjusting the composition of the lipid membrane. The inactivation performance of the photoreactors and the synergistic interactions between the released compounds were characterized. In addition to planktonic bacteria, the antibacterial effect of the photoreactors was also quantified against colonized bacteria in a biofilm as a proof-of-concept study for materials surface sterilization.

3.1.1 Design and Preparation

A similar nanocomposite design of the photoreactor bactericide nanocomposite to the nanopigment as introduced in section **2.1.1** is utilized in this work.[29] $[Ru(bpy)_3]^{2+}$ is localized around a Ag nanoantenna core (around 45 nm in diameter) by a self-assembled hybrid lipid layer (**Fig. 3.1.1A**), which ensures both biocompatibility of the hybrid structure and pins the photocatalyst within the enhanced E-field of the plasmonic nanoantenna when irradiated. The spectral overlap between the LSPR of Ag NPs and the MLCT band of $[Ru(bpy)_3]^{2+}$ enables a substantial resonant plasmonic enhancement of the MLCT and photoreactivity of $[Ru(bpy)_3]^{2+}$, as has been previously demonstrated.[29, 46] The composition of the lipid layer was inspired by biological membranes,[17] and are customized with a high degree of unsaturated membrane component, as they have been shown to undergo peroxidation[209] for a light-controlled release of Ag^+ and $[Ru(bpy)_3]^{2+}$. An increased concentration of $[Ru(bpy)_3]^{2+}$ is incorporated compared to section **2.1** in order to facilitate a stronger photocatalytic release. Specifically, the membrane contained 47 mol% zwitterionic lipid DPPC, 4.5 mol% negatively charged lipid DOPS, 35 mol % cholesterol, and 13.5 mol% $[Ru(bpy)_3]^{2+}$. An octadecanethiol (ODT) layer that binds covalently to the metal and sustains hydrophobic interaction with the lipids was still used as an intermediate layer in the hybrid membrane. High-resolution transmission electron microscopy (HRTEM) image of the photoreactor nanocomposites confirms a uniform self-assembled lipid membrane close to the Ag surfaces (**Fig. 3.1.1B**). Statistical analysis of 30 randomly chosen NPs reveals an average membrane width of 5.7 ± 1.3 nm. As demonstrated in our previous work and introduced in section **2.1**,[29] the preferential localization of $[Ru(bpy)_3]^{2+}$ in the direct vicinity of the metal NPs enables an efficient E-field-enhanced photoexcitation of $[Ru(bpy)_3]^{2+}$. This is confirmed by the UV-vis absorbance spectra measurements, where substantial enhancement of the absorbance band for the photocatalysts MLCT in the photoreactors (red) is observed around 430 nm compared to an aqueous solution of $[Ru(bpy)_3]^{2+}$ (orange, inset), or a simple mixture control of Ag colloid and $[Ru(bpy)_3]^{2+}$ solution (purple) (**Fig. 3.1.1C**). All control groups possess identical Ag and/or Ru concentrations as the photoreactor nanocomposite.

Element mapping results generated by EDX provide evidence of the spatial colocalization of Ru and Ag within the photoreactor nanocomposite boundary (**Fig. 3.1.1D**), further corroborating the successful wrapping of the photocatalyst $[Ru(bpy)_3]^{2+}$ around Ag NP cores. The concentration of the specific compositions of the photoreactor nanocomposites were quantified by measurement of the element concentration with inductively coupled plasma-mass spectrometry (ICP-MS). An average ^{107}Ag concentration of 3835 ± 262 ppb and ^{101}Ru concentration of 528 ± 4 ppb were measured for the photoreactor suspension, which were used throughout this work for standard photoreactor bactericides and controls unless otherwise noted.

The E-field-enhanced photocatalytic properties of the photoreactors provide a rational strategy for triggering the release of Ag^+ and $[Ru(bpy)_3]^{2+}$ through a visible light-induced, $[Ru(bpy)_3]^{2+}$-catalyzed oxidation of the hybrid lipid membrane. The release of Ag^+ (**Fig. 3.1.2A, B**) and $[Ru(bpy)_3]^{2+}$ (**Fig. 3.1.2C**) from the photoreactors upon illumination with 430 nm LED (power density: 9.76 mW cm^{-2}) or in the dark as a function of time was quantified through ICP-MS. ^{107}Ag and ^{101}Ru concentrations in the supernatant after

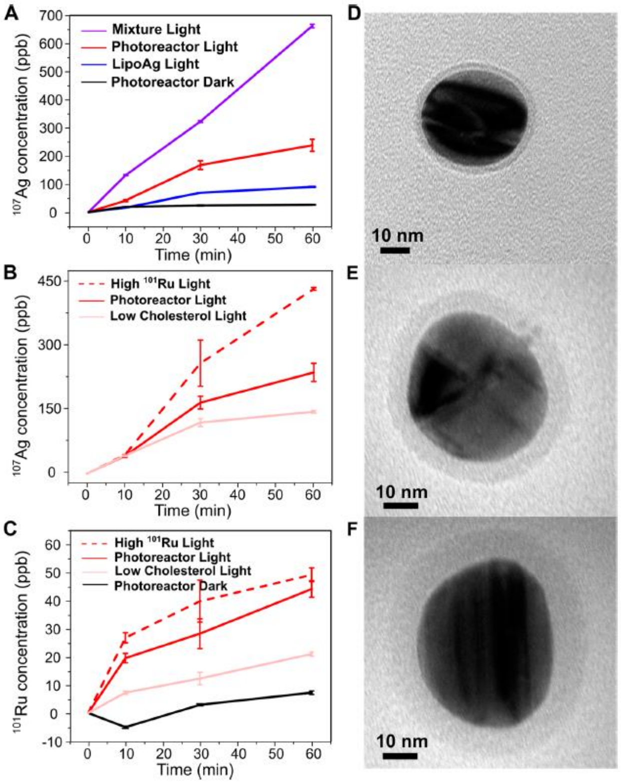

Figure 3.1.2 Characterization of the Light-Induced Ion Release by the Photoreactor Bactericides. Reproduced with permission from Ref. 52, Copyright (2020) by American Chemical Society. (A-C) ICP-MS results of Ag^+ release measured by ^{107}Ag concentration (A and B) and $[Ru(bpy)_3]^{2+}$ release measured by ^{101}Ru concentration (C) over time. "Mixture Light": simple mixture control of unwrapped Ag NPs and $[Ru(bpy)_3]^{2+}$ with light; "High ^{101}Ru Light": photoreactor control with 857 ppb ^{101}Ru with light; "LipoAg Light": lipid-wrapped Ag NPs without $[Ru(bpy)_3]^{2+}$ with light; "Low Cholesterol Light": photoreactor control with 20 mol% cholesterol with light. Error bars: Mean ± standard deviation of 3 independent tests. (D-F) TEM images of the photoreactor bactericides before illumination (D), after illumination for 1 hour (E), and for 3 hours (F). Scale bars: 10 nm.

removal of the nanocomposites through centrifugation were measured to account for the released molecular or ion concentrations. Almost no release from photoreactors could be observed in dark (black). Upon illumination, the plasmonic photoreactors ("Photoreactor Light", red) exhibited fast release for both elements. The release rates are evidently larger than that of the lipid-wrapped Ag NPs control with no $[Ru(bpy)_3]^{2+}$ under the same illumination condition ("LipoAg Light", blue). After LED illumination for 1 hour, 237 ppb

^{107}Ag and 44 ppb ^{101}Ru were released from the photoreactor nanocomposite into the solution, respectively representing 6.2% and 8.3% of the total.

Importantly, the release rate of the ions could be controlled by altering the concentration of the photocatalyst loaded in the membrane. This is evidenced by the faster release of Ag^+ and $[Ru(bpy)_3]^{2+}$ by control photoreactors containing a higher photocatalyst loading (^{101}Ru concentration of 857 ppb) ("High ^{101}Ru Light", dashed red line, **Fig. 3.1.2B, C**) than regular photoreactors (528 ppb). The concentration of the unsaturated components, such as cholesterol in the photoreactor membrane also has a significant effect on the light-mediated release rate. A larger release is observed from a membrane-wrapped nanocomposite with a larger cholesterol input (**Fig. 3.1.2B, C**).

The release of cations from the photoreactors results from morphological changes and increase in permeability of the hybrid lipid membrane induced by photo-oxidation. This can be evidenced by the TEM images of the membrane layer before or after illumination. Before illumination, a uniform, an intact lipid membrane layer is observed on the photoreactor surface (**Fig. 3.1.2D**). However, after illumination for 1 hour, the density of the membrane layer around the NPs started to decrease, indicated by the lower electron contrast; while its width increased from 5.7 ± 1.3 nm to 7.7 ± 2.5 nm. These observations points at a less densely packed membrane layer (**Fig. 3.1.2E**). After 3 hours of illumination, the density of the membrane layer further decreased (**Fig. 3.1.2F**). This photoinduced change in the density and morphology of the photoreactor lipid membrane can accounted for by a continuous lipid peroxidation. As has been previously demonstrated,[209-212] the peroxidation of unsaturated phospholipids (*e.g.*, DOPS) and cholesterol by reactive oxygen species (ROS) and/or photosensitizers can result in the generation of negatively charged carboxylates, lipid hydroperoxides such as 6-OOH-cholesterol or PS-OOH, and truncated lipid aldehydes.[209] The migration of lipid peroxidation products to the membrane/water interface as well as the electrostatic repulsion of the negatively charged peroxidation products can lead to an increase in membrane surface area and membrane thickness, consistent with our observations. The photo-driven lipid peroxidation of the photoreactor lipid membrane transforms the membrane from a dense, closely packed state into a disordered, expanded state with a lower density, increasing the ion permeability and leading to ion leakage across the partially photo-oxidized membrane architecture. Thus, the photoreactor nanocomposites serves as Ag^+ and $[Ru(bpy)_3]^{2+}$ reservoirs in dark, while visible light illumination triggers the change in the membrane permeability to induce the release of Ag^+ and $[Ru(bpy)_3]^{2+}$ into the solution.

3.1.2 Characterization of Antibacterial Effect in Solution

The visible light-induced morphological transformation of the membrane provides a reliable control mechanism for regulating Ag^+ and $[Ru(bpy)_3]^{2+}$ release both spatially and temporally through an external cue, and could potentially enable an effective antibacterial pathway. To quantify the bactericidal efficacy of the photoreactor bactericides in solutions, we first used *Arthrobacter sp.*, a Gram-positive soil bacterium, as test species. *Arthrobacter sp.* has been shown to chemically reduce high-valence metal cations, and, therefore, presents a relevant and meaningful test case for metal-based bactericides.[213-214] The

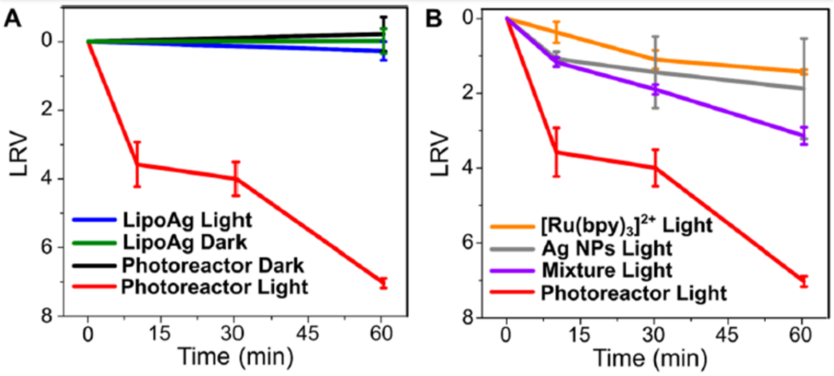

Figure 3.1.3 Characterization of the Antibacterial Property of the Photoreactor Bactericides. Reproduced with permission from Ref. 52, Copyright (2020) by American Chemical Society. (A) Inactivation LRV curves for *Arthrobacter sp.* with photoreactor bactericides and LipoAg control with or without 430 nm LED photoactivation. (B) Inactivation LRV curves for *Arthrobacter sp.* with control groups of Ag NPs only, $[Ru(bpy)_3]^{2+}$ only, and a simple mixture control of Ag NPs and $[Ru(bpy)_3]^{2+}$. All controls possess identical Ag and/or Ru concentrations and illumination condition with the 430 nm LED. Error bars: Mean ± standard deviation of 3 independent tests.

antibacterial effect of the photoreactor bactericides and controls were recorded either in the dark or with illumination from a 430 nm LED. A photoreactor NP:bacterium ratio of 100:1 was used, and the log reduction values (LRVs) of colony-forming units (CFUs) were calculated as a function of time to quantify bacterial inactivation efficacy according to **Eq. 1.12**. An LRV ≥ 3 is considered standard for bactericidal activity.[109, 215] The antibacterial effect of the 430 nm LED illumination alone was subtracted from all experimental conditions with illumination to exclude inactivation caused by illumination only.

As shown in **Fig. 3.1.3A**, the photoreactor bactericide does not achieve any measurable inactivation in dark (black) as expected, which confirms the high biocompatibility that arises from the hybrid lipid architecture. Importantly, when illuminated, the photoreactor bactericides (red) demonstrate a rapid inactivation of *Arthrobacter sp.*, and an LRV of 7.03 (± 0.14) is determined after photoactivation for 1 hour. In sharp contrast, the LipoAg

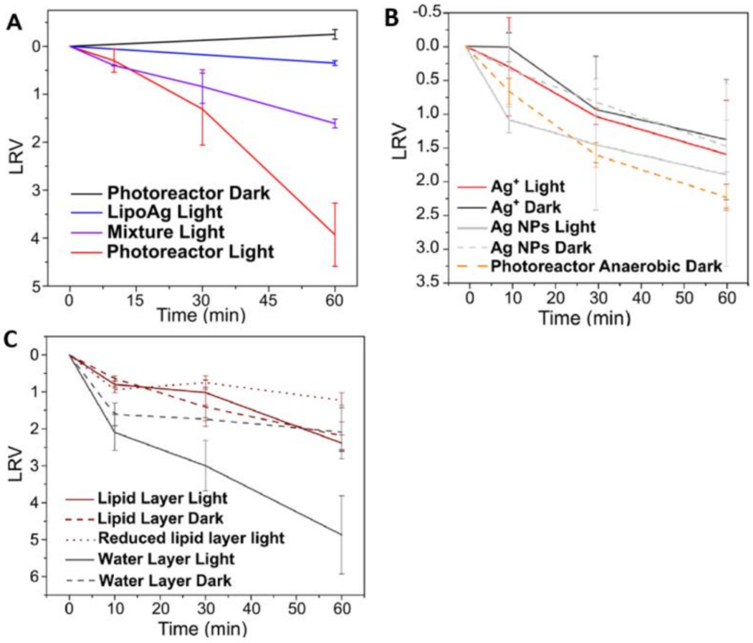

Figure 3.1.4 Supplemental Characterization of the Antibacterial Property of the Photoreactor Bactericides. Reproduced with permission from Ref. 52, Copyright (2020) by American Chemical Society. (A) Antimicrobial LRV curves against Gram-Negative bacteria *E. coli*. (B, C) Inactivation LRV curves of *Arthrobacter sp.* with control conditions. Error bars: Mean ± standard deviation of 3 independent tests.

control did not show any significant bacterial inactivation, which proves that it is indeed the plasmon-enhanced photocatalysis of $[Ru(bpy)_3]^{2+}$ that led to the bactericidal performance instead of photothermal effect or optically induced hot carrier redox chemistry.

A Gram-negative bacterium strain, *E. coli* was also used as test case in order to probe the broad-band inactivation efficacy of the photoreactors (**Fig. 3.1.4A**). An LRV of 3.93 (± 0.66) was recorded for this group after photoactivation for 1 hour. The LRV against *E. coli* is lower compared to that of *Arthrobacter sp.* This can be partly ascribed to the presence of an extra outer membrane layer in *E. coli*, which is absent in Gram-positive strains and makes the Gram-negative strain more resistant.[12, 109, 216]

To understand the role of the individual components of the photoreactor nanocomposite in the inactivation process, the LRVs were measured with *Arthrobacter sp.* from each of the individual components or simple mixture controls. As shown in **Fig. 3.1.3B** and **Fig. 3.1.4B**, neither did Ag NPs or Ag^+ alone at the same concentration as used in the photoreactors (with or without illumination) achieved significant inactivation effect. Both groups led to low LRVs < 2, likely due to the reducing power and metal resistance of *Arthrobacter sp*. The free $[Ru(bpy)_3]^{2+}$ complex achieved LRVs of 1.43 (± 0.06) after photo-activation for 1 hour (**Fig. 3.1.3B**, orange) and 0.66 (± 0.23) in the dark. The inactivation performance in dark indicates toxicity of the complex due to ground state reactivity. The simple "mixture" control (**Fig. 3.1.3B**, purple), which lacks the preferential localization of $[Ru(bpy)_3]^{2+}$ within the evanescent E-field of the Ag NPs, achieves an LRV of 3.14 (± 0.23) with light, which is almost 4 orders of magnitude weaker than the photoreactor bactericides (LRV = 7.03). This dramatic difference further emphasizes the importance of the hierarchical photoreactor structure for maximizing antibacterial efficacy.

Since the peroxidized lipid components could also be bactericidal, these compounds were separated from the photoreactor bactericide with chloroform after photo-activation for 1 hour, and their LRVs against *Arthrobacter sp.* were determined (**Fig. 3.1.4C**). LRVs of 2.19 (± 0.38) and 2.39 (± 0.22) were obtained respectively without and with 430 nm LED photoexcitation. The similar values with or without light for the peroxidized lipids indicates that the effect of these compounds is largely light-independent. The antibacterial effect of the peroxidized lipids was further corroborated by adding a reducing agent to the isolated compounds prior to their incubation with the bacteria, in order to remove the peroxidized products. This treatment reduced the rate of bacterial inactivation of the peroxidation products by 1 order of magnitude (LRV = 1.23 ± 0.20) (**Fig. 3.1.4C**, dotted brown curve) with *Arthrobacter sp.*, confirming that the peroxidized lipid species indeed contributed to the net antibacterial effect. Importantly, the LRV of the photoreactor (7.03) significantly exceeds the sum of individual components of Ag NPs, $[Ru(bpy)_3]^{2+}$, and peroxidized lipid components (5.53), which indicates a strong synergistic gain between the released bactericidal chemicals.

To further characterize the light-controlled Ag^+ and $[Ru(bpy)_3]^{2+}$ release pathway and associated inactivation mechanisms, the bacterial inactivation experiments were repeated with photoreactors under anaerobic conditions. The photoreactor-associated LRV for *Arthrobacter sp.* was 2.21 ± 0.19 without light (**Fig. 3.1.4B**), and 2.13 ± 0.44 with 430 nm LED illumination (**Fig. 3.1.5A**, red dashed line) after treatment under anaerobic conditions for 1 hour. These reduced values compared to aerobic conditions clearly show that O_2 is a key factor in the activation of the antibacterial properties of the photoreactors. The low LRVs achieved under anaerobic conditions could be due to the light-independent ground state reactivity of the photocatalyst, and/or formation of ROS from reactions with H_2O molecules through photoinduced water oxidation reactions. Based on these observations, we hypothesized that the photoreactivity of $[Ru(bpy)_3]^{2+}$ in the presence of O_2 can lead to production of ROS, which then induces lipid membrane peroxidation in the photoreactors and subsequently initiates membrane permeabilization and the release of antibacterial Ag^+ and $[Ru(bpy)_3]^{2+}$ into the ambient solution.

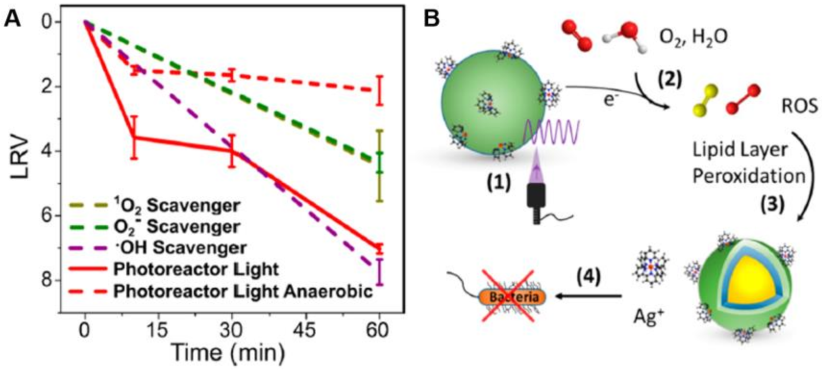

Figure 3.1.5 Characterization of the Antibacterial Mechanisms of the Photoreactor Bactericides. Reproduced with permission from Ref. 52, Copyright (2020) by American Chemical Society. (A) Inactivation curves for *Arthrobacter sp.* with photoreactor bactericides under anaerobic conditions or with singlet oxygen ($^1O_2$), superoxide (O_2•$^-$), and hydroxyl radical (•OH) scavengers. Error bars: Mean ± standard deviation of 3 independent tests. (B) Scheme for the light-controlled cation release and inactivation pathway of the photoreactor bactericides.

To evidence our hypothesis of the role of ROS, the inactivation assays were next performed in the presence of ROS scavengers. The effect of three types of ROS that are likely to be generated from $[Ru(bpy)_3]^{2+}$ in H_2O in the presence of O_2: singlet oxygen ($^1O_2$), superoxide anion ($O_2^{\bullet-}$), and/or hydroxyl radicals (•OH) are probed.[217-219] ROS scavengers sodium azide (for $^1O_2$), MnTBAP (for $O_2^{\bullet-}$), and mannitol (for •OH) were applied, as demonstrated previously.[40] As shown in **Fig. 3.1.5A**, both $^1O_2$ (dashed brown line) and $O_2^{\bullet-}$ (dashed green line) scavengers significantly reduce the levels of inactivation of the bactericides to similar extent, which indicates that these two types of ROS could be generated. •OH scavengers (dashed purple) do not obviously affect the antibacterial activities. This could be due to the relatively short lifetime of •OH (half-life of 10^{-9} s) compared to those of the other two species (half-lives of 10^{-6} s).[220]

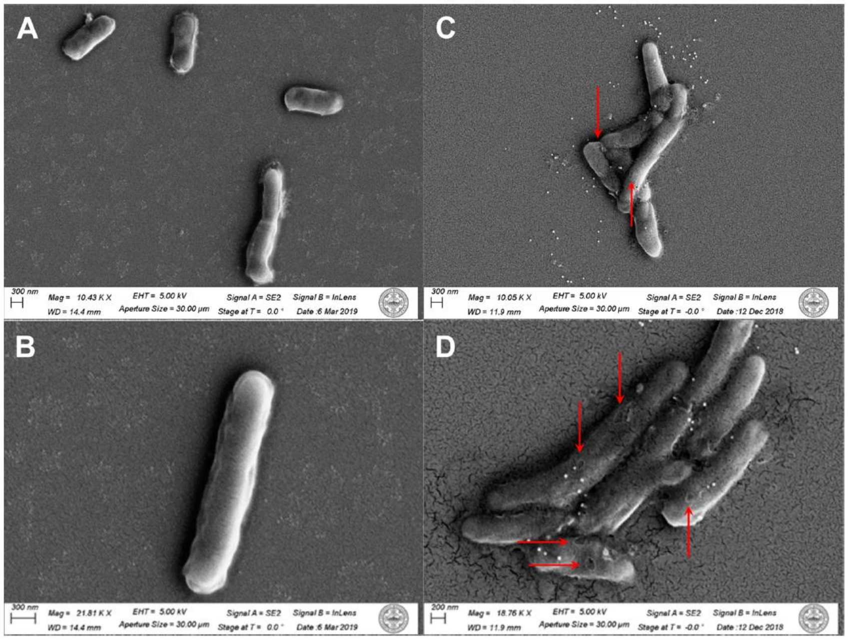

Figure 3.1.6 Characterization of Bacterial Surface Structural Damage After Photoreactor Bactericides Treatment. Reproduced with permission from Ref. 52, Copyright (2020) by American Chemical Society. (A-D) SEM images of *Arthrobacter sp.* without inactivation (A, B) or after illumination for 1 hour in the presence of photoreactor bactericides (C, D).

These released ROS and cations can lead to surface structural damage on *Arthrobacter sp.* cells, as indicated by a comparison of SEM images of the cell morphology before and after inactivation (**Fig. 3.1.6**). Intact bacteria cell surface can be seen without any inactivation (**Fig. 3.1.6A, B**). Notably, after inactivation with the photoreactors and LED illumination, a large number of pores appeared on the bacterial surface (**Fig. 3.1.6C, D**), which indicates that the effect of the photoreactors is localized on the surface of the bacteria. The surface structural damage observation is consistent with earlier Ag-based antibacterial research.[140] Ag^+ cations can bind to surface proteins that contain amino acids with thiol (-SH) groups, such as cysteine.[221] The oxidative properties of the released photocatalyst molecule $[Ru(bpy)_3]^{2+}$ in our case could further accelerate the membrane perforation effect through inducing photoredox-associated peroxidation processes[209, 211] and, thus, contribute to the experimentally observed efficient membrane perforation. Such damage to the cell surface affects the osmotic pressure balance across the cell membrane. Furthermore, damage of the cell surface could also cause permeation of the bactericidal components into bacteria cells for intracellular damage. Both factors could eventually lead to cell death.

On the basis of the analyses presented above, the inactivation mechanism of the photoreactor bactericides could be summarized in **Fig. 3.1.5B**. Upon resonant illumination of the Ag NPs LSPR, an intense E-field can be generated for resonant enhancement of the photoexcitation of $[Ru(bpy)_3]^{2+}$ MLCT. This process generates Ru*(II) photoexcited state, which can react primarily with O_2 to produce various ROS. ROS can then induce peroxidation of cholesterol and unsaturated phospholipids in the hybrid lipid layer of the photoreactors, and change the chemical composition and permeability of the hybrid lipid membrane. These changes result in the release of Ag^+ ions, membrane-bound $[Ru(bpy)_3]^{2+}$, and peroxidized lipid products into the aqueous solution. In the medium, the ions can subsequently achieve superior and synergistic antibacterial effects through inducing structural damage on the cell surfaces. The visible light-controlled ion release is subject to spatial and temporal control through the chosen illumination conditions, which could be used to localize the antibacterial effect.[52]

3.1.3 Characterization of Antibacterial Effect against Biofilms

The superb inactivation performance of the photoreactor bactericides against planktonic bacteria in solution motivates further characterization of their efficacy against bacterial

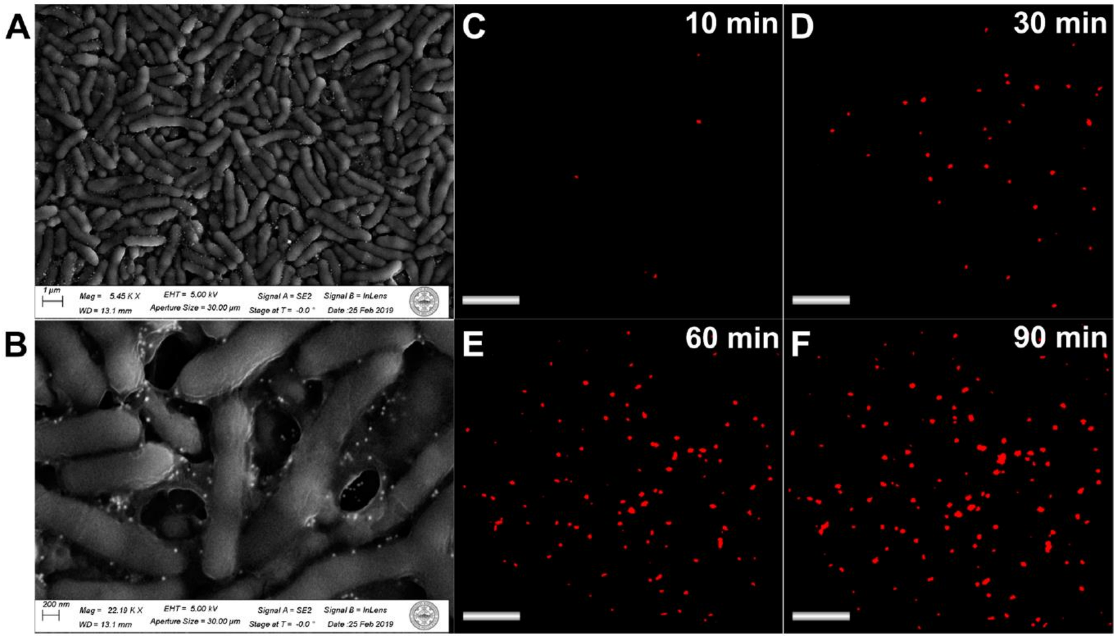

Figure 3.1.7 Characterization of Inactivation of Bacterial Biofilm by Photoreactor Bactericides. Reproduced with permission from Ref. 52, Copyright (2020) by American Chemical Society. (A, B) SEM images of the biofilm incubated with photoreactor bactericides before inactivation. (C−F) Fluorescence images of the biofilm after staining with propidium iodide and after illumination by white light from the halogen lamp and inactivation for 10 (C), 30 (D), 60 (E), and 90 (F) min. Scale bars: 4 µm.

biofilms. Biofilms contain bacteria embedded in a complex extracellular matrix (ECM), which is composed of polysaccharides, proteins, and nucleic acids secreted by the cells. Biofilms are very meaningful test targets for bactericides because the protective function of the ECM could typically render bacteria in a biofilm more resilient against conventional antibacterial agents.[222-223] Thus, growth of biofilms on materials surfaces, particularly on the surfaces of tubings and medical appliances, can pose serious threats to human health. These factors motivate the development of new strategies for combating bacterial biofilms.

In this section, the efficacy of the photoreactor bactericides against resilient bacterial biofilms is tested. *Arthrobacter sp.* was cultured into biofilms on silicon wafers and glass

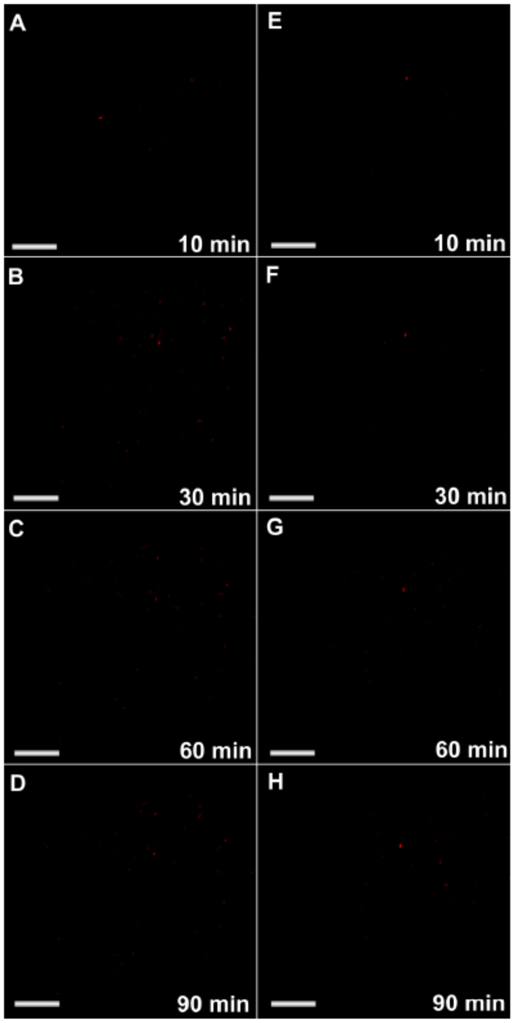

Figure 3.1.8 Characterization of Inactivation of Bacterial Biofilm by Control Nanocomposites. Reproduced with permission from Ref. 52, Copyright (2020) by American Chemical Society. (A-D) Fluorescence images of the biofilm with white light illumination from the halogen lamp but with no photoreactor nanocomposites taken at 10 min (A), 30 min (B), 60 min (C) and 90 min (D). (E-H) Fluorescence images of the biofilm with photoreactor nanocomposites in dark taken at 10 min (E), 30 min (F), 60 min (G) and 90 min (H). Scales bars: 4 μm.

slide substrates in peptone yeast extract glucose medium for 7 days in the dark at 28 °C according to previously reported protocol.[222] The biofilm was then incubated with the photoreactor bactericides (10^{10} NPs mL^{-1}) at room temperature for 1 hour. Densely packed bacteria connected by the ECM can be observed in the biofilm after culture from scanning electron microscopy (SEM) micrographs (**Fig. 3.1.7A, B**). The photoreactor-treated bacterial biofilm samples were then covered by a glass slide and illuminated with white light from a halogen lamp (power density: 105 mW cm^{-2} in the sample plane) for 90 min for inactivation. Afterwards, propidium iodide (PI) staining and FL imaging were used to monitor the inactivation efficacy at 10, 30, 60, and 90 min (**Fig. 3.1.7C−F**). PI cannot permeate intact cell membranes, and is thus specific to dead or dying cells. An increase in PI fluorescence intensity in the film is observed as a function of time, confirming that the photoreactors are effective against the biofilm. Control groups were also tested with (a) biofilms exposed to visible light illumination in the absence of photoreactors, and (b) biofilms mixed with photoreactors but without photo-activation. Neither control demonstrated noticeable FL signal from the PI staining associated with inactivation even after 90 min (**Figure 3.1.8**), confirming that the inactivation performance indeed results from the photo-induced effect of the photoreactor bactericides.

In summary, we have demonstrated in this section visible light-controlled bacteria inactivation through a hybrid photoreactor bactericide architecture incorporating Ag NPs as plasmonic nanoantenna and $[Ru(bpy)_3]^{2+}$ as a photoredox catalyst.[52] The hybrid nanostructures are stable and biocompatible in the absence of illumination, while low-power visible illumination is able to initiate the release of Ag^+, $[Ru(bpy)_3]^{2+}$, and peroxidized lipids from the photoreactors into ambient medium through photocatalytic permeabilization of the hybid lipid membrane. These released species can cause structural damage to bacterial surface, and ultimately leads to cell death. Our photoreactor bactericide approach is effective against both planktonic Gram-positive and -negative bacteria. > 7 orders of magnitude reduction in *Arthrobacter sp.* CFUs and ∼4 orders of magnitude reduction for *E. coli* were recorded. In addition, the photoreactor nanocomposites also achieved effective inactivation of colonized bacteria in the form of a biofilm and is potentially relevant for sterilization of biofilm-plagued materials surfaces.

3.2 Plasmonic Antibacterial Coating Enabled by Plasmonic Photoreactors

Bacterial colonization on materials surfaces could be a major health risk to humans. Thus, sterilization of materials surfaces is important to prevent the infection of microbial pathogens and the spread of infectious diseases.[224-225] In particular, sterilization of plastic surfaces is crucial, as plastics are ubiquitous in many sensitive daily applications, such as as catheters;[226-227] or as integral components of medical devices or industrial instruments.[228-231] In these applications, plastic devices are routinely sterilized through conventional sterilization techniques. However, microbial colonization and biofilm formation could still occur under continuous use. This is well recognized and led to the development of numerous antimicrobial coatings for polymer and other sensitive surfaces.[225, 232-235]

Antibacterial coatings are generally classified into two categories.[232-234] The first type are “passive” coatings that repel bacteria, typically through nanostructured hydrophobic compounds that induce anti-fouling properties and trigger bacterial growth inhibition.[236-238] On the other hand, the second category are “active” coatings that directly inactivate the microbes. This can be achieved through different strategies including antibacterial polymers, peptides and surfactants;[239-242] carbon-based materials such as graphene and fullerene;[243-244] or metal-based nanostructures that can release metal cations as bactericides or that trigger photophysical inactivation pathways,[227, 232, 245] as introduced in section **1.4**. Silver is among one of the most commonly used metal-based antimicrobial coating materials.[227, 232, 244, 246-247] Microbicidal compound-releasing materials scaffolds are another notable example of active antimicrobial coatings.[248-249] These scaffolds have, in some cases, been combined with release strategies triggered by external cues for controlled bactericidal performances.[250]

These antimicrobial coating materials developed in previous research have been shown to be useful for the disinfection of sensitive materials surfaces as well as for preventing microbial infection in both *in vitro* and *in vivo* tests. Furthermore, antibacterial coatings, particularly those with active bactericidal properties, have also enabled flow-through bacteria inactivation devices.[251-253] These flow devices reported thus far utilize (a) light illumination-induced photoreactivity either enhanced in the presence of wide-bandgap semiconductors[251] or non-enhanced,[254] or (b) photothermal effects by plasmonic and carbon-based materials[252-253] to potentially achieve efficient and broad-band inactivation of microbes in contaminated water, other liquids, and in air.

However, despite these great achievements, several important factors still limit the development and efficacy of current antibacterial drugs, coatings, and other strategies. Firstly, rapidly evolving microbial resistances jeopardize the efficacy of current antimicrobials.[12] Furthermore, although effective, many of the conventional antimicrobial strategies lack degrees of specificity in their effect, which excludes them from numerous applications. As one example, the effect of conventional sterilization techniques based on heat, high pressure, or UV radiation are typically non-discriminative. Thus, although they are efficient in inactivating bacteria, they could also lead to collateral damage to mammal cell components, and are thus challenging to sterilize media containing sensitive biologics, such as monoclonal antibodies, due to loss of activity; or protein-rich foods, such as soymilk, without denaturation of macromolecular nutrients.[255-256] Nor are they applicable to sterilization of infected wounds in mammals without inducing severe collateral damage to healthy mammal cells. Given these challenges, there is a need for robust, selective and energy-efficient alternatives that ideally combine both active and passive antibacterial capabilities and that provide a strong antibacterial effect without the need of dedicated or energy-intensive equipment.[257]

The superb visible light-controlled bactericidal properties of the plasmonic photoreactors introduced in section **3.1**[52] indicates great promise as an antimicrobial coating that combines active and passive bactericidal functionalities. In this section, we assess the effect of the plasmonic photoreactors as an antimicrobial coating material on plastic surfaces, and implement effective flow sterilizers for flow-through bacteria inactivation based on photoreactors-coated plastic tubings.[53] We demonstrate that the plasmonic photoreactor coating achieves (a) active flow-through inactivation of bacteria suspensions up to LRVs around 5 for both Gram-positive and -negative bacterial suspensions; and (b) passive biofilm growth inhibition on plastic slides in the presence of ambient light. The shelf life and recycled use performance of the flow sterilizer are assessed. Importantly, antibodies in the bacteria-containing medium do not show evident functional degradation during the antibacterial treatment, indicating that the plasmonic antimicrobial flow sterilizers are applicable for sterilizing sensitive biologics without detrimental effects on their functions. The photoreactor coatings also show a much weaker reduction of the growth of mammal cells cultured on the coated surfaces compared with bacteria, which reveals degrees of selectivity of the approach against bacterial cells.[53]

3.2.1 Design and Preparation

Plasmonic photoreactor nanocomposites were prepared and characterized in similar approaches as previously reported[29, 52] and as described in section **3.1.1**. Each nanocomposite comprises a Ag NP core encapsulated by a $[Ru(bpy)_3]^{2+}$-loaded hybrid lipid membrane, which contains an outer lipid monolayer assembled on an inner octadecanethiol (ODT) layer (**Fig. 3.2.1A, B**). Average hydrodynamic diameters of 57.3 ± 6.8 nm, ζ-potential of -30.5 ± 7.8 mV, and membrane width of 3.1 ± 1.1 nm were measured for the nanocomposites.

Two plastic components and topologies, low-density polyethylene (LDPE) tubing and polyvinyl chloride (PVC) slides were chosen as test platforms to evaluate the photoreactors coatings' role as antimicrobial layer for plastics. PVC slides were purchased from VWR (82027-788), and LDPE tubings from Scientific Commodities, Inc. (0.023'' inner diameter: Catalog #BB31695-PE/3; 0.066'' inner diameter: Catalog #BB31695-PE/11). Both polymers are frequently used polymers for daily appliances and biomedical equipment[229-230] and are meaningful test targets for materials surface sterilization. The

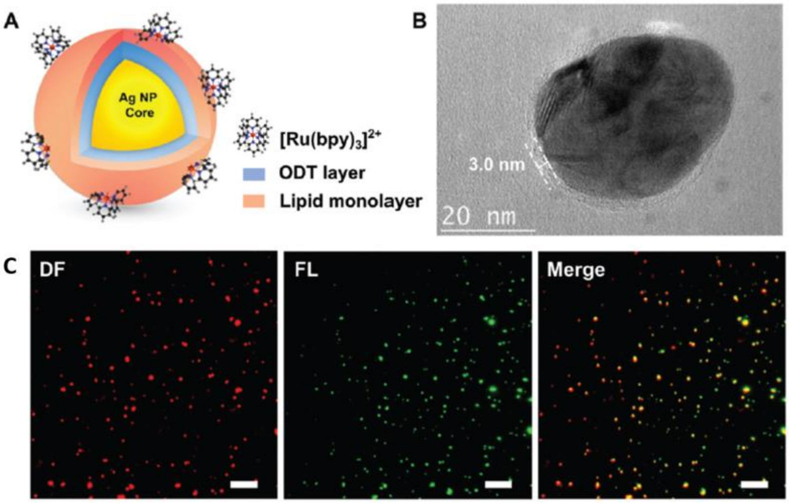

Figure 3.2.1 Characterization of Plasmonic Photoreactor Bactericide Nanocomposite and Coated Plastic Surfaces. Reproduced with permission from Ref. 53, Copyright (2022) by The Royal Society of Chemistry. (A, B) Structural scheme (A) and high-resolution TEM micrograph (B) of a plasmonic photoreactor nanocomposite. (C) Correlated darkfield (left) and fluorescent (middle) images, and the merged channel (right) of a random area on the plastic slide surface coated with dye-labelled plasmonic photoreactors; scale bars: 10 µm.

plastic surfaces were coated with 0.1% (w/v) poly-L-lysine water solution (Sigma) for 15 min before being incubated with 100 pM (particle concentration) aqueous suspension of the photoreactor nanocomposites for 1 hour. The solution was drop-casted onto a slide or injected into a tubing with a syringe. The aqueous suspension was then removed, and the incubation was repeated with a 100 pM suspension of fresh photoreactors in water to increase the bound photoreactor density. After removal of the suspension, the photoreactor-coated samples were stored at RT for structural characterization or for the inactivation experiments. Very close particle binding densities of around 1 x 10^9 NP cm^{-2} were calculated respectively for the coated plastic tubing and slide surfaces.

The coating on the plastic slide surfaces was further characterized by correlated Darkfield (DF) / Fluorescence (FL) imaging using dye-labelled photoreactor nanocomposites (**Fig.**

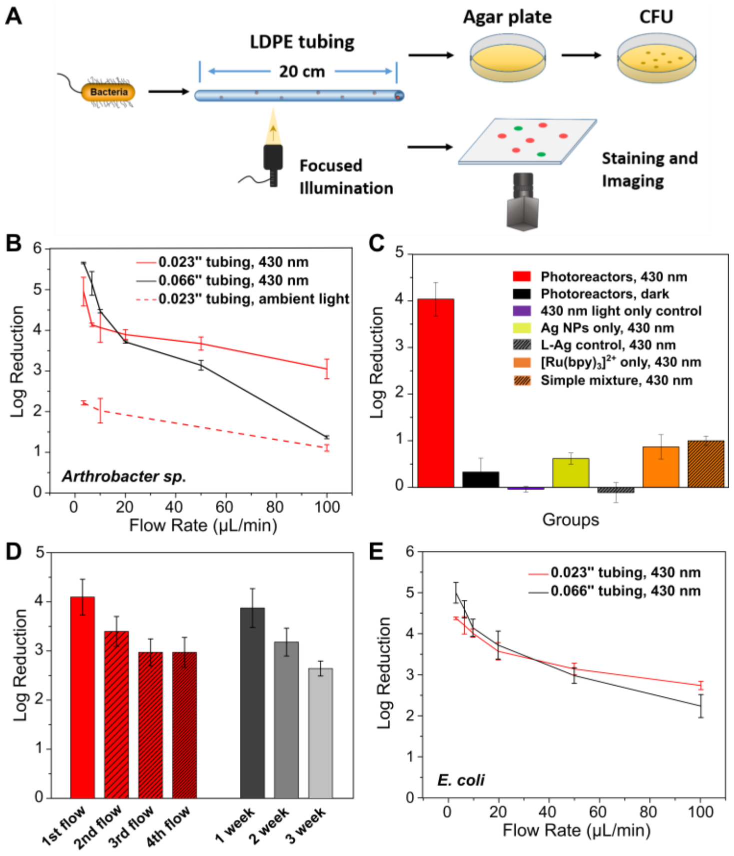

Figure 3.2.2. Bacteria Flow Inactivation with Antimicrobial Flow Sterilizer. Reproduced with permission from Ref. 53, Copyright (2022) by The Royal Society of Chemistry. (A) Schematic illustration of the antimicrobial flow sterilizer and the flow inactivation processes. (B) Log reduction values (LRVs) for Gram-positive *Arthrobacter sp.* after flow inactivation with antimicrobial flow sterilizers of different inner diameters and with specified flow rates and illumination conditions. (C) Comparison of LRVs of *Arthrobacter sp.* with LDPE tubing (ID=0.023'') coated with plasmonic photoreactor (antimicrobial flow sterilizers) or control groups at a flow rate of 10 µL/min. (D) LRVs of *Arthrobacter sp.* after flow inactivation with LDPE tubing (ID=0.023'') coated with freshly prepared plasmonic photoreactors in the 1st, 2nd, 3rd or the 4th flow (left four columns); or in the 1st flow with plasmonic photoreactors with 1, 2, or 3-week shelf life (right three columns). All groups were measured at a flow rate of 10 µL/min. (E) LRVs of Gram-negative *E. coli* CFU population after flow inactivation with antimicrobial flow sterilizers of different inner diameters at different flow rates. Error bars: Mean ± standard deviation of 3 independent tests.

3.2.1C). A strong spatial colocalization between the DF signal from the metal cores in the nanocomposites and the FL membrane signal from the membrane dye incorporated in the hybrid lipid membranes proves a successful wrapping of the plasmonic photoreactors on the ensemble level. The optical images also revealed an even coating of the nanocomposites on the plastic surfaces.

3.2.1 Characterization of the Active and Passive Antibacterial Effect

The active antibacterial performance of the photoreactor coating with LDPE tubing, namely, the flow sterilizer, was first characterized for flow-through bacteria inactivation. Gram-positive *Arthrobacter sp.*, a ubiquitous soil bacterium was still used as test microbe. As introduced in section **3.1**, it has been shown to possess metal cation-reducing capability[213-214] and is thus a desirable test platform for metal-based plasmonic photoreactors. During the flow inactivation, the bacteria suspension was manually injected into photoreactor-coated LDPE tubing with a total length of 20 cm. Light from a 430 nm LED was focused on the tubing (**Fig. 3.2.2A**). Tubings with two different inner diameters (ID), 0.023'' (inches) and 0.066'', were tested with flow rates of 3.33, 6.67, 10, 20, 50 or 100 $\mu L\ min^{-1}$. LRVs were calculated by plating the flowed-through bacteria suspension and counting the colony-forming unit (CFU) population after culture according to **Eq. 1.12**.

Overall, higher LRVs are observed at slower flow rates for both tubing diameters (**Fig. 3.2.2B**). At 3.33 $\mu L\ min^{-1}$, a superb LRV of around 5.5 is reached for both tubing diameters. This reduction is comparable to the effect of state-of-the-art metal-based bactericides in suspension within the same treatment times.[50-52] For the 0.023'' tubing, LRVs above 3 are measured at all tested flow rates. For the 0.066'' tubing, LRVs > 3 were achieved with flow rates $\leq 50\ \mu L\ min^{-1}$. Control groups included (a) a dark control of photoreactors-coated flow sterilizers; (b) LED only control of uncoated LDPE tubing; (c) polylysine-

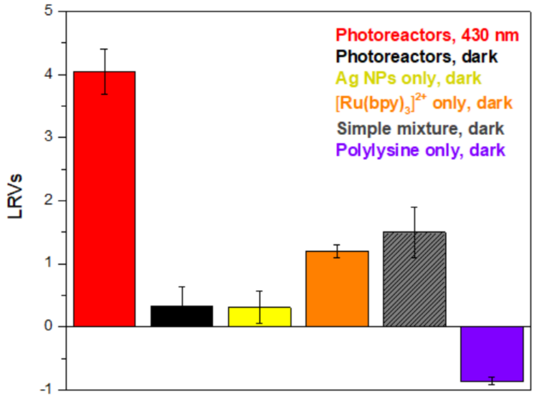

Figure 3.2.3 Comparison of LRVs of *Arthrobacter sp.* with LDPE tubing (ID = 0.023'') Coated with Plasmonic Photoreactors or Control Groups. Reproduced with permission from Ref. 53, Copyright (2022) by The Royal Society of Chemistry. Flow rate for all groups: 10 µL min^{-1}. Error bars: Mean ± standard deviation of 3 independent tests.

treated tubing only with light; or tubing coated with (d) "bare" Ag NPs without any lipid membranes (Ag NPs only control), (e) lipid-wrapped Ag NPs (L-Ag), (f) [Ru(bpy)$_3$]$^{2+}$, and (g) a simple mixture of L-Ag and [Ru(bpy)$_3$]$^{2+}$ with and without illumination from a 430 nm LED (**Fig. 3.2.2C** and **Fig. 3.2.3**). All control groups, if applicable, were prepared to have identical Ag and/or Ru concentration as the plasmonic antimicrobial photoreactors. Very low reductions in *Arthrobacter sp.* CFUs are obtained for all dark controls. This finding confirms that the antibacterial effect of the antimicrobial plasmonic photoreactor is "switched on" by visible illumination. LRVs below or close to 1.5 were obtained for all control conditions, which evidences the synergistic gain in activity that arises from a combination of L-Ag NPs and [Ru(bpy)$_3$]$^{2+}$ into functional units in the plasmonic photoreactor.

Interestingly, the tubing with a larger ID (0.066'') achieves stronger antibacterial effects at lower flow rates (3.33, 6.67 and 10 µL min^{-1}) than the thinner tubing (0.023''), whereas the thinner tubing is more effective at higher flow rates (20, 50, 100 μL min^{-1}) (**Fig. 3.2.2B**). These trends could be due to a tradeoff between flow rate and mass transport in the flow sterilizers. As described in our previous work[52] and in section **3.1**, the plasmonic photoreactors provide a visible light-induced release of various bactericidal compounds including Ag^+, $[Ru(bpy)_3]^{2+}$ and peroxidized lipids due to photogenerated ROS. These bactericidal compounds are released at the photoreactor-coated surface of the tubing, and diffuse into the interior volume of the flow sterilizer where they take effect. Consequently, for the larger diameter tubing, it is to be expected that the longer diffusion length could impede the accumulation of high bactericide concentrations in the interior volume at high lateral flow rates. However, at slower flow rates, the mass transport of the bactericidal compounds is no longer a rate-limiting factor. Thus, a stronger antibacterial effect can be achieved in the tubing with larger diameter since it has a larger inner surface area coated with the photoreactors, and that it also offers a larger illuminated area for converting light energy into reactive chemical species.

The reproducibility of the bactericidal properties under repeated use as well as the shelf life of the antimicrobial flow sterilizers are two important parameters for their practical applications. To assess these aspects, we respectively measured LRVs of *Arthrobacter sp.* in 4 subsequent flow inactivation runs with the flow sterilizer, and with different flow sterilizers stored for 1-3 weeks under ambient conditions (**Fig. 3.2.2D**). These experiments were performed with the thinner tubing (0.023’’) at a bacteria flow rate of 10 μL min^{-1}. Although the LRV decreased by approximately 1 when the same antimicrobial flow sterilizer was reused, LRVs above or close to 3 were obtained in all subsequent flow inactivations (**Fig. 3.2.2D**, left). The antibacterial efficacy also decreased with increasing shelf life, due to gradual photobleaching of the active components when stored in ambient conditions as well as a slow detachment of the coating from the surface over time. Yet a substantial inactivation with a LRV of around 2.5 was still achieved after 3 weeks. These results indicate that the plasmonic antimicrobial photoreactors can be reused for multiple times, and that the photoreactor coating retains significant bactericidal properties for weeks.

For completeness, we also assessed the flow inactivation efficacy of the photoreactor-coated tubing (0.023'') under ambient illumination from incandescent lamps (**Fig. 3.2.2B**, dashed curve). Although not as efficient as with the focused 430 nm LED, a bacterial inactivation with LRVs of up to 2 was still obtained with the low-power ambient light, which indicates that it is possible to develop the plasmonic flow sterilizers into on-site sterilization devices that do not require any extra equipment. To validate that the antimicrobial effect of the plasmonic photoreactor coating is effective against different types of bacteria, Gram-negative *E. coli* was also tested on (**Fig. 3.2.2E**). LRVs > 5 were achieved for *E. coli* with the larger tubing diameter at the flow rate of 3.33 µL min^{-1}. This evidences that the antimicrobial coating based on the photoreactor nanocomposites possesses general antibacterial properties. For *E.coli*, similar correlations between LRV and tubing diameter or flow rates were observed as for *Arthrobacter sp.*, although the LRVs for the Gram-negative bacteria are slightly lower than for the Gram-positive specie, which could be owing to differences in the cell surface structure and the known stronger resistance of Gram-negative bacteria against metal-based bactericides.[12, 109, 216]

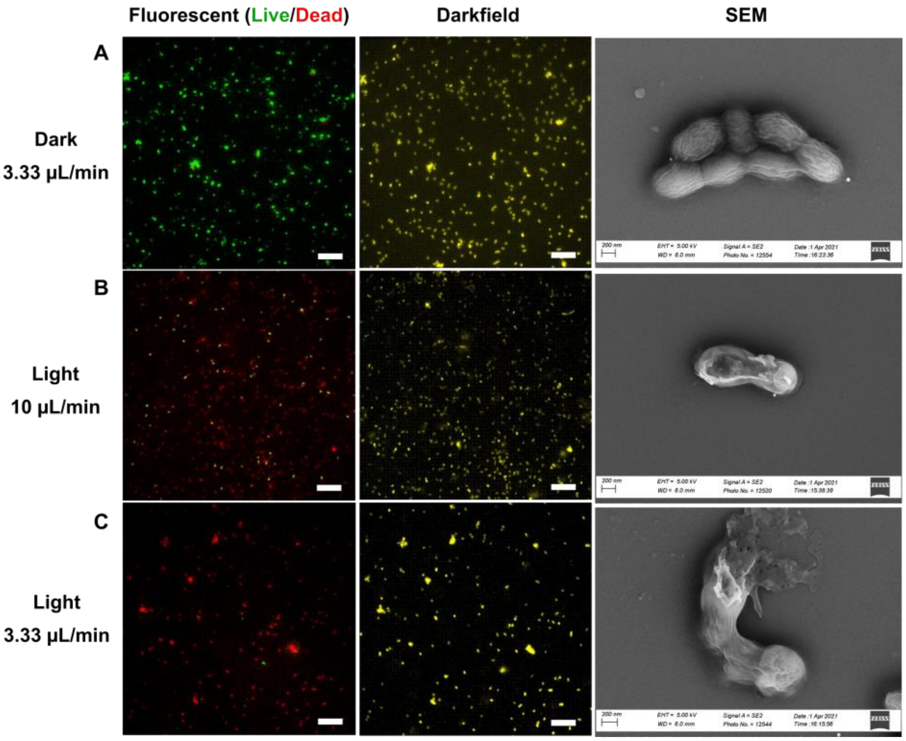

Figure 3.2.4 Characterization of *Arthrobacter sp.* Bacteria After Flow Inactivation. Reproduced with permission from Ref. 53, Copyright (2022) by The Royal Society of Chemistry. (A-C) Characterization of *Arthrobacter sp*. bacteria after flowing through plasmonic photoreactor-coated flow sterilizers (ID = 0.023’’) in dark at 3.33 µL min^{-1} flow rate (A), with 430 nm illumination at 10 µL min^{-1} (B), and with 430 nm illumination at 3.33 µL min^{-1} (C). Left column: a merged FL image of live (green) and dead (red) fluorescent signals of the collected bacteria after staining with the BacLight Live/Dead stain; middle column: darkfield images of the same field of view; right column: SEM micrographs of bacteria collected for the specified conditions. Scale bars = 10 µm for FL and DF images.

To further evidence the bactericidal effect of the photoreactors-based flow sterilizers, BacLight Live/Dead staining (ThermoFisher) and fluorescence microscopy as well as SEM imaging were used to characterize flowed-through *Arthrobacter sp.* bacteria collected after flow inactivation. After *Arthrobacter sp.* bacteria were flowed through the plasmonic antimicrobial flow sterilizer (0.023’’) in dark, a dominance of strong green fluorescence signals was observed in the FL channel (**Fig. 3.2.4A**, left), which is indicative of live bacteria. The green FL signal overlaps well with the bacteria cells seen in the DF channel

(**Fig. 3.2.4A**, middle). Corresponding SEM images show intact bacteria cell morphology and surface structure (**Fig. 3.2.4A**, right). These results further corroborate that in the absence of illumination, the antimicrobial coating barely has any detrimental effect, and the collected flowed-through bacteria are viable. If the bacteria suspension was flushed through the plasmonic antimicrobial flow sterilizer with a flow rate of 10 µL min^{-1} under 430 nm LED illumination, a larger fraction of bacterial cells stained red, indicative of dead cells (**Fig. 3.2.4B**, left). This fraction further increased with a slower flow rate of 3.33 µL min^{-1} under illumination (**Fig. 3.2.4C**, left). SEM images of these cells reveal significant structural damage, which includes peeling and perforation of the cell surface at the faster flow rate (**Fig. 3.2.4B**, right) and complete disintegration of the cell body with the slower flow (**Fig. 3.2.4C**, right). These observations are consistent with previous findings on how metal-based antibacterial agents take effect.[140, 258] Detrimental interactions between metal ions and surface proteins or other cell wall and membrane components can cause surface structural damage to bacteria cells, which accounts for the observed surface morphological change.[52, 109]

In addition to the active bactericidal function, plasmonic photoreactor antimicrobial coatings are also able to provide unique capabilities as “passive” antimicrobial coatings, namely, to inhibit bacterial colonization of plastic surfaces. For this purpose, we incubated PVC slides coated with plasmonic photoreactor nanocomposites in *Arthrobacter sp.* suspension in growth medium at a concentration of 10^7 bac mL^{-1} for 2 days at 25 ^{o}C with or without ambient irradiation. Control conditions included: (a) slides treated with polylysine but without antibacterial coating (referred to as uncoated plastic slides), (b)

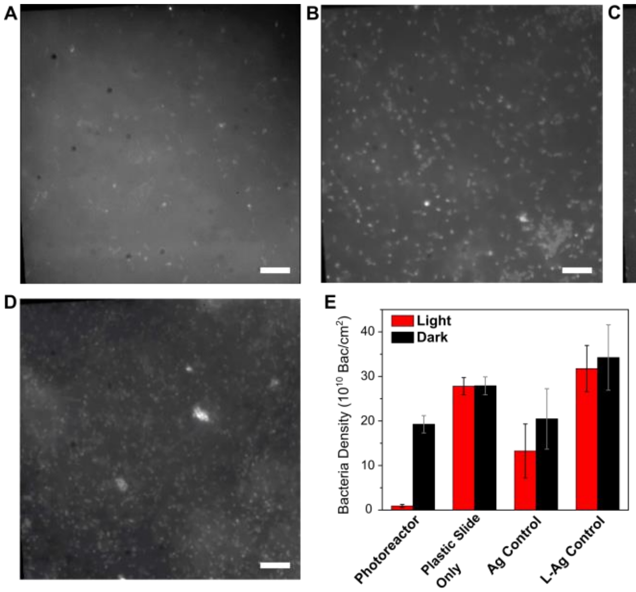

Figure 3.2.5 Bacterial Growth Inhibition on Photoreactors-Coated Plastic Surfaces. Reproduced with permission from Ref. 53, Copyright (2022) by The Royal Society of Chemistry. (A-D) DF images of bacterial growth on different PVC slide surfaces that are coated with plasmonic photoreactors (A), uncoated (B), coated with the Ag control (C), or coated with the L-Ag control (D), after seeding with *Arthrobacter sp.* at a concentration of 10^7 bac mL^{-1} and cultured for two days at 25 ^{o}C with ambient light. Scale bars = 10 μm. (E) Average bacteria density on PVC slide surfaces coated with (from left to right): photoreactors, uncoated, Ag NPs, or L-Ag NPs controls. The slides were seeded with *Arthrobacter sp.* (10^7 bac mL^{-1}) and cultured for two days at 25 ^{o}C with ambient light (red) or in the dark (black). The data represent mean ± standard deviation of 6 DF images from 3 independent measurements.

slides coated with citrate-stabilized, "bare" Ag NPs (Ag control; same Ag concentration as for the photoreactor coating), and (c) slides coated with lipid-wrapped Ag NPs (L-Ag control).

Slides coated with the photoreactor bactericide coating and irradiated with ambient light (**Fig. 3.2.5A**) results in a significantly lower density of bacteria than control conditions or when kept in the dark (**Fig. 3.2.5B-D**, **Fig. 3.2.6**), which indicates great inhibitory effect of bacteria colonization. The surface densities of bacteria on the plastic slide surfaces in the recorded darkfield images were quantified for the different experimental conditions (**Fig.**

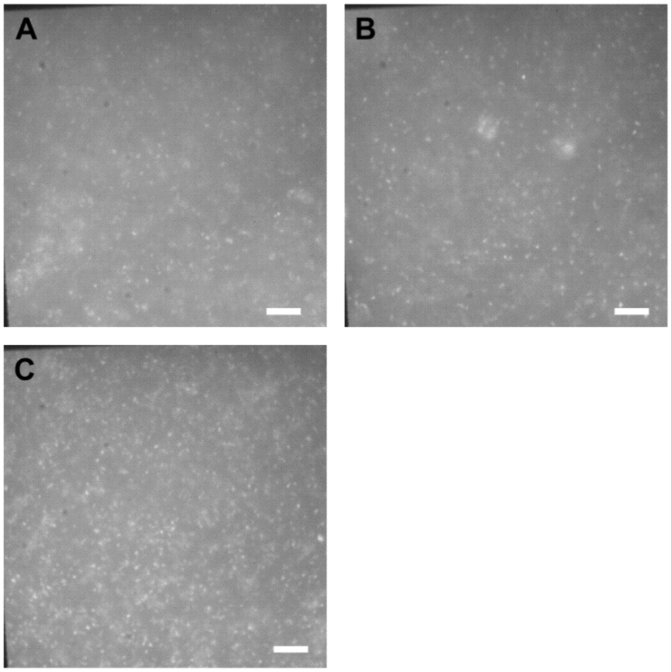

Figure 3.2.6 Supplemental Characterizations of Bacterial Growth Inhibition on Plastic Surfaces. Reproduced with permission from Ref. 53, Copyright (2022) by The Royal Society of Chemistry. (A-C) Darkfield images of plastic slide surfaces that are coated with plasmonic photoreactors (A), with Ag NPs control (B), or with L-Ag controls (C) after seeding with 10^7 bacteria mL^{-1} *Arthrobacter sp.* and left at RT for two days in dark. Scale bars = 10 µm.

3.2.5E). Under ambient illumination, the plasmonic photoreactor-coated surfaces show a 1.49-log reduction in the bacteria density. Due to the bactericidal properties of Ag NPs and released Ag^+, the Ag NPs only control also provides a measurable decrease in bacterial density with ambient light (0.32-log reduction), although the effect is evidently weaker than for the photoreactors. L-Ag control, possessing favorable biocompatibility and stabilizing effect from the lipid architecture that precludes any evident Ag^+ release and cytotoxicity, yielded a similar bacteria density as the uncoated plastic slide with ≤ 0.2 log reduction in the population of visible bacteria from the DF images. Overall, these observations confirm the efficacy of the photoreactor coating for inhibiting bacterial colonization switched on by ambient visible-light illumination.

3.2.3 Characterization of Toxicity and Collateral Damage of the Photoreactor Bactericide Coating and Application in Biologics Sterilization

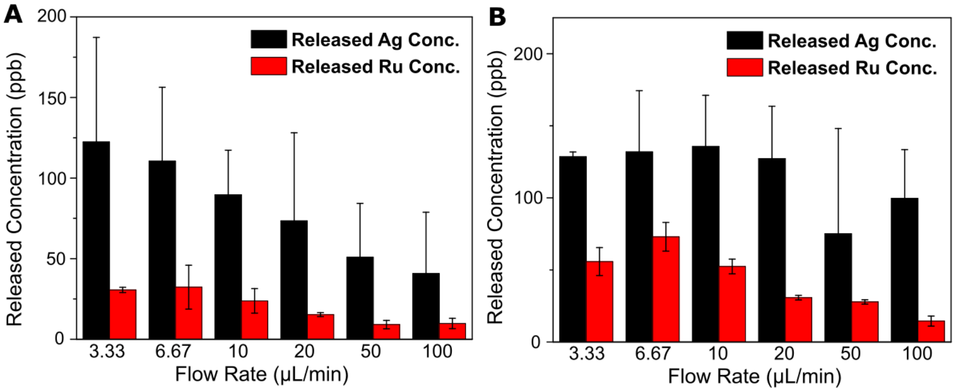

Figure 3.2.7 Measurements of the Released Ion Concentrations in Dark. Reproduced with permission from Ref. 53, Copyright (2022) by The Royal Society of Chemistry. (A-B) MP-AES results of released Ag and Ru concentrations in the bacteria suspension after flow inactivation assay with plasmonic photoreactor-coated LDPE tubings (antimicrobial flow sterilizers) with inner diameters (ID) of 0.023'' (A) and 0.066'' (B) in dark. Error bars: Mean ± standard deviation of 3 independent measurements.

Free plasmonic photoreactor bactericides in solution take effect as they harvest the ROS produced by photoexcited $[Ru(bpy)_3]^{2+}$ to induce the permeabilization of the hybrid lipid membrane and to trigger the release of bactericidal compounds into the ambient medium.[52] When formed into the antimicrobial coating on plastic surfaces, it is very likely that the flow sterilizers retain this visible light-induced release mechanism. To quantify the concentration of the released Ag and Ru species from the plasmonic photoreactor coating in the flow sterilizer, 100 μL bacteria-containing medium was flowed through 0.023'' or 0.066'' tubing under ambient illumination, with 430 nm LED irradiation or in dark, and

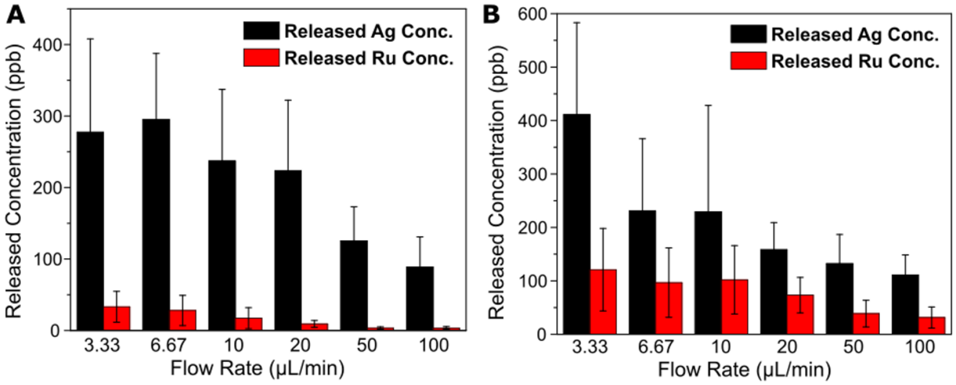

Figure 3.2.8 Measurements of the Released Ion Concentrations from the 0.023'' Tubing. Reproduced with permission from Ref. 53, Copyright (2022) by The Royal Society of Chemistry. (A-B) Released Ag and Ru concentrations quantified by MP-AES in bacteria suspensions collected after flow inactivation in plasmonic photoreactors-coated LDPE tubing (ID = 0.023'') with ambient light (A) or with 430 nm illumination (B) at different flow rates.

the released ion concentrations were quantified through Microwave Plasma-Atomic Emission Spectroscopy (MP-AES) (**Fig. 3.2.7 - 3.2.9**). In general, the factors associated with larger released ion concentrations include slower flow rates, larger tubing diameters, and resonant illumination. Amongst these factors, the flow rate-dependence is likely due to the increased dwell time of the bacteria suspension in the reactor at a slower flow; while the tubing diameter-dependence is the result of the larger surface area for the larger diameter tubing, as is also mentioned in section **3.2.2**.

The measured release concentrations in dark define a baseline for the Ag NPs and $[Ru(bpy)_3]^{2+}$ flushed out by the applied flow in the absence of light-induced reactions, since no light-induced photoreactivity takes place in dark. For the 0.023'' flow sterilizer in dark, a flow rate of 3.33 μL min^{-1} led to average released Ag and Ru concentrations of 122 ppb Ag and 30 ppb Ru (**Fig. 3.2.7**). As expected, both types of illumination can trigger a faster ion release for both elements. For the 0.023'' flow sterilizer with a flow rate of 3.33 μL

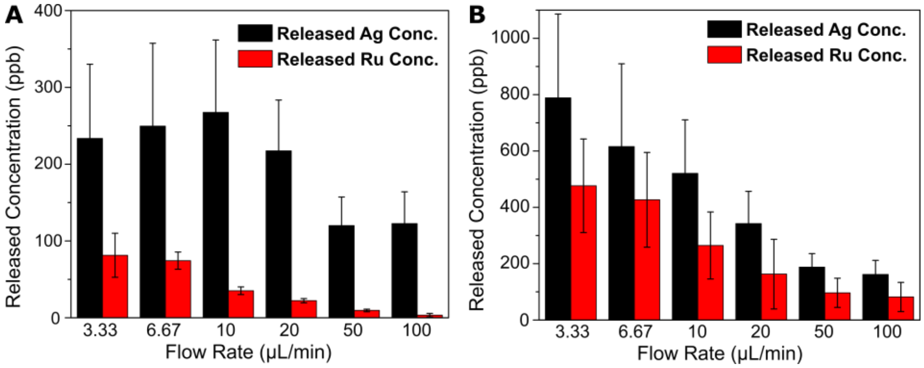

Figure 3.2.9 Measurements of the Released Ion Concentrations from the 0.066'' Tubing. Reproduced with permission from Ref. 53, Copyright (2022) by The Royal Society of Chemistry. (A-B) MP-AES measurements of released Ag and Ru concentrations in the bacteria suspension after flow inactivation assay with plasmonic photoreactors-coated LDPE tubing (ID = 0.066'') at different flow rates with ambient light (A) or with 430 nm illumination (B).

min^{-1}, the concentrations of released Ag and Ru species increased to 277 ppb and 33 ppb, respectively, under irradiation with ambient light (**Fig. 3.2.8A**); and to 411 ppb and 121 ppb, respectively, with 430 nm LED irradiation (**Fig. 3.2.8B**). This difference is consistent with the stronger bactericidal effect obtained with plasmonic photoreactors for LED illumination when compared to ambient light illumination as shown in **Fig. 3.2.2B**.

Overall, the released concentrations of Ag^+ (~102 ppb) and $[Ru(bpy)_3]^{2+}$ (~10-100 ppb) in combination with the generation of ROS through the plasmonic photoreactors provide a strong synergistic bactericidal effect. The concentrations are, however, significantly below typical half-maximal inhibitory concentration (IC_{50}) values for mammalian cells and are thus unlikely to induce significant collateral damage to mammalian cell components. The highest released Ag^+ concentration from the 0.023'' flow sterilizer (411 ppb) is almost 2 orders of magnitude lower than the $AgNO_3$ IC_{50} value of 157 μM (1.7 x 10^4 ppb Ag) determined with HeLa cells.[259] Similarly, the largest released Ru concentration stemming

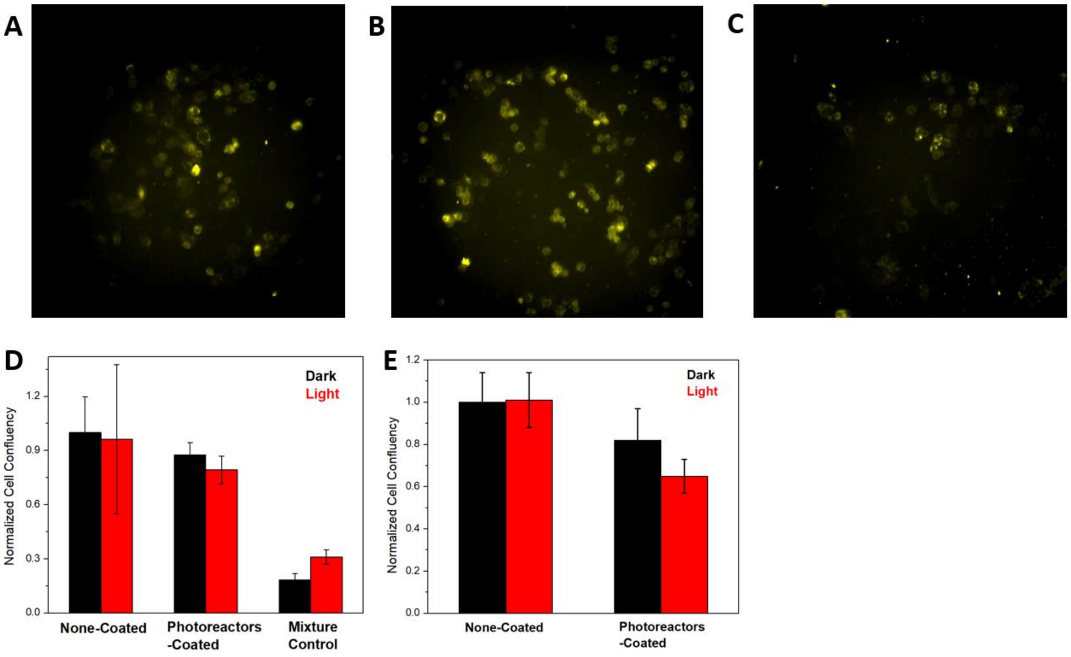

Figure 3.2.10 Characterization of Cancer Cell Confluency on Photoreactor-Coated Slides and Controls. Reproduced with permission from Ref. 53, Copyright (2022) by The Royal Society of Chemistry. (A-C) Darkfield images of the surfaces of PVC slides that are uncoated (A), coated with plasmonic photoreactors (B), or coated with the same concentration of a simple mixture control of Ag NPs and $[Ru(bpy)_3]^{2+}$ (C) after culturing with MDA-MB-468 cells with ambient light for 2 days at 37 ^{o}C. (D) Normalized cell confluency of MDA-MB-468 cells after culturing on PVC slides coated with photoreactor nanocomposites or controls with (red) or without (black) ambient light for 2 days at 37 ^{o}C. (E) Normalized cell confluency of MDA-MB-231 cells after culturing on PVC slides that are none-coated or coated with photoreactor nanocomposites with (red) or without (black) ambient light.

from $[Ru(bpy)_3]^{2+}$ from the 0.023'' flow sterilizer (121 ppb) remains significantly below the typical IC_{50} values of similar complexes that lie in the range between 10s and 100s of µM (10^3 - 10^4 ppb Ru).[260-261]

The detrimental effect of photoreactor coating against mammalian cells was further probed by quantifying the confluency of MDA-MB-468 breast cancer cells cultured on plastic slides that are (a) uncoated, (b) coated with the photoreactor nanocomposites, or (c) coated with a simple mixture of Ag NPs and $[Ru(bpy)_3]^{2+}$ with identical concentrations as for the hybrid plasmonic photoreactor bactericides with or without ambient illumination (**Fig. 3.2.10**). PVC slides were sterilized with 75% ethanol and coated as described above. MDA-MB-468 cells (ATCC, HTB-132) were seeded at a density of 1 x 10^5 cells mL^{-1} in advanced Dulbecco's Modified Eagle Medium (DMEM) supplemented with 10% (v) fetal bovine serum (FBS), 2 mM L-glutamine, and 50 units mL^{-1} penicillin-streptomycin on uncoated slides, photoreactors-coated slides, and slides coated with a simple mixture control of Ag NPs and $[Ru(bpy)_3]^{2+}$ at the identical concentration as in the nanocomposites. The cells were cultured in a 37 ^oC incubator in dark or with ambient light for 2 days and imaged under the Olympus IX71 Inverted Microscope for DF imaging with an Olympus 10x air objective. Cell confluency were measured by the area density of the cells from 4 independent DF images, and normalized by dividing with the area density of the cells on the none-coated plastic slides cultured in dark. Notably, the cancer cells cultured on photoreactor-coated slides maintained high cell confluency, achieving 87.6% of the confluency of the no treatment reference in the dark. When illuminated, the confluency dropped slightly to 79.3%. In contrast, due to a lack of the protective hybrid lipid membrane that provides adequate light-control and biocompatibility in dark, the simple mixture-coated control of Ag NPs and $[Ru(bpy)_3]^{2+}$ led to a much larger decrease in cancer cell confluency down to 31.1% in the dark, and 18.4% with light. A similar trend was also observed for another mammalian cell line, MDA-MB-231 (**Fig. 3.2.10E**), where the decrease in cell confluency was merely 18% when cultured on photoreactor-coated plastic slides in dark and 35% with light. In practice, the difference in the growth inhibiting effect on mammalian (decrease in confluency by 21% and 35%) and bacterial cells (decrease in surface density by 1.49 orders of magnitude) on the PVC slides provides some selectivity for the plasmonic photoreactor nanocomposites. The difference in the growth inhibiting effect of the photoreactor bactericide coating on plastic surface against mammalian cells and bacteria is intriguing and indicates some degree of selectivity for the effect of plasmonic photoreactor nanocomposites. Potential reasons for this selectivity could be related to the smaller size of the bacteria. The larger surface to volume ratio could make bacteria more susceptible to surface damage by the molecular bactericidal agents released by the plasmonic photoreactor coating, including Ag^+, $[Ru(bpy)_3]^{2+}$, peroxidized lipid components, and ROS. Furthermore, differences in the structure[12, 109] and surface charge[262] of bacterial cell surfaces when compared to mammalian cells can result in different binding affinities and different chemical interactions. These factors could lead to different damage thresholds for these different types of cells. In addition, differences in the efficacy of cellular repair mechanisms could also contribute to the observed selectivity.

One important potential field of application for the plasmonic antimicrobial flow sterilizers is in small-scale sterilization of biologics, such as monoclonal antibodies, which are valuable compounds for both scientific research and biomedical applications, but their safe sterilization is challenging.[263] One crucial prerequisite for these applications is that the antimicrobial effect of the photoreactor nanocomposites and the flow sterilizers do not negatively impact the function of the biologics. To this end, we first assessed whether the bactericidal effect of the antimicrobial coating and flow sterilizers could be maintained in the presence of monoclonal antibodies against Epidermal Growth Factor Receptor (EGFR), which were chosen as test case to evaluate the effect of the sterilization process on sensitive

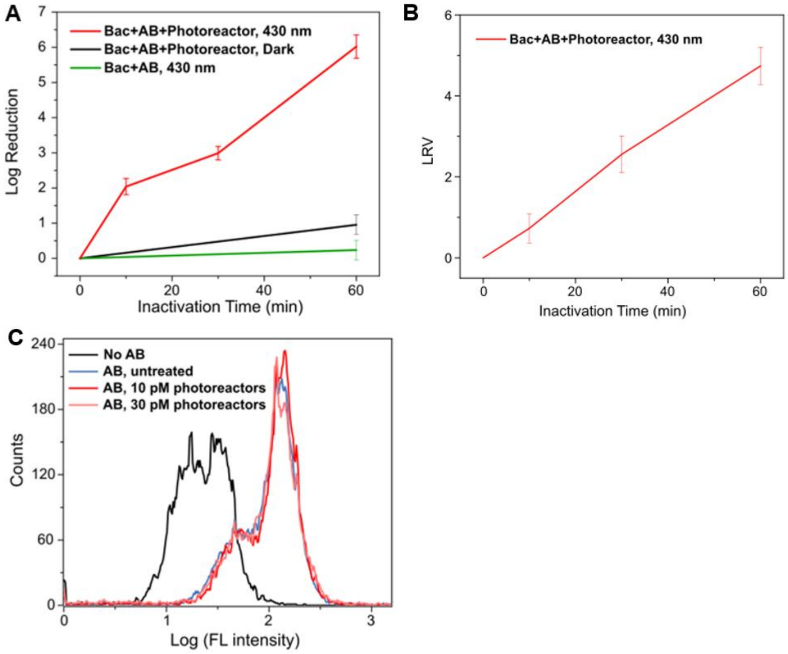

Figure 3.2.11 Characterization of the Effect of Plasmonic Photoreactors in the Presence of EGFR Antibody. Reproduced with permission from Ref. 53, Copyright (2022) by The Royal Society of Chemistry. (A) Inactivation of Gram-positive *Arthrobacter sp.* with plasmonic photoreactors in the presence of 100 µL 0.05 mg mL^{-1} EGFR antibody (AB). LRVs are given as function of time for mixtures of bacteria and ABs treated with photoreactors and 430 nm irradiation (red), treated with photoreactors in dark (black), and irradiated at 430 nm without photoreactors (green). (B) Inactivation of Gram-negative *E. coli.* with plasmonic photoreactors in the presence of 100 µL 0.05 mg mL^{-1} EGFR antibody (AB). (C) Flow cytometry histograms of fluorescence intensity of MDA-MB-468 cells (black), after incubating with untreated dye-labelled EGFR antibody (blue), and after incubating with dye-labelled EGFR antibody co-illuminated at 430 nm with 10 pM (red) or 30 pM (pink) plasmonic photoreactors. Error bars: mean ± standard deviation of 3 independent measurements.

biologics; and whether they would also induce damage to the antibodies. Biotinylated Epidermal Growth Factor Receptor (EGFR) antibody cocktail (ThermoFisher, MA5-13266) was added to the inactivation colloid. In this experiment, 100 µL bacteria suspension with an estimated concentration of 10^{10} Bac mL^{-1} by the absorbance optical density at 600 nm (OD_{600}), 100 µL media, 100 µL 30 pM photoreactor nanocomposite suspension, and 100 µL 0.05 mg mL^{-1} antibody were added to a glass cuvette, mixed, and illuminated under stirring with the 430 nm LED for 1 hour. The reaction mixture was fetched at 10, 30 and 60 min to be serial-diluted, plated, colony counted and calculated for LRVs as described above. As shown in **Fig. 3.2.11A**, a superb LRV of around 6 is achieved with *Arthrobacter sp.* after 1 hour of illumination. Similarly, a high inactivation is also observed for Gram-negative *E. coli* in the presence of antibody (**Fig. 3.2.11B**). The LRVs in both cases are similar to the reported values when no antibodies were added,[52] which indicates that the bactericidal properties have been maintained in the presence of the antibodies.

Next, the binding affinity of the biotinylated EGFR-antibodies to MDA-MB-468 cells, an EGFR-overexpressing breast cancer cell line,[264] was quantified through flow cytometry and compared before and after illumination with 430 nm light in the presence of 10 or 30 pM photoreactor nanocomposites. Dye-labelled streptavidin (ThermoFisher, S11227) was used as fluorescence marker for the biotinylated EGFR. In this experiment, a reaction mixture of 100 µL PBS, 100 µL 10 or 30 pM photoreactor nanocomposite suspension, and 100 µL 0.05 mg mL^{-1} antibody were added to a glass cuvette, mixed, and illuminated under stirring with the 430 nm LED for 30 min. To prevent contamination to the later cell culture, no bacteria were added in this step. Afterwards, the antibody mixtures after treatment with photoreactors, as well as an untreated control, were centrifuged to remove the photoreactor nanocomposites, redispersed in PBS, and then incubated with MDA-MB-468 cells at 37 ^{o}C for 3 hours for specific binding. MDA-MB-468 cells were cultured according to previously developed protocols[59] in advanced Dulbecco’s Modified Eagle Medium (DMEM) supplemented with 10% (v) fetal bovine serum (FBS), 2 mM L-glutamine, and 50 units mL^{-1} penicillin-streptomycin, and grown in a 37 ^{o}C incubator with 5% CO_2 and

95% relative humidity. Experiments were performed when cells reached 80% confluency. After incubation with the treated antibodies or controls, the cells were washed with Hank's Balanced Salt Solution (HBSS) buffer and incubated with 0.5 mg mL^{-1} Streptavidin-Alexa Fluor 594 dye for 1 hour at 37 ^{o}C. Subsequently, the cells were washed with HBSS buffer and detached from plates using Accutase cell dissociation reagent (ThermoFisher) and fixed with 4% (w/v) pierce formaldehyde (ThermoFisher) for 10 min before washed with PBS buffer. The fluorescence intensity of the cells were measured by flow cytometry.

The fluorescence intensity histograms shown in **Fig. 3.2.11C** reveal similar FL intensities for antibodies before (blue) and after (red and pink) treatment, which suggests that the photoreactor-driven bacteria inactivation does not lead to measurable decrease in the binding affinity of the antibodies. These results are encouraging as the lack of a substantial decrease in antibody functionality suggests that the effect of the plasmonic photoreactor bactericides do not affect the functional, and thus structural integrity of the antibody.

In summary, we have demonstrated in this section the visible light-driven active and passive antibacterial properties of antimicrobial coatings based on plasmonic photoreactor nanocomposites. Under visible illumination, the photoreactor coating releases a combination of bactericidal chemical compounds, which interact synergistically to induce bacterial surface damage and lead to a strong bactericidal effect. The flow sterilizer is able to reduce the population of both Gram-positive and -negative bacteria (*Arthrobacter sp.* and *E.coli*) by over 5 orders of magnitude (LRV > 5) under focused 430 nm LED irradiation. Irradiation with ambient light was sufficient for the photoreactor coating to achieve a measurable inhibition of *Arthrobacter sp.* colonization of plastic surfaces. The antimicrobial performance of the flow sterilizers is robust, allowing multiple re-uses and having a shelf-life of at least 3 weeks under ambient conditions. The plasmonic antimicrobial flow sterilizers did not significantly deteriorate the function of monoclonal antibodies that were contained in a bacteria-spiked medium, and demonstrated degrees of selectivity in its toxicity against bacterial pathogens compared to mammal cells.

3.3 Summary of Chapter 3

We have demonstrated in this chapter the development of an effective plasmonic photoreactor bactericide composed of Ag NP cores and molecular photocatalyst $[Ru(bpy)_3]^{2+}$ that are integrated with a hybrid lipid membrane architecture. We quantify in section **3.1** the mechanism of light-controlled photocatalytic release of bactericidal compounds Ag^+, $[Ru(bpy)_3]^{2+}$ and peroxidized lipids induced by the photogenerated reactive oxygen species; the performance of the photoreactor bactericides against planktonic bacteria; as well as their efficacy against a bacterial biofilm.[52] Applied to plastic tubing, the nanocomposites generate plasmonic antimicrobial flow sterilizers. In section **3.2**, we characterize the effect of the photoreactor bactericide nanocomposites as an antimicrobial coating material for plastic surfaces that combines active and passive bactericidal properties, and further illustrate the cation release mechanism as well as its cytotoxicity against mammal cells and collateral damage in sterilization of biologics.[53]

The photoreactor composites released low concentrations of ^{101}Ru (44 ppb) and require low light power densities (< 10 mW cm^{-2}) to achieve reliable bacterial inactivation. In contrast to conventional light-based bacteria flow inactivation approaches that rely on high energetic UV irradiation or heat, the plasmonic photoreactor bactericide and the antimicrobial flow sterilizers operate with visible light, which helps to minimize light-based collateral damage. The visible light dependence of the cation release provides a reliable control mechanism for the initiation of inactivation, which paves the way for spatial and temporal regulation of the antibacterial activity.[52-53]

The photoreactor bactericides introduced in this chapter also represent an alternative broad-band antimicrobial strategy with a broad range of applications, ranging from the inactivation of bacteria on surfaces and medical devices to potential wound sterilization. The development of plasmonic antimicrobial coatings and the implementation of plasmonic antimicrobial flow sterilizers has implications not only for flow-based sterilization of food, water, fluids, or biologics; but also for protection of plastic surfaces in medical devices against bacterial colonization. Sterilization of valuable biologics using only the plasmonic antimicrobial flow sterilizer and light is of special interest as it can be combined with emerging on-chip biologics fabrication strategies,[265-266] paving the path to integrated solutions for the fabrication of safe and sterile biologics on demand. Furthermore, plasmonic antimicrobial flow sterilizers provide a portable and easy approach to implement small scale sterilization strategy for biologics in field applications or in emergency situations where dedicated laboratory equipment is not available.[53]

Chapter 4. SERS Characterization of Orientational and Functional Dimorphism of Sterol-Derived Raman Tags in Lipid-Coated Nanoparticles

Nanoplasmonics have been utilized extensively for the enhancement of optical microscopy and spectroscopy, for instance, through surface-enhanced Raman spectroscopy (SERS), where the inelastic scattering cross-sections of molecules placed in the vicinity of plasmonic nanostructures could be significantly augmented the resonant electromagnetic field.[69, 267-269] With intricate designs of SERS substrates, the enhancement factors (EFs) of Raman signatures of molecules could be extremely high.[73-75] Spontaneous or enhanced Raman spectroscopy therefore represents an important approach to obtain sensitive molecular structural and physicochemical information, including the bonding information,[270-271] structural conformation,[272-273] hydration,[274] and orientation[275-277] of molecules. As lipid-coated noble metal NPs (L-NPs) achieve precise positioning of molecules within the E-fields of plasmonic NP cores via the lipid architecture, they thus possess great potentials as bright and effective SERS probes that provide unique imaging or spectroscopy modality.

As introduced in section **1.5**, sterols and terpenoids represent an effective platform for introducing functionality onto the surface of L-NPs and other membrane-based materials. Chemical derivatization of these molecules can also induce significant impact on interactions with the lipid molecules and/or the hydrogen-bonding network (HBN) at the lipid-water interface.[278-280] A rational engineering of the interactions with the HBN provides control over the molecular orientation of sterols in the lipid coating and facilitates configurable surface properties that adjust in response to external cues. Therefore, chemical derivatization of these essential membrane components presents a promising strategy for controlling the membrane properties of L-NPs. The control of the surface properties combined with the plasmonic signal enhancement through the NP core can also grant L-NPs with multiple distinct functionalities as Raman probes,[76, 167] chemical reactors,[52] drug carriers,[159-160] and/or catalysts.[29]

In this chapter, we demonstrate that through chemical derivatization of cholesterol and betulin, three modified tag molecules (Tag-1 to Tag-3) can be generated with side chains that differ in polarity and lengths.[56] These tags all contain a terminal alkyne group, which provides a reliable moiety for bio-orthogonal chemical conjugation, as well as a strong and unique Raman signature. The local chemical environment of the tag molecules could affect the precise Raman stretching frequencies of the alkyne signature. The tag structure as well as the solvation properties of the modified side chains impact their interactions with surrounding lipids and water, determine their orientation in the membrane, and thus directly affect the surface chemical properties of the L-NPs. The integration of these tags into the hybrid lipid membrane of L-NPs is investigated. The orientations of Tag-1 to Tag-3 in the NP-supported lipid membrane are probed with SERS, and the underlying mechanisms that determine the orientation of the tags in the membrane are elucidated. The tags-incorporating L-NPs were then utilized to engineer plasmon-enhanced Raman probes for the detection and Raman imaging of epidermal growth factor receptor (EGFR)-overexpressing cancer cells at single cell level.

This chapter was reproduced and adapted from Ref. 56, Copyright (2021) by National Academy of Sciences.

4.1 Design and Preparation of Tag Molecules and Tag-Incorporating L-NPs

Three tag molecules were synthesized and characterized in this study: cholesteryl hexynoate (Tag-1), cholesterol succinoylpropargyl amide (Tag-2), and betulin 28-succinoylpropargyl amide (Tag-3) (**Fig. 4.1A**). The tags were prepared following established procedures[281-282] or by applying routine synthesis protocols (**Fig. 4.2**) by our collaborators Prof. John Snyder, Taranee Puri, Taimeng Liang and Zhiliang He, and were characterized by ^{1}H- and ^{13}C-nuclear magnetic resonance (NMR) spectroscopy, as well as high-resolution mass spectrometry (HRMS). ^{1}H- and ^{13}C-NMR spectra were recorded at 117.5 kG (^{1}H-NMR 500 MHz, ^{13}C-NMR 125 MHz) or 70.5 kG (^{1}H NMR 300 MHz) as noted at ambient temperature. Chemical shifts (in parts per million) are referenced to the residual protio solvent for the proton reference, and the center line of the solvent multiplet for the carbon reference (^{1}H/^{13}C $CDCl_3$, 7.26/77.23, and ^{1}H/^{13}C CD_3OD, 7.26/77.23). Betulin was isolated from the bark of *Beula alba*, collected in Harvard, MA, as previously reported.[283] Other commercially available reagents were used without further purification; thin-layer chromatography (TLC) visualization was accomplished with $KMnO_4$ stain. High resolution mass spectrometry data was obtained on a Qtof (hybrid quadrupole time-of-flight) API US system by electrospray ionization (ESI) in the positive mode. Mass correction was done by an external reference using a Lockspray accessory. Mobile phases were water and acetonitrile with 0.1% formic acid. The MS settings were: capillary voltage

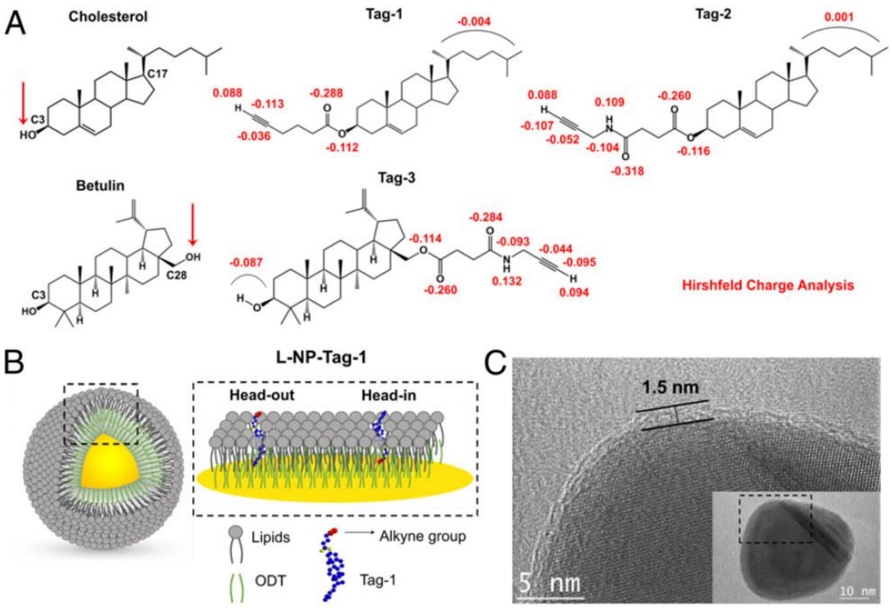

Figure 4.1 Molecular Structures of Tags-1-3 and Structural Characterizations of L-NP-Tag-1. Reproduced with permission from Ref. 56. Copyright (2021) by National Academy of Sciences. (A) Molecular Structures of cholesterol, betulin, and alkyne-modified Tags-1-3 with Hirshfeld Partial Charge Calculations. (B) Scheme of L-NP-Tag-1. (C) TEM micrographs of L-NP-Tag-1. Inset: A zoom-out view of imaged nanocomposite, with the zoomed in area indicated by the black rectangle.

= 3kV, cone voltage = 35, source temperature = 120 °C and dissolvation temperature = 350 °C.

Tag-1, Cholesteryl Hex-5-ynoate, [(3*S*,10*R*,13*R*,17*R*)-10,13-dimethyl-17-((*R*)-6-methylheptan-2-yl)-2,3,4,7,8,9,10,11,12,13,14,15,16,17-tetradecahydro-1*H*-cyclopenta[*a*] phenanthren-3-yl hex-5-ynoate] is synthesized as described below.[281] To a solution of cholesterol (386.7 mg, 1.0 mmol) in dichloromethane (DCM, 5 mL) heated to reflux (40 ^{o}C) was added sequentially hex-5-ynoic acid (134.6 mg, 1.2 mmol), 4-*N*,*N*-dimethylaminopyridine (DMAP, 122.2 mg, 1.0 mmol), and 1-ethyl-3-(3-dimethylaminopropyl)-carbodiimide (EDCI, 186.3 mg, 1.2 mmol). The reaction was stirred under reflux until TLC (DCM:MeOH, 95:5) showed all cholesterol had reacted (2.5

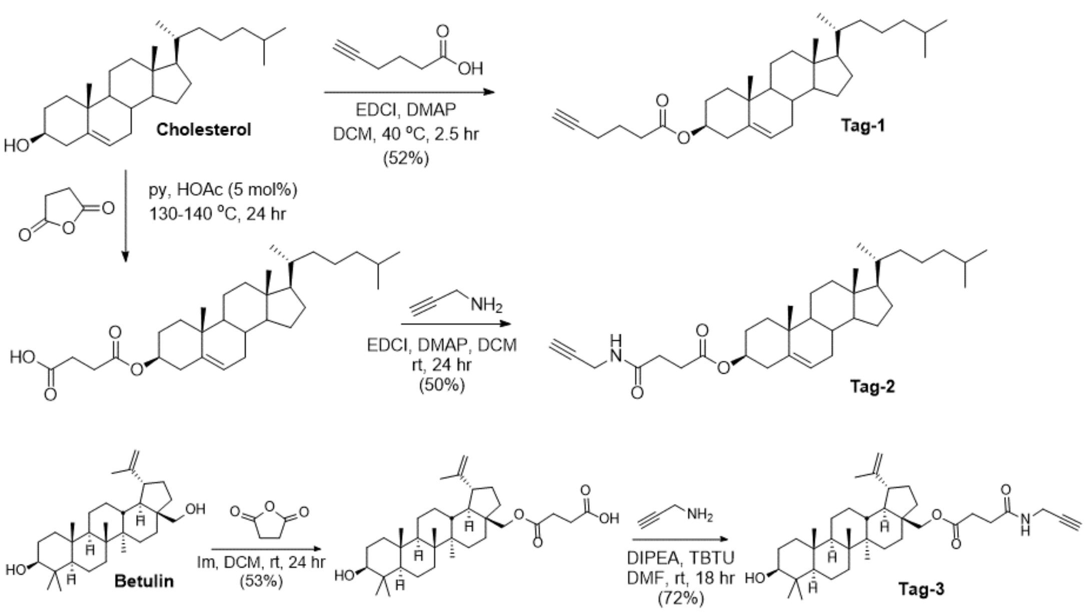

Figure 4.2 Synthesis Schemes of Tags-1, 2 and 3. Reproduced with permission from Ref. 56. Copyright (2021) by National Academy of Sciences.

hours). After cooling, the reaction mixture was washed with H_2O (3 x 2 mL), 1N HCl (2 x 3 mL), and H_2O (3 x 2 mL). The solvent was removed in vacuo (rotary evaporator) to yield Tag-1 (240 mg, 52% crude yield), shown to be >95% pure by NMR. Further purification could be accomplished by flash chromatography (DCM:MeOH, 95:5, R_f 0.43). ^{1}H-NMR (500 MHz, $CDCl_3$) δ 0.67 (s, 3H), 0.86 (d, *J* = 6.6 Hz, 3H), 0.87 (d, *J* = 6.6 Hz, 3H), 0.91 (d, *J* = 6.6 Hz, 3H), 1.01 (s, 3H), 1.778 - 1.89 (overlapped, 6H), 1.97 (t, *J* = 2.6 Hz, 1H), 1.93 - 2.04 (overlapped, 2H under 1.97 t), 2.26 (td, *J* = 7.0, 2.6 Hz, 2H), 2.29 - 2.34 (overlapped, 2H), 2.42, (t, *J* = 7.4 Hz, 2H), 4.62 (m, 1H), 5.37 (br d, *J* = 5.4 Hz, 1H). ^{13}C NMR (125 MHz, $CDCl_3$) δ 12.1, 18.1, 18.9, 19.5, 21.2, 22.8, 23.1, 23.9, 24.0, 24.5, 28.0, 28.2, 28.5, 32.06, 32.12, 33.5, 36.0, 36.4, 36.8, 37.2, 38.3, 39.7, 39.9, 42.5, 50.2, 56.3, 56.9, 69.3, 74.2, 83.6, 122.9, 139.8, 172.7.

For synthesis of Tag-2, Cholesteryl Hemisuccinate was first prepared in an adapted approach as previously reported.[284] Cholesterol (1 g, 2.6 mmol) and succinic anhydride (0.775 g, 7.7 mmol, 3 eq) in anhydrous pyridine (60 mL) were placed into a two-neck round bottom flask. Acetic acid (two drops) was added, then the reaction mixture was refluxed with stirring for 24 hours monitored by TLC (DCM:MeOH, 9:1). After cooling to RT, $NaHCO_3$ solution (5%, 200 mL) was added to the reaction mixture, then the pH was adjusted to 5 by the addition of 6N HCl. Diethyl ether (100 ml) was added, then the organic layer was separated, and the aqueous layer extracted twice with additional diethyl ether (50 mL). The combined ether layers were dried over Na_2SO_4, then the solvent removed in vacuo. The residue was purified by flash chromatography (DCM:MeOH, 9:1, $R_{f.}$ = 0.43), or could be used directly in the next step without further purification. After purification, the esterified cholesterol (0.635 g, 51 % yield) was isolated as a white solid. ^{1}H-NMR (300 MHz, $CDCl_3$) δ 0.68 (s, 3H), 0.86 (d, *J* = 6.6 Hz, 3H), 0.87 (d, *J* = 6.6 Hz, 3H), 0.91 (d, *J* = 6.6 Hz, 3H), 1.01 (s, 3H), 0.86 (d, *J* = 6.6 Hz, 3H), 0.87 (d, *J* = 6.6 Hz, 3H), 0.91 (d, *J* = 6.5 Hz, 3H), 1.02 (s, 3H), 2.26 – 2.36 (overlapped, 2H), 2.55 - 2.72 (overlapped, 4H), 4.63 (m, 1H), 5.37 (br m, 1H).

Tag-2 [(3S,10R,13R,17R)-10,13-dimethyl-17-((R)-6-methylheptan-2-yl)-2,3,4,7,8,9,10, 11,12,13,14,15,16,17-tetradecahydro-1H-cyclopenta[a]phenanthren-3-yl 4-oxo-4-(prop-2-yn-1-ylamino) butanoate] was prepared through amidation of the cholesteryl hemisuccinate.[284] Propargylamine (822 mmol) and DMAP (1.133 mmol, 0.13 mol%) were dissolved in a sufficient amount of DCM to dissolve all solids with ultrasound assistance. To the mixture was added the cholesteryl hemisuccinate (0.82 mmol, 1 equivalent, 400 mg) and then EDCI (1.133 mmol, 0.13 mol%). The reaction mixture was stirred for 18 hours at RT. Once the reaction had gone to completion, monitored using TLC (DCM:MeOH, 95:5), the mixture was then washed with 10% acetic acid, followed by distilled water, sodium bicarbonate and finally brine. The combined organic layers were dried over sodium sulfate and concentrated in vacuo. The product is a white powder (0.215 g, 50.0% yield) and purification via column chromatography was accomplished using hexanes:ethyl acetate (1:1)). ^{1}H-NMR (500 MHz, $CDCl_3$) δ 0.67 (s, 3H), 0.86 (d, *J* = 6.6 Hz, 3H), 0.87 (d, *J* = 6.6 Hz, 3H), 0.91 (d, J = 6.6 Hz, 3H), 1.01 (s, 3H), 2.22 (t, *J* = 2.6 Hz, 1H), 2.29 - 2.34 (overlapped, 2H), 2.48 (t, *J* = 6.7 Hz, 2H), 2.65 (t, *J* = 6.7 Hz, 2H), 4.05 (dd, *J* = 5.2, 2.6 Hz, 2H), 4.62 (m, 1H); 5.37 (br d, *J* = 4.8 Hz, 1H), 5.89 (br s, N*H*). HRMS (ESI QToF) *m/z* 524.4118 ($[M + H]^+$, 100%), calculated for $C_{34}H_{54}NO_3$ 524.4104.

For synthesis of Tag-3, an intermediate was first synthesized following a previous report.[285] To a solution of betulin (0.490 g, 1.1 mmol) in dry DCM (40 mL), succinic anhydride (0.129 g, 1.3 mmol) and imidazole (0.230 g, 3.3 mmol) were added. The reaction was stirred at RT for 24 hours, after which it was quenched with 3% aqueous hydrochloric acid (5 mL). The organic layer was separated and washed twice with 3% aqueous hydrochloric acid (5 mL), and then dried over $MgSO_4$. The solvent was removed in vacuo, and the crude product was triturated with a minimum amount of acetone. Vacuum filtration yielded pure product (0.317 g, 53%). ^{1}H-NMR (500 MHz, CD_3OD) δ 0.76 (s, 3H), 0.82 (s, 3H), 0.96 (s, 3H), 0.97 (s, 3H), 1.02 (s, 3H), 1.68 (s, 3H), 2.43 (ddd, *J* = 11.1, 11.1, 5.6 Hz, 1H), 2.64 - 2.74 (AA'BB'-system, 4H), 3.18 (dd, *J* = 11.5, 4.6 Hz, 1H), 3.91 (d, *J* = 11.4 Hz, 1H), 4.30 (d, *J* = 11.4 Hz, 1H), 4.58 (br s, 1H), 4.68 (br s, 1H).

Tag-3, (1*R*,3a*S*,5a*R*,5b*R*,7a*R*,9*S*,11a*R*,13b*R*)-9-hydroxy-5a,5b,8,8,11a-pentamethyl-1-(prop-1-en-2-yl)-icosahydro-1H-cyclopenta[a]chrysen-3a-yl]methyl 3-[(prop-2-yn-1-yl)carbamoyl]propa-noate, was synthesized through amidation of 28-hemisuccinylbetulin.[282] To a stirred solution of 28-hemisuccinylbetulin (0.140 g, 0.26 mmol) in dry dimethylformamide (DMF, 3 mL) was added *N*,*N*-diisopropylethylamine (DIPEA, 0.1 mL, 0.57 mmol) and 2-(1*H*-benzotriazole-1-yl)-1,1,3,3-tetramethylaminium tetrafluoroborate (TBTU, 0.097 g, 0.3 mmol) at 0 °C. The reaction mixture was stirred for 30 minutes followed by the addition of propargylamine (0.05 mL, 0.78 mmol), after which it was allowed to warm to RT and stirred overnight (18 hours). The reaction was quenched by the addition of saturated sodium bicarbonate (3 mL) and the mixture was extracted with methylene chloride (10 mL). The organic layer was washed with cold water (3 mL) and brine (3 mL), then dried over $MgSO_4$. After filtering, removal of the solvent in vacuo yielded the crude product. The solid was purified using flash chromatography (95:5 chloroform:methanol) to yield pure Tag-3 (0.108 g, 72%). ^{1}H-NMR (500 MHz, $CDCl_3$) δ 0.75 (s, 3H), 0.81(s, 3H), 0.96 (s, 6H), 1.02 (s, 3H), 1.67 (s, 3H), 2.23 (t, *J* = 2.5 Hz, 1H) 2.42 (ddd, *J* = 11.0, 11.0, 5.6 Hz, 1H), 2.50 (t, *J* = 6.7 Hz, 2H), 2.71 (t, *J* = 6.7 Hz, 2H), 3.18 (br d, *J* = 11.0 Hz, 1H), 3.87 (d, *J* = 11.1 Hz, 1H), 4.05.(dd, *J* = 5.2, 2.5 Hz, 1H) 4.38 (d, *J* = 11.1 Hz, 1H), 4.58 (br s, 1H), 4.68 (br s, 1H), 5.88 (br s, N*H*). HRMS (ESI QToF) *m/z* 580.4388 ($[M + H]^+$, 100%), calculated for $C_{37}H_{58}NO_4$ 580.4366.

The tags retain the lipophilic terpenoid ring structure of cholesterol or betulin, which allows them to integrate into lipid membranes and stabilize lipid organization and packing, as is known from unmodified sterols. The hydroxyl group on cholesterol C3 or betulin C28 (**Fig.**

4.1A, red arrows) are derivatized to introduce side chains of different lengths and polarity as well as the terminal alkyne group. Compared to Tag-1, the modified side chains for Tag-2 and Tag-3 are longer and contain an additional amide group that increases the polarity and the number of hydrogen bond donors/acceptors in the side chain. The partial charge distribution in the modified side chains is illustrated by Hirshfeld charge analyses,[286] performed by our collaborator, James McNeely, for all tags under lipid membrane-mimicking conditions with a dielectric constant ε = 2 (**Fig. 4.1A**).

Tag-1 to Tag-3 were incorporated into the lipid membrane of an L-NP architecture in a modified one-pot self-assembly approach as previously reported.[17, 29, 52] In this work, 40 nm Ag NP cores and a lipid composition of 55 mol% zwitterionic 1,2- dipalmitoyl-sn-glycero-3-phosphocholine (DPPC), 5 mol% anionic 1,2-dioleoyl-sn-glycero-3-phospho-L-serine (DOPS), and 40 mol% of one of the three tag species were used as the major L-NP composition. A similar hybrid membrane to described in previous chapters is produced that contains an outer lipid monolayer tethered through hydrophobic interactions to an inner octadecanethiol (ODT) layer, which is covalently bound to the metal NP surfaces (**Fig. 4.1B**). As introduced earlier, in this or similar hybrid membrane models, the intermediate layer and lipid layers interdigitate, leaving no interstitial space between the two sublayers.[157-158] This can be evidenced by transmission electron microscopy (TEM) micrographs of L-NP-Tag-1 (**Fig. 4.1C**), which show a uniform lipid membrane around the NP core with an average thickness of 2.2 ± 0.4 nm, This membrane thickness is smaller than what would be expected based on a simple addition of the thicknesses of a DPPC monolayer (16.1 Å)[287] and an ODT layer (16.0 Å).[288] A nearly identical membrane width of 2.3 ± 0.4 nm is measured for L-NP-Chol control composed of the same lipids but unmodified cholesterol instead of the tag molecules.

Table 4.1 Summary of Hydrodynamic Diameters and ζ-Potentials of L-NP Composites. Reproduced with permission from Ref. 56. Copyright (2021) by National Academy of Sciences.

Groups	**Hydrodynamic Diameter (nm)**	**ζ-Potential (mV)**
L-NP-Chol control	61.3 ± 9.6	-33.9 ± 0.9
L-NP-Tag-1	56.7 ± 4.8	-31.1 ± 1.3
$\mathbf{L_{DSPA}}$-NP-Tag-1	59.0 ± 2.4	-63.3 ± 1.2
Liposome-Tag-1	107.8 ± 1.7	-47.8 ± 2.5
L-NP-Tag-2	53.4 ± 3.4	-15.5 ± 0.5
L-NP-Tag-3	59.7 ± 2.7	-11.8 ± 1.3

Successful lipid membrane formation in L-NPs was demonstrated using fluorescence-labeled lipids through optical colocalization of fluorescent membrane signal and NP scattering signal in correlated fluorescence (FL) and darkfield (DF) imaging of surface-immobilized L-NPs. Images were analyzed by ImageJ, and Manders' coefficients[189] were calculated with the JACoP ImageJ plugin.[289] For nanocomposites with all three modified tags, a strong spatial correlation of the DF signal from the metal core and the FL signal from the membrane layer was observed with high Manders' correlation coefficients comparable to that of the regular L-NP-Chol control (**Fig. 4.3**). The average hydrodynamic diameters of the nanocomposites were measured to be 56.7 ± 4.8 nm for Tag-1-containing L-NPs (L-NP-Tag-1), 53.4 ± 3.4 nm (L-NP-Tag-2), and 59.7 ± 2.7 nm (L-NP-Tag-3). These diameters are similar to that of L-NP-Chol (61.3 ± 9.6) (**Table 4.1**).

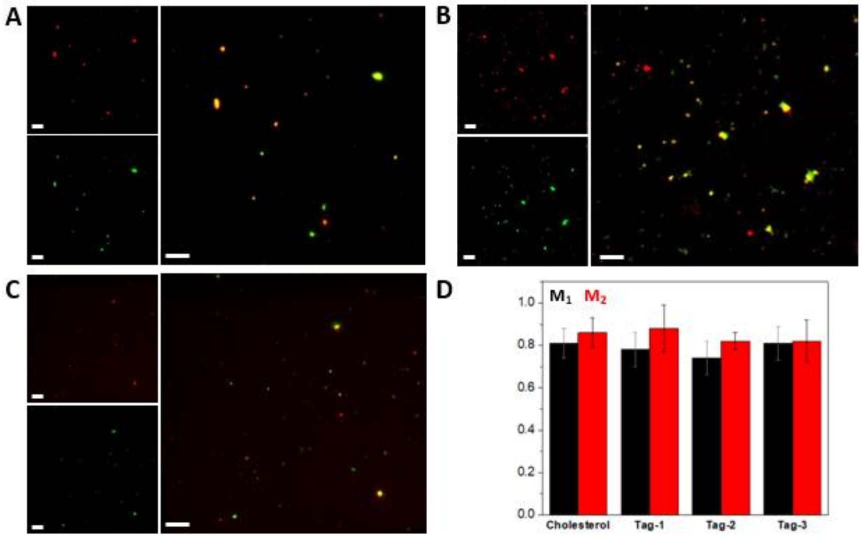

Figure 4.3 Evidence of Successful L-NP Membrane Formation with Tags-1-3. Reproduced with permission from Ref. 56. Copyright (2021) by National Academy of Sciences. (A-C) Correlated DF (top left), FL images (bottom left) and a channel merge (right) of L-NP-Tag-1 (A), L-NP-Tag-2 (B) and L-NP-Tag-3 (C) colloids with a membrane dye. Scale bars=10 µm. (D) Manders correlation coefficients M_1 (black, correlation of DF signals with FL) and M_2 (red, correlation of FL with DF) calculated from the correlated DF/FL images with membrane dye for L-NP-Chol, and L-NP-Tags-1-3.

To probe the availability of alkyne groups on the surface of L-NP-Tag-1, a fluorescent click assay (FCA) based on the azide-alkyne click reaction[290] was designed and performed. The FCA conjugates alkyne groups with fluorescent azide molecules (**Fig. 4.4**). Aliquoted reaction mixtures containing 30 µL water suspension of L-NP-Tags, 60 µL 10 mM azide-PEG$_3$-biotin (Sigma Aldrich) in 0.5x phosphate-buffered saline (PBS) buffer and 6 µL catalyst solution containing 1:1 (volume/volume) 0.005 M Cu(II)$SO_4 \cdot 5H_2O$ (Sigma Aldrich) and 0.05 M L-ascorbic acid (Sigma Aldrich) were prepared and kept at RT for 2 days before being dialyzed with nuclepore track-etched membranes (Whatman, pore size: 0.03 µm) in 0.1x PBS overnight. The dialyzed products were analyzed with Raman spectroscopy or further incubated with 1 mg mL^{-1} 0.5x PBS solution of the streptavidin

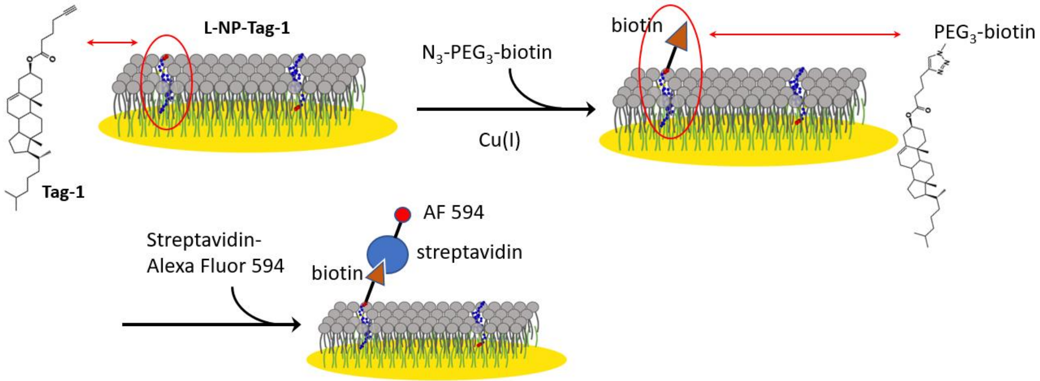

Figure 4.4 Scheme of the Fluorescent Click Assay for Click Conjugation of a Dye-Labelled Azide to L-NP-Tag-1 Surface. Reproduced with permission from Ref. 56. Copyright (2021) by National Academy of Sciences.

Alexa Fluor 594 (Thermo Fisher Scientific) for correlated DF/FL imaging under an Olympus IX71 Inverted Microscope. After the click reaction, correlated DF/FL imaging on L-NP-Tag-1 colloids reveals a strong spatial correlation of DF and FL signals (**Fig. 4.5A**). Overall, these data confirm the presence of solvent-accessible terminal alkyne groups in L-NP-Tag-1 that facilitate a successful click conjugation.

Next, Raman spectra were recorded for drop-casted thin films of Tag-1, L-NP-Tag-1, and a liposome-Tag-1 control (**Fig. 4.5B**). The liposome-Tag-1 control possessed conventional liposome structure with lipid bilayers and identical lipid compositions (**Fig. 4.6A**). The average width of the lipid bilayer membrane in the liposome controls was determined from TEM images as 6.1 ± 1.0 nm (**Fig. 4.6B**). Raman spectra were obtained on a Renishaw InVia Raman Microscope with 100x air objective (Leica, Numerical Aperture=0.85); a 2400 l/mm diffraction grating for the 532 nm excitation laser, or a 1200 l/mm diffraction grating for 633 and 785 nm lasers. 30-seconds exposure time and laser powers of $1.6\text{x}10^3$ μW (for 532 nm excitation), 504.0 μW (for 633 nm) and $5.9\text{x}10^3$ μW (for 785 nm) were

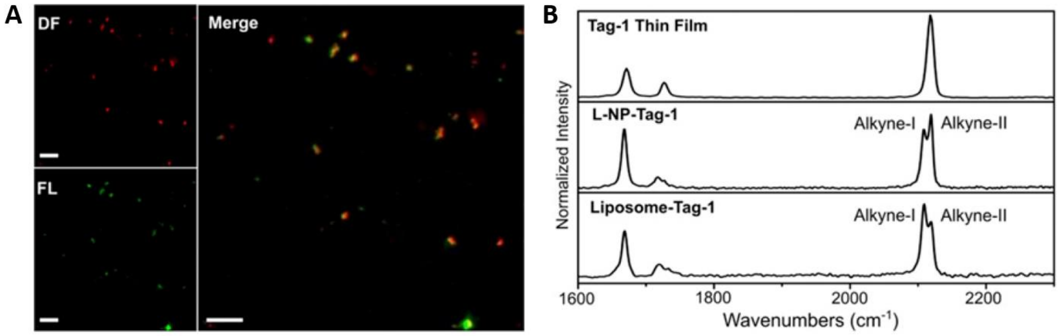

Figure 4.5 Microscopy and Raman Characterizations of L-NP-Tag-1. Reproduced with permission from Ref. 56. Copyright (2021) by National Academy of Sciences. (A) Correlated DF (top left), FL (bottom left) images and a channel merge (right) of L-NP-Tag-1 after the fluorescent click assay. Scale bars = 10 µm. (B) Raman spectra of Tag-1 (top), L-NP-Tag-1 (middle) and Liposome-Tag-1 (bottom).

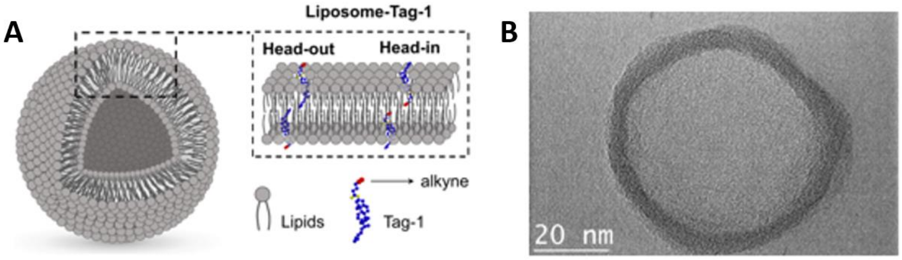

Figure 4.6 Characterizations of Liposome-Tag-1 Control. Reproduced with permission from Ref. 56. Copyright (2021) by National Academy of Sciences. (A, B) Structural scheme (A) and TEM micrograph (B) of Liposome-Tag-1.

used. Each spectrum was calibrated with the Si peak from Si wafer substrate at 522 cm^{-1}, and Lorentzian peak fitting of Raman spectra was performed in Origin for calculation of peak positions, peak FWHMs as well as the integrated peak areas. The Raman spectrum of the Tag-1 thin film contains a well-defined alkyne-stretching peak at 2118.4 ± 1.0 cm^{-1} with a narrow full width at half maximum (FWHM) of 9.9 ± 1.3 cm^{-1} (**Fig. 4.5B**, Top; see also **Fig. 4.7A**). In addition, a distinct C=C-stretching band at 1667.8 ± 0.9 cm^{-1} as well as a carbonyl-stretching band at 1717.1 ± 1.1 cm^{-1} can also be observed from these functional groups in Tag-1. Intriguingly, different from the Tag-1 thin film, the alkyne-stretching

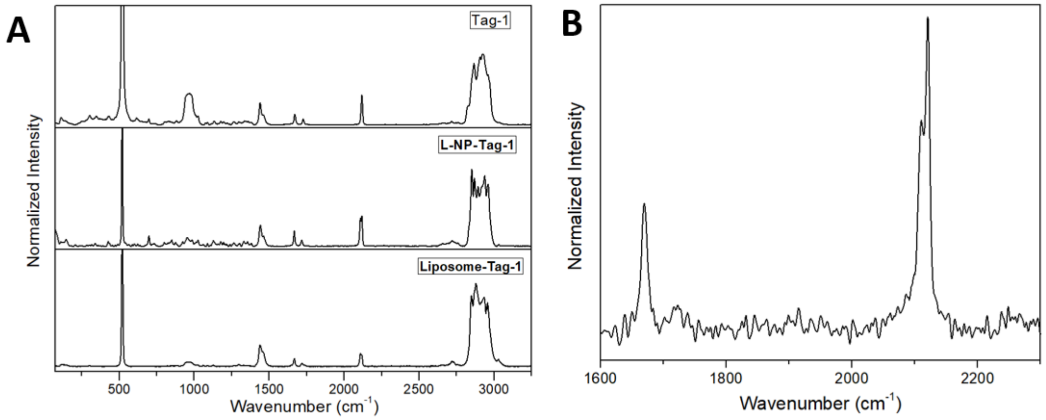

Figure 4.7 Raman Characterization of L-NP-Tag-1 and Controls. Reproduced with permission from Ref. 56. Copyright (2021) by National Academy of Sciences. (A) Extended Raman spectra of Tag-1 (top), L-NP-Tag-1 (middle) and Liposome-Tag-1 (bottom) drop-coated on Si substrates measured with 532 nm excitation. The peak at 522 cm^{-1} is from Silicon wafer substrate and was used to calibrate the peak frequencies. (B) Raman spectrum of an aqueous suspension of L-NP-Tag-1 acquired with 532 nm excitation laser.

bands of L-NP-Tag-1 (**Fig. 4.5B**, Middle) and liposome-Tag-1 (**Fig. 4.5B**, Bottom) are split into a doublet shape with two distinct peaks. For L-NP-Tag-1, the peak stretching frequencies are respectively 2108.8 ± 0.8 cm^{-1} and 2118.6 ± 0.8 cm^{-1}, with FWHMs of 9.5 ± 1.2 cm^{-1} and 10.3 ± 1.4 cm^{-1}. These two peaks are referred to as alkyne-I and alkyne-II, respectively, throughout this chapter. An ensemble-averaged SERS enhancement factor of 3.9×10^4 is calculated for L-NP-Tag-1 based on the alkyne-II peak intensity with 532 nm excitation. Raman spectra of aqueous suspensions of L-NP-Tag-1 were also recorded (**Fig. 4.7B**) and were found to exhibit an identical doublet peak shape for the alkyne-stretching band with peak maxima at 2108.8 ± 0.8 and 2119.9 ± 0.7 cm^{-1}.

This peak splitting behavior is not limited to L-NP-Tag-1 prepared with Ag NP core or Liposome-Tag-1. Similar doublet peak shapes were also recorded for other types of lipid-coated, Tag-1-incorporating control nanocomposites, prepared with cores of different

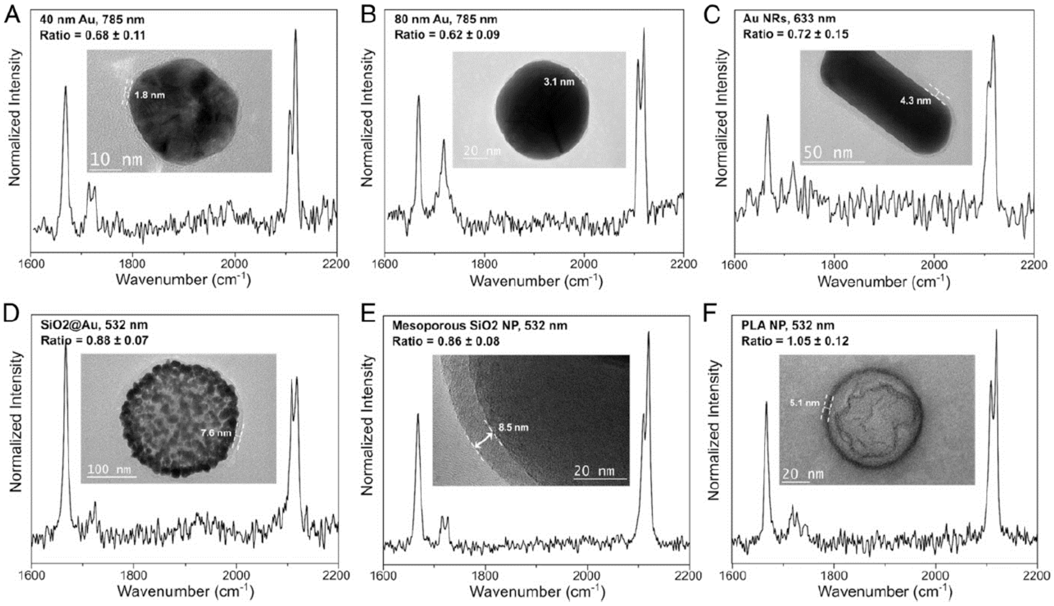

Figure 4.8 Characterization of Different Tag-1-Incorporating Nanocomposites. Reproduced with permission from Ref. 56. Copyright (2021) by National Academy of Sciences. (A-F) Raman spectra of lipid-wrapped, Tag-1-incorporating nanocomposites with 40 nm Au NPs (A), 80 nm Au NPs (B), Au nanorods (NRs) (C), SiO_2-Au core-shell NPs (D), mesoporous SiO_2 NPs (E), and PLA NPs (F) as cores at indicated excitation wavelengths. Alkyne-I/alkyne-II-integrated intensity ratios are calculated by peak areas from Lorentzian peak fits from 10 spectra obtained in three independent experiments.

sizes, shapes, and compositions (**Fig. 4.8**). Nanocomposites containing Au NPs (40 and 80 nm), Au nanorods, SiO_2-Au core-shell NPs, mesoporous SiO_2 NPs, or polylactic acid (PLA) NPs as cores were found to exhibit similar spectral features in the alkyne-stretching region as L-NP-Tag-1.

As Raman spectroscopy can provide detailed structural information and can resolve molecular orientations in membranes, one possible explanation for the observed splitting of the alkyne-stretching band in L-NP-Tag-1 is that the tag molecule exhibits two preferential orientations in the lipid membrane. Previous studies on unmodified cholesterol have shown that while sterols most likely tend to take on an orientation (a) where the sterol lies parallel to the lipid molecules and the cholesterol hydroxyl group is positioned close to lipid head groups; two other orientations are also likely: (b) an inverse orientation to (a) where the sterol lies parallel to the lipid but the hydroxyl is placed close to lipid tails, and (c) when the sterol sits in the interstice between the two lipid leaflets of a lipid bilayer and perpendicular to lipid molecules.[291-294] A coexistence of different orientations is likely to occur in membranes with high levels of unsaturated lipids[292, 294] or when the sterol hydroxyl is substituted with less polar functional groups.[295-296]

Based on these previous findings, we tentatively attribute the splitting of the alkyne-stretching band in the L-NP-Tag-1 Raman spectra to a coexistence of two distinct orientations. A "head-out" orientation corresponding to the (a) mode of unmodified cholesterol, in which the tag lies parallel to the lipid and the terminal alkyne group points toward the lipid-water interface is very likely to exist in our case; and a "head-in" orientation corresponding to the (b) mode, where the alkyne points toward the metal core is also feasible (**Fig. 4.1B**, Right). Because of an absence of an interstitial space in the interdigitated lipid-ODT hybrid membrane architecture as evidenced above, significant contributions from the (c) mode (horizontal sterol orientation) can be excluded for L-NPs.

4.2 Evidence of Tag Orientation in Lipid Membranes

To determine the specific tag orientations associated with alkyne-I and alkyne-II modes in L-NP-Tag-1, we first measured the alkyne-stretching frequencies of Tag-1 dissolved in solvents with different polarities,[297] including ethanol, acetone, and chloroform (**Fig. 4.9A**), in order to imitate the dielectric environments of the lipid head groups or lipid tails

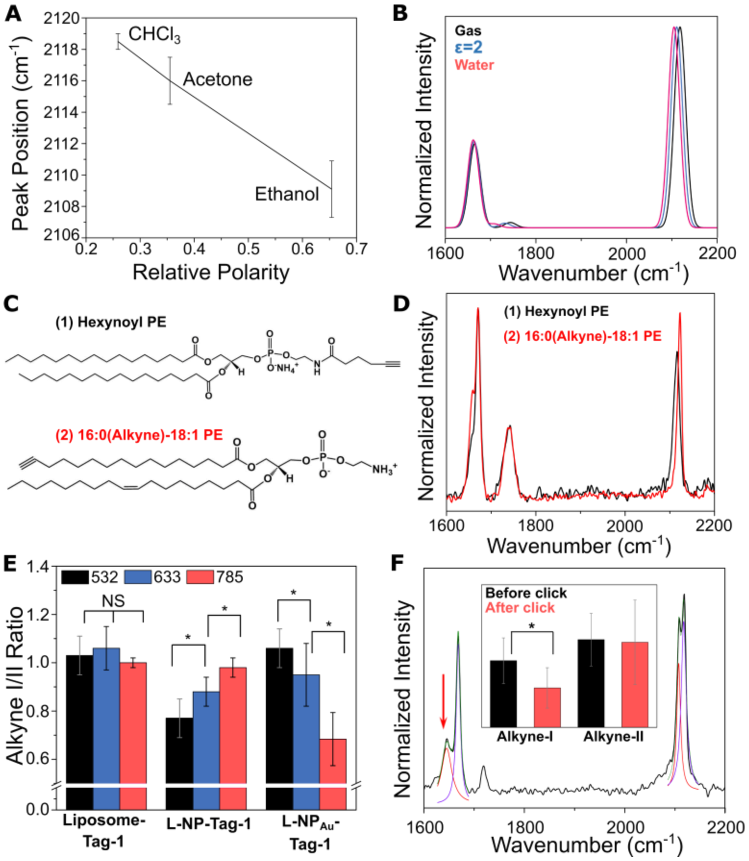

Figure 4.9 Evidence for Tag-1 Orientation in Lipid Membranes. Reproduced with permission from Ref. 56. Copyright (2021) by National Academy of Sciences. (A) Plot of the alkyne stretching frequencies of Tag-1 dissolved in different solvents versus relative solvent polarity. (B) BP86/DEF2-SV(P)/D3BJ[/CPCM(H_2O/ε=2)] calculations of Raman vibrational frequencies of Tag-1 alkyne stretching peak in gas phase (black), in a lipid membrane mimic with ε=2 (blue), and with an CPCM implicit solvation of water (red). (C-D) Molecular structures (C) of hexynoyl PE (1,2-dipalmitoyl-sn-glycero-3-phosphoethanolamine-N-(5-hexynoyl)) (top) and 16:0(alkyne)-18:1 PE (1-hexdec-15-ynoyl-2-oleoyl-sn-glycero-3-phosphoethanolamine) (bottom), and Raman spectra of liposome containing the two lipids (D). (E) Alkyne-I/alkyne-II integrated intensity ratios with different excitation wavelengths for Liposome-Tag-1, L-NP-Tag-1, and L-NP$_{Au}$-Tag-1; *: significant difference at p=0.01; NS: non-significant difference at p=0.5. (F) Raman spectrum and Lorentzian fits of L-NP-Tag-1 after click conjugation of azide-PEG-biotin; inset: integrated peak intensity ratios of alkynes-I or -II to lipid -CH_2- stretching internal standard before (black) or after (red) click reaction.

and to estimate the spectral shift in the alkyne-stretching frequency. The alkyne-stretching band of Tag-1 exhibits a single, symmetric peak in all solvents, and the peak stretching frequency shifts towards higher wavenumbers in solvents that are less polar. When the solvent is changed from the more polar solvent ethanol to the relatively nonpolar solvent chloroform, the stretching frequency of the alkyne-stretching peak shifts from 2109.1 ± 2.1 cm^{-1} to 2118.5 ± 0.5 cm^{-1}. These stretching frequencies are essentially identical to those determined for alkyne-I (2108.8 ± 0.8 cm^{-1}) and alkyne-II (2118.6 ± 0.8 cm^{-1}) in L-NP-Tag-1. A similar test was also conducted with Tag-3, and a nearly identical trend was observed (**Fig. 4.10A**).

The Raman spectra of Tag-1 were also calculated through BP86/DEF2-SV(P)/D3BJ calculations by our collaborator Dr. James McNeely in 1) the gas phase; 2) a conductor-like polarizable continuum model (CPCM) with a dielectric constant $\varepsilon = 2$, mimicking the hydrophobic condition of lipid tails; and 3) a CPCM model of water (**Fig. 4.9B**). These calculations predict that in the gas phase, the alkyne-stretching frequency Tag-1 is located at 2118 cm^{-1}, which shifts to 2111 cm^{-1} in the dielectric medium with $\varepsilon = 2$, and to 2105 cm^{-1} in water. Both the experimental and calculated relationship between the alkyne-stretching peak frequency and the dielectric environment are consistent with an assignment of the alkyne-I peak to the head-out orientation of Tag-1, sampling the lipid head groups with relatively polar moieties; and the alkyne-II peak to the head-in orientation, sampling the lipid tails of the membrane with relatively less polar environment.

Another piece of evidence supporting this peak assignment stems from another experiment where control liposomes were prepared with unmodified cholesterol and alkyne-conjugated lipids that contain an alkyne group respectively in the lipid head group [(i) hexynoyl PE, **Fig. 4.9C**, Top] or in the lipid tail [(ii) 16:0(alkyne)–18:1 PE, **Fig. 4.9C**,

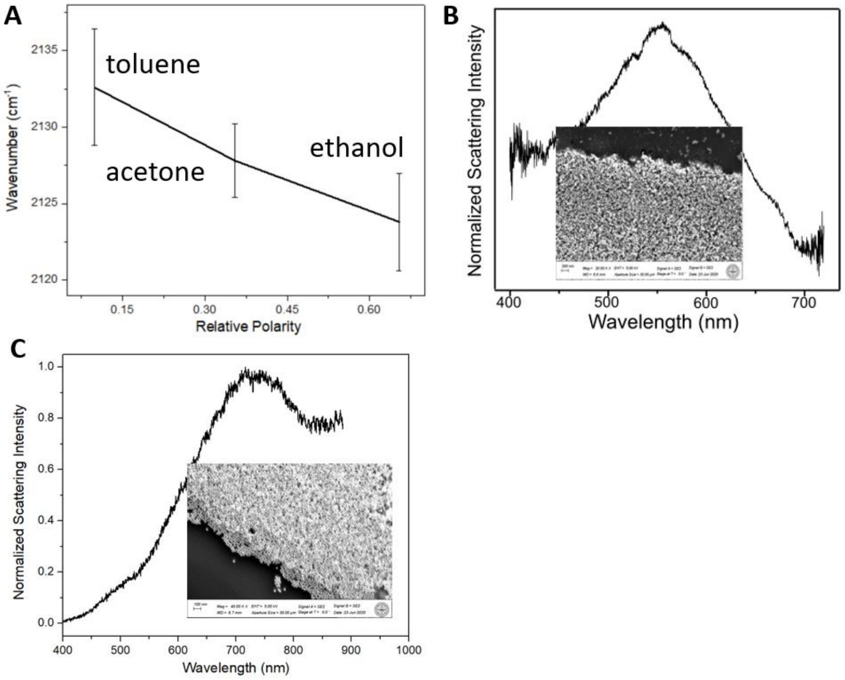

Figure 4.10 Supplemental Evidence for Tag Orientations in Lipid Membranes. Reproduced with permission from Ref. 56. Copyright (2021) by National Academy of Sciences. (A) Plot of the alkyne stretching frequencies of Tag-3 dissolved in different solvents versus the relative solvent polarity. (B, C) Elastic scattering spectra and SEM images (insets) of L-NP-Tag-1 (B) and L-NP$_{Au}$-Tag-1 control with 40 nm Au NPs cores (C) thin films drop-coated on glass (spectrum) or silicon (image) substrates.

Bottom]. The spectrum of (i) exhibits an alkyne-stretching peak at 2112 ± 1.2 cm^{-1}, which is similar to the alkyne-I peak observed for L-NP-Tag-1; whereas the spectrum of (ii) contains an alkyne-stretching peak at 2119.5 ± 2.1 cm^{-1}, close to the alkyne-II peak of L-NP-Tag-1 (**Fig. 4.9D**). The spectra of the modified lipids confirm that the stretching frequency of the alkyne groups shifts to higher wavenumbers when localized in the hydrophobic region of the membrane.

The relative SERS enhancement could provide another set of evidence to our peak assignment in the alkyne stretching region. As the resonant SERS signal amplification scales with the fourth power of the E-field (E^4),[107, 267-268] and that the E-field intensity rapidly decreases as the separation from the NP surface increases,[107] a strong distance-dependence in the extent of enhancement exists. Consequently, even relatively small changes in separation between a Raman-active group and the NP surface can result in significant differences in the recorded signal intensity. Based on the length of the sterol molecule, the difference in the distance between the metal surface and the alkyne group respectively in the head-out and head-in orientations of Tag-1 is estimated to be > 1.5 nm.[291] Consequently, we expect the alkyne-II peak, which is associated with the head-in orientation and positions the alkyne moiety closer to the metal NP, to experience on average a stronger SERS signal amplification under resonant excitation than the alkyne-I peak associated with the head-out orientation. To test this hypothesis, the integrated intensity ratios of the alkyne-I to alkyne-II bands at three different excitation wavelengths (532, 633, and 785 nm) were calculated for L-NP-Tag-1, and were compared to control groups of liposome-Tag-1 and an L-NP$_{Au}$-Tag-1 control. The L-NP$_{Au}$-Tag-1 control was prepared with the identical lipid membrane but using a 40 nm Au NP core instead of Ag NP. The reason why these controls were used is to provide SERS response from different spectra regions. The plasmon resonance maxima of L-NP-Tag-1 and L-NP$_{Au}$-Tag-1 thin films were measured to be around 550 and 750 nm, respectively (**Fig. 4.10B, C**).

All three investigated groups exhibit a distinct doublet shape in the alkyne-stretching region. For liposome-Tag-1, the alkyne I/alkyne II Raman intensity ratios (**Fig. 4.9E**) show no noticeable difference between the three excitation wavelengths. As no plasmonic NP cores are present for this group and no SERS enhancement factors are involved, the observed intensity ratios close to 1 for all wavelengths in this group indicate that, during the formation of the lipid membranes, head-out and head-in orientations are equally favored in the lipid layer. Importantly, for both L-NP-Tag-1 and L-NP$_{Au}$-Tag-1, the alkyne-I/alkyne-II ratio evidently deviates from around 1 in the liposome case. Both ratios drops significantly when the excitation wavelength overlaps with the plasmon resonance of the drop-casted L-NP films (i.e., at 532 nm with L-NP-Tag-1 and 785 nm with L-NP$_{Au}$-Tag-1) (**Fig. 4.9E**). As the LSPR band of the films are broad, the 633 nm excitation also overlaps weakly with both Ag and Au L-NPs, and the integrated peak intensity ratios also decreased relative to the "off-resonance" conditions (785 nm for silver and 532 nm for gold) but not as much as for the "on-resonance" conditions. Notably, in both L-NP-Tag-1 and L-NP$_{Au}$-Tag-1, alkyne-I/alkyne-II intensity ratios of around 0.7 for on-resonance conditions are consistent with a 1.5- to 2-fold lower SERS signal enhancement for alkyne-I compared to alkyne-II, predicted by the distance dependence of the E-field intensity around individual Au NPs in a Au NP film.[298]

As the head-out orientation of Tag-1 presents the terminal alkyne at the lipid-solution interface, it is very likely that these alkyne groups can react with azides in solution to form a triazole product through click chemistry,[290] whereas the head-in orientation is protected by the lipid layer and not readily accessible for chemical reactions. After click reaction of L-NP-Tag-1 with azides, the Raman spectra contain a new peak in the C=C-stretching range at 1644.2 ± 2.7 cm^{-1} (**Fig. 4.9F**, red arrow), which is very likely to derive from the formation of the triazole product.[299] The lipid -CH$_2$- symmetric stretching band at 2850 cm^{-1} was then used as internal standard,[300] and the alkyne peak intensity was normalized based on the internal standard. After normalization, a significant decrease in intensity was revealed for alkyne-I, whereas the alkyne-II peak intensity remains almost unchanged (**Fig. 4.9F**, Inset). These observations further confirm our orientation assignment of alkyne-I to head-out and alkyne-II to head in. Overall, the experimental data point toward a coexistence of the head-in and head-out orientations as the most likely cause of the observed doublet shape in the alkyne-stretching region for L-NP-Tag-1.

4.3 Effect of Hydrogen Bonding Network on Tag Orientations

To acquire further information on the stability and thermodynamics of the two distinct Tag-1 orientations, we next measured the integrated intensity ratios of alkyne-I and alkyne-II in the Raman spectra of L-NP-Tag-1 as a function of temperature. A water suspension of L-NP-Tag-1 colloid was heated continuously *in situ* from RT up to 65 °C, and its Raman spectra were measured while the temperature was increased. The most notable observation in the heating experiment is that the alkyne-I peak intensity as well as the alkyne-I/II intensity ratio gradually decrease as the temperature increases (**Fig. 4.11A**). At 63.7 ^{o}C and above, alkyne-I peak is completely gone and only a single alkyne-stretching peak remains at 2118.7 ± 0.4 cm^{-1}, which is essentially identical to the alkyne-II peak (head-in mode) at RT (2118.6 ± 0.8 cm^{-1}). This observation suggests that the heating to a certain transition temperature induces a reorientation of Tag-1 in the lipid membrane from head-out to head-in. This reorientation is further corroborated by the FCA, as introduced in **Fig. 4.4**, performed on L-NP-Tag-1 after heating. Correlated DF/FL imaging showed only weak FL

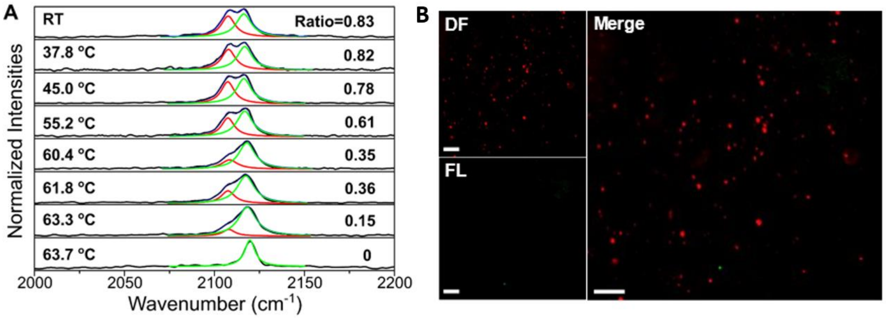

Figure 4.11 Characterization of Thermal-Induced Orientation Change of Tag-1 in L-NP-Tag-1. Reproduced with permission from Ref. 56. Copyright (2021) by National Academy of Sciences. (A) Raman spectra and Lorentzian peak fits of the alkyne stretching bands of L-NP-Tag-1 colloid suspension under *in-situ* heating to different temperatures. (B) Correlated DF/FL images and a channel merge for the Fluorescent Click Assay with L-NP-Tag-1 after heating to > 63.7 ºC for 30 min. Scale bars = 10 µm.

signals with poor colocalization with DF signals ($M_1 = 0.03 \pm 0.05$ and $M_2 = 0.01 \pm 0.01$) (**Fig. 4.11B**). The poor click conjugation efficiency confirms the absence of the head-out orientation for successful click reaction to happen.

The driving forces for the heat-induced reorientation of Tag-1 in NP-supported lipid membranes were next investigated. It has been previously established that the zwitterionic lipids in L-NPs can form an extensive hydrogen-bonding network (HBN) at the interface between lipid head groups and interfacial water molecules located in the immediate vicinity of the lipid membrane.[278-280] The strong interfacial HBN have been characterized in prior works through sum-frequency generation spectroscopy, and it has been determined to effectively repels solute molecules that would perturb and weaken the HBN, which has enabled anti-fouling properties of lipid membranes in some studies.[279-280] In our work, the interaction with the HBN is very likely to impact the orientation of Tag-1 in L-NP membrane. In the head-out orientation, the modified side chain conjugated to the cholesterol C3 in Tag-1 positions the alkyne group into the plane containing the lipid head

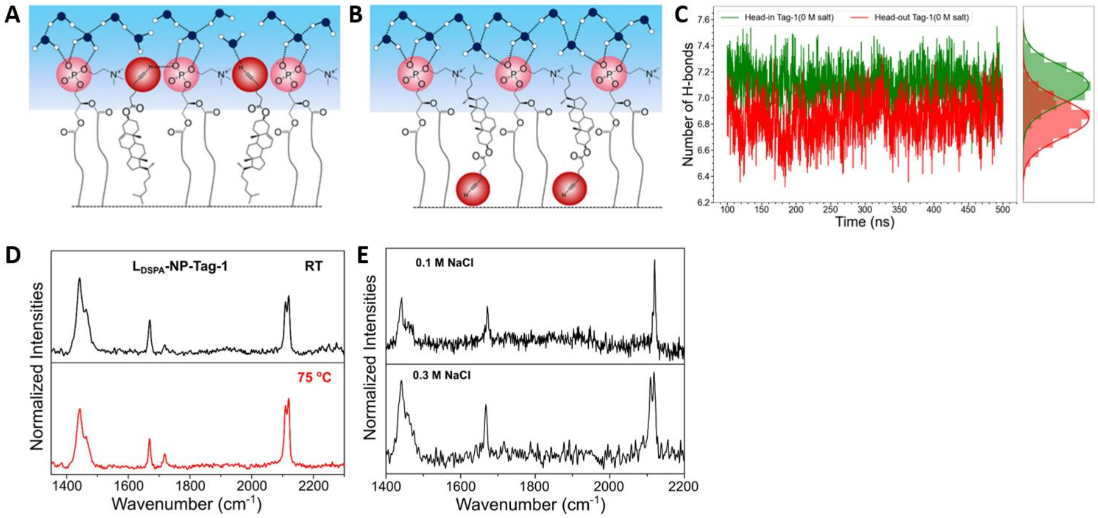

Figure 4.12 Characterization of the Hydrogen Bonding Network. Reproduced and adapted with permission from Ref. 56. Copyright (2021) by National Academy of Sciences. (A, B) Graphical representations of the HBN between DPPC head group and interfacial water molecules with Tag-1 head-out (A) or head-in (B) conformation of Tag-1. (C) Instantaneous average number of hydrogen bonds formed between a single DPPC lipid and interfacial water molecules for a lipid membrane containing Tag-1 head-in (green) or head-out (red) orientations. (D) Raman spectra of L_{DSPA}-NP-Tag-1 control composite before and after heating to 75 °C for 30 min. (E) Raman spectra of L-NP-Tag-1 after heating to 75 °C for 30 min in 0.1M (top) or 0.3 M (bottom) NaCl.

groups. As the side chains contains polar function groups, it can form weak hydrogen bonds with water or lipid molecules (**Fig. 4.12A** and **Fig. 4.13A**). In contrast, in the head-in orientation where the nonpolar carbon chain in position C17 is close to the HBN (**Fig. 4.12B**), it does not engage in evident hydrogen bond formation; as such, it does not evidently impact the strong interfacial water-lipid HBN as much as the modified side chain in the head-out mode. Consequently, we hypothesized that the observed head-out to head-in conversion could be accounted for by the fact that the interfacial HBN is more strongly restructured and perturbed with the head-out orientation of Tag-1 than with head-in.

To substantiate this hypothesis, our collaborator Dr. John Straub and Ayan Majumder performed all-atomic molecular dynamic (MD) simulations of the Tag-1 embedded in a lipid bilayer membrane model, and calculated the number of hydrogen bonds formed between the zwitterionic DPPC lipid head group, interfacial water molecules, and Tag-1 respectively in head-in and head-out orientation in order to characterize the HBN. These calculations reveal that an increased number of hydrogen bonds are formed between each DPPC lipid molecule and interfacial water molecules when Tag-1 is in the head-in orientation (7.1 hydrogen bonds per DPPC molecule), compared to head-out (6.8 per DPPC) (**Fig. 4.12C**). This observation confirms that Tag-1 in the head-out orientation has a stronger disruptive effect on the lipid-water HBN. To estimate the energy associated with this difference, we used the previously reported value of the change in Gibbs free energy associated with the formation of hydrogen bonds between zwitterionic lipids and interfacial waters around -12 kJ/mol at RT,[301] and a typical lipid-grafting density on the surface of our L-NP model of one lipid molecule per 40 Å^2,[302-303] maximization of the HBN achieved by the conversion of head-out to head-in orientation represents a thermodynamic driving force of -4.15×10^{-17} J per particle.

The liquid crystal order parameter was also calculated for a lipid bilayer with identical compositions, and very high values were derived for a lipid membrane containing both tag orientations (**Fig. 4.13B**). These results suggest that the hybrid membrane considered here is in a liquid-ordered phase at RT.[164] Under these conditions, there is a substantial energy barrier for the transition of Tag-1 from head-out to head-in orientation. Therefore, at room temperature, the close packing of the lipids in the hybrid lipid membrane as well as the associated high activation energy barrier could suppress the head-out to head-in transition and effectively break the ergodicity of the system, accounting for the observed doublet

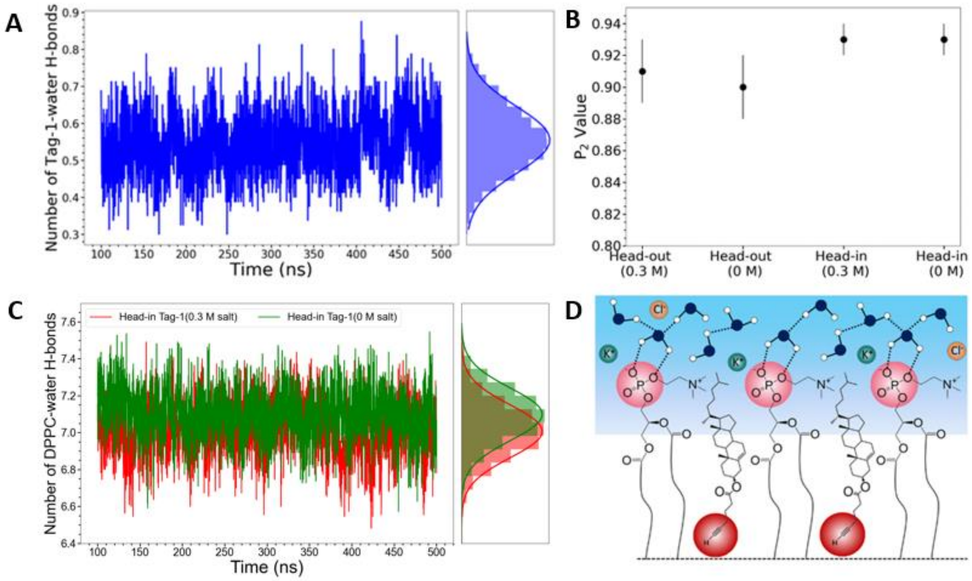

Figure 4.13 Supplemental Characterization of the Lipid-Water HBN. Reproduced with permission from Ref. 56. Copyright (2021) by National Academy of Sciences. (A) MD simulation results for the instantaneous average number of hydrogen bonds formed between a single Tag-1 molecule in the head-out orientation of a model DPPC-Tag-1 bilayer and interfacial water molecules at 0 M salt concentration at RT. (B) Average liquid crystal order parameter (P_2) obtained from MD simulations of lipid bilayers containing Tag-1 head-out or head-in orientations, respectively, and 0 M or 0.3 M salt concentrations at RT. (C) MD simulation results for the instantaneous average number of hydrogen bonds formed between the head group of a single DPPC lipid and interfacial water molecules at 0.3 M and 0 M salt concentration, respectively, with Tag-1 in the head-in orientation. (D) Graphical representation of HBN of DPPC-water affected by the ion concentration with Tag-1 in the head-in conformation.

alkyne stretching Raman peak shape. However, at elevated temperatures, the membrane undergoes a transition into a liquid disordered phase, which could lower the activation barrier for Tag-1 reorientation. The lower activation barrier and the higher available thermal energy facilitate the reorientation of Tag-1 into the preferred head-in orientation, minimizing the disruption of the HBN.

The role of the HBN in the Tag-1 reorientation was also probed experimentally. As shown in previous works, the HBN can be effectively weakened by replacing zwitterionic lipids in the membrane with lipids that carry a net charge.[278-279] Thus, we next tested whether through weakening of the HBN, the stability of the respective orientations of Tag-1 could be affected. A first control nanocomposite, L_{DSPA}-NP-Tag-1, was assembled, which contained the saturated, negatively charged lipid 1,2-distearoyl-sn-glycero-3-phosphate (DSPA) instead of the zwitterionic DPPC as the lipid skeletal component in order to increase the net charge of the lipid membrane. A much more negative ζ-potential was measured for this group than for the regular L-NP-Tag-1, as was expected (**Table 4.1**). At RT, the alkyne-stretching band of L_{DSPA}-NP-Tag-1 shows a pronounced doublet shape with peak frequencies of 2109.3 ± 0.4 cm^{-1} and 2119.8 ± 0.4 cm^{-1}, similar to the alkyne-I and -II modes of L-NP-Tag-1 (**Fig. 4.12D**, top). However, unlike in the case of L-NP-Tag-1, after heating to 75 °C for 30 min, which is above the 63.7 °C transition temperature for regular L-NP-Tag-1, the doublet peak shape is retained for the alkyne-stretching band in L_{DSPA}-NP-Tag-1 (**Fig. 4.12D**, bottom), indicating that the reorientation has been eliminated.

An alternative strategy of weakening the HBN can be achieved by increasing the electrolyte concentration in the aqueous medium around the L-NP-Tag-1 in order to favor the electrostatic interactions in the system.[278-279] This is also evidenced by our MD studies, in which a higher salt concentration in the ambient medium results in a general decrease in hydrogen bond formation at the lipid-water interface (**Fig. 4.13C, D**). When the salt concentration is increased from 0 M (as used in all previous experiments) to 0.1 M NaCl, heating of L-NP-Tag-1 to 75 °C for 30 min still induces some degree of head-out to head-in transition in the alkyne-stretching frequencies of its Raman spectra, but the conversion is not complete, as an evident alkyne-I feature still remains after heating (**Fig. 4.12E**, Top). Importantly, when the salt concentration is further increased to 0.3 M NaCl, no evident transition could be observed any longer (**Fig. 4.12E**, Bottom). Both these experimental results shown above confirms that the HBN is indeed the determining factor for the tag orientation and that the HBN induced the head-out to head-in reorientation at elevated temperatures in the hybrid lipid membrane of L-NP-Tag-1.

The head-out to head-in reorientation and the predominance of the head-in mode in L-NP-Tag-1 at higher temperatures due to interactions of Tag-1 with the HBN suggests that it is feasible to control the preferential orientation of the tag molecules in the membrane by means of altering the size and structure of the side chain in the tag molecule. This could potentially open up great potentials for modulation of the surface properties of L-NPs. To probe this possibility, we tested two other tag molecules, Tags-2 and -3, in which side chains containing an overall increased polarity and a larger number of charge centers for increased hydrogen bonding with the water network are included (**Fig. 4.1A**). As an increased hydrogen bonding is expected for both of these two tags, we expect both tags to favor the head-out orientation in the hybrid lipid membrane.

The Raman spectra at RT for both Tag-2 and Tag-3 (**Fig. 4.14A**), and L-NP-Tag-2 and L-NP-Tag-3 (**Fig. 4.14B**) contain only one distinct, symmetric alkyne-stretching peak. Peak-stretching frequencies were 2131.4 ± 1.9 cm^{-1} (L-NP-Tag-2) and 2124.0 ± 1.6 cm^{-1} (L-NP-Tag-3), respectively. This indicates one dominant orientation of the tags in the membrane for both nanocomposites.

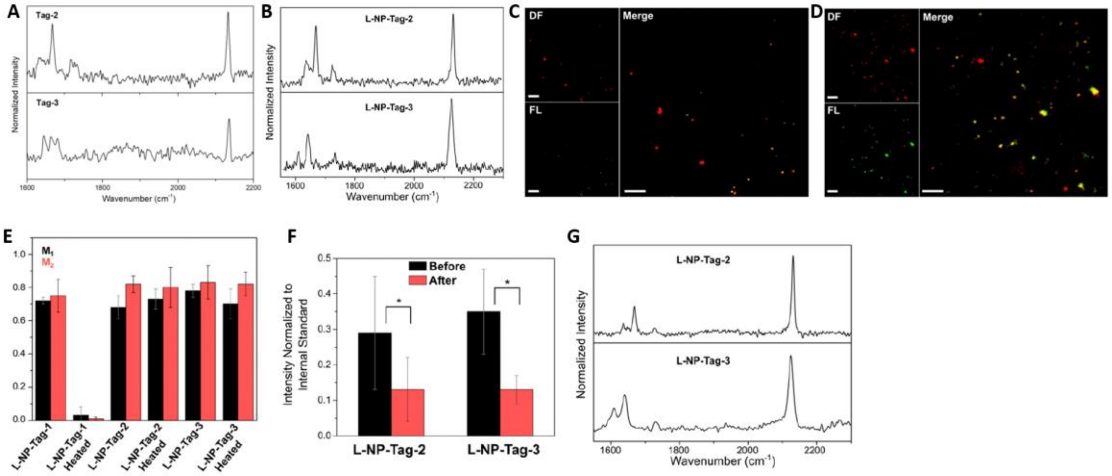

Figure 4.14 Characterization of Orientations of L-NP-Tags-2 and -3. Reproduced and adapted with permission from Ref. 56. Copyright (2021) by National Academy of Sciences. (A, B) Raman spectra of Tag-2 (top) and Tag-3 (bottom) (A), or L-NP-Tag-2 (top) and L-NP-Tag-3 (bottom) (B) drop-coated on Si substrates. (C, D) Correlated DF (top left), FL images (bottom left) and a channel merge (right) of L-NP-Tag-2 (C) or L-NP-Tag-3 (D) colloids after the fluorescent click assay; scale bars=10 µm. (E) Plot of Manders' coefficients M_1 (correlation of DF with FL signals, black) and M_2 (correlation of FL with DF, red) after the fluorescent click assay for L-NP-Tags-1-3 and L-NP-Tags-1-3 after heating. (F) Plot of the integrated peak intensity of the alkyne stretching band of L-NP-Tags-2 and -3 before (black) and after (red) click reaction normalized to the lipid -CH_2- internal standard. (G) Raman spectra of L-NP-Tag-2 (top) and L-NP-Tag-3 (bottom) drop-coated on Si substrates after heated to 75 ºC for 30 min.

To determine what the preferential tag orientation is, the fluorescent click assay was next exploited in order to probe the solvent-accessible alkyne concentration on the nanocomposites. Strong spatial correlation of DF and FL signals were observed in both cases after the fluorescent click (**Fig. 4.14C, D**). High Manders' colocalization coefficients were also calculated from the DF/FL images for L-NP-Tag-2 and L-NP-Tag-3 (**Fig. 4.14E**). These evidence confirm that the tag orientation in both nanocomposites possess the solvent-accessible alkyne moieties that facilitate a successful click conjugation. Furthermore, the Raman spectra of these nanocomposites show a measurable reduction in the normalized integrated peak intensity of the alkyne-stretching mode after the click reaction (**Fig. 4.14F**). These observations imply a head-out orientation. Heating of L-NP-Tag-2 and L-NP-Tag-3 to 75 °C for 30 min did not affect the multiplicity and stretching frequency of the alkyne-stretching peak (**Fig. 4.14G**), which implies that the head-out orientation in L-NP-Tag-2 and Tag-3 is very stable, and is maintained even at higher temperatures. The difference in the preferential membrane orientation between Tag-1 (head-in) and Tag-2 and Tag-3 (head-out) confirms that side chains with overall higher polarity that can form a larger number of hydrogen bonds with the interfacial HBN succeed in stabilizing the tags in the head-out orientation.

4.4 Targeted Cancer Cell Raman Imaging with Tag-Incorporating L-NPs

Targeted Raman imaging of cancer cells using molecular or nanoscale probes that recognize certain cellular biomarkers is a promising strategy for cancer detection and studies at the single-cell level.[304-305] As L-NP-Tag-1 sustains a coexistence of head-out and head-in orientation of Tag-1 at RT, it can provide both (a) surface-accessible alkyne moieties for chemical conjugation and introduction of specific targeting functionalities through click chemistry, and (b) protected alkyne groups that can grant the nanocomposites with a characteristic, plasmon-enhanced spectral signature in Raman imaging experiments. Thus, L-NP-Tag-1 is likely to serve as a novel, efficient and effective probe for targeted cancer cell imaging.

Epidermal growth factor receptor (EGFR)-overexpressing cancer cells were chosen as the targets for the single-cell level Raman imaging tests, as it provides abundant EGFR on the cell surface as a biomarker for molecular recognition. The alkynes in head-out orientation were clicked with azide-functionalized epidermal growth factor (EGF) to introduce the specific EGFR recognition element on the L-NP surfaces. Azide-functionalized EGF was first synthesized through acylation of primary amines. A total of 0.5 mL 1 mg mL^{-1} 1× PBS solution of EGF recombinant human protein (Thermo Fisher Scientific) was mixed with 3% (volume/volume) 0.44 M Dimethyl sulfoxide (DMSO) solution of azido-$dPEG_8$-NHS ester (Sigma Aldrich) and kept in ice bath for 6 hours. Azide-functionalized EGF product was then dialyzed with D-Tube dialyzers (Millipore) overnight to remove excessive unreacted azido-$dPEG_8$-NHS ester. Click reaction between L-NP-Tag-1 and azide-functionalized EGF was performed in reaction mixtures containing 50 μL L-NP-Tag-1 water suspensions, 50 μL azide-functionalized EGF, and 6 μL catalyst solution as described for the Fluorescent Click Assay section. The click and subsequent dialysis procedures are also identical to the fluorescent click process.

The clicked nanocomposites are referred to as L-NP-Tag-1-EGF. These nanoconjugates were then applied to two EGFR-overexpressing breast cancer cell lines, MDA-MB-468 (1.9×10^6 EGFR/cell)[264] and MDA-MB-231 (7.0×10^5 EGFR/cell),[306] as well as to HeLa cells with physiological EGFR expression levels (on the level of 10^4 EGFR/cell)[307] as a negative control. An L-NP-Tag-1-EGF concentration of 100 pM (particle concentration), corresponding to an approximate tag concentration of 0.5 μM, was used in all cell experiments. MDA-MB-468 (ATCC, HTB-132), MDA-MB-231 (ATCC, HTB-26), and HeLa (gift from Sam Thiagalingam, Boston Unviersity) cells were cultured in advanced Dulbecco's Modified Eagle Medium (DMEM) supplemented with 10% (v) fetal bovine serum (FBS), 2 mM L-glutamine, and 50 units/mL penicillin-streptomycin, and grown in

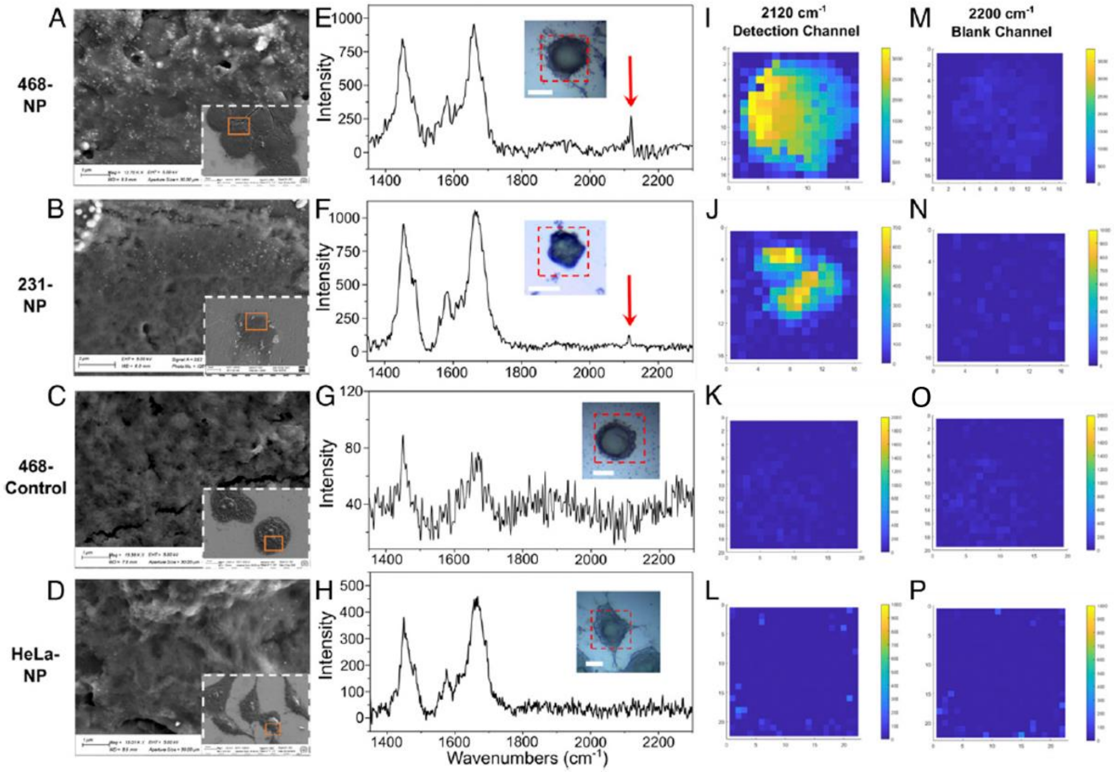

Figure 4.15 Targeted Raman Imaging of Cancer Cells with 468-NP (Top Row), 231-NP (2^nd^ Row), 468-Control (3^rd^ Row) and HeLa-NP (Bottom Row). Reproduced and adapted with permission from Ref. 56. Copyright (2021) by National Academy of Sciences. (A-D) SEM images of cell surfaces after incubation with 100 pM L-NP-Tag-1-EGF for 468-NP (A), 231-NP (B), and HeLa-NP (D), or with 100 pM L-NP-Tag-1 control for 468-Control (C). Insets: Zoomed-out views of the imaged cells, with the zoomed-in area indicated by orange rectangles. (E-H) Raman spectra of single cells. Insets: optical images of the imaged cells in Raman mapping experiments and Raman imaging areas (red dashed squares). Scale bars in insets: 10 µm. (I-P) Raman maps generated from the detection channel at 2120 cm^{-1} (I-L), and from the blank channel at 2200 cm^{-1} (M-P).

a 37 ^{o}C incubator with 5% CO_2 and 95% relative humidity. For SEM and Raman spectroscopy and mapping experiments, the cells were seeded at a density of 1 x 10^5 cells/mL on poly-L-lysine (PLL, Sigma Aldrich)-coated Si substrates, whereas for DF imaging, cells are plated on PLL-coated glass slides at the same concentration. Before the experiments, cells were starved in serum-free media for 24 hours. Experiments were performed when cells reached 80% confluency. L-NP-Tag-1-EGF suspension or controls were diluted to 100 pM with fresh media for incubation with MDA-MB-468, -231, or HeLa cells on substrates at 4 ^{o}C for 2.5 hours. HBSS buffer was used to wash the cells and remove unbound composites after incubations. The cells were fixed with 4% (w/v) pierce formaldehyde (ThermoFisher) for 10 min before used for imaging or spectroscopic measurements. Raman spectra and maps of cells were obtained with the Renishaw InVia Raman Microscope with 50× air objective (Leica, NA = 0.75), 532 nm excitation laser, and a diffraction grating of 2400 I/mm.

MDA-MB-468 and MDA-MB-231 cells incubated with L-NP-Tag-1-EGF, referred to as 468-NP and 231-NP in the following, both show a high concentration of NP binding on the cell surfaces, as indicated in Scanning electron microscope (SEM) images (**Fig. 4.15A, B**). In contrast, MDA-MB-468 cells that were incubated with L-NP-Tag-1 without EGF (468-Control) showed almost no NP binding to the cell surface (**Fig. 4.15C**), indicating that non-specific binding is negligible. HeLa cells incubated with L-NP-Tag-1-EGF (HeLa-NP) showed a much lower NP-binding density on the cell surface (**Fig. 4.15D**) than observed for the 468-NP and 231-NP groups. This is as expected because of the lower binding affinity of L-NP-Tag-1-EGF to physiological EGFR expressors than to overexpressing cells.

The Raman spectra of individual cells of the 468-NP and 231-NP both provide sufficient signal-to-noise for the detection of a single, alkyne-stretching peak at around 2119.3 cm^{-1} (indicated by red arrows in **Fig. 4.15E, F**). According to the stretching frequency, this peak corresponds to the alkyne II-stretching mode of Tag-1, which was assigned to the head-in orientation. The predominance of the alkyne-II peak is consistent with our design that the head-out orientation (alkyne-I) is consumed in the click conjugation of azide-functionalized EGF. In contrast, neither did the spectra of the 468-control (**Fig. 4.15G**) nor of HeLa-NP (**Fig. 4.15H**) contain any observable features in the alkyne-stretching frequency range.

The specificity of the alkyne-II signal of L-NP-Tag-1-EGF for EGFR-overexpressing cells makes it a useful marker for identifying EGFR-overexpressors at the single-cell level through Raman imaging. To obtain Raman images, a combination of 1 μm step width, 10 second accumulation time, and 270.4 μW laser power were used for each mapped pixel. Raman maps were generated on Matlab. A Savitzky-Golay filter was applied to smooth the data. The alkyne-II-stretching mode at around 2120 cm^{-1} of the L-NP-Tag-1-EGF nanocomposite was used as a "detection" channel; whereas a frequency of 2200 cm^{-1}, which is void of any specific Raman features, was used as a "blank" channel. The signal intensity at the studied channels ± 5 cm^{-1} (2115 to 2125 cm^{-1} for detection channel and 2195 to 2205 cm^{-1} for blank channel) were integrated in each pixel to account for any systematic errors in peak stretching frequencies. The mean + SD of the Raman signal intensity in each measured spectrum between 1800 and 1900 cm^{-1} is used as a threshold for that pixel in the generation of the map to preclude the contribution from the noise in the baseline; signals below the threshold are set to 0.

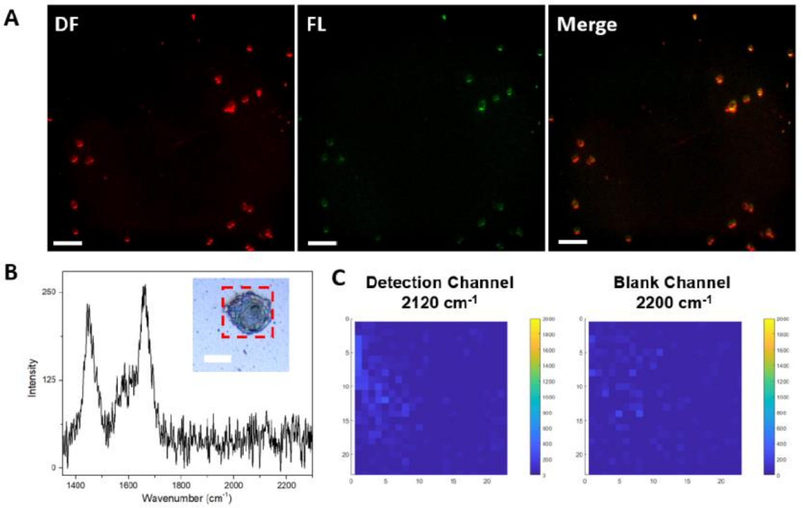

Figure 4.16 Characterization of 468-Liposome Group. Reproduced with permission from Ref. 56. Copyright (2021) by National Academy of Sciences. (A) Correlated DF/FL images of MDA-MB-468 cells after incubation with 100 pM dye-labelled Liposome-Tag-1-EGF. Scale bars = 50 µm. (B) Raman spectra of MDA-MB-468 after incubation with Liposome-Tag-1-EGF. Insets: optical image of the mapped cell in with the mapped area in dashed squares. Scale bar in inset: 10 µm. (C) Raman maps generated from the detection channel at 2120 cm^{-1} (left), and the blank channel at 2200 cm^{-1} (right).

For the 468-NP group, high signal intensities in the detection channel (**Fig. 4.15I**) were observed across the entire mapped cell area (**Fig. 4.15E**, Inset). These favorable results are consistent with a successful labeling of the MDA-MB-468 cell surface by nanocomposite Raman probes. Only very low-signal intensities were observed in the blank channel (**Fig. 4.15M**). For the other EGFR-overexpressing cell line MDA-MB-231, very similar observations were made with the 231-NP group (**Fig. 4.15J, N**), which indicates that the observed imaging effect is effective for EGFR-overexpressing cancer cells in general. However, in the case of both 468-Control and HeLa-NP, no significant signal intensity was detected in either detection or blank channel (**Fig. 4.15K, L, O, and P**). The negligible alkyne-II signal in these cases is also as expected as they are consistent with a low nanocomposite binding for these groups.

Another control group where EGF was clicked to Liposome-Tag-1 was also used as a no-enhancement control that does not possess any plasmonic NP cores. MDA-MB-468 cells incubated with Liposome-Tag-1-EGF (468-liposome) demonstrated a high degree of binding, as indicated in the fluorescence imaging experiments where a fluorescent dye was included in the liposomes (**Fig. 4.16A**). However, the alkyne-stretching signal intensity detected from the cells (**Fig. 4.16B**) was much lower than for 468-NP, which consequently led to almost no imaging contrast for the targeted cancer cell (**Fig. 4.16C**). The significant gain in Raman signal intensity for 468-NP further illustrates the necessity of the electromagnetic enhancement of the alkyne signal through the metal NP in L-NP-Tag-1, which makes these nanocomposites more effective Raman probes.

Our Raman imaging experiments confirm that EGF-conjugated L-NP-Tag-1 facilitate the specific detection of EGFR-overexpressing cancer cell lines, Raman imaging of the target cells at the single-cell level, and their differentiation from cells with physiological expression levels.

4.5 Summary of Chapter 4

Sterol molecules are integral components of both biological and artificial lipid membrane architectures, and their chemical derivatization provides a facile synthetic platform to control the surface properties of lipid-coated metal composite systems on molecular length scales. We have demonstrated in this chapter that the chemical modification of sterols or other terpenoid derivatives into tag molecules with side chains possessing a terminal alkyne group as well as distinct solvent properties can modulate their orientation in hybrid lipid membranes assembled around a metal NP core in the L-NP model, and thus directly affect the surface properties of L-NPs.[56] The specific orientations of the investigated Tag-1 to Tag-3 probes were shown to depend on the structure and interaction with the hydrogen bonding network at the lipid-water interface. Tag-1 contains a side chain with a low number of hydrogen bond donors and acceptors that perturb the HBN. Under physiological conditions, Tag-1 shows a coexistence of head-in and head-out orientations in the hybrid membrane architecture of L-NPs. Above the transition temperature of (63.7 °C), Tag-1 molecules with head-out orientation can overcome the energetic barrier associated with the reorientation in the membrane and convert into the head-in mode, which sustains less perturbation of the lipid-water HBN. For Tags-2 and -3, a larger number of polar charge centers than in Tag-1 are included in the modified side chain, and thus interfacial hydrogen bonding is favored. Consequently, unlike Tag-1, Tag-2 and Tag-3 show a strong preference for the head-out orientation at both RT and elevated temperatures.

The coexistence of head-out and head-in orientations in L-NP-Tag-1 at RT provides the dual functionalities of (a) the chemical conjugation of a molecular, cell-binding ligand *via* the solvent-accessible terminal alkyne groups in the head-out orientation through click chemistry, and (b) plasmon-enhanced Raman imaging contrast through “protected” alkyne groups in the head-in orientation. This functional duality was utilized in this chapter to generate specific molecular Raman labels that produce bio-orthogonal signals for the targeted Raman imaging of EGFR-overexpressing breast cancer cell lines. MDA-MB-468 and MDA-MB-231 were used in the imaging experiments, and the L-NP-based Raman probes were also able to distinct them from cancer cells with physiological EGFR expression levels. L-NP-Tag-1 represents a promising diagnostic probe that enhances the sensitivity of cancer Raman imaging and enables cancer detection and identification at the single-cell level.

Chapter 5. Summary and Outlook

5.1 Summary

In summary, in this dissertation, we outline the fundamental photophysical responses of nanoplasmonics including the E-field localization and plasmonic hot charge carrier production, and illustrate how they could be modulated and applied in plasmonic photocatalysis, as plasmonic nano-antimicrobials, and for SERS imaging of cancer cells. Lipid-coated noble metal nanoparticles (L-NPs) consisting of silver or gold NP cores and hybrid lipid membranes that comprises an alkylthiol inner layer and a lipid monolayer were exploited as a major materials platform to implement the structural modulation, to probe the structure-function relationship of the hybrid composite material, and to carry out the proposed applications. The hybrid lipid membrane can serve multiple roles, including as a platform for integration of molecular or nanoscale cargo materials, such as photocatalysts, drugs or tag molecules; as a spacer for precise localization of the molecules at certain distances to the surface of the metal cores; and as a scaffold that grants the nanocomposites with favorable structural and photoelectrochemical stability.

We demonstrate plasmonic photocatalysis through both a E-field enhanced mechanism,[29] and a plasmonic hot charge carrier-mediated pathway.[78] For the former case, lipid-coated Ag NPs present an effective nanoantenna, and the E-field localized by them is able to sustain strong resonant enhancement of the excitation and intramolecular transition of a molecular photocatalyst $[Ru(bpy)_3]^{2+}$ that is pinned by the hybrid membrane layer in a plasmonic “sweet spot” around 3 nm away from the Ag surface. This distance is associated with both intense E-field intensity for resonant enhancement and limited quenching of the photoexcited states through metal-induced non-radiative decay pathways. These factors enable a significant augmentation of the photocatalytic performance of the hybrid lipid-Ag NP-$[Ru(bpy)_3]^{2+}$ nanopigment for the urea oxidation reaction and implementation of a visible light-driven direct urea fuel cell.[29] These applications are meaningful for both urea-containing wastewater treatment and light energy conversion. For the latter pathway of plasmonic photocatalysis, we demonstrate that through construction of a hybrid plasmonic heterostructure containing multiple plasmonic building blocks, Au nanorods and chalcopyrite nanocrystals, a wavelength-dependent excitation of both resonance mode could be achieved that produces different types of charge carriers on the surface of the nanocomposite. This diversified charge carrier production provides distinct opportunities to catalyze both an oxidation and a reduction reaction on the same structural building block, and is utilized for the catalysis of both half reactions in the water splitting reaction with visible light.

Nanoplasmonics also enables effective nano-antimicrobials. We discovered that through modulation of the unsaturated lipid components and photosensitizer molecule concentration in the hybrid lipid-Ag-$[Ru(bpy)_3]^{2+}$ nanocomposite, a light-controlled permeation of the membrane layer and photocatalytic cationic release of Ag^+ and $[Ru(bpy)_3]^{2+}$ could be initiated by the production of reactive oxygen species. This light-controlled release pathway provides desirable spatial and temporal controllability over the antimicrobial effect, and led to a superb inactivation log reduction value > 7 for Gram-negative bacteria species, and ~4 for Gram-positive species in aqueous suspensions *in* *vitro*. The lipid-Ag-$[Ru(bpy)_3]^{2+}$ nano-antimicrobial was also shown to be effective towards colonized bacterial biofilms that are more resilient against conventional bactericidal agents than bacterial suspensions in medium. This is relevant for sterilization of materials surfaces and prevention of bacterial infection.[52] The hybrid plasmonic nano-antimicrobials we designed is also efficient as a multifunctional antibacterial coating for plastic surfaces that combines active and passive bactericidal performances. Applied to plastic tubings, the lipid-Ag-$[Ru(bpy)_3]^{2+}$ composite enables flow sterilizers for efficient and robust bacteria flow-sterilization. The nanocomposites coating effectively prevents the colonization of bacteria on plastic surface with ambient light. Importantly, the nanocomposite antimicrobials exhibit degrees of selectivity of their detrimental effect against bacterial cells compared to mammal cells; and their effect do not evidently impact the functionality of biologics, including monoclonal antibodies. These factors indicate great promises for potential *in vivo* applications as well as for the specific application of sterilization of biologics that are sensitive to conventional antibacterial strategies.[53]

The strong resonant E-field generated by the plasmonic NP core in the L-NP model also provide unique opportunities for plasmon-enhanced spectroscopy and microscopy, and for characterization of the physicochemical properties of the membrane layer through surface-enhanced Raman spectroscopy. We demonstrate that through designs of three sterol-based tag molecules derivatized through addition of side chains possessing a terminal alkyne group and different solvent properties, integration of these molecules into the hybrid lipid membrane and their interaction with the hydrogen bonding network at the lipid-water interface could be effectively modulated, which consequently could affect the orientation of the tag molecules in the membrane layer as well as the specific surface properties and functionalities of the L-NP. We discovered that when incorporated in the hybrid membrane, Tag-1, cholesteryl hexynoate, takes on both a head-in and a head-out orientation at room temperature, while a reorientation takes place at higher temperature than 63.7 ^{o}C and only head-in still exists due to the repulsion of the modified side chain by the hydrogen bonding network. The orientational dimorphism of L-NP-Tag-1 at RT was utilized to give the dual functionality of chemical conjugation and Raman imaging contrast for the single-cell, targeted imaging of EGFR-overexpressing cancer cells as well as for their distinction from cancer cell lines with physiological EGFR expressing levels.[56]

5.2 Outlook

Nanoplasmonics and the L-NP model present versatile platforms to integrate various functionalities and a synergistic combination of them to be customized towards different applications. For both plasmonic photocatalysis pathways introduced in this dissertation, the structural building blocks are not limited to the Ag NPs/$[Ru(bpy)_3]^{2+}$ or the Au NRs/chalcopyrite NCs pairs as used in the specific projects in this dissertation. For the E-field enhancement mechanism, different structural components could be exploited in future works that satisfy the spectral overlap requirement for resonant energy transfer and gain in absorption. Gold nanostructures and dye molecules with absorption bands that overlap with the LSPR of Au, for instance, could be exploited to achieve photoexcitation with even longer wavelengths and thus lower energy than the Ag/$[Ru(bpy)_3]^{2+}$ pair. This could potentially allow the harvesting of a broader range of the visible region in the electromagnetic spectrum. For the charge carrier-induced wavelength-controlled catalysis, different plasmonic components that can lead to hot electron or hot hole production could also be explored, although the efficacy of the charge transfer and catalysis would also be dependent on the energy barrier at the interfaces between the individual components. In addition, as nanoplasmonics entails broad-band catalytic properties that can cover a wide range of redox potentials, a number of chemical reactions could potentially be facilitated, which includes organic synthetic reactions,[2] fuel cell half reactions,[1] reactions for environment remediation[191, 253] etc. It is foreseeable that a library for catalyst and facilitated reactions could be constructed to further augment the efficiency of both the catalyzed reaction processes and industrial as well as commercial manufacturing processes. Future efforts in plasmonic photocatalysis could focus on further enhancement of the energy transfer efficacy by a more precise positioning of the photocatalyst molecule in the enhancement "sweet spot" within sub-nanometer precision through one-pot synthesis approaches. Besides, novel photocatalysts that contain conventional transitional metal components could be utilized to further reduce the cost of the hybrid catalysts.

Plasmonic nano-antimicrobials have presented great advantages compared to conventional antibacterial approaches including UV or X-ray treatment, autoclaving, bleaching etc (**Table 5.1**). In the case of our Ag/$[Ru(bpy)_3]^{2+}$-based nano-antimicrobials and coatings, very low metal concentrations, low-power illumination in the visible range, and no complicated infrastructures are adequate to induce significant and reliable antimicrobial performances. Despite the numerous advantages of our system and of plasmonic nano-antimicrobials in general, several important challenges still exist.[109] Firstly, the light-induced plasmonic nano-antimicrobial inactivation mechanisms requires efficient illumination of the NPs, which can make it difficult for prospective *in vivo* applications in mammals, if the sites of infections are not readily accessible. Although in our studies it has been shown that ambient illumination is adequate to induce significant antimicrobial effect, yet it still requires intricate designs to achieve minimalized invasion in *in vivo* applications in order to deliver the illumination to deeper tissues. One important potential solution is through the use of NIR-responsive materials, such as nanorods or bipyramids,[40-41] due to the larger tissue penetration depths at these wavelengths.[99] Up-conversion strategies through resonant energy transfers between NIR-responsive light donors and UV- or visible-responsive materials have also been shown to allow for photoexcitation with higher wavelengths.[308]

Table 5.1 Comparison of Plasmonic Nano-Antimicrobials with Other Antimicrobial Strategies. Reproduced with permission from Ref. 109, Copyright (2021) by The Royal Society of Chemistry.

	Conventional Sterilization Techniques	**Plasmonic Nano-Antimicrobials**	**Other Nanoscale Antimicrobials**	**Molecular Antimicrobial Drugs or Peptides**	**Macroscale Antimicrobial Materials or Coatings**
Broad-band antimicrobial efficacy	√	√	√	√	√
Visible light responsivity		√√	√		
Resilience against microbial resistance development	√	√	√		√
Large-scale and repeatable i*n vitro* inactivation effect	√	√	√	√	√

Specificity in *in vivo* disinfection applications				√	
Sensing and theranostic capability		√√	√		√
Low cost and low energy and environmental hazards				√	√

Another important challenge for plasmonic nano-antimicrobials is the generation of undesired collateral cytotoxicity by plasmonic NPs, photosensitizers and/or photocatalysts. Although it has been shown in section **3.2.3** that the released concentrations are limited to well below the IC_{50} values of Ag and Ru species, yet there could still be some detrimental effect against mammal cells in potential sterilization applications. One strategy to minimize the collateral damage is to further increase the plasmonic enhancement as well as the efficacy of the inactivation mechanisms so that the required dosage of microbicidal components can be further reduced. In addition, localizing the antimicrobial effect by selective pathogen targeting, or passivating the plasmonic nanostructures by encapsulation in liposomes or polymersome could also contribute to limiting the collateral damage of plasmonic nano-antimicrobials.[52, 54, 309]

Finally, the development of resistance against metal cation-based inactivation strategies is a concern for some types of plasmonic nano-antimicrobials. Several studies have reported altered gene expression levels or other cellular changes indicative of emerging resistances against metal cations.[310-311] These resistances can, however, be overcome by “multimodal” inactivation strategies that provide a more resilient microbicidal effect as they can affect multiple structural or metabolistic aspects of the pathogens simultaneously.

To harness the full potential of plasmonic nano-antimicrobials, future work should focus on further improving the efficacy of a broad range of diverse microbial pathogens in biological medium, reducing the time required for complete inactivation, and limiting the collateral damage by active targeting of the microbial pathogens or enhancing the selectivity of the antimicrobial effects.

The large optical cross-sections, E-field enhancement, and increased local density of electromagnetic states (LDOS) derived from the plasmon resonance effect can not only enable these diverse antimicrobial properties, but are also shown to facilitate unique biosensing and imaging modalities, such as through plasmon-enhanced fluorescence imaging, SERS spectroscopy and imaging, LSPR sensing, or plasmon coupling microscopy. Thus, the potential of plasmonic nano-antimicrobials as theranostic tools that enable simultaneous pathogen inactivation and monitoring of the inactivation process through plasmon-enhanced microscopic or spectroscopic approaches could also be explored and exploited.[109]

In our work for SERS characterization of tag orientation in hybrid lipid membrane and application for targeted cancer imaging, although our characterization experiments and Raman imaging application mostly utilized nanocomposites with a 40 nm Ag NP core, our results indicate that the coexistence of head-out and head-in orientations of Tag-1, and thus the functional duality is characteristic of a broad range of lipid-coated nanostructures with different core sizes, shapes, and compositions, including metal or polymer cores (see **Fig. 4.8**). In addition, both the hybrid lipid membrane and the click conjugation reactivity by the head-out alkynes provide means for the integration of distinct surface biomarkers other than the EGF-EGFR interaction utilized in our work. This could allow targeting, characterization, and imaging of different categories of cells that sustain expression of that specific biomarker on the cell surface. Modified sterols and terpenoids could, thus, provide a general strategy to modulate the surface chemical properties of lipid-coated NPs, to understand the structure-function relationship of various types of L-NPs, and to probe particle-cell interaction modes of various types of cells.

The ability to control molecular orientation on the surface of L-NPs also has general relevance beyond the specific application as Raman tag. For instance, the modulation of sterol orientation in L-NPs is meaningful for many sensing, diagnostic, and therapeutic strategies. In addition, it could also enable applications such as smart sampling and plasmonic nanoreactors. It is conceivable that through the integration of multiple sterols that undergo orientational changes in response to defined external cues (e.g., temperature and irradiation) into L-NP platforms, the surface properties and, thus, the ability to interact with their environment can actively evolve to carry out different tasks as a function of location and time. It is conceivable that the lipid layer in L-NPs is more than a biomimetic surface coating, as it provides a matrix for active surface control whose abilities remain to be fully explored in the future.

APPENDIX

The data presented in this dissertation can be found on the Boston University Research Drive for the Reinhard research group (U:/eng_research_reinhard) in the folder named "AN, Xingda". Additional inquiries or request for data can also be sent to me *via* email to: xingda@bu.edu; or xda0907@126.com.

As a brief introduction to the folder on the Research Drive, the "AN, Xingda" folder contains 6 subfolders. "Data" contains raw and processed data in different projects categorized by the specific instrumentation or research approach, and further by research projects; "Dissertation related" contains draft, figures and other related files for dissertation and defense; "Files" contains miscellaneous academic files including protocols, course slides, purchase orders and etc.; "Literature" contains relevant literatures organized by project or by year; "Manuscripts" contains the draft, figures, processed data and other related files for my publications; "Research update slides" contains update and summary slides in group meetings or individual meetings with Prof. Reinhard.

REFERENCE

1. Zhang, Y.; He, S.; Guo, W.; Hu, Y.; Huang, J.; Mulcahy, J. R.; Wei, W. D., Surface-plasmon-driven hot electron photochemistry. *Chemical reviews* **2017,** *118* (6), 2927-2954.

2. Wang, C.; Astruc, D., Nanogold plasmonic photocatalysis for organic synthesis and clean energy conversion. *Chemical Society Reviews* **2014,** *43* (20), 7188-7216.

3. Shi, J.; Wang, Y.; Yang, W.; Tang, Y.; Xie, Z., Recent advances of pore system construction in zeolite-catalyzed chemical industry processes. *Chemical Society Reviews* **2015,** *44* (24), 8877-8903.

4. Jiao, X.; Zheng, K.; Liang, L.; Li, X.; Sun, Y.; Xie, Y., Fundamentals and challenges of ultrathin 2D photocatalysts in boosting CO 2 photoreduction. *Chemical Society Reviews* **2020,** *49* (18), 6592-6604.

5. Liu, J.; Qiao, S. Z.; Budi Hartono, S.; Lu, G. Q., Monodisperse yolk–shell nanoparticles with a hierarchical porous structure for delivery vehicles and nanoreactors. *Angewandte Chemie International Edition* **2010,** *49* (29), 4981-4985.

6. Kim, K. T.; Meeuwissen, S. A.; Nolte, R. J.; van Hest, J. C., Smart nanocontainers and nanoreactors. *Nanoscale* **2010,** *2* (6), 844-858.

7. Elani, Y.; Trantidou, T.; Wylie, D.; Dekker, L.; Polizzi, K.; Law, R. V.; Ces, O., Constructing vesicle-based artificial cells with embedded living cells as organelle-like modules. *Scientific reports* **2018,** *8* (1), 1-8.

8. Mura, S.; Nicolas, J.; Couvreur, P., Stimuli-responsive nanocarriers for drug delivery. *Nature materials* **2013,** *12* (11), 991-1003.

9. Ma, Y.; Nolte, R. J.; Cornelissen, J. J., Virus-based nanocarriers for drug delivery. *Advanced drug delivery reviews* **2012,** *64* (9), 811-825.

10. Sun, Y.; Gao, S.; Xie, Y., Atomically-thick two-dimensional crystals: electronic structure regulation and energy device construction. *Chemical Society Reviews* **2014,** *43* (2), 530-546.

11. Peng, X.; Peng, L.; Wu, C.; Xie, Y., Two dimensional nanomaterials for flexible supercapacitors. *Chemical Society Reviews* **2014,** *43* (10), 3303-3323.

12. Gupta, A.; Mumtaz, S.; Li, C.-H.; Hussain, I.; Rotello, V. M., Combatting antibiotic-resistant bacteria using nanomaterials. *Chemical Society Reviews* **2019,** *48* (2), 415-427.

13. Jaque, D.; Maestro, L. M.; del Rosal, B.; Haro-Gonzalez, P.; Benayas, A.; Plaza, J.; Rodríguez, E. M.; Solé, J. G., Nanoparticles for photothermal therapies. *nanoscale* **2014,** *6* (16), 9494-9530.

14. Yang, B.; Chen, Y.; Shi, J., Reactive oxygen species (ROS)-based nanomedicine. *Chemical reviews* **2019,** *119* (8), 4881-4985.

15. Li, Z.; Zhang, L.; Liu, Y.; Shao, C.; Gao, Y.; Fan, F.; Wang, J.; Li, J.; Yan, J.; Li, R., Surface - Polarity - Induced Spatial Charge Separation Boosts Photocatalytic Overall Water Splitting on GaN Nanorod Arrays. *Angewandte Chemie* **2020,** *132* (2), 945-952.

16. Guo, Y.; Xu, K.; Wu, C.; Zhao, J.; Xie, Y., Surface chemical-modification for engineering the intrinsic physical properties of inorganic two-dimensional nanomaterials. *Chemical Society Reviews* **2015,** *44* (3), 637-646.

17. Yu, X.; Xu, F.; Ramirez, N.-G. P.; Kijewski, S. D.; Akiyama, H.; Gummuluru, S.; Reinhard, B. M., Dressing up nanoparticles: A membrane wrap to induce formation of the virological synapse. *ACS nano* **2015,** *9* (4), 4182-4192.

18. Khanehzar, A.; Fraire, J. C.; Xi, M.; Feizpour, A.; Xu, F.; Wu, L.; Coronado, E. A.; Reinhard, B. M., Nanoparticle–cell interactions induced apoptosis: a case study with nanoconjugated epidermal growth factor. *Nanoscale* **2018,** *10* (14), 6712-6723.

19. Zhu, X.; Guo, Y.; Cheng, H.; Dai, J.; An, X.; Zhao, J.; Tian, K.; Wei, S.; Cheng Zeng, X.; Wu, C., Signature of coexistence of superconductivity and ferromagnetism in two-dimensional NbSe2 triggered by surface molecular adsorption. *Nature communications* **2016,** *7* (1), 1-8.

20. Eshaghi, B.; Alsharif, N.; An, X.; Akiyama, H.; Brown, K. A.; Gummuluru, S.; Reinhard, B. M., Stiffness of HIV ‐ 1 Mimicking Polymer Nanoparticles Modulates Ganglioside ‐ Mediated Cellular Uptake and Trafficking. *Advanced Science* **2020,** *7* (18), 2000649.

21. Alsharif, N.; Eshaghi, B.; Reinhard, B. M.; Brown, K. A., Physiologically Relevant Mechanics of Biodegradable Polyester Nanoparticles. *Nano letters* **2020,** *20* (10), 7536-7542.

22. Hong, Y.; Reinhard, B. M., Optoplasmonics: basic principles and applications. *Journal of Optics* **2019,** *21* (11), 113001.

23. Zhao, X.; Reinhard, B. M., Switchable chiroptical hot-spots in silicon nanodisk dimers. *ACS Photonics* **2019,** *6* (8), 1981-1989.

24. Link, S.; El-Sayed, M. A., Spectral properties and relaxation dynamics of surface plasmon electronic oscillations in gold and silver nanodots and nanorods. ACS Publications: 1999; Vol. 103, pp 8410-8426.

25. Link, S.; El-Sayed, M. A., Shape and size dependence of radiative, non-radiative and photothermal properties of gold nanocrystals. *International reviews in physical chemistry* **2000,** *19* (3), 409-453.

26. Nordlander, P. J.; Prodan, E. In *Optical properties of metallic nanoshells*, Properties of Metal Nanostructures, SPIE: 2002; pp 91-98.

27. Murphy, C. J.; Sau, T. K.; Gole, A.; Orendorff, C. J., Surfactant-directed synthesis and optical properties of one-dimensional plasmonic metallic nanostructures. *MRS bulletin* **2005,** *30* (5), 349-355.

28. Maier, S. A., *Plasmonics: fundamentals and applications*. Springer: 2007; Vol. 1.

29. An, X.; Stelter, D.; Keyes, T.; Reinhard, B. M., Plasmonic photocatalysis of urea oxidation and visible-light fuel cells. *Chem* **2019,** *5* (8), 2228-2242.

30. Susman, M. D.; Feldman, Y.; Vaskevich, A.; Rubinstein, I., Chemical deposition and stabilization of plasmonic copper nanoparticle films on transparent substrates. *Chemistry of Materials* **2012,** *24* (13), 2501-2508.

31. Agrawal, A.; Cho, S. H.; Zandi, O.; Ghosh, S.; Johns, R. W.; Milliron, D. J., Localized surface plasmon resonance in semiconductor nanocrystals. *Chemical reviews* **2018,** *118* (6), 3121-3207.

32. Luther, J. M.; Jain, P. K.; Ewers, T.; Alivisatos, A. P., Localized surface plasmon resonances arising from free carriers in doped quantum dots. *Nature materials* **2011,** *10* (5), 361-366.

33. Xi, M.; Reinhard, B. M., Localized surface plasmon coupling between mid-IR-resonant ITO nanocrystals. *The Journal of Physical Chemistry C* **2018,** *122* (10), 5698-5704.

34. Baffou, G.; Quidant, R.; García de Abajo, F. J., Nanoscale control of optical heating in complex plasmonic systems. *ACS nano* **2010,** *4* (2), 709-716.

35. Ingram, D. B.; Linic, S., Water splitting on composite plasmonic-metal/semiconductor photoelectrodes: evidence for selective plasmon-induced formation of charge carriers near the semiconductor surface. *Journal of the American Chemical Society* **2011,** *133* (14), 5202-5205.

36. Linic, S.; Chavez, S.; Elias, R., Flow and extraction of energy and charge carriers in hybrid plasmonic nanostructures. *Nature Materials* **2021,** *20* (7), 916-924.

37. Kale, M. J.; Avanesian, T.; Christopher, P., Direct photocatalysis by plasmonic nanostructures. *Acs Catalysis* **2014,** *4* (1), 116-128.

38. Chen, X.; Chen, Y.; Yan, M.; Qiu, M., Nanosecond photothermal effects in plasmonic nanostructures. *ACS nano* **2012,** *6* (3), 2550-2557.

39. Boulais, E.; Lachaine, R.; Hatef, A.; Meunier, M., Plasmonics for pulsed-laser cell nanosurgery: Fundamentals and applications. *Journal of Photochemistry and Photobiology C: Photochemistry Reviews* **2013,** *17*, 26-49.

40. Nazari, M.; Xi, M.; Lerch, S.; Alizadeh, M.; Ettinger, C.; Akiyama, H.; Gillespie, C.; Gummuluru, S.; Erramilli, S.; Reinhard, B. M., Plasmonic enhancement of selective photonic virus inactivation. *Scientific reports* **2017,** *7* (1), 1-10.

41. Nazari, M.; Xi, M.; Aronson, M.; Mcrae, O.; Hong, M. K.; Gummuluru, S.; Sgro, A. E.; Bird, J. C.; Ziegler, L. D.; Gillespie, C., Plasmon-Enhanced Pan-Microbial Pathogen Inactivation in the Cavitation Regime: Selectivity Without Targeting. *ACS Applied Nano Materials* **2019,** *2* (4), 2548-2558.

42. Boulais, É.; Lachaine, R.; Meunier, M., Plasma mediated off-resonance plasmonic enhanced ultrafast laser-induced nanocavitation. *Nano letters* **2012,** *12* (9), 4763-4769.

43. Li, X.; Wang, Y.; Zaytsev, M. E.; Lajoinie, G.; Le The, H.; Bomer, J. G.; Eijkel, J. C.; Zandvliet, H. J.; Zhang, X.; Lohse, D., Plasmonic bubble nucleation and growth in water: Effect of dissolved air. *The Journal of Physical Chemistry C* **2019,** *123* (38), 23586-23593.

44. Freestone, I.; Meeks, N.; Sax, M.; Higgitt, C., The Lycurgus cup—a roman nanotechnology. *Gold bulletin* **2007,** *40* (4), 270-277.

45. Morones-Ramirez, J. R.; Winkler, J. A.; Spina, C. S.; Collins, J. J., Silver enhances antibiotic activity against gram-negative bacteria. *Science translational medicine* **2013,** *5* (190), 190ra81-190ra81.

46. Mori, K.; Kawashima, M.; Che, M.; Yamashita, H., Enhancement of the Photoinduced Oxidation Activity of a Ruthenium (II) Complex Anchored on Silica ‐

Coated Silver Nanoparticles by Localized Surface Plasmon Resonance. *Angewandte Chemie* **2010,** *122* (46), 8780-8783.

47. Dishing, S. K.; Li, J.; Meng, F.; Senty, T. R.; Suri, S.; Zhi, M.; Li, M.; Bristow, A. D.; Wu, N., Photocatalytic activity enhanced by plasmonic resonant energy transfer from metal to semiconductor. *Journal of the American Chemical Society* **2012,** *134* (36), 15033-15041.

48. Li, J.; Cushing, S. K.; Zheng, P.; Meng, F.; Chu, D.; Wu, N., Plasmon-induced photonic and energy-transfer enhancement of solar water splitting by a hematite nanorod array. *Nature communications* **2013,** *4* (1), 1-8.

49. Li, J.; Cushing, S. K.; Meng, F.; Senty, T. R.; Bristow, A. D.; Wu, N., Plasmon-induced resonance energy transfer for solar energy conversion. *Nature Photonics* **2015,** *9* (9), 601-607.

50. Planas, O.; Macia, N.; Agut, M.; Nonell, S.; Heyne, B., Distance-dependent plasmon-enhanced singlet oxygen production and emission for bacterial inactivation. *Journal of the American Chemical Society* **2016,** *138* (8), 2762-2768.

51. Macia, N.; Bresoli-Obach, R.; Nonell, S.; Heyne, B., Hybrid silver nanocubes for improved plasmon-enhanced singlet oxygen production and inactivation of bacteria. *Journal of the American Chemical Society* **2018,** *141* (1), 684-692.

52. An, X.; Naowarojna, N.; Liu, P.; Reinhard, B. M., Hybrid plasmonic photoreactors as visible light-mediated bactericides. *ACS Applied Materials & Interfaces* **2019,** *12* (1), 106-116.

53. An, X.; Cheng, R.; Liu, P.; Reinhard, B. M., Plasmonic photoreactors-coated plastic tubing as combined-active-and-passive antimicrobial flow sterilizer. *Journal of Materials Chemistry B* **2022,** 10(12), 2001-2010.

54. Geilich, B. M.; van de Ven, A. L.; Singleton, G. L.; Sepúlveda, L. J.; Sridhar, S.; Webster, T. J., Silver nanoparticle-embedded polymersome nanocarriers for the treatment of antibiotic-resistant infections. *Nanoscale* **2015,** *7* (8), 3511-3519.

55. Pornpattananangkul, D.; Zhang, L.; Olson, S.; Aryal, S.; Obonyo, M.; Vecchio, K.; Huang, C.-M.; Zhang, L., Bacterial toxin-triggered drug release from gold nanoparticle-stabilized liposomes for the treatment of bacterial infection. *Journal of the American Chemical Society* **2011,** *133* (11), 4132-4139.

56. An, X.; Majumder, A.; McNeely, J.; Yang, J.; Puri, T.; He, Z.; Liang, T.; Snyder, J. K.; Straub, J. E.; Reinhard, B. M., Interfacial hydration determines orientational and functional dimorphism of sterol-derived Raman tags in lipid-coated nanoparticles. *Proceedings of the National Academy of Sciences* **2021,** *118* (33), e2105913118.

57. Mayer, K. M.; Hafner, J. H., Localized surface plasmon resonance sensors. *Chemical reviews* **2011,** *111* (6), 3828-3857.

58. Zhang, S.; Reinhard, B. M., Characterizing large-scale receptor clustering on the single cell level: a comparative plasmon coupling and fluorescence superresolution microscopy study. *The Journal of Physical Chemistry B* **2019,** *123* (26), 5494-5505.

59. Zhang, Q.; Reinhard, B. M., Ligand density and nanoparticle clustering cooperate in the multivalent amplification of epidermal growth factor receptor activation. *ACS nano* **2018,** *12* (10), 10473-10485.

60. Wu, L.; Xu, F.; Reinhard, B. M., Nanoconjugation prolongs endosomal signaling of the epidermal growth factor receptor and enhances apoptosis. *Nanoscale* **2016,** *8* (28), 13755-13768.

61. Yu, X.; Feizpour, A.; Ramirez, N.-G. P.; Wu, L.; Akiyama, H.; Xu, F.; Gummuluru, S.; Reinhard, B. M., Glycosphingolipid-functionalized nanoparticles recapitulate CD169-dependent HIV-1 uptake and trafficking in dendritic cells. *Nature communications* **2014,** *5* (1), 1-12.

62. Xu, F.; Reiser, M.; Yu, X.; Gummuluru, S.; Wetzler, L.; Reinhard, B. M., Lipid-mediated targeting with membrane-wrapped nanoparticles in the presence of corona formation. *ACS nano* **2016,** *10* (1), 1189-1200.

63. Li, J.; Cushing, S. K.; Zheng, P.; Senty, T.; Meng, F.; Bristow, A. D.; Manivannan, A.; Wu, N., Solar hydrogen generation by a CdS-Au-TiO2 sandwich nanorod array enhanced with Au nanoparticle as electron relay and plasmonic photosensitizer. *Journal of the American Chemical Society* **2014,** *136* (23), 8438-8449.

64. Bian, Z.; Tachikawa, T.; Zhang, P.; Fujitsuka, M.; Majima, T., Au/TiO2 superstructure-based plasmonic photocatalysts exhibiting efficient charge separation and unprecedented activity. *Journal of the American Chemical Society* **2014,** *136* (1), 458-465.

65. Priebe, J. B.; Karnahl, M.; Junge, H.; Beller, M.; Hollmann, D.; Brückner, A., Water reduction with visible light: synergy between optical transitions and electron transfer in Au ‐ TiO2 catalysts visualized by in situ EPR spectroscopy. *Angewandte Chemie International Edition* **2013,** *52* (43), 11420-11424.

66. Müller, P.; Brettel, K., [Ru (bpy) 3] 2+ as a reference in transient absorption spectroscopy: differential absorption coefficients for formation of the long-lived 3 MLCT excited state. *Photochemical & Photobiological Sciences* **2012,** *11* (4), 632-636.

67. Cushing, S. K.; Li, J.; Meng, F.; Senty, T. R.; Suri, S.; Zhi, M.; Li, M.; Bristow, A. D.; Wu, N., Photocatalytic activity enhanced by plasmonic resonant energy transfer from metal to semiconductor. *Journal of the American Chemical Society* **2012,** *134* (36), 15033-15041.

68. Kern, A. M.; Meixner, A. J.; Martin, O. J., Molecule-dependent plasmonic enhancement of fluorescence and Raman scattering near realistic nanostructures. *ACS nano* **2012,** *6* (11), 9828-9836.

69. Camden, J. P.; Dieringer, J. A.; Zhao, J.; Van Duyne, R. P., Controlled plasmonic nanostructures for surface-enhanced spectroscopy and sensing. *Accounts of chemical research* **2008,** *41* (12), 1653-1661.

70. Zhao, X.; Alizadeh, M.; Reinhard, B. M., Harnessing leaky modes for fluorescence enhancement in gold-tipped silicon nanowires. *The Journal of Physical Chemistry C* **2016,** *120* (37), 20555-20562.

71. Wang, H.; Rong, G.; Yan, B.; Yang, L.; Reinhard, B. M., Optical sizing of immunolabel clusters through multispectral plasmon coupling microscopy. *Nano letters* **2011,** *11* (2), 498-504.

72. Zhang, Q.; Reinhard, B. M., Characterizing nanoplastics - induced stress and its SERS fingerprint in an intestinal membrane model. *Nano Select* **2021,** *2* (9), 1707-1722.

73. Zhang, R.; Hong, Y.; Reinhard, B. M.; Liu, P.; Wang, R.; Dal Negro, L., Plasmonic nanotrough networks for scalable bacterial Raman biosensing. *ACS applied materials & interfaces* **2018,** *10* (33), 27928-27935.

74. Yang, L.; Yan, B.; Premasiri, W. R.; Ziegler, L. D.; Negro, L. D.; Reinhard, B. M., Engineering nanoparticle cluster arrays for bacterial biosensing: the role of the building block in multiscale SERS substrates. *Advanced Functional Materials* **2010,** *20* (16), 2619-2628.

75. Yan, B.; Thubagere, A.; Premasiri, W. R.; Ziegler, L. D.; Dal Negro, L.; Reinhard, B. M., Engineered SERS substrates with multiscale signal enhancement: nanoparticle cluster arrays. *ACS Nano* **2009,** *3* (5), 1190-1202.

76. Cormode, D. P.; Skajaa, T.; van Schooneveld, M. M.; Koole, R.; Jarzyna, P.; Lobatto, M. E.; Calcagno, C.; Barazza, A.; Gordon, R. E.; Zanzonico, P., Nanocrystal core high-density lipoproteins: a multimodality contrast agent platform. *Nano letters* **2008,** *8* (11), 3715-3723.

77. Allijn, I. E.; Leong, W.; Tang, J.; Gianella, A.; Mieszawska, A. J.; Fay, F.; Ma, G.; Russell, S.; Callo, C. B.; Gordon, R. E., Gold nanocrystal labeling allows low-density lipoprotein imaging from the subcellular to macroscopic level. *ACS nano* **2013,** *7* (11), 9761-9770.

78. An, X.; Kays, J. C.; Lightcap, I. V.; Ouyang, T.; Dennis, A. M.; Reinhard, B. M., Wavelength-Dependent Bifunctional Plasmonic Photocatalysis in Au/Chalcopyrite Hybrid Nanostructures. *ACS nano* **2022,** *16* (4), 6813-6824.

79. Van Turnhout, L.; Hattori, Y.; Meng, J.; Zheng, K.; Sá, J., Direct Observation of a Plasmon-Induced Hot Electron Flow in a Multimetallic Nanostructure. *Nano letters* **2020,** *20* (11), 8220-8228.

80. Graf, M.; Vonbun-Feldbauer, G. B.; Koper, M. T., Direct and broadband plasmonic charge transfer to enhance water oxidation on a gold electrode. *ACS nano* **2021,** *15* (2), 3188-3200.

81. Hou, Y.; Li, X.; Zhao, Q.; Chen, G.; Raston, C. L., Role of hydroxyl radicals and mechanism of Escherichia coli inactivation on Ag/AgBr/TiO2 nanotube array electrode under visible light irradiation. *Environmental science & technology* **2012,** *46* (7), 4042-4050.

82. Liga, M. V.; Bryant, E. L.; Colvin, V. L.; Li, Q., Virus inactivation by silver doped titanium dioxide nanoparticles for drinking water treatment. *Water research* **2011,** *45* (2), 535-544.

83. Adhikari, S.; Banerjee, A.; Eswar, N. K.; Sarkar, D.; Madras, G., Photocatalytic inactivation of E. Coli by ZnO–Ag nanoparticles under solar radiation. *RSC Advances* **2015,** *5* (63), 51067-51077.

84. Anger, P.; Bharadwaj, P.; Novotny, L. In *Enhancement and Quenching of Single Molecule Fluorescence near a Gold Nanoparticle*, Laser Science, Optical Society of America: 2005; p LTuC3.

85. Anger, P.; Bharadwaj, P.; Novotny, L., Enhancement and quenching of single-molecule fluorescence. *Physical review letters* **2006,** *96* (11), 113002.

86. Hong, Y. Development and characterization of metallo-dielectric hybrid nanomaterials. 2016.

87. Baffou, G.; Quidant, R., Thermo‐plasmonics: using metallic nanostructures as nano‐sources of heat. *Laser & Photonics Reviews* **2013,** *7* (2), 171-187.

88. Johnson, P. B.; Christy, R.-W., Optical constants of the noble metals. *Physical review B* **1972,** *6* (12), 4370.

89. Palik, E. D., *Handbook of optical constants of solids*. Academic press: 1998; Vol. 3.

90. Gaspari, R.; Della Valle, G.; Ghosh, S.; Kriegel, I.; Scotognella, F.; Cavalli, A.; Manna, L., Quasi-static resonances in the visible spectrum from all-dielectric intermediate band semiconductor nanocrystals. *Nano Letters* **2017,** *17* (12), 7691-7695.

91. Ghosh, S.; Avellini, T.; Petrelli, A.; Kriegel, I.; Gaspari, R.; Almeida, G.; Bertoni, G.; Cavalli, A.; Scotognella, F.; Pellegrino, T., Colloidal CuFeS2 nanocrystals: intermediate Fe d-band leads to high photothermal conversion efficiency. *Chemistry of Materials* **2016,** *28* (13), 4848-4858.

92. Sugathan, A.; Bhattacharyya, B.; Kishore, V.; Kumar, A.; Rajasekar, G. P.; Sarma, D.; Pandey, A., Why does CuFeS2 resemble gold? *The journal of physical chemistry letters* **2018,** *9* (4), 696-701.

93. Eustis, S.; El-Sayed, M. A., Why gold nanoparticles are more precious than pretty gold: noble metal surface plasmon resonance and its enhancement of the radiative and

nonradiative properties of nanocrystals of different shapes. *Chemical society reviews* **2006,** *35* (3), 209-217.

94. Jain, P. K.; El-Sayed, M. A., Plasmonic coupling in noble metal nanostructures. *Chemical Physics Letters* **2010,** *487* (4-6), 153-164.

95. Xi, M.; Reinhard, B. M., Evolution of near-and far-field optical properties of Au bipyramids upon epitaxial deposition of Ag. *Nanoscale* **2020,** *12* (9), 5402-5411.

96. Jain, P. K.; Lee, K. S.; El-Sayed, I. H.; El-Sayed, M. A., Calculated absorption and scattering properties of gold nanoparticles of different size, shape, and composition: applications in biological imaging and biomedicine. *The journal of physical chemistry B* **2006,** *110* (14), 7238-7248.

97. Chan, G. H.; Zhao, J.; Schatz, G. C.; Van Duyne, R. P., Localized surface plasmon resonance spectroscopy of triangular aluminum nanoparticles. *The Journal of Physical Chemistry C* **2008,** *112* (36), 13958-13963.

98. Zheng, Z.; Tachikawa, T.; Majima, T., Single-particle study of Pt-modified Au nanorods for plasmon-enhanced hydrogen generation in visible to near-infrared region. *Journal of the American Chemical Society* **2014,** *136* (19), 6870-6873.

99. Zhao, J.; Zhong, D.; Zhou, S., NIR-I-to-NIR-II fluorescent nanomaterials for biomedical imaging and cancer therapy. *Journal of Materials Chemistry B* **2018,** *6* (3), 349-365.

100. Li, W.; Wang, J.; Ren, J.; Qu, X., Near‐infrared‐ and pH‐responsive system for reversible cell adhesion using graphene/gold nanorods functionalized with i‐motif DNA. *Angewandte Chemie* **2013,** *125* (26), 6858-6862.

101. de Miguel, I.; Prieto, I.; Albornoz, A.; Sanz, V.; Weis, C.; Turon, P.; Quidant, R., Plasmon-based biofilm inhibition on surgical implants. *Nano letters* **2019,** *19* (4), 2524-2529.

102. Poletti, A.; Fracasso, G.; Conti, G.; Pilot, R.; Amendola, V., Laser generated gold nanocorals with broadband plasmon absorption for photothermal applications. *Nanoscale* **2015,** *7* (32), 13702-13714.

103. Zheng, X.; Shen, Z.-p.; Cheng, C.; Shi, L.; Cheng, R.; Dong, J., Electrospinning Cu–TiO 2 nanofibers used for photocatalytic disinfection of bacteriophage f2: preparation, optimization and characterization. *RSC advances* **2017,** *7* (82), 52172-52179.

104. Mo, S.; Chen, X.; Chen, M.; He, C.; Lu, Y.; Zheng, N., Two-dimensional antibacterial Pd@ Ag nanosheets with a synergetic effect of plasmonic heating and Ag+ release. *Journal of Materials Chemistry B* **2015,** *3* (30), 6255-6260.

105. Boriskina, S. V.; Reinhard, B. M., Molding the flow of light on the nanoscale: from vortex nanogears to phase-operated plasmonic machinery. *Nanoscale* **2012,** *4* (1), 76-90.

106. Lerch, S.; Reinhard, B. M., Quantum Plasmonics: Optical Monitoring of DNA‐Mediated Charge Transfer in Plasmon Rulers. *Advanced Materials* **2016,** *28* (10), 2030-2036.

107. Hao, E.; Schatz, G. C., Electromagnetic fields around silver nanoparticles and dimers. *The Journal of chemical physics* **2004,** *120* (1), 357-366.

108. Linic, S.; Christopher, P.; Ingram, D. B., Plasmonic-metal nanostructures for efficient conversion of solar to chemical energy. *Nature materials* **2011,** *10* (12), 911-921.

109. An, X.; Erramilli, S.; Reinhard, B. M., Plasmonic nano-antimicrobials: properties, mechanisms and applications in microbe inactivation and sensing. *Nanoscale* **2021,** *13* (6), 3374-3411.

110. Wellstood, F.; Urbina, C.; Clarke, J., Hot-electron effects in metals. *Physical Review B* **1994,** *49* (9), 5942.

111. Kazuma, E.; Jung, J.; Ueba, H.; Trenary, M.; Kim, Y., Real-space and real-time observation of a plasmon-induced chemical reaction of a single molecule. *Science* **2018,** *360* (6388), 521-526.

112. Manjavacas, A.; Liu, J. G.; Kulkarni, V.; Nordlander, P., Plasmon-induced hot carriers in metallic nanoparticles. *ACS nano* **2014,** *8* (8), 7630-7638.

113. Tan, S.; Argondizzo, A.; Ren, J.; Liu, L.; Zhao, J.; Petek, H., Plasmonic coupling at a metal/semiconductor interface. *Nature Photonics* **2017,** *11* (12), 806-812.

114. Tagliabue, G.; DuChene, J. S.; Abdellah, M.; Habib, A.; Gosztola, D. J.; Hattori, Y.; Cheng, W.-H.; Zheng, K.; Canton, S. E.; Sundararaman, R., Ultrafast hot-hole injection modifies hot-electron dynamics in Au/p-GaN heterostructures. *Nature Materials* **2020,** *19* (12), 1312-1318.

115. Zhang, Q.; Li, R.; Lee, E.; Luo, T., Optically driven gold nanoparticles seed surface bubble nucleation in plasmonic suspension. *Nano Letters* **2021,** *21* (13), 5485-5492.

116. Nazari, M.; Li, X.; Alibakhshi, M. A.; Yang, H.; Souza, K.; Gillespie, C.; Gummuluru, S.; Hong, M. K.; Reinhard, B. M.; Korolev, K. S., Femtosecond photonic viral inactivation probed using solid-state nanopores. *Nano Futures* **2018,** *2* (4), 045005.

117. Neumann, O.; Urban, A. S.; Day, J.; Lal, S.; Nordlander, P.; Halas, N. J., Solar vapor generation enabled by nanoparticles. *ACS nano* **2013,** *7* (1), 42-49.

118. Boulais, É.; Lachaine, R.; Meunier, M., Plasma-mediated nanocavitation and photothermal effects in ultrafast laser irradiation of gold nanorods in water. *The Journal of Physical Chemistry C* **2013,** *117* (18), 9386-9396.

119. Choi, K. M.; Kim, D.; Rungtaweevoranit, B.; Trickett, C. A.; Barmanbek, J. T. D.; Alshammari, A. S.; Yang, P.; Yaghi, O. M., Plasmon-enhanced photocatalytic CO2 conversion within metal–organic frameworks under visible light. *Journal of the American Chemical Society* **2017,** *139* (1), 356-362.

120. Persson, B., Polarizability of small spherical metal particles: influence of the matrix environment. *Surface Science* **1993,** *281* (1-2), 153-162.

121. Lee, S. Y.; Tsalu, P. V.; Kim, G. W.; Seo, M. J.; Hong, J. W.; Ha, J. W., Tuning chemical interface damping: interfacial electronic effects of adsorbate molecules and sharp tips of single gold bipyramids. *Nano letters* **2019,** *19* (4), 2568-2574.

122. Foerster, B.; Joplin, A.; Kaefer, K.; Celiksoy, S.; Link, S.; Sönnichsen, C., Chemical interface damping depends on electrons reaching the surface. *ACS nano* **2017,** *11* (3), 2886-2893.

123. Aruda, K. O.; Tagliazucchi, M.; Sweeney, C. M.; Hannah, D. C.; Schatz, G. C.; Weiss, E. A., Identification of parameters through which surface chemistry determines the

lifetimes of hot electrons in small Au nanoparticles. *Proceedings of the National Academy of Sciences* **2013,** *110* (11), 4212-4217.

124. Shi, Z.; Li, Y.; Li, S.; Li, X.; Wu, D.; Xu, T.; Tian, Y.; Chen, Y.; Zhang, Y.; Zhang, B., Localized surface plasmon enhanced all ‐ inorganic perovskite quantum dot light ‐ emitting diodes based on coaxial core/shell heterojunction architecture. *Advanced Functional Materials* **2018,** *28* (20), 1707031.

125. Xu, S.; Guo, L.; Sun, Q.; Wang, Z. L., Piezotronic effect enhanced plasmonic photocatalysis by AuNPs/BaTiO3 heterostructures. *Advanced Functional Materials* **2019,** *29* (13), 1808737.

126. Jiang, X.; Zong, S.; Chen, C.; Zhang, Y.; Wang, Z.; Cui, Y., Gold–carbon dots for the intracellular imaging of cancer-derived exosomes. *Nanotechnology* **2018,** *29* (17), 175701.

127. Tanaka, A.; Teramura, K.; Hosokawa, S.; Kominami, H.; Tanaka, T., Visible light-induced water splitting in an aqueous suspension of a plasmonic Au/TiO 2 photocatalyst with metal co-catalysts. *Chemical science* **2017,** *8* (4), 2574-2580.

128. Mubeen, S.; Lee, J.; Singh, N.; Krämer, S.; Stucky, G. D.; Moskovits, M., An autonomous photosynthetic device in which all charge carriers derive from surface plasmons. *Nature nanotechnology* **2013,** *8* (4), 247-251.

129. Wilson, A. J.; Jain, P. K., Light-induced voltages in catalysis by plasmonic nanostructures. *Accounts of chemical research* **2020,** *53* (9), 1773-1781.

130. Huang, X.; Li, H.; Zhang, C.; Tan, S.; Chen, Z.; Chen, L.; Lu, Z.; Wang, X.; Xiao, M., Efficient plasmon-hot electron conversion in Ag–CsPbBr3 hybrid nanocrystals. *Nature communications* **2019,** *10* (1), 1-8.

131. Guo, X.; Hao, C.; Jin, G.; Zhu, H. Y.; Guo, X. Y., Copper nanoparticles on graphene support: an efficient photocatalyst for coupling of nitroaromatics in visible light. *Angewandte Chemie International Edition* **2014,** *53* (7), 1973-1977.

132. Robatjazi, H.; Bao, J. L.; Zhang, M.; Zhou, L.; Christopher, P.; Carter, E. A.; Nordlander, P.; Halas, N. J., Plasmon-driven carbon–fluorine (C (sp3)–F) bond activation with mechanistic insights into hot-carrier-mediated pathways. *Nature Catalysis* **2020,** *3* (7), 564-573.

133. Chen, Y.; Zhai, Y.; Deng, L.; Wang, N.; Mao, Y.; Yang, J.; Huang, Y., Optimizing Ag-Pt core-shell nanostructures for solar energy conversion, plasmonic photocatalysis, and photothermal catalysis. *Applied Physics Letters* **2019,** *114* (18), 183902.

134. Wang, F.; Huang, Y.; Chai, Z.; Zeng, M.; Li, Q.; Wang, Y.; Xu, D., Photothermal-enhanced catalysis in core–shell plasmonic hierarchical Cu 7 S 4 microsphere@ zeolitic imidazole framework-8. *Chemical science* **2016,** *7* (12), 6887-6893.

135. Chuang, C.-C.; Chu, H.-C.; Huang, S.-B.; Chang, W.-S.; Tuan, H.-Y., Laser-induced plasmonic heating in copper nanowire fabric as a photothermal catalytic reactor. *Chemical Engineering Journal* **2020,** *379*, 122285.

136. Robatjazi, H.; Zhao, H.; Swearer, D. F.; Hogan, N. J.; Zhou, L.; Alabastri, A.; McClain, M. J.; Nordlander, P.; Halas, N. J., Plasmon-induced selective carbon dioxide

conversion on earth-abundant aluminum-cuprous oxide antenna-reactor nanoparticles. *Nature communications* **2017,** *8* (1), 1-10.

137. Zou, J.; Si, Z.; Cao, Y.; Ran, R.; Wu, X.; Weng, D., Localized surface plasmon resonance assisted photothermal catalysis of CO and toluene oxidation over Pd–CeO2 catalyst under visible light irradiation. *The Journal of Physical Chemistry C* **2016,** *120* (51), 29116-29125.

138. Li, X.; Everitt, H. O.; Liu, J., Synergy between thermal and nonthermal effects in plasmonic photocatalysis. *Nano Research* **2020,** *13* (5), 1268-1280.

139. Luo, S.; Ren, X.; Lin, H.; Song, H.; Ye, J., Plasmonic photothermal catalysis for solar-to-fuel conversion: current status and prospects. *Chemical Science* **2021,** *12* (16), 5701-5719.

140. Liu, Y.; Wang, X.; Yang, F.; Yang, X., Excellent antimicrobial properties of mesoporous anatase TiO2 and Ag/TiO2 composite films. *Microporous and Mesoporous Materials* **2008,** *114* (1-3), 431-439.

141. Kuo, W.-S.; Chang, C.-N.; Chang, Y.-T.; Yeh, C.-S., Antimicrobial gold nanorods with dual-modality photodynamic inactivation and hyperthermia. *Chemical communications* **2009,** (32), 4853-4855.

142. Ding, R.; Yu, X.; Wang, P.; Zhang, J.; Zhou, Y.; Cao, X.; Tang, H.; Ayres, N.; Zhang, P., Hybrid photosensitizer based on amphiphilic block copolymer stabilized silver nanoparticles for highly efficient photodynamic inactivation of bacteria. *RSC advances* **2016,** *6* (24), 20392-20398.

143. Tahir, K.; Nazir, S.; Li, B.; Khan, A. U.; Khan, Z. U. H.; Ahmad, A.; Khan, Q. U.; Zhao, Y., Enhanced visible light photocatalytic inactivation of Escherichia coli using silver nanoparticles as photocatalyst. *Journal of Photochemistry and Photobiology B: Biology* **2015,** *153*, 261-266.

144. Khan, S.; Runguo, W.; Tahir, K.; Jichuan, Z.; Zhang, L., Catalytic reduction of 4-nitrophenol and photo inhibition of Pseudomonas aeruginosa using gold nanoparticles as photocatalyst. *Journal of Photochemistry and Photobiology B: Biology* **2017,** *170*, 181-187.

145. Jijie, R.; Dumych, T.; Chengnan, L.; Bouckaert, J.; Turcheniuk, K.; Hage, C.-H.; Heliot, L.; Cudennec, B.; Dumitrascu, N.; Boukherroub, R., Particle-based photodynamic therapy based on indocyanine green modified plasmonic nanostructures for inactivation of a Crohn's disease-associated Escherichia coli strain. *Journal of Materials Chemistry B* **2016,** *4* (15), 2598-2605.

146. Turcheniuk, K.; Turcheniuk, V.; Hage, C.-H.; Dumych, T.; Bilyy, R.; Bouckaert, J.; Héliot, L.; Zaitsev, V.; Boukherroub, R.; Szunerits, S., Highly effective photodynamic inactivation of E. coli using gold nanorods/SiO 2 core–shell nanostructures with embedded verteporfin. *Chemical Communications* **2015,** *51* (91), 16365-16368.

147. Ibelli, T.; Templeton, S.; Levi-Polyachenko, N., Progress on utilizing hyperthermia for mitigating bacterial infections. *International Journal of Hyperthermia* **2018,** *34* (2), 144-156.

148. Lara, H. H.; Ayala-Nuñez, N. V.; Ixtepan-Turrent, L.; Rodriguez-Padilla, C., Mode of antiviral action of silver nanoparticles against HIV-1. *Journal of nanobiotechnology* **2010,** *8* (1), 1-10.

149. Rivas Aiello, M. B.; Ghilini, F.; Martínez Porcel, J. n. E.; Giovanetti, L.; Schilardi, P. L.; Mártire, D. O., Riboflavin-mediated photooxidation of gold nanoparticles and its effect on the inactivation of bacteria. *Langmuir* **2020,** *36* (28), 8272-8281.

150. Li, F.; Lei, C.; Shen, Q.; Li, L.; Wang, M.; Guo, M.; Huang, Y.; Nie, Z.; Yao, S., Analysis of copper nanoparticles toxicity based on a stress-responsive bacterial biosensor array. *Nanoscale* **2013,** *5* (2), 653-662.

151. Zhang, Y.; Sun, P.; Zhang, L.; Wang, Z.; Wang, F.; Dong, K.; Liu, Z.; Ren, J.; Qu, X., Silver‐infused porphyrinic metal–organic framework: Surface‐adaptive, on‐demand nanoplatform for synergistic bacteria killing and wound disinfection. *Advanced functional materials* **2019,** *29* (11), 1808594.

152. Sontakke, S.; Modak, J.; Madras, G., Photocatalytic inactivation of Escherischia coli and Pichia pastoris with combustion synthesized titanium dioxide. *Chemical engineering journal* **2010,** *165* (1), 225-233.

153. Wang, Y.; Ding, X.; Chen, Y.; Guo, M.; Zhang, Y.; Guo, X.; Gu, H., Antibiotic-loaded, silver core-embedded mesoporous silica nanovehicles as a synergistic antibacterial agent for the treatment of drug-resistant infections. *Biomaterials* **2016,** *101*, 207-216.

154. Song, Z.; Ma, Y.; Xia, G.; Wang, Y.; Kapadia, W.; Sun, Z.; Wu, W.; Gu, H.; Cui, W.; Huang, X., In vitro and in vivo combined antibacterial effect of levofloxacin/silver co-

loaded electrospun fibrous membranes. *Journal of Materials Chemistry B* **2017,** *5* (36), 7632-7643.

155. Zhang, H.; Yang, Z.; Ju, Y.; Chu, X.; Ding, Y.; Huang, X.; Zhu, K.; Tang, T.; Su, X.; Hou, Y., Galvanic Displacement Synthesis of Monodisperse Janus‐ and Satellite‐Like Plasmonic–Magnetic Ag–Fe@ Fe3O4 Heterostructures with Reduced Cytotoxicity. *Advanced Science* **2018,** *5* (8), 1800271.

156. Xu, F.; Bandara, A.; Akiyama, H.; Eshaghi, B.; Stelter, D.; Keyes, T.; Straub, J. E.; Gummuluru, S.; Reinhard, B. M., Membrane-wrapped nanoparticles probe divergent roles of GM3 and phosphatidylserine in lipid-mediated viral entry pathways. *Proceedings of the National Academy of Sciences* **2018,** *115* (39), E9041-E9050.

157. Fan, H.; Yang, K.; Boye, D. M.; Sigmon, T.; Malloy, K. J.; Xu, H.; López, G. P.; Brinker, C. J., Self-assembly of ordered, robust, three-dimensional gold nanocrystal/silica arrays. *Science* **2004,** *304* (5670), 567-571.

158. Guo, Y.; Terazzi, E.; Seemann, R.; Fleury, J. B.; Baulin, V. A., Direct proof of spontaneous translocation of lipid-covered hydrophobic nanoparticles through a phospholipid bilayer. *Science advances* **2016,** *2* (11), e1600261.

159. Li, P.; Li, D.; Zhang, L.; Li, G.; Wang, E., Cationic lipid bilayer coated gold nanoparticles-mediated transfection of mammalian cells. *Biomaterials* **2008,** *29* (26), 3617-3624.

160. Shen, Z.; Loe, D. T.; Awino, J. K.; Kröger, M.; Rouge, J. L.; Li, Y., Self-assembly of core-polyethylene glycol-lipid shell (CPLS) nanoparticles and their potential as drug delivery vehicles. *Nanoscale* **2016,** *8* (31), 14821-14835.

161. Tatur, S.; Maccarini, M.; Barker, R.; Nelson, A.; Fragneto, G., Effect of functionalized gold nanoparticles on floating lipid bilayers. *Langmuir* **2013,** *29* (22), 6606-6614.

162. Ohvo-Rekilä, H.; Ramstedt, B.; Leppimäki, P.; Slotte, J. P., Cholesterol interactions with phospholipids in membranes. *Progress in lipid research* **2002,** *41* (1), 66-97.

163. Gleason, M. M.; Medow, M.; Tulenko, T. N., Excess membrane cholesterol alters calcium movements, cytosolic calcium levels, and membrane fluidity in arterial smooth muscle cells. *Circulation Research* **1991,** *69* (1), 216-227.

164. Pantelopulos, G. A.; Nagai, T.; Bandara, A.; Panahi, A.; Straub, J. E., Critical size dependence of domain formation observed in coarse-grained simulations of bilayers composed of ternary lipid mixtures. *The Journal of Chemical Physics* **2017,** *147* (9), 095101.

165. Guan, X. L.; Souza, C. M.; Pichler, H.; Dewhurst, G.; Schaad, O.; Kajiwara, K.; Wakabayashi, H.; Ivanova, T.; Castillon, G. A.; Piccolis, M., Functional interactions between sphingolipids and sterols in biological membranes regulating cell physiology. *Molecular biology of the cell* **2009,** *20* (7), 2083-2095.

166. Bandara, A.; Panahi, A.; Pantelopulos, G. A.; Nagai, T.; Straub, J. E., Exploring the impact of proteins on the line tension of a phase-separating ternary lipid mixture. *The Journal of chemical physics* **2019,** *150* (20), 204702.

167. Mei, R.; Wang, Y.; Liu, W.; Chen, L., Lipid Bilayer-Enabled Synthesis of Waxberry-like Core–Fluidic Satellite Nanoparticles: Toward Ultrasensitive Surface-Enhanced Raman Scattering Tags for Bioimaging. *ACS applied materials & interfaces* **2018,** *10* (28), 23605-23616.

168. Yoshimura, A.; Hoffman, M. Z.; Sun, H., An evaluation of the excited state absorption spectrum of Ru (bpy) 32+ in aqueous and acetonitrile solutions. *Journal of Photochemistry and Photobiology A: Chemistry* **1993,** *70* (1), 29-33.

169. Mujumdar, R. B.; Ernst, L. A.; Mujumdar, S. R.; Lewis, C. J.; Waggoner, A. S., Cyanine dye labeling reagents: sulfoindocyanine succinimidyl esters. *Bioconjugate chemistry* **1993,** *4* (2), 105-111.

170. Ozer, G.; Valeev, E. F.; Quirk, S.; Hernandez, R., Adaptive steered molecular dynamics of the long-distance unfolding of neuropeptide Y. *Journal of Chemical Theory and Computation* **2010,** *6* (10), 3026-3038.

171. Jarzynski, C., Nonequilibrium equality for free energy differences. *Physical Review Letters* **1997,** *78* (14), 2690.

172. Park, S.; Schulten, K., Calculating potentials of mean force from steered molecular dynamics simulations. *The Journal of chemical physics* **2004,** *120* (13), 5946-5961.

173. Ma, Z.; LeBard, D. N.; Loverde, S. M.; Sharp, K. A.; Klein, M. L.; Discher, D. E.; Finkel, T. H., TCR triggering by pMHC ligands tethered on surfaces via poly (ethylene glycol) depends on polymer length. *PloS one* **2014,** *9* (11), e112292.

174. Hill, R. T.; Mock, J. J.; Hucknall, A.; Wolter, S. D.; Jokerst, N. M.; Smith, D. R.; Chilkoti, A., Plasmon ruler with angstrom length resolution. *ACS nano* **2012,** *6* (10), 9237-9246.

175. Kerr, E.; Doeven, E. H.; Wilson, D. J.; Hogan, C. F.; Francis, P. S., Considering the chemical energy requirements of the tri-n-propylamine co-reactant pathways for the judicious design of new electrogenerated chemiluminescence detection systems. *Analyst* **2016,** *141* (1), 62-69.

176. Boggs, B. K.; King, R. L.; Botte, G. G., Urea electrolysis: direct hydrogen production from urine. *Chemical Communications* **2009,** (32), 4859-4861.

177. Zhu, X.; Dou, X.; Dai, J.; An, X.; Guo, Y.; Zhang, L.; Tao, S.; Zhao, J.; Chu, W.; Zeng, X. C., Metallic nickel hydroxide nanosheets give superior electrocatalytic oxidation of urea for fuel cells. *Angewandte Chemie International Edition* **2016,** *55* (40), 12465-12469.

178. Vedharathinam, V.; Botte, G. G., Understanding the electro-catalytic oxidation mechanism of urea on nickel electrodes in alkaline medium. *Electrochimica Acta* **2012,** *81* (none).

179. Chen, S.; Duan, J.; Vasileff, A.; Qiao, S. Z., Size fractionation of two‐dimensional sub‐nanometer thin manganese dioxide crystals towards superior urea electrocatalytic conversion. *Angewandte Chemie International Edition* **2016,** *55* (11), 3804-3808.

180. Esposito, D. V.; Levin, I.; Moffat, T. P.; Talin, A. A., H2 evolution at Si-based metal–insulator–semiconductor photoelectrodes enhanced by inversion channel charge collection and H spillover. *Nature materials* **2013,** *12* (6), 562-568.

181. Sun, K.; Park, N.; Sun, Z.; Zhou, J.; Wang, J.; Pang, X.; Shen, S.; Noh, S. Y.; Jing, Y.; Jin, S., Nickel oxide functionalized silicon for efficient photo-oxidation of water. *Energy & Environmental Science* **2012,** *5* (7), 7872-7877.

182. Prier, C. K.; Rankic, D. A.; MacMillan, D. W., Visible light photoredox catalysis with transition metal complexes: applications in organic synthesis. *Chemical reviews* **2013,** *113* (7), 5322-5363.

183. You, S.; Gong, X.; Wang, W.; Qi, D.; Wang, X.; Chen, X.; Ren, N., Enhanced cathodic oxygen reduction and power production of microbial fuel cell based on noble - metal - free electrocatalyst derived from metal - organic frameworks. *Advanced Energy Materials* **2016,** *6* (1), 1501497.

184. Bhattacharyya, B.; Pandey, A., CuFeS2 quantum dots and highly luminescent CuFeS2 based core/shell structures: synthesis, tunability, and photophysics. *Journal of the American Chemical Society* **2016,** *138* (32), 10207-10213.

185. Kumar, P.; Uma, S.; Nagarajan, R., Precursor driven one pot synthesis of wurtzite and chalcopyrite CuFeS 2. *Chemical Communications* **2013,** *49* (66), 7316-7318.

186. Xie, H.; Su, X.; Zheng, G.; Zhu, T.; Yin, K.; Yan, Y.; Uher, C.; Kanatzidis, M. G.; Tang, X., The role of Zn in chalcopyrite CuFeS2: enhanced thermoelectric properties of

Cu1–xZnxFeS2 with in situ nanoprecipitates. *Advanced Energy Materials* **2017,** *7* (3), 1601299.

187. Yu, H.; Xu, P.; Lee, D.-W.; Li, X., Porous-layered stack of functionalized AuNP–rGO (gold nanoparticles–reduced graphene oxide) nanosheets as a sensing material for the micro-gravimetric detection of chemical vapor. *Journal of Materials Chemistry A* **2013,** *1* (14), 4444-4450.

188. Hsieh, Z.-L.; Lin, M.-C.; Uan, J.-Y., Rapid direct growth of Li–Al layered double hydroxide (LDH) film on glass, silicon wafer and carbon cloth and characterization of LDH film on substrates. *Journal of Materials Chemistry* **2011,** *21* (6), 1880-1889.

189. Manders, E.; Verbeek, F.; Aten, J., Measurement of co‐localization of objects in dual‐colour confocal images. *Journal of microscopy* **1993,** *169* (3), 375-382.

190. Oguchi, T.; Sato, K.; Teranishi, T., Optical reflectivity spectrum of a CuFeS2 single crystal. *Journal of the Physical Society of Japan* **1980,** *48* (1), 123-128.

191. Ge, Q.; Feng, X.; Wang, R.; Zheng, R.; Luo, S.; Duan, L.; Ji, Y.; Lin, J.; Chen, H., Mixed redox-couple-involved chalcopyrite phase CuFeS2 quantum dots for highly efficient Cr (VI) removal. *Environmental Science & Technology* **2020,** *54* (13), 8022-8031.

192. Kumar, B.; Singh, S. V.; Chattopadhyay, A.; Biring, S.; Pal, B. N., Scalable Synthesis of a Sub-10 nm Chalcopyrite (CuFeS2) Nanocrystal by the Microwave-Assisted Synthesis Technique and Its Application in a Heavy-Metal-Free Broad-Band Photodetector. *ACS omega* **2020,** *5* (40), 25947-25953.

193. Gabka, G.; Bujak, P.; Żukrowski, J.; Zabost, D.; Kotwica, K.; Malinowska, K.; Ostrowski, A.; Wielgus, I.; Lisowski, W.; Sobczak, J. W., Non-injection synthesis of monodisperse Cu–Fe–S nanocrystals and their size dependent properties. *Physical Chemistry Chemical Physics* **2016,** *18* (22), 15091-15101.

194. Wang, S. S.; Jiao, L.; Qian, Y.; Hu, W. C.; Xu, G. Y.; Wang, C.; Jiang, H. L., Boosting Electrocatalytic Hydrogen Evolution over Metal–Organic Frameworks by Plasmon‐Induced Hot‐Electron Injection. *Angewandte Chemie* **2019,** *131* (31), 10823-10827.

195. Li, Y.; Qian, G.; Brown, P. L.; Gerson, A. R., Chalcopyrite dissolution: Scanning photoelectron microscopy examination of the evolution of sulfur species with and without added iron or pyrite. *Geochimica et Cosmochimica Acta* **2017,** *212,* 33-47.

196. Nishikawa, M.; Nomoto, K.; Kume, S.; Nishihara, H., Reversible copper (II)/(I) electrochemical potential switching driven by visible light-induced coordinated ring rotation. *Journal of the American Chemical Society* **2012,** *134* (25), 10543-10553.

197. Navon, N.; Golub, G.; Cohen, H.; Paoletti, P.; Valtancoli, B.; Bencini, A.; Meyerstein, D., Design of ligands that stabilize Cu (I) and shift the reduction potential of the CuII/I couple cathodically in aqueous solutions. *Inorganic chemistry* **1999,** *38* (15), 3484-3488.

198. Yin, Q.; Vaughan, D.; England, K.; Kelsall, G.; Brandon, N., Surface oxidation of chalcopyrite (CuFeS2) in alkaline solutions. *Journal of the Electrochemical Society* **2000,** *147* (8), 2945.

199. Grimaud, A.; Diaz-Morales, O.; Han, B.; Hong, W. T.; Lee, Y.-L.; Giordano, L.; Stoerzinger, K. A.; Koper, M. T.; Shao-Horn, Y., Activating lattice oxygen redox reactions in metal oxides to catalyse oxygen evolution. *Nature chemistry* **2017,** *9* (5), 457-465.

200. Amiri, M.; Fallahi, M.; Bezaatpour, A.; Jijie, R.; Nozari-Asbmarz, M.; Rouhi, M.; Boukherroub, R.; Szunerits, S., Solution processable Cu (II) macrocycle for the formation of Cu2O thin film on indium tin oxide and its application for water oxidation. *The Journal of Physical Chemistry C* **2018,** *122* (29), 16510-16518.

201. Drosou, M.; Kamatsos, F.; Ioannidis, G.; Zarkadoulas, A.; Mitsopoulou, C. A.; Papatriantafyllopoulou, C.; Tzeli, D., Reactivity and Mechanism of Photo-and Electrocatalytic Hydrogen Evolution by a Diimine Copper (I) Complex. *Catalysts* **2020,** *10* (11), 1302.

202. Zhu, D.; Wang, L.; Yu, W.; Xie, H., Intriguingly high thermal conductivity increment for CuO nanowires contained nanofluids with low viscosity. *scientific reports* **2018,** *8* (1), 1-12.

203. Liu, H.; Xie, J.; Liu, P.; Dai, B., Effect of Cu+/Cu2+ ratio on the catalytic behavior of anhydrous nieuwland catalyst during dimerization of acetylene. *Catalysts* **2016,** *6* (8), 120.

204. Shah, P. M.; Burnett, J. W.; Morgan, D. J.; Davies, T. E.; Taylor, S. H., Ceria–zirconia mixed metal oxides prepared via mechanochemical grinding of carbonates for the total oxidation of propane and naphthalene. *Catalysts* **2019,** *9* (5), 475.

205. Peng, C.-Y.; Hou, C.-C.; Chen, Q.-Q.; Wang, C.-J.; Lv, X.-J.; Zhong, J.; Fu, W.-F.; Che, C.-M.; Chen, Y., Cu (OH) 2 supported on Fe (OH) 3 as a synergistic and highly

efficient system for the dehydrogenation of ammonia-borane. *Science Bulletin* **2018,** *63* (23), 1583-1590.

206. Deng, Y.; Handoko, A. D.; Du, Y.; Xi, S.; Yeo, B. S., In situ Raman spectroscopy of copper and copper oxide surfaces during electrochemical oxygen evolution reaction: identification of CuIII oxides as catalytically active species. *Acs Catalysis* **2016,** *6* (4), 2473-2481.

207. Giester, G.; Libowitzky, E., Crystal structures and Raman spectra of Cu (OH) F and Cu3 (OH) 2F4. *Zeitschrift für Kristallographie-Crystalline Materials* **2003,** *218* (5), 351-356.

208. Kim, T. W.; Choi, K.-S., Nanoporous BiVO4 photoanodes with dual-layer oxygen evolution catalysts for solar water splitting. *Science* **2014,** *343* (6174), 990-994.

209. Yin, H.; Xu, L.; Porter, N. A., Free radical lipid peroxidation: mechanisms and analysis. *Chemical reviews* **2011,** *111* (10), 5944-5972.

210. Girotti, A. W., Photosensitized oxidation of membrane lipids: reaction pathways, cytotoxic effects, and cytoprotective mechanisms. *Journal of Photochemistry and Photobiology B: Biology* **2001,** *63* (1-3), 103-113.

211. Bacellar, I. O.; Oliveira, M. C.; Dantas, L. S.; Costa, E. B.; Junqueira, H. C.; Martins, W. K.; Durantini, A. M.; Cosa, G.; Di Mascio, P.; Wainwright, M., Photosensitized membrane permeabilization requires contact-dependent reactions between photosensitizer and lipids. *Journal of the American Chemical Society* **2018,** *140* (30), 9606-9615.

212. Bacellar, I. O.; Baptista, M. S., Mechanisms of photosensitized lipid oxidation and membrane permeabilization. *Acs Omega* **2019,** *4* (26), 21636-21646.

213. Margesin, R.; Schinner, F., Heavy metal resistant Arthrobacter sp.—A tool for studying conjugational plasmid transfer between Gram ‐ negative and Gram ‐ positive bacteria. *Journal of basic microbiology* **1997,** *37* (3), 217-227.

214. Prasad, K. S.; Ramanathan, A.; Paul, J.; Subramanian, V.; Prasad, R., Biosorption of arsenite (As+ 3) and arsenate (As+ 5) from aqueous solution by Arthrobacter sp. biomass. *Environmental technology* **2013,** *34* (19), 2701-2708.

215. Mascio, C. T.; Alder, J. D.; Silverman, J. A., Bactericidal action of daptomycin against stationary-phase and nondividing Staphylococcus aureus cells. *Antimicrobial agents and chemotherapy* **2007,** *51* (12), 4255-4260.

216. Silhavy, T. J., Classic spotlight: Gram-negative bacteria have two membranes. Am Soc Microbiol: 2016; Vol. 198, pp 201-201.

217. Parakh, P.; Gokulakrishnan, S.; Prakash, H., Visible light water disinfection using [Ru (bpy) 2 (phendione)](PF6) 2· 2H2O and [Ru (phendione) 3] Cl2· 2H2O complexes and their effective adsorption onto activated carbon. *Separation and Purification Technology* **2013,** *109*, 9-17.

218. Abreu, F. D.; Diógenes, I. C. N.; de França Lopes, L. G.; Sousa, E. H. S.; de Carvalho, I. M. M., Ruthenium (II) bipyridine complexes with pendant anthracenyl and naphthyl moieties: A strategy for a ROS generator with DNA binding selectivity. *Inorganica Chimica Acta* **2016,** *439*, 92-99.

219. da Silva, R. S.; Marchesi, M. S. P.; Tedesco, A. C.; Mikhailovsky, A.; Ford, P. C., Generation of reactive oxygen species by photolysis of the ruthenium (ii) complex Ru (NH 3) 5 (pyrazine) 2+ in oxygenated solution. *Photochemical & Photobiological Sciences* **2007,** *6* (5), 515-518.

220. Papuc, C.; Goran, G. V.; Predescu, C. N.; Nicorescu, V., Mechanisms of oxidative processes in meat and toxicity induced by postprandial degradation products: A review. *Comprehensive Reviews in food science and food safety* **2017,** *16* (1), 96-123.

221. Xu, Q.; Ke, X.; Cai, D.; Zhang, Y.; Fu, F.; Endo, T.; Liu, X., Silver-based, single-sided antibacterial cotton fabrics with improved durability via an l-cysteine binding effect. *Cellulose* **2018,** *25* (3), 2129-2141.

222. Dey, S.; Paul, A., Influence of metal ions on biofilm formation by Arthrobacter sp. SUK 1205 and evaluation of their Cr (VI) removal efficacy. *International biodeterioration & biodegradation* **2018,** *132*, 122-131.

223. Whitehead, K. A.; Verran, J., Formation, architecture and functionality of microbial biofilms in the food industry. *Current Opinion in Food Science* **2015,** *2*, 84-91.

224. Hall-Stoodley, L.; Costerton, J. W.; Stoodley, P., Bacterial biofilms: from the natural environment to infectious diseases. *Nature reviews microbiology* **2004,** *2* (2), 95-108.

225. Chouirfa, H.; Bouloussa, H.; Migonney, V.; Falentin-Daudré, C., Review of titanium surface modification techniques and coatings for antibacterial applications. *Acta biomaterialia* **2019,** *83*, 37-54.

226. Lopez-Lopez, G.; Pascual, A.; Perea, E., Effect of plastic catheter material on bacterial adherence and viability. *Journal of medical microbiology* **1991,** *34* (6), 349-353.

227. Roe, D.; Karandikar, B.; Bonn-Savage, N.; Gibbins, B.; Roullet, J.-B., Antimicrobial surface functionalization of plastic catheters by silver nanoparticles. *Journal of antimicrobial chemotherapy* **2008,** *61* (4), 869-876.

228. Lin, Y.; Chen, J.; Tavakoli, M. M.; Gao, Y.; Zhu, Y.; Zhang, D.; Kam, M.; He, Z.; Fan, Z., Printable fabrication of a fully integrated and self‐powered sensor system on plastic substrates. *Advanced Materials* **2019,** *31* (5), 1804285.

229. Paxton, N. C.; Allenby, M. C.; Lewis, P. M.; Woodruff, M. A., Biomedical applications of polyethylene. *European Polymer Journal* **2019,** *118*, 412-428.

230. Tickner, J. A.; Schettler, T.; Guidotti, T.; McCally, M.; Rossi, M., Health risks posed by use of Di‐2‐ethylhexyl phthalate (DEHP) in PVC medical devices: A critical review. *American journal of industrial medicine* **2001,** *39* (1), 100-111.

231. Jenke, D., Evaluation of the chemical compatibility of plastic contact materials and pharmaceutical products; safety considerations related to extractables and leachables. *Journal of pharmaceutical sciences* **2007,** *96* (10), 2566-2581.

232. Sileika, T. S.; Kim, H.-D.; Maniak, P.; Messersmith, P. B., Antibacterial performance of polydopamine-modified polymer surfaces containing passive and active components. *ACS applied materials & interfaces* **2011,** *3* (12), 4602-4610.

233. Balaure, P. C.; Grumezescu, A. M., Recent advances in surface nanoengineering for biofilm prevention and control. part i: Molecular basis of biofilm recalcitrance. passive anti-biofouling nanocoatings. *Nanomaterials* **2020,** *10* (6), 1230.

234. Balaure, P. C.; Grumezescu, A. M., Recent advances in surface nanoengineering for biofilm prevention and control. Part II: active, combined active and passive, and smart bacteria-responsive antibiofilm nanocoatings. *Nanomaterials* **2020,** *10* (8), 1527.

235. Vasilev, K., Nanoengineered antibacterial coatings and materials: A perspective. *Coatings* **2019,** *9* (10), 654.

236. Park, S.; Kim, H.-h.; Yang, S. B.; Moon, J.-H.; Ahn, H.-W.; Hong, J., A polysaccharide-based antibacterial coating with improved durability for clear overlay appliances. *ACS applied materials & interfaces* **2018,** *10* (21), 17714-17721.

237. Diaz Blanco, C.; Ortner, A.; Dimitrov, R.; Navarro, A.; Mendoza, E.; Tzanov, T., Building an antifouling zwitterionic coating on urinary catheters using an enzymatically triggered bottom-up approach. *ACS Applied Materials & Interfaces* **2014,** *6* (14), 11385-11393.

238. Yu, K.; Lo, J. C.; Yan, M.; Yang, X.; Brooks, D. E.; Hancock, R. E.; Lange, D.; Kizhakkedathu, J. N., Anti-adhesive antimicrobial peptide coating prevents catheter associated infection in a mouse urinary infection model. *Biomaterials* **2017,** *116*, 69-81.

239. Asri, L. A.; Crismaru, M.; Roest, S.; Chen, Y.; Ivashenko, O.; Rudolf, P.; Tiller, J. C.; van der Mei, H. C.; Loontjens, T. J.; Busscher, H. J., A shape ‐ adaptive, antibacterial ‐ coating of immobilized quaternary ‐ ammonium compounds tethered on hyperbranched

polyurea and its mechanism of action. *Advanced Functional Materials* **2014,** *24* (3), 346-355.

240. Yu, H.; Liu, L.; Li, X.; Zhou, R.; Yan, S.; Li, C.; Luan, S.; Yin, J.; Shi, H., Fabrication of polylysine based antibacterial coating for catheters by facile electrostatic interaction. *Chemical Engineering Journal* **2019,** *360*, 1030-1041.

241. Li, P.; Poon, Y. F.; Li, W.; Zhu, H.-Y.; Yeap, S. H.; Cao, Y.; Qi, X.; Zhou, C.; Lamrani, M.; Beuerman, R. W., A polycationic antimicrobial and biocompatible hydrogel with microbe membrane suctioning ability. *Nature materials* **2011,** *10* (2), 149-156.

242. Liu, Y.; Li, J.; Cheng, X.; Ren, X.; Huang, T., Self-assembled antibacterial coating by N-halamine polyelectrolytes on a cellulose substrate. *Journal of Materials Chemistry B* **2015,** *3* (7), 1446-1454.

243. Han, W.; Wu, Z.; Li, Y.; Wang, Y., Graphene family nanomaterials (GFNs)—promising materials for antimicrobial coating and film: A review. *Chemical Engineering Journal* **2019,** *358*, 1022-1037.

244. Moor, K. J.; Osuji, C. O.; Kim, J.-H., Dual-functionality fullerene and silver nanoparticle antimicrobial composites via block copolymer templates. *ACS Applied Materials & Interfaces* **2016,** *8* (49), 33583-33591.

245. Benetti, G.; Cavaliere, E.; Brescia, R.; Salassi, S.; Ferrando, R.; Vantomme, A.; Pallecchi, L.; Pollini, S.; Boncompagni, S.; Fortuni, B., Tailored Ag–Cu–Mg multielemental nanoparticles for wide-spectrum antibacterial coating. *Nanoscale* **2019,** *11* (4), 1626-1635.

246. Huang, Y.-H.; Chen, M. H.-C.; Lee, B.-H.; Hsieh, K.-H.; Tu, Y.-K.; Lin, J.-J.; Chang, C.-H., Evenly distributed thin-film Ag coating on stainless plate by tricomponent Ag/Silicate/PU with antimicrobial and biocompatible properties. *ACS Applied Materials & Interfaces* **2014,** *6* (22), 20324-20333.

247. Taheri, S.; Cavallaro, A.; Christo, S. N.; Majewski, P.; Barton, M.; Hayball, J. D.; Vasilev, K., Antibacterial plasma polymer films conjugated with phospholipid encapsulated silver nanoparticles. *ACS Biomaterials Science & Engineering* **2015,** *1* (12), 1278-1286.

248. Li, Z.; Lee, D.; Sheng, X.; Cohen, R. E.; Rubner, M. F., Two-level antibacterial coating with both release-killing and contact-killing capabilities. *Langmuir* **2006,** *22* (24), 9820-9823.

249. Yu, H.; Liu, L.; Yang, H.; Zhou, R.; Che, C.; Li, X.; Li, C.; Luan, S.; Yin, J.; Shi, H., Water-insoluble polymeric guanidine derivative and application in the preparation of antibacterial coating of catheter. *ACS applied materials & interfaces* **2018,** *10* (45), 39257-39267.

250. Wang, B.; Liu, H.; Wang, Z.; Shi, S.; Nan, K.; Xu, Q.; Ye, Z.; Chen, H., A self-defensive antibacterial coating acting through the bacteria-triggered release of a hydrophobic antibiotic from layer-by-layer films. *Journal of Materials Chemistry B* **2017,** *5* (7), 1498-1506.

251. Pal, A.; Pehkonen, S. O.; Yu, L. E.; Ray, M. B., Photocatalytic inactivation of airborne bacteria in a continuous-flow reactor. *Industrial & engineering chemistry research* **2008,** *47* (20), 7580-7585.

252. Loeb, S.; Li, C.; Kim, J.-H., Solar photothermal disinfection using broadband-light absorbing gold nanoparticles and carbon black. *Environmental science & technology* **2018,** *52* (1), 205-213.

253. Loeb, S. K.; Kim, J.; Jiang, C.; Early, L. S.; Wei, H.; Li, Q.; Kim, J.-H., Nanoparticle enhanced interfacial solar photothermal water disinfection demonstrated in 3-D printed flow-through reactors. *Environmental Science & Technology* **2019,** *53* (13), 7621-7631.

254. Amsberry, A.; Tyler, C.; Steinhauff, W.; Pommerenck, J.; Yokochi, A. T., Simple continuous-flow device for combined solar thermal pasteurization and solar disinfection for water sterilization. *Journal of Humanitarian Engineering* **2015,** *3* (1).

255. Zhang, H.; Li, L.; Tatsumi, E.; Isobe, S., High-pressure treatment effects on proteins in soy milk. *LWT-Food Science and Technology* **2005,** *38* (1), 7-14.

256. Cruz, N.; Capellas, M.; Hernández, M.; Trujillo, A.; Guamis, B.; Ferragut, V., Ultra high pressure homogenization of soymilk: Microbiological, physicochemical and microstructural characteristics. *Food research international* **2007,** *40* (6), 725-732.

257. Chu, C.; Ryberg, E. C.; Loeb, S. K.; Suh, M.-J.; Kim, J.-H., Water disinfection in rural areas demands unconventional solar technologies. *Accounts of Chemical Research* **2019,** *52* (5), 1187-1195.

258. Tallósy, S. P.; Janovák, L.; Nagy, E.; Deák, Á.; Juhász, Á.; Csapó, E.; Buzás, N.; Dékány, I., Adhesion and inactivation of Gram-negative and Gram-positive bacteria on photoreactive TiO2/polymer and Ag–TiO2/polymer nanohybrid films. *Applied Surface Science* **2016,** *371*, 139-150.

259. Miura, N.; Shinohara, Y., Cytotoxic effect and apoptosis induction by silver nanoparticles in HeLa cells. *Biochemical and biophysical research communications* **2009,** *390* (3), 733-737.

260. Lo, K. K.-W.; Lee, T. K.-M.; Lau, J. S.-Y.; Poon, W.-L.; Cheng, S.-H., Luminescent biological probes derived from ruthenium (II) estradiol polypyridine complexes. *Inorganic chemistry* **2008,** *47* (1), 200-208.

261. Mattsson, J.; Govindaswamy, P.; Renfrew, A. K.; Dyson, P. J.; Stepnicka, P.; Süss-Fink, G.; Therrien, B., Synthesis, molecular structure, and anticancer activity of cationic arene ruthenium metallarectangles. *Organometallics* **2009,** *28* (15), 4350-4357.

262. Zhu, C.; Yang, Q.; Liu, L.; Lv, F.; Li, S.; Yang, G.; Wang, S., Multifunctional cationic poly (p‐phenylene vinylene) polyelectrolytes for selective recognition, imaging, and killing of bacteria over mammalian cells. *Advanced Materials* **2011,** *23* (41), 4805-4810.

263. Maity, J. P.; Chakraborty, S.; Kar, S.; Panja, S.; Jean, J.-S.; Samal, A. C.; Chakraborty, A.; Santra, S. C., Effects of gamma irradiation on edible seed protein, amino acids and genomic DNA during sterilization. *Food chemistry* **2009,** *114* (4), 1237-1244.

264. Filmus, J.; Pollak, M. N.; Cailleau, R.; Buick, R. N., MDA-468, a human breast cancer cell line with a high number of epidermal growth factor (EGF) receptors, has an amplified EGF receptor gene and is growth inhibited by EGF. *Biochemical and biophysical research communications* **1985,** *128* (2), 898-905.

265. Balakrishnan, H. K.; Doeven, E. H.; Merenda, A.; Dumée, L. F.; Guijt, R. M., 3D printing for the integration of porous materials into miniaturised fluidic devices: A review. *Analytica Chimica Acta* **2021,** *1185*, 338796.

266. Liu, J.; Hwang, H. H.; Wang, P.; Whang, G.; Chen, S., Direct 3D-printing of cell-laden constructs in microfluidic architectures. *Lab on a Chip* **2016,** *16* (8), 1430-1438.

267. Haynes, C. L.; McFarland, A. D.; Van Duyne, R. P., Surface-enhanced: Raman spectroscopy. *Analytical Chemistry* **2005,** *77* (17), 338 A-346 A.

268. Jackson, J. B.; Halas, N. J., Surface-enhanced Raman scattering on tunable plasmonic nanoparticle substrates. *Proceedings of the National Academy of Sciences* **2004,** *101* (52), 17930-17935.

269. Schlücker, S., Surface‐Enhanced raman spectroscopy: Concepts and chemical applications. *Angewandte Chemie International Edition* **2014,** *53* (19), 4756-4795.

270. Asher, S. A.; Schuster, T. M., Resonance Raman examination of axial ligand bonding and spin-state equilibriums in metmyoglobin hydroxide and other heme derivatives. *Biochemistry* **1979,** *18* (24), 5377-5387.

271. Tsubaki, M.; Srivastava, R. B.; Yu, N. T., Resonance Raman investigation of carbon monoxide bonding in (carbon monoxy) hemoglobin and-myoglobin: detection of iron-carbon monoxide stretching and iron-carbon-oxygen bending vibrations and influence of the quaternary structure change. *Biochemistry* **1982,** *21* (6), 1132-1140.

272. ZOU, S.-Z.; ZHANG, Y.-H.; CHEN, Y.-X.; TIAN, Z.-Q., SERS Studies on the Orientation and Structure of Absorbed Water at Ag Electrodes—— Effects of Electrode

Potential and NaClO_4 Concentrations. *CHEMICAL RESEARCH IN CHINESE UNIVERSITIES* **1995**.

273. Kister, G.; Cassanas, G.; Vert, M., Effects of morphology, conformation and configuration on the IR and Raman spectra of various poly (lactic acid) s. *Polymer* **1998,** *39* (2), 267-273.

274. Guo, C.; Wang, J.; Liu, H.-z.; Chen, J.-y., Hydration and conformation of temperature-dependent micellization of PEO− PPO− PEO block copolymers in aqueous solutions by FT-Raman. *Langmuir* **1999,** *15* (8), 2703-2708.

275. Muniz-Miranda, M.; Puggelli, M.; Ricceri, R.; Gabrielli, G., SERS and Molecular Orientation in Langmuir− Blodgett Films Deposited onto Smooth Copper Surfaces. *Langmuir* **1996,** *12* (18), 4417-4420.

276. Huang, M.; Yan, H.; Chen, C.; Song, D.; Heinz, T. F.; Hone, J., Phonon softening and crystallographic orientation of strained graphene studied by Raman spectroscopy. *Proceedings of the National Academy of Sciences* **2009,** *106* (18), 7304-7308.

277. Ling, X.; Wu, J.; Xu, W.; Zhang, J., Probing the effect of molecular orientation on the intensity of chemical enhancement using graphene ‐ enhanced Raman spectroscopy. *Small* **2012,** *8* (9), 1365-1372.

278. Dogangun, M.; Ohno, P. E.; Liang, D.; McGeachy, A. C.; Be, A. G.; Dalchand, N.; Li, T.; Cui, Q.; Geiger, F. M., Hydrogen-bond networks near supported lipid bilayers from vibrational sum frequency generation experiments and atomistic simulations. *The Journal of Physical Chemistry B* **2018,** *122* (18), 4870-4879.

279. Dalchand, N.; Dogangun, M.; Ohno, P. E.; Ma, E.; Martinson, A. B.; Geiger, F. M., Perturbation of hydrogen-bonding networks over supported lipid bilayers by poly (allylamine hydrochloride). *The Journal of Physical Chemistry B* **2019,** *123* (19), 4251-4257.

280. Leng, C.; Hung, H.-C.; Sun, S.; Wang, D.; Li, Y.; Jiang, S.; Chen, Z., Probing the surface hydration of nonfouling zwitterionic and PEG materials in contact with proteins. *ACS applied materials & interfaces* **2015,** *7* (30), 16881-16888.

281. Boeck, F.; Kribber, T.; Xiao, L.; Hintermann, L., Mixed phosphane η5-CpRuCl (PR3) 2 complexes as ambifunctional catalysts for anti-Markovnikov hydration of terminal alkynes. *Journal of the American Chemical Society* **2011,** *133* (21), 8138-8141.

282. Yang, S.-J.; Liu, M.-C.; Xiang, H.-M.; Zhao, Q.; Xue, W.; Yang, S., Synthesis and in vitro antitumor evaluation of betulin acid ester derivatives as novel apoptosis inducers. *European Journal of Medicinal Chemistry* **2015,** *102*, 249-255.

283. Deng, Y.; Snyder, J. K., Preparation of a 24-nor-1, 4-dien-3-one triterpene derivative from betulin: A new route to 24-nortriterpene analogues1. *The Journal of Organic Chemistry* **2002,** *67* (9), 2864-2873.

284. Zhang, C.; Liu, D.; Zhou, B.; Deng, J.; Yang, W., Poly (N-propargylamide) s bearing cholesteryl moieties: Preparation and optical activity. *Reactive and Functional Polymers* **2012,** *72* (11), 832-838.

285. Šilhár, P.; Alakurtti, S.; Čapková, K.; Xiaochuan, F.; Shoemaker, C. B.; Yli-Kauhaluoma, J.; Janda, K. D., Synthesis and evaluation of library of betulin derivatives

against the botulinum neurotoxin A protease. *Bioorganic & medicinal chemistry letters* **2011,** *21* (8), 2229-2231.

286. Hirshfeld, F. L., Bonded-atom fragments for describing molecular charge densities. *Theoretica chimica acta* **1977,** *44* (2), 129-138.

287. Smondyrev, A. M.; Berkowitz, M. L., Structure of dipalmitoylphosphatidylcholine/cholesterol bilayer at low and high cholesterol concentrations: molecular dynamics simulation. *Biophysical Journal* **1999,** *77* (4), 2075-2089.

288. Rao, N.; Plant, A. L.; Silin, V.; Wight, S.; Hui, S. W., Characterization of biomimetic surfaces formed from cell membranes. *Biophysical journal* **1997,** *73* (6), 3066-3077.

289. Bolte, S.; Cordelières, F. P., A guided tour into subcellular colocalization analysis in light microscopy. *Journal of microscopy* **2006,** *224* (3), 213-232.

290. Moses, J. E.; Moorhouse, A. D., The growing applications of click chemistry. *Chemical Society Reviews* **2007,** *36* (8), 1249-1262.

291. Marquardt, D.; Kučerka, N.; Wassall, S. R.; Harroun, T. A.; Katsaras, J., Cholesterol's location in lipid bilayers. *Chemistry and Physics of Lipids* **2016,** *199*, 17-25.

292. Harroun, T. A.; Katsaras, J.; Wassall, S. R., Cholesterol hydroxyl group is found to reside in the center of a polyunsaturated lipid membrane. *Biochemistry* **2006,** *45* (4), 1227-1233.

293. Shaikh, S. R.; Cherezov, V.; Caffrey, M.; Soni, S. P.; LoCascio, D.; Stillwell, W.; Wassall, S. R., Molecular organization of cholesterol in unsaturated

phosphatidylethanolamines: X-ray diffraction and solid state 2H NMR reveal differences with phosphatidylcholines. *Journal of the American Chemical Society* **2006,** *128* (16), 5375-5383.

294. Marrink, S. J.; de Vries, A. H.; Harroun, T. A.; Katsaras, J.; Wassall, S. R., Cholesterol shows preference for the interior of polyunsaturated lipid membranes. *Journal of the American chemical society* **2008,** *130* (1), 10-11.

295. Allhusen, J. S.; Kimball, D. R.; Conboy, J. C., Structural origins of cholesterol accelerated lipid flip-flop studied by sum-frequency vibrational spectroscopy. *The Journal of Physical Chemistry B* **2016,** *120* (12), 3157-3168.

296. Rog, T.; Stimson, L. M.; Pasenkiewicz-Gierula, M.; Vattulainen, I.; Karttunen, M., Replacing the cholesterol hydroxyl group with the ketone group facilitates sterol flip-flop and promotes membrane fluidity. *The journal of physical chemistry B* **2008,** *112* (7), 1946-1952.

297. Reichardt, C.; Welton, T., *Solvents and solvent effects in organic chemistry*. John Wiley & Sons: 2011.

298. Goul, R.; Das, S.; Liu, Q.; Xin, M.; Lu, R.; Hui, R.; Wu, J. Z., Quantitative analysis of surface enhanced Raman spectroscopy of Rhodamine 6G using a composite graphene and plasmonic Au nanoparticle substrate. *Carbon* **2017,** *111*, 386-392.

299. Zhang, K.; Lu, J.; Li, J.; Zhang, D.; Gao, L.; Zhou, H., An improved approach to prepare triazole protective film by click-assembly on copper surface. *Corrosion Science* **2020,** *164*, 108352.

300. Larsson, K.; Rand, R., Detection of changes in the environment of hydrocarbon chains by Raman spectroscopy and its application to lipid-protein systems. *Biochimica et Biophysica Acta (BBA)-Lipids and Lipid Metabolism* **1973,** *326* (2), 245-255.

301. Srivastava, A.; Debnath, A., Hydration dynamics of a lipid membrane: Hydrogen bond networks and lipid-lipid associations. *The Journal of Chemical Physics* **2018,** *148* (9), 094901.

302. Hu, M.; Stanzione, F.; Sum, A. K.; Faller, R.; Deserno, M., Design principles for nanoparticles enveloped by a polymer-tethered lipid membrane. *ACS nano* **2015,** *9* (10), 9942-9954.

303. Olenick, L. L.; Troiano, J. M.; Vartanian, A.; Melby, E. S.; Mensch, A. C.; Zhang, L.; Hong, J.; Mesele, O.; Qiu, T.; Bozich, J., Lipid corona formation from nanoparticle interactions with bilayers. *Chem* **2018,** *4* (11), 2709-2723.

304. Tian, S.; Li, H.; Li, Z.; Tang, H.; Yin, M.; Chen, Y.; Wang, S.; Gao, Y.; Yang, X.; Meng, F., Polydiacetylene-based ultrastrong bioorthogonal Raman probes for targeted live-cell Raman imaging. *Nature communications* **2020,** *11* (1), 1-9.

305. Abramczyk, H.; Brozek-Pluska, B., Raman Imaging in Biochemical and Biomedical Applications. Diagnosis and Treatment of Breast Cancer. *Chemical Reviews* **2013,** *113* (8), 5766-5781.

306. Fitzpatrick, S. L.; LaChance, M. P.; Schultz, G. S., Characterization of epidermal growth factor receptor and action on human breast cancer cells in culture. *Cancer research* **1984,** *44* (8), 3442-3447.

307. Berkers, J. A.; en Henegouwen, P. v. B.; Boonstra, J., Three classes of epidermal growth factor receptors on HeLa cells. *Journal of Biological Chemistry* **1991,** *266* (2), 922-927.

308. Zhao, Y.; Hu, M.; Zhang, Y.; Liu, J.; Liu, C.; Choi, S. K.; Zhang, Z.; Song, L., Multifunctional therapeutic strategy of Ag-synergized dual-modality upconversion nanoparticles to achieve the rapid and sustained cidality of methicillin-resistant Staphylococcus aureus. *Chemical Engineering Journal* **2020,** *385*, 123980.

309. Liu, Y.; Lin, A.; Liu, J.; Chen, X.; Zhu, X.; Gong, Y.; Yuan, G.; Chen, L.; Liu, J., Enzyme-responsive mesoporous ruthenium for combined chemo-photothermal therapy of drug-resistant bacteria. *ACS applied materials & interfaces* **2019,** *11* (30), 26590-26606.

310. Nagy, A.; Harrison, A.; Sabbani, S.; Munson Jr, R. S.; Dutta, P. K.; Waldman, W. J., Silver nanoparticles embedded in zeolite membranes: release of silver ions and mechanism of antibacterial action. *International journal of nanomedicine* **2011,** *6*, 1833.

311. Hamida, R. S.; Ali, M. A.; Goda, D. A.; Khalil, M. I.; Al-Zaban, M. I., Novel biogenic silver nanoparticle-induced reactive oxygen species inhibit the biofilm formation and virulence activities of Methicillin-Resistant Staphylococcus aureus (MRSA) strain. *Frontiers in Bioengineering and Biotechnology* **2020,** *8*, 433.

CURRICULUM VITAE

[redacted]

[redacted]

[redacted]